# In-Situ Polymerization and Characterization of Polyethylene-Clay Nanocomposites

by

Sang-Young Anthony Shin

A thesis
presented to the University of Waterloo
in fulfillment of the
thesis requirements of the degree of
Doctor of Philosophy
in
Chemical Engineering

Waterloo, Ontario, Canada, 2007

# AUTHOR'S DECLARATION

I hereby declare that I am the sole author of this thesis. This is a true copy of the thesis, including any required final revisions, as accepted by my examiners.

I understand that my thesis may be made electronically available to the public.

# Abstract

Chapter 1 provides an overview of this study and a literature review. Emphasis is put on the materials used, the different processes available to synthesize polymer-clay nanocomposites, analytical methods to characterize nanophase materials and on the impact of the nanophase on the final physical properties of polymer-clay nanocomposites.

Chapter 2 discusses PE-clay nanocomposites which were synthesized using metallocene and Ni-diimine catalysts through in-situ polymerization. Morphological studies were carried out by XRD, SEM, EDX, and TEM to investigate the intercalation and exfoliation mechanism. Prior to its injection into the polymerization reactor, montmorillonite (MMT) was treated with triisobutyl aluminum and undecylenyl alcohol (UOH). Triisobutyl aluminum (TIBA) can react with hydroxyl groups on the surface of MMT and UOH is able to react with TIBA on the MMT surface. An alkoxy bond is generated by the reaction of the hydroxyl groups of UOH with the TIBA on the surface of MMT. A single site catalyst was then supported on the MMT/TIBA/UOH support, generating a MMT/TIBA/UOH/CAT system. The free vinyl groups of the surface UOH molecules can be copolymerized with ethylene, leading to the formation of chemical bonds between the MMT surface and polyethylene (PE). Ethylene polymerizations with the MMT/TIBA/UOH/CAT system were compared with ethylene polymerization with unsupported catalysts. The resulting PE-clay nanocomposites were analyzed with electronic and optical microscopes to confirm the nanophase distribution of MMT platelets in the polymer matrix. TEM images showed that the exfoliated MMT layers appeared as single layers or aggregated layers in the polyethylene matrix. After Soxhlet extraction with boiling 1,2,4-trichlorobenzene, the morphology of the residue particles remaining the thimble showed polymer fibrils stemming from the MMT surface, providing direct evidence of the chemical bonds between MMT surfaces and polymer matrix. Some residue particles also show PE-

clay hybrid fibers between the particles. Through SEM/EDX analysis, it was confirmed that the fiber's composition possessed silicone atoms together with carbon atoms.

Chapter 3 discusses the results of in-situ polymerizations in gas-phase. The same catalyst systems and polymerization conditions discussed in Chapter 2 for slurry polymerization were applied to the gas-phase polymerization in order to investigate the particle fragmentation mechanism. After gas-phase polymerization at atmospheric pressure, the surface morphologies were investigated by SEM and TEM. In the case of the MMT/TIBA/UOH/$Cp_2ZrCl_2$ system, small particles (< 10μm) were shattered from the larger particles (> 100 μm) in the early stages of polymerization. After 24-hours of continuous polymerization, polymer fibrils growing from the inside of the MMT particles were observed by SEM. After further investigation with TEM, the cross-section profile of the particles showed curved bundles of MMT platelets, which illustrates exfoliation starting from the edges of the MMT particles. The MMT/TIBA/UOH/Ni-diimine system shows a different surface morphology after polymerization. In the early stages of the polymerization, polymer films were generated from the inside of the particles. After further polymerization, the MMT particles shattered and formed aggregates of PE-clay nanocomposites, similar to the ones proposed in the multigrain model.

Chapter 4 discusses the copolymerization of ethylene and acrylonitrile. Ethylene/acrylonitrile copolymers were produced in the presence of a Ni-diimine/EASC catalyst system without the use of supports. Polymerizations of ethylene and acrylonitrile showed comparable activities in low concentrations of acrylonitrile. However, in higher concentrations, acrylonitrile induced a reductive elimination of the alkyl groups in the activated nickel-diimine catalyst. Conclusively, GPC analyses showed that acrylonitrile behaves as a chain transfer agent, showing reductive elimination of alkyl groups in the catalytic active center. The polymerization product morphology was analyzed by SEM and TEM. Polyacrylonitrile domains were observed in the polyethylene matrix and confirmed its nanosize distribution in the polyethylene matrix. DSC analysis of ethylene/acrylonitrile copolymers shows that an exothermic reaction takes place from 300 °C to

370 °C. This exotherm band detected by DSC can be related to the cyclization and aromatization of the nitrile groups of polyacrylonitrile. Through IR analysis of the ethylene and acrylonitrile polymer under high temperatures, this cyclization and aromatization was confirmed to be the cause of the decrease of the nitrile band (at 2244 $cm^{-1}$) and increase of the vinyl bands (at 1640 $cm^{-1}$). In addition, thermal treatment in DSC and successive XRD analysis showed the formation of the lamellar structures in the polyethylene matrix, reported as lamellar formation of polyacrylonitrile due to cyclization and aromatization of nitrile groups. The decomposition temperatures measured by TGA increased up to 50 °C due to the presence of the nitrile groups in the polymer matrix. Tensile testing showed that the modulus increased, together with the yield strength and elongation. This phenomenon supports that strong interfacial interactions exist between the polyethylene matrix and polyacrylonitrile domains, as confirmed by TEM and IR analysis.

Chapter 5 introduces the idea of acrylonitrile as a clay surface modifier. MMT was treated with acrylonitrile, using the same modification method of MMT that was applied in the MMT/TIBA/UOH/CAT system in Chapter 2. The nitrile groups in PE-MMT/TIBA/AN/CAT composites were confirmed at 2244 $cm^{-1}$ by IR analysis. DSC analysis of PE-MMT/TIBA/AN/CAT showed that an exothermic reaction takes place from 300 °C to 375 °C. Successive DSC analysis with the same sample showed a new glass transition temperature band, induced by the reduction of polymer chain mobility. The basal diffraction band disappeared due to the exfoliation of MMT. Tensile tests showed an increase in modulus, without sacrificing the yield strength and elongation of PE-clay hybrid composites. Through these analyses, it was confirmed that strong interfacial forces exist between the polyethylene matrix and MMT layers in these PE-clay nanocomposites.

# Acknowledgements

I would like to extend a big 'thank-you' to my supervisor Dr. Soares for providing me with a plethora of conveniences to start my career as a PhD student at the University of Waterloo. I cannot emphasize the importance of his involvement in my graduate career. In addition, I would like to gratefully acknowledge the enthusiastic supervision of Dr. Simon during the past five years. Dr. Simon was also an excellent supervisor who truly helped me through five years of amazing research work. My overwhelming thanks go out to Dr. Simon. This thesis grew out of a series of remarkable conversations with these supervisors, all of which brought me closer to the reality that I had initially perceived. I would also like to specially thank Professor Günter Scholz for his kind guidance and assistance on X-ray diffraction and transmittance electron microscope analysis. I also would like to acknowledge the support provided by Prof. Timothy McKenna, who gladly allowed me to use his lab facilities without any charge and provided valuable insight regarding the operation of the turbosphere reactor.

They made the experience of being a graduate student very fulfilling by always encouraging my everyday work, by exposing me to different aspects of academia, by supporting my broad interests and every little progress, and by countless other little things that I cannot put into words. I am forever indebted for their guidance and encouragement.

Many thanks to my lab colleagues, William Ripmeester, Deborah Sarzotti, and Aaron Law for providing me with excellent technical support on GPC, TGA and DSC. They never hesitated to offer their full assistance, for which I am extremely grateful.

In particular, thanks Andrea Schoeller for helping me with my thesis revision.

Last, but not least, heartfelt thanks go out to my family, whose steadfast support was the driving force behind the completion of this thesis.

# Dedication

This thesis belongs to my wife, Geumhee Lee, and my sons Hyun Wook and Hyun June for their trust in me as a husband and a father. My wife Geumhee Lee inspired and encouraged me to get to this point - a part of this thesis belongs to all of you.

Finally, I would like to dedicate this thesis to my parents, late Daeil Shin, Youngja Lee, Jongho Lee and Taeok Yoon, who helped me embrace my research at Waterloo. To all of you, I extend my sincerest appreciation.

# Table of Contents

# List of Figures

# List of Tables

# Nomenclature

| | |
|---|---|
| 24 HP | Polymerization for 24 hours |
| 3 HP | Polymerization for 3 hours |
| AN | Acrylonitrile |
| ASTM | American Standards Testing Method |
| ATR | Attenuated total reflectance |
| ATRP | Atom transfer free-radical polymerization |
| CEC | Cation exchange capacity |
| Cp | Cyclopentadienyl |
| $Cp_2ZrCl_2$ | Cyclopentadienyl zirconium dichloride |
| DCP | Direct current plasma-atomic emission |
| DSC | Differential scanning calorimetry |
| EASC | Ethyl aluminum sesquichloride |
| EDX | Energy dispersive X-ray spectroscopy |
| FT-IR | Fourier transform infrared spectroscopy |
| GPC | Gel permeation chromatography |
| MAO | Methylaluminoxane |
| MMT/TIBA | Montmorillonite modified with triisobutylaluminum |
| MMT/TIBA/UOH | Montmorillonite modified with triisobutylaluminum and 10-undecene-1-ol |
| MMT/TIBA/UOH/CAT | Montmorillonite modified with triisobutylaluminum, 10-undecene-1-ol and catalyst |
| MMT/TIBA/UOH/Pex | Polyethylene extracted from PE-clay nanocomposites by Soxhlet extraction |
| MMT | Montmorillonite |

| | |
|---|---|
| MW | Molecular Weight |
| MWD | Molecular weight distribution |
| Ni-diimine | (1,4-bis(2,6-diisopropylphenyl)-acenaphthenediimine) dichloro nickel |
| NMR | Nuclear magnetic resonance |
| PAN | Polyacrylonitrile |
| PDI | Polydispersity index |
| PE | Polyethylene |
| PEex | Polyethylene extracted from PE-clay nanocomposites by Soxhlet extraction |
| PE-MMT/TIBA/UOH/CAT | PE-clay nanocomposite made by MMT/TIBA/UOH/CAT |
| PET | Polyethylene terephthalate |
| SAX | Small angle X-Ray crystallography |
| SEM | Scanning electron microscopy |
| SMAO | Silica-supported methylaluminoxane |
| TCB | 1,2,4-Trichlorobenzene |
| TEA | Triethylaluminum |
| TEM | Transmission electron microscopy |
| TGA | Thermal gravimetric analysis |
| TIBA | Triisobutylaluminum |
| $T_m$ | Melting temperature |
| TMA | Trimethylaluminum |
| UOH | 10-undecene-1-ol |
| WAX | Wide angle X-ray crystallography |
| XRD | X-ray diffraction |

| | |
|---|---|
| Z-N | Ziegler-Natta |

# Chapter 1
# Introduction

## 1.1 Overview

The term *nanocomposite* defines a composite in which one substance is dispersed in another one and one of the phases has at least one dimension smaller than 100 nm (Giannelis, 1996). Polymer nanocomposites are commonly based on polymer matrices reinforced with nanosize fillers such as silica, metal oxides (Motomatsu, 1997), zeolites (Frisch et al., 1996), and clay (Pinnavaia et al., 2000), as well as colloidal dispersions of rigid polymers (Ruckenstein et al., 1997). Among the nanosize fillers, clay has been studied for several decades because of its several advantages such as enhanced gas barrier properties, reduced flammability, lower coefficient of thermal expansion, and higher UV resistance.

In the early eighties, researchers at Toyota discovered how to produce nanostructures based on polyamide-6 and montmorillonite (MMT) modified with ammonium cations (Okada et al., 1990). These products showed significant improvements in mechanical properties (tensile strength and modulus) and heat distortion temperature without a loss in impact resistance. All of these property improvements were attributed to the distribution of nanosize MMT particles in the polyamide matrix (Theng, 1979).

Figure 1-1 shows how the clay particle distribution within the polymer matrix is used to classify polymer-clay composites: (a) *aggregated structures* have clay distributed in the micrometer scale acting as a conventional filler; (b) *intercalated nanocomposites* consists of a regular insertion of the polymer chains between the clay layers; and (c) *exfoliated nanocomposites* have 1 nm-thick clay layers dispersed homogeneously throughout the polymer matrix. Morphologies (b) and (c) are considered nanocomposites of particular interest because they enhance polymer-clay interactions due to the larger surface area of the clay layers, as compared to conventional composites of type (a).

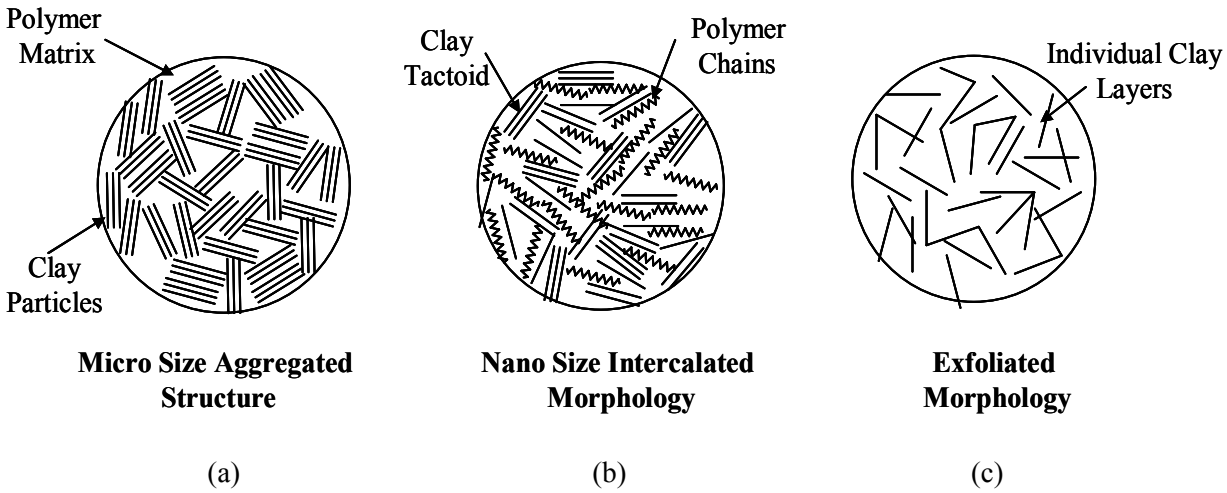


**Figure 1-1.** The three idealized polymer-clay composite structures.

In certain clays, like MMT, the surface of individual layers is charged and naturally occurring ions balance out the charge between two layers, thus keeping these layers together. The surface of layered clays is naturally hydrophilic. In their natural stage they are poorly suited for mixing with hydrophobic polymers, which causes phase separation between clay and polymer leading to structures of type (a) in Figure 1-1. Treatment of clays with organic compounds prior to the preparation of the polymer-clay nanocomposites is necessary to improve the compatibility between both phases.

Therefore, making a nanocomposite out of the untreated clay would result in poor interaction between the hydrophobic polyolefin matrix and the hydrophilic surface of layered clays. In the case of polyolefin-MMT nanocomposites, the enhancement in physical properties has been reported to be lower than those of clay nanocomposites prepared with polar polymers, such as polyamide-6/MMT nanocomposites (Okada et al., 1990).

We propose a novel methodology for the preparation of polyethylene-clay nanocomposites using in situ polymerization in this thesis. In this method, polyethylene chains are polymerized in the presence of organically modified montmorillonite. Several strategies will be considered to improve

the dispersion of clay at the nanoscale and to increase the surface interaction between polyethylene and MMT.

Chapter 1 provides an overview of this study and reviews the relevant previous literature in the area. Emphasis is put on the materials used, the different processes available to synthesize polymer-clay nanocomposites, the analytical methods used to characterize nanophase materials, and the impact of the nanophase on the final physical properties of polymer-clay nanocomposites

## 1.2 Clays

The purpose of this section is to describe the characteristics and properties of natural clay and its crystal structure. Montmorillonite (MMT) was selected among smectite natural clays for the preparation of polyolefin-clay nanocomposites in this study.

### 1.2.1. Clay Groups

Clays have layered silicate structures and can be divided into two groups: smectites and illites. Smectite clays are composed of units made up of two silica tetrahedral sheets with a central alumina octahedral sheet. Illite clays are composed of one silica tetrahedral sheet and one octahedral sheet. This classification determines the feasibility for intercalation and exfoliation of platelets because of different levels of electrostatic interaction between the cationic species and the anionic-charged surfaces of clay plates. Illite clays, such as mica and bentonite, cannot be exfoliated, whereas smectite clays, such as MMT or synthetic layered clays like fluorohectorite (Kaviratna et al., 1996; de Silva et al., 2002), can be exfoliated. Because they can be exfoliated, smectite clays have been explored as the major materials for the synthesis of polymer-clay nanocomposites.

Considerable work on the structure of clays and the feasibility for intercalation (addition of ions, molecules or atoms between the layers) was done using X-ray diffraction methods simply by hydration of the clay (intercalation of water) in order to assign basal plane diffraction bands. Natural

clays exist together and form mixtures of several clays because of natural crystallization mechanisms. In the case of MMT, there are several impurities that can be observed in X-ray diffractograms.

### 1.2.2. MMT Crystal Structure

The MMT three-layered crystal structure is composed of two tetrahedral silica outer layers separated by one octahedral alumina layer, as illustrated in Figure 1-2. Many of these layers are stacked on top of one another to form larger crystals. This structure is called a *tactoid*. Isomorphous substitutions of $Si^{+4}$ with $Al^{+3}$ in the tetrahedral layer, and of $Al^{+3}$ with $Mg^{+2}$ in the octahedral layer, cause an excess of negative charges within the MMT layers. These negative charges are counterbalanced by cations such as calcium ($Ca^{+2}$), sodium ($Na^{+}$), magnesium ($Mg^{+2}$), copper ($Cu^{+2}$), iron ($Fe^{+2}$), and other positively charged ions. While these ions are in the space between the crystalline layers, they are not specifically bonded to the crystalline surface; they form a positively charged layer between the negatively charged surfaces of MMT platelets. Water molecules are usually also present between the MMT platelets. Stacking of the layers leads to regular van der Waals gaps called *interlayers* or *galleries*. The sum of the single platelets thickness (9.6 Å) and the interlayer gap represents the repeat unit in this multilayer material, also known as *d-spacing* or *basal spacing*. This is calculated from the (001) harmonics obtained from X-ray diffraction patterns. The d-spacing between platelets (the silica-alumina-silica units) for Na-MMT varies from 9.6 Å in the collapsed state to 20 Å when the clay is dispersed in water (Mering, 1946).

.

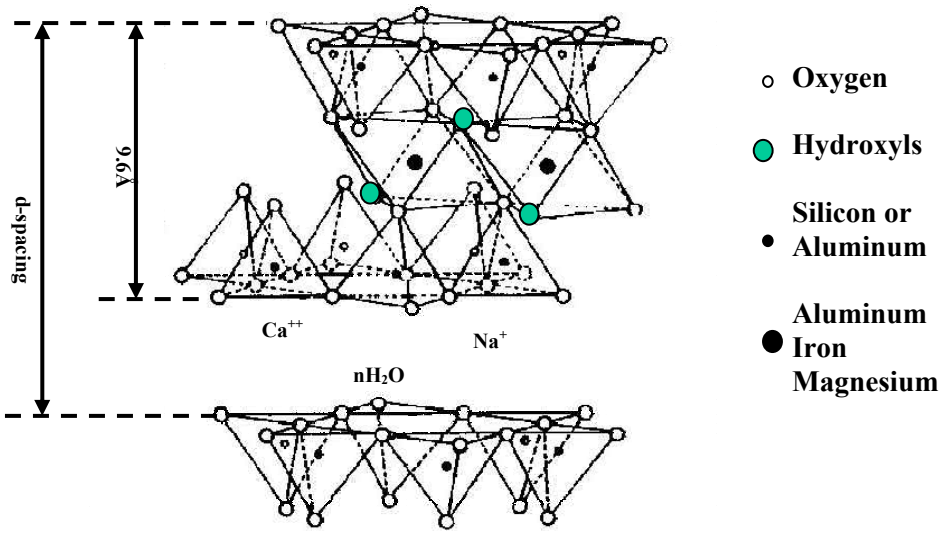


**Figure 1-2.** Idealized structure for MMT proposed by Hoffmann, Endell and Wilm (Brindley al., 1980), showing the (001) plane of the plate which consists of two tetrahedral sheets fused to one octahedral sheet. The black dots indicate the locations of isomorphous substitutions in the octahedral and tetrahedral sites, respectively.

### 1.2.3. Location of Hydroxyl Groups in MMT

The location and concentration of hydroxyl groups is important because hydroxyl group modification is commonly used for in-situ polymerization with homogeneous catalysts. Figure 1-3 (a) illustrates the porous surface structure of MMT. Through this model of the (100) plane of MMT, the location of the hydroxyl groups is shown at the edge of the hexagonal units covered with six tetrahedral silicone cages. The detailed structure is expanded in Figure 1-3 (b). Most –OH groups are buried within the layered framework. The small number of –OH groups located on the edge of the layers are more accessible for chemical modification of the clay platelets.

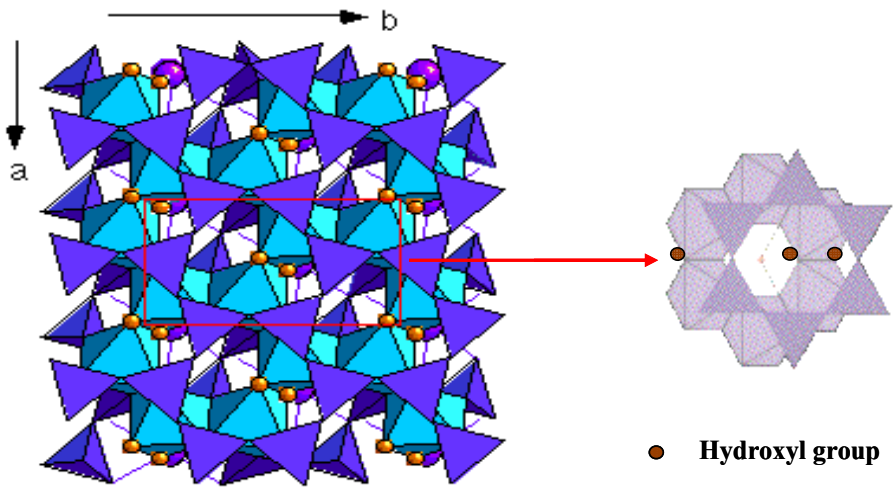


(a) (b)

**Figure 1-3**. Structure of MMT surface ((100) plane): Hydroxyl groups (brown circles) are located in the octahedral units inside or outside the hexagon of silicone tetrahedrons (http://www.geoclassroom.com/mineralogy/ phyllosilicates.html).

The surface modification of silica with alkyl aluminum compounds is a well known method for evaluating the population of the silanol groups on the silica surfaces. Triisobutylaluminum in heptane solution was used by Liefländer and Stöber (1960) to react with surface silanol groups, as shown in Figure 1-4. After thorough washing with heptane to remove excess reagent, the surface retained 5.7 micromoles of Al after dehydrolysis in TGA.

$$Si_8OH + AlR_3 \xrightarrow{-RH} Si_8OAlR_2 \xrightarrow{+H_2O} Si_8OAl(OH)_2 + 2\,RH$$

**Figure 1-4**. Theoretical chemical reaction on the surface of silica (Iler, 1979).

This technique has been applied to support metallocene catalyst on silica surfaces after treatment with alkyl aluminums. Modification of the MMT surface with alkyl aluminum compounds has also been reported for supporting metallocene catalysts (Ferreira et. al., 2000).

A similar technique was reported for supporting metallocene catalysts on MMT. Prior to the alkyl aluminum reactions with the MMT surface, MMT was treated with HCl or $H_2SO_4$ (Weiss et. al., 2002). This process dissolves part of the aluminum octahedral structures between the two insoluble silicate layers.

### 1.2.4. MMT Layered Structure

On a larger scale, each MMT layer can be seen as a high aspect ratio lamella about 100-200 nm in length/width (the natural structures are irregular) and 1 nm in thickness, as shown in Figure 1-5 (Kornmann, 2001). The grey circles in the primary particle represent the intercalated cations ($Na^+$,$Ca^{2+}$, $K^+$) (Mathieu-Sicaud et al., 1951) and the lines represent the individual layers. Five to ten crystalline layers are associated by interlayer ions to form a *primary particle* (8-10 nm in the "transverse" direction) (Mathieu-Sicaud et al., 1951) which, in turn, get together to form larger irregular aggregates (0.1-10 μm in diameter), giving the clay its aggregate structure (Sides et al., 1971). The primary particles are also called tactoids.

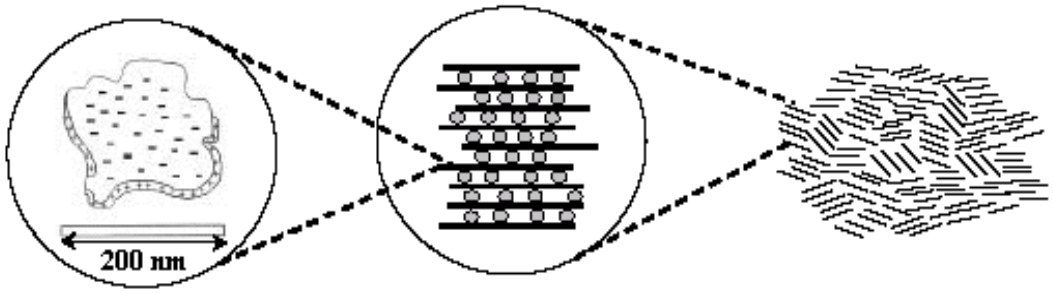


| Lamella | Primary particle | Aggregate |
|---|---|---|
| (1 nm) | (8 ~ 10 nm) | (0.1 ~ 10 μm) |

**Figure 1-5.** Model for the morphology of MMT (Kornmann, 2001; Akelah, et al., 1994).

A characteristic feature of MMT is its ability to absorb and retain certain cations reversibly. These intercalated cations can be exchanged by treatment with other cations in solution. Recently, several kinds of exchangeable cations, from alkali earth metal to organic cations, were reported. Figure 1-6 shows the equilibrium between $Na^+$ cations in MMT with quaternary alkyl ammonium cations, $NH_{(4-x)}R_x^+$ (H= hydrogen, R=alkyl groups, $1 \leq x \leq 4$) in electrolytes. Depending on the layer charge density of the clay, the alkylammonium ions adopt different configurations between the clay layers: monolayers, bilayers, pseudo-trimolecular layers, or paraffin type monolayers (Lagaly, 1986).

In Figure 1-6, the alkylammonium ions adopt a paraffin-type configuration and the spacing between the clay layers increases over 10 Å; this process is called *intercalation*. As indicated, this reaction is in dynamic equilibrium and the extent to which the reaction proceeds from the left to the right depends on the nature of the cations, on their relative concentrations, and often on secondary hydration reactions (Pinnavaia, 1983). In Figure 1-6, the equilibrium of the reaction can be shifted to the right by increasing the concentration of the added $NH_{(4-x)}R_x^+$ cation (Khalil et. al., 2005; Worall, 1968).

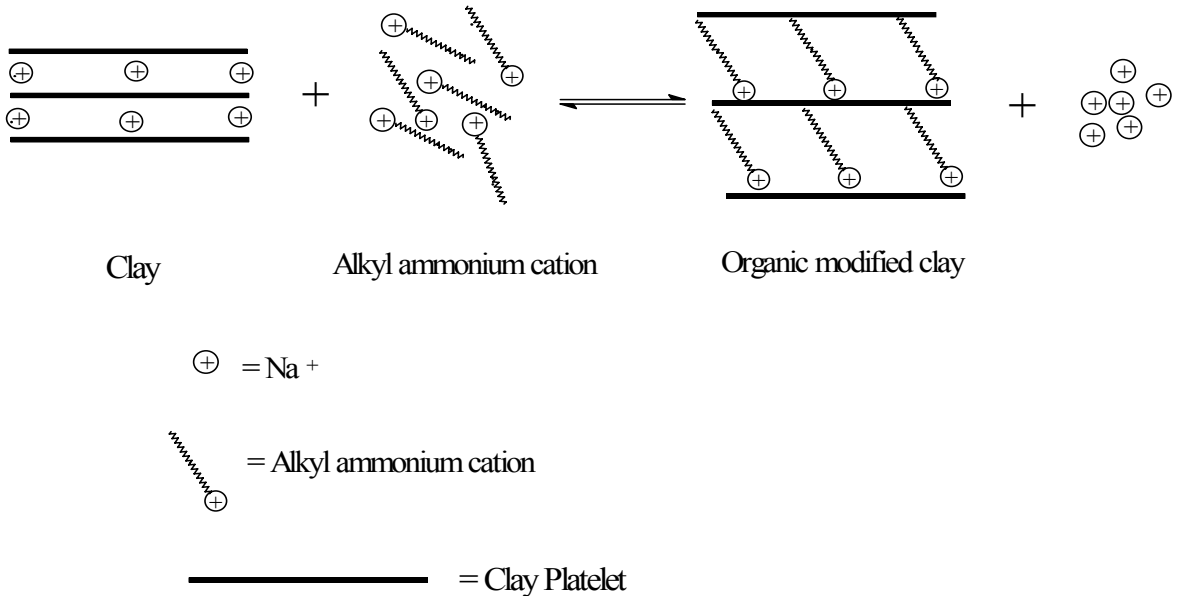


**Figure 1-6.** Cation exchange between sodium cations in MMT and quaternary alkyl ammonium cations in an electrolyte (Khalil et. al., 2005).

For a given clay, the maximum amount of cations that can be taken up is constant and known as the *cation-exchange capacity* (CEC). However, determination of the CEC is considered inaccurate. The measurement is generally made by saturating the clay with $NH_4^+$ or $Ba^{2+}$ ions and determining the amount held at pH 7 by conductmetric titration (Busenberg et al., 1973). Another method consists in saturating the clay with alkylammonium ions and evaluating the quantity of ions intercalated by combustion of the sample (McAtee, 1959). The result is measured in milliequivalents per gram (meq/g) or more frequently per 100g (meq/100g). Although the convention is to use meq/g units, the CEC can also be reported as electrical charge per unit mass. In SI units, it is expressed in coulombs per unit mass, /g. A CEC of 1 meq/g is equivalent to 96.5 C/g in SI units. The CEC of MMT varies from 80 to 150 meq/100g.

### 1.2.5. Molecular Orientation in the Clay Galleries

Organic modification can be used to improve the affinity between polymer and clay. Together with CEC, the orientation of organic molecules in the clay galleries is an important parameter when synthesizing polymer-clay nanocomposites. The shape or orientation of molecules within the galleries is directly related to the d-spacing of the galleries, also interpreted as intercalation or exfoliation of the composite materials.

Structural characterization has been used to determine the orientation and arrangement of the alkyl chains based on X-ray diffraction and FT-IR analysis. The orientation of the tetraalkylammonium compound ($N(R_3)_4^+$ where R = alkyl, hydrocarbon chain) was suggested by the increase of the d-spacing of the clay, depending on the packing density, temperature and chain length. The hydrocarbon chains of tetraalkylammonium are thought to lie either parallel to the clay layers, forming lateral mono- or bilayers, or to radiate away from the surface, forming extended (paraffin-type) mono- or bimolecular arrangements (Lagaly, 1981; Largaly, 1986; Weiss, 1963; Vaia et al., 1994).

In the case of aromatic compounds, benzene rings assumed several different orientations between clay lamellae, depending on the orientation of the benzene rings to the (001) axis of clay crystal. Three types of orientation have been reported: type A, perpendicular to the (001) axis; type B, parallel to the (001) axis; and type C, tilted to the (001) plane. Generally, it has been known that type B orientation occurs at a higher concentration of the organic compounds in the clay lamellae. Type A orientation has a d-spacing of 1.25 nm, type B has a d-spacing of 1.5-1.54 nm and type C, tilted to the (001) plane, has a d-spacing of 1.44nm (Lagaly et al., 1975; Khalil et al., 2005).

## 1.3. Coordination Catalysts

In this section, the catalyst systems used for olefin polymerization will be introduced. Several single-site catalysts used to make polyethylene and polypropylene are soluble in the polymerization medium. These catalysts can be immobilized on inorganic substrates (silica or magnesia, for example) producing a heterogeneous catalyst. One of the key advantages of the heterogeneous system is the easy recovery of the products.

### 1.3.1. Metallocene Catalysts

Several metallocene and other single-site catalysts have been developed since the early 1980's (Kaminsky et al., 1985). Among them, metallocene catalysts have been extensively studied due to their high activity, and ability to produce polyolefins with controlled molecular weight distribution (MWD), uniform chemical composition distribution (CCD) (Zambelli et al., 1986; Chien, et al., 1991; Uozumi et al., 1992; Tsutsui et al., 1988), and high stereospecificity (Coates, 2000). Moreover, single-site catalysts are based on relatively stable metal complexes that can be easily stored and handled in inert atmospheres.

The general structure of a metallocene catalyst precursor is illustrated in Figure 1-7.a. The metal center is bonded to two cyclopentadienyl anions in a $\pi$- or $\eta^5$-mode. Furthermore, the carbon atoms of the cyclopentadienyl-type ligands can bear substituents other than hydrogen, namely alkyl,

aryl or silyl groups. The cyclopentadienyl-type ligands can be linked by one or more atoms to yield complexes that are commonly referred to as *ansa*-metallocenes. Among metallocene catalysts, the majority used for the polymerization of olefins comprises transition metal complexes of group 4 (Ti, Zr, Hf).

Once the catalyst precursor is activated with a cocatalyst, usually methylaluminoxane (MAO), it can polymerize olefin monomers. Generation of an active site requires a reaction between one or both of the σ-bonded ligands of the metallocene catalyst precursor and the cocatalyst, resulting in a species containing a vacant site capable of coordinating an olefin and a ligand adjacent to the vacant site into which the olefin can be inserted, usually an alkyl or hydride substituent (Figure 1-7. b). The cocatalyst is often a strong Lewis acid (most often an alkyl aluminum or aluminoxane), which by abstracting an anion (halide ion) from the catalytic complex, leaves it not only with a vacant site, but also with a highly Lewis acidic, cationic metal centre, that has an affinity for nucleophilic olefins.

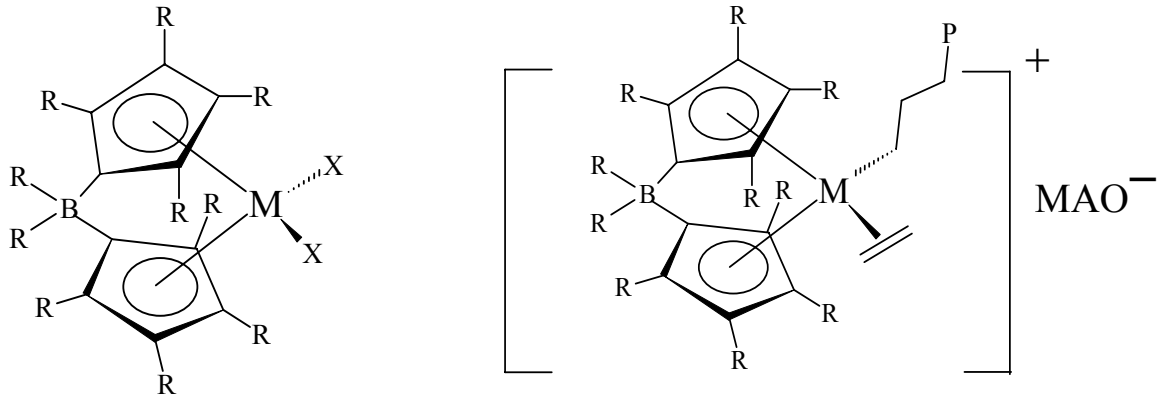


(a) (b)

**Figure 1-7.** (a) Generalized structure of a metallocene catalyst; (b) Schematic diagram of a cationic metallocene active site with olefin coordinated to the metal center and growing polymer chain bonded to the metal center. The counter ion stabilizes the charge. (M: transition metal center, X: halogen, R: alkyl or aromatic ligand, B: bridging group, P: polymer chain, $MAO^-$: counter anion based on methylalumoxane).

MAO, produced by the controlled hydrolysis of trimethylaluminum (TMA), is the most widely used cocatalyst. Although the mechanism of catalyst activation by MAO is not entirely clear yet, the accepted mechanism of active site formation is shown schematically in Figure 1-8.

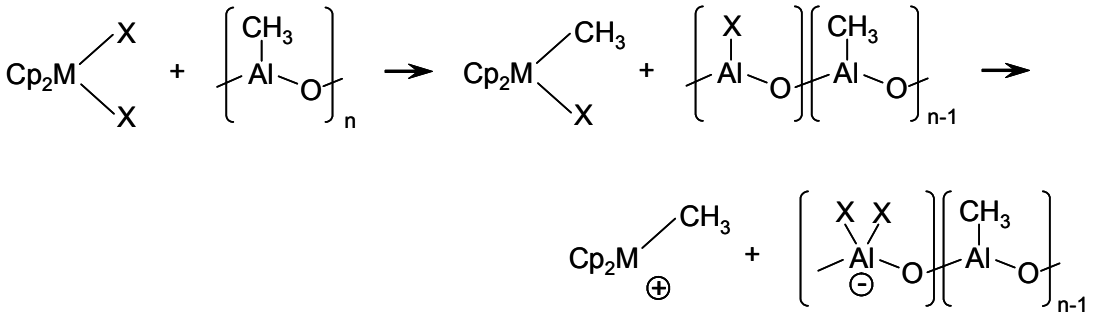


**Figure 1-8.** Accepted mechanism for active site formation with MAO (Resconi et al., 2000).

### 1.3.2. Non-Metallocene Catalysts

Since the mid 1990's, catalysts based on non-cyclopentadienyl ligands have received much attention as the next generation of coordination catalysts for olefin polymerization (Johnson et al., 1995; Johnson et al., 1996; Killian et al., 1996; Mecking et al., 1998). Late transition metal catalysts are particularly attractive because of their additional tolerance to heteroatom functionalities. Under appropriate conditions, they can copolymerize olefins (ethylene, propylene) and polar comonomers (vinyl alcohol, acrylates). Catalysts developed by Brookhart and coworkers, consisting of a late transition metal such as nickel (II) or palladium (II) and a bulky diimine ligand, are examples of late transition metal catalysts that yield high molecular weight polyolefins with unique microstructures (Johnson et al., 1995). Figure 1-9 shows two typical examples of these catalysts. Because of the bulky aryl groups on the diimine ligand, the rates of associative displacement and chain transfer are greatly diminished and substantially longer chains are produced on ethylene polymerizations. On the other hand, diimido ligands without bulky aryl groups are known for the oligomerization of olefins.

This catalyst system produces a wide range of materials from highly branched amorphous polyethylene (70 branches per 1000 carbon atoms) to linear semicrystalline high-density polyolefins by simply varying polymerization temperature, ethylene pressure, and ligand architecture. This capacity to produce short chain branches without addition of α-olefins is attributed to the *chain-walking* mechanism (Johnson et al., 1995; Simon et al., 2001). During polymerization, the active site undergoes position isomerization, moving from the end of the growing polymer chain and performing a random-walk on the chain backbone. After this change in position, the addition of ethylene to the chain and subsequent growth creates a branch.

These catalysts can also copolymerize functionalized vinyl monomers with α-olefins and are less sensitive to poisons (oxygen, water or other electron donor groups) than Ziegler-Natta and metallocene catalysts. This tolerance to functionalized vinyl monomers makes late transition metal catalysts very attractive for producing polyolefins containing heteroatoms.

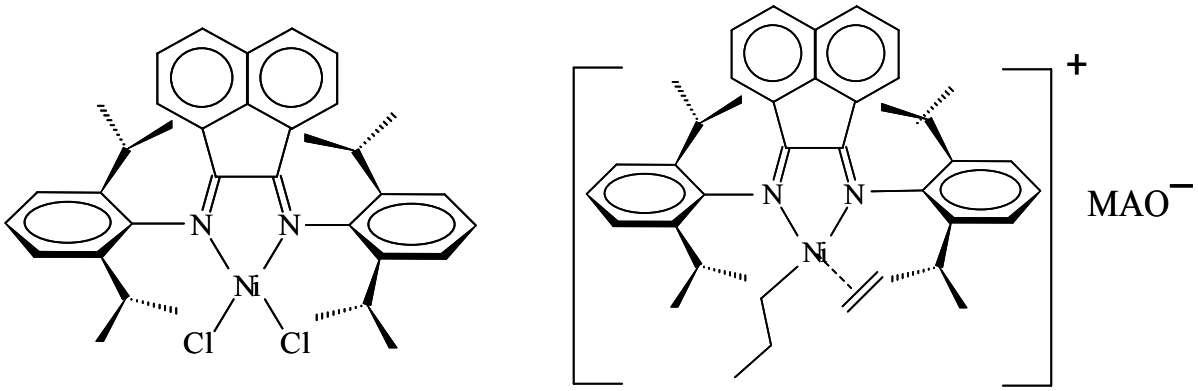


(a) (b)

**Figure 1-9.** Examples of late transition metal catalysts: (a)1,4-bis(2,6-diisopropylphenyl)-acenaphthenediimine-dichloronickel (II); (b) a schematic of a nickel catalyst active site.

## 1.4. Copolymerization of Ethylene with Polar Vinyl Monomers

Polar vinyl monomers are good candidates as surface modifiers for MMT. The polar group can be chemically bonded to the surface of clay and the vinyl group can be copolymerized with ethylene through in-situ polymerization. Homogeneous catalysts for the copolymerization of ethylene with 10-undecen-1-ol has already been studied and reported by other groups (Marques et. al., 1999).

### 1.4.1. Copolymerization of Ethylene with 10-undecen-1-ol

Polyolefins with functional groups along their backbone are of great interest because of their many desirable properties such as toughness, adhesion, barrier properties, paintability, printability, solvent resistance, and miscibility with other polar polymers (Boffa and Novak, 2000). Unfortunately, since Ziegler-Natta catalysts are highly oxophilic, they are easily inhibited by oxygen-containing functionalities in the monomer. However, metallocene catalyst based on Ti, Zr and Hf can tolerate functional monomers if the oxo or hydroxyl groups are protected with alkyl aluminum complexes (Marques et al., 1999). It is also known that an alkyl chain spacer between the polar group and the vinyl double bond has a beneficial influence on polar comonomer incorporation and catalyst activity (Boffa and Novak, 2000).

On the other hand, the cationic nickel or palladium α-diimine complexes are remarkably functional-group tolerant. Ethylene polymerizations with polar monomers, such as ethers, organic esters and acids, have been reported in the literature (Johnson et al., 1995; Johnson et al., 1996).

### 1.4.2. Copolymerization of Ethylene with Acrylonitrile

It has been reported that copolymers of acrylonitrile can be obtained from the copolymerization of polar monomers such as acrylate, methyl acrylate or methyl methacrylate by free radical polymerization (Gridnev et al., 2001; Li et al., 2006). The copolymerization of olefins, styrene and acrylonitrile were successfully achieved through atom transfer radical polymerization (Matyjaszewski et al., 2001). These types of copolymers, containing blocks or random acrylonitrile units, can be used

to manufacture fibers to make knitted clothing, such as socks and sweaters, as well as outdoor products like tents.

On the other hand, many research groups have tried to copolymerize olefins and acrylonitrile with transition metal catalysts. The goal to develop a new method to synthesize copolymers of ethylene and acrylonitrile is still highly desirable because of the physical properties of the final products: the brittleness of polyacrylonitrile and the ductility of polyolefins. Unfortunately, there has been no report containing successful experimental results for the copolymerization of ethylene and acrylonitrile with coordination catalysts.

## 1.5. Modification of Clay Surface and its Intercalation

Clays do not disperse well in polyolefins, unless a compatibilizing agent is present. There are two possible strategies: a) to chemically-modify the polyolefin with functional groups; or b) to modify the inorganic clay with surfactant-like quaternary ammonium salts. Compatibilizers usually have bifunctionality: the hydrophobic "tail" has affinity for polyolefins, while the hydrophilic "head" has affinity for the ionic inorganic species at the clay surface.

The first compatibilizing agents used in the synthesis of nylon nanocomposites (polyamide-6-clay hybrids) were amino acids (Laus et al., 1998). Since then, several other kinds of compatibilizing agents have been. The most popular ones are alkylammonium ions because they can be exchanged easily with the cations situated between the clay layers. Silanes have also been used because of their ability to react with the hydroxyl groups located at the clay surface and at the edges of the clay layers (Weimer et al., 1999). MMT exchanged with long chain alkylammonium ions can be dispersed in polar organic liquids forming a suspension with high liquid content. This property was first discovered by Jordan (Jordan, 1949) and summarized later by Weiss (Weiss, 1963). Alkylammonium ions can be intercalated easily between the clay layers and offer a good alternative to amino acids for the synthesis of nanocomposites based on polyamide-6.

The most widely used alkylammonium ions are primary alkylamines treated in acidic medium to protonate the amine function. Their basic formula is $CH_3$-$(CH_2)_n$-$NR_3^+$ where n is between 1 and 18 and R is any hydrocarbon. It is interesting to note that the length of the ammonium ions has a strong impact on the resulting nanocomposite structures. Lan and coworkers (Lan et al., 1995) showed that alkylammonium ions with chain length longer than eight carbon atoms produced exfoliated nanocomposites, whereas alkylammonium ions with shorter chains made intercalated nanocomposites. Alkylammonium ions based on secondary amines have also been used to produce nanocomposites (Wang et al., 1998). The cation-exchange process with linear alkylammonium ions has already been depicted in Figure 1-6.

Other compatibilizing agents have recently been introduced to synthesize polymer-clay hybrid nanocomposites because they can either participate directly in the polymerization process or initiate it. For example, polystyrene-clay nanocomposites have been prepared with aminomethyl-styrene (Laus et al., 1998). A detailed review gives further information about other methods for organic modification of clays or suitable compatibilizing agents for the synthesis of nanocomposites (Ogawa et al., 1997).

## 1.6. Methods for Manufacturing Polymer-Clay Nanocomposites

The two general methods for the preparation of polymer-clay nanocomposites are: (a) melt compounding; and (b) in-situ polymerization.

Since melt intercalation process was first introduced by Vaia and his colleagues, it has become a mainstream in the preparation of intercalated polymer nanocomposites (Vaia, et al., 1993, 1996). The melt intercalation process involves mixing clay with the polymer and heating the mixture above the softening point of the polymers, as described in Figure 1-10.

The proposed driving force for this mechanism is the enthalpic contribution of the polymer-organic clay interaction during the blending and annealing steps. Polymer chains can undergo center of mass transport between the clay layers; note that the radius of gyration of the polymer is roughly

an order of magnitude greater than the basal spacing. For the more precise relationship between shear force and basal distance between clay platelets, Rheometric study combined with XRD analysis was reported. To increase the uniformity of the layer distribution in the polymer matrix, it needs appropriate shear force and basal distance (Busmina, 2006).

A wide range of thermoplastics, from polyamide 6 (Chow, et al., 2003; Lui, et al., 1999) to polystyrene (Vaia, et al., 1996) have been melt-intercalated between clay layers. However, a partly intercalated and partly exfoliated structure has been usually obtained by melt mixing. Also, the collapsed structure of the clay galleries was reported by the degradation of modifiers in the galleries. It might be due to the spot generations during melt processing in the barrel. Clays in polyolefins, which represent the largest volume of polymer nanocomposites produced, have not been intercalated very successfully by this approach so far (Kawasumi et al., 1997).

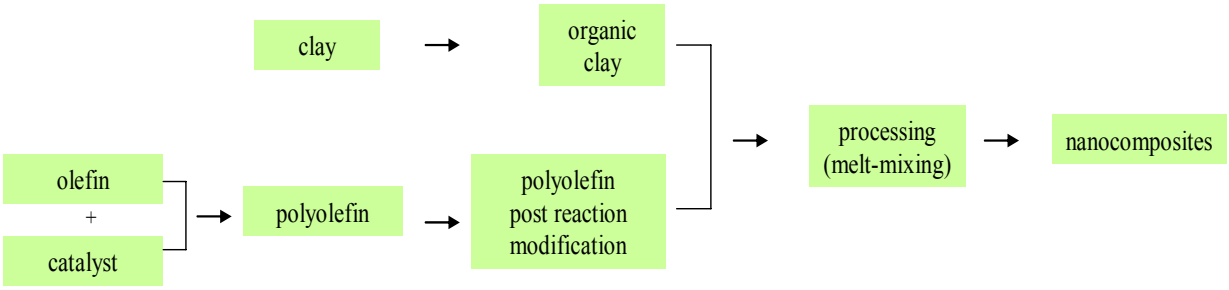


**Figure 1-10.** Flow diagram of the melt compounding method for the production of polyolefin-clay nanocomposites.

The first step for in-situ polymerization is to swell the organoclay with the monomer. This step requires a certain amount of time, which depends on the polarity of the monomer molecules, the surface treatment of the organoclay, and the swelling temperature. After swelling, the polymerization is initiated. The key is to control the polymerization occurring between the layers (intragallery polymerization), so that exfoliation of the clay takes place effectively. Therefore, one needs to find

ways to favor the intragallery polymerization as compared with the extragallery polymerization (Tudor et al., 1996). In-situ polymerization is described in Figure 1-11.

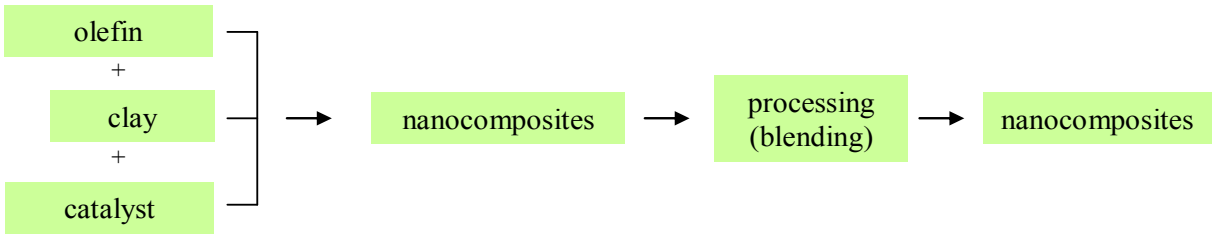


**Figure 1-11.** Flow diagram of the in-situ polymerization process for the production of polyolefin-clay nanocomposites.

Figure 1-12 shows how $TiCl_4$ can be supported within the galleries of MMT modified with hydroxyl ammonium ions (Jin et al., 2002). After reaction of $TiCl_4$ with the hydroxyl groups on the clay surface and in-situ polymerization with ethylene, the layered clays were fully exfoliated and distributed in the polymer matrix. It was recently reported that the polymerization of olefins using MAO-activated transition-metal catalysts incorporated between clay layers caused their exfoliation. According to the literature, the dispersion of clay obtained using the in-situ polymerization method showed better nanosize exfoliation than that produced with the melt intercalation method (Usuki et al, 1997; Kato et al., 1997; Hasegawa et al., 1998; Kawasumi et al., 1997; Heinemann et al., 1999).

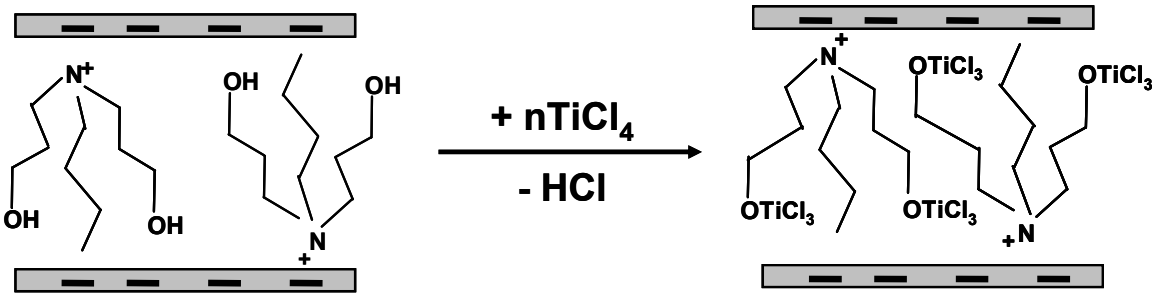


**Figure 1-12.** $TiCl_4$ supporting in the galleries of modified MMT layers (Jin et al., 2002).

## 1.7. Characterization of Polymer-Clay Nanocomposites

Two main techniques are used to characterize the morphology and exfoliation of polymer-clay nanocomposites. The most straightforward one is X-ray diffraction (XRD) because it can measure the spacing between the clay layers at the nanoscale and, therefore, quantify the exfoliation process. Transmission electron microscopy (TEM) gives a direct measurement of the spatial distribution of the layers, but requires substantial skill to prepare and analyze the nanocomposite specimens. Other techniques relevant to this project are related to the characterization of the microstructure and morphology of polymer particles, and testing of thermal and mechanical properties of polymer samples.

### 1.7.1. X-Ray Diffraction (XRD)

The XRD patterns of clay samples give information on their crystallographic structures (Brindley et. al, 1980; Wang et al., 1993). Some concepts must be introduced in this section to clarify how X-rays can be used to define the structure of PE-clay nanocomposites.

Crystalline structures are described by their lattices. These lattices can be separated into unit cells which are the simplest repeating unit in a given lattice. The corners of the unit cell mark the location of the lattice points, which are defined as array of points in space so arranged that each point has identical surroundings. The lattice parameters describe the relation between adjacent lattice points.

Since these lattice points are arranged in a periodic pattern, these points produce a plane in three-dimensions. These planes are known as lattice planes and are described by the Miller indices. These indices are defined as the reciprocals of the fractional intercepts which the plane makes with the crystallographic axes denoted by (100) and (200), as shown in Figure 1-13.

The distance, d, between adjacent planes in the set (hkl), as in a crystal in the cubic system, is calculated by Equation (1-1):

$$\frac{1}{d^2} = \frac{h^2 + k^2 + l^2}{a^2} \tag{1-1}$$

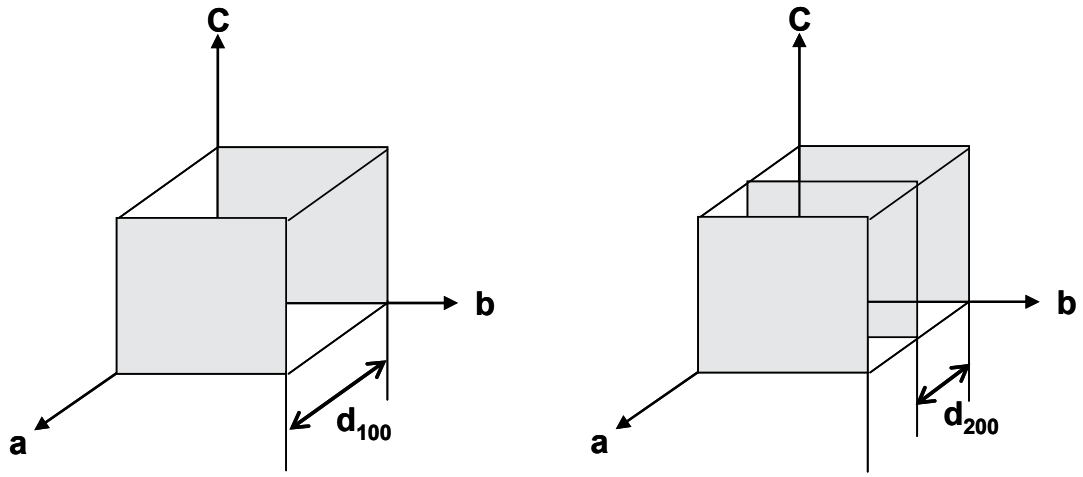


(a) (b)

**Figure 1-13.** Determination of Miller indices; (a) Plane (100), (b) Plane (200).

When X-rays hit atoms (or, more precisely, electrons) they scatter. In other words, when X-rays of close proximity hit an area embedded with atoms they collectively scatter. This area of atoms can be seen as a series of lattice planes since there is a periodic arrangement of atoms on a 2-dimentional sheet. When the waves that are close together reflect, they interfere. This interference is best outlined by the Bragg relation, shown in Equation (1-2):

$$n\lambda = 2d\sin\theta \tag{1-2}$$

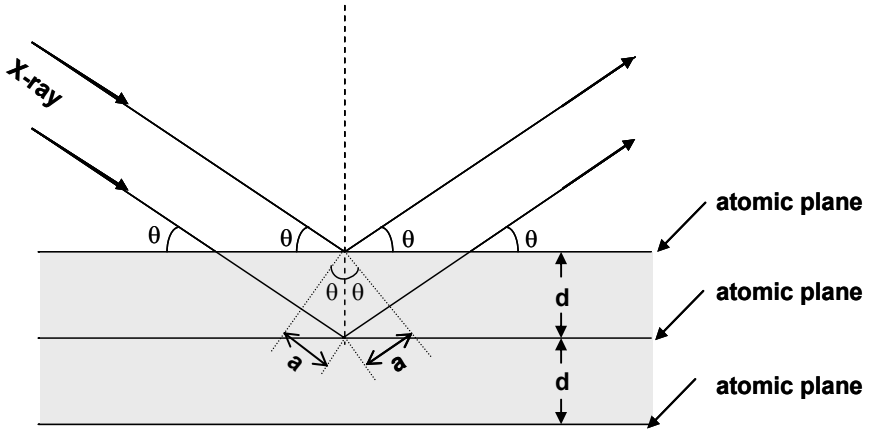


**Figure 1-14.** Diffraction for the (001) crystal planes.

For constructive interference, the path difference between the two waves (2d sinθ) must be equal to some integral of the wavelength. When the Bragg condition is met, a diffraction pattern will be produced, which conventionally is recorded on film and then analyzed by various techniques (Figure 1-14).

One of the most common sample analysis methods is the use of powder diffraction. This method is particularly convenient because samples are not always found in pure crystal form, but instead in powder form. Each powder particle is, in itself, a minute crystal with some random orientation with respect to the incident beam. Incidentally, some of these particles or tiny crystals, will be in the correct orientation such that they can reflect the incident beam off its (001) planes. Other particles will be oriented such that their (110) planes reflect. The result is such that every set of lattice planes will be capable of reflection.

In the case of MMT, the distance between two layers is called d-spacing, which is derived from the diffraction of the X-ray beam from the MMT layers. The diffraction of the lowest 2θ value is produced by the scattering from planes of the greatest spacing. So, its diffraction band is called

basal diffraction. For example, in a cubic system d is greatest when $(h^2+k^2+l^2)$ is minimum, therefore the reflection with the lowest 2θ value corresponds to the low value of $(00\ell)$ in $(00\ell)$ set of planes (see Equation (1-1)).

The X-ray powder diffraction profiles (Figure 1-15) are for MMT and hydrated MMT. These profiles show that the peak located at 2θ° = 6.6° (12.5 Å) in raw-MMT, characteristic of a monolayer of water molecules between the clay layers, moves to 5.7° (15.02 Å) in hydrated MMT, corresponding to a bilayer of water molecules between the clay layers (Earley et al., 1953). Other crystalline phases such as quartz, feldspath and calcite, also present in raw-MMT, were identified by assignment of its characteristic bands. Table 1-1 shows characteristic diffraction bands of other phases also present in the MMT particles.

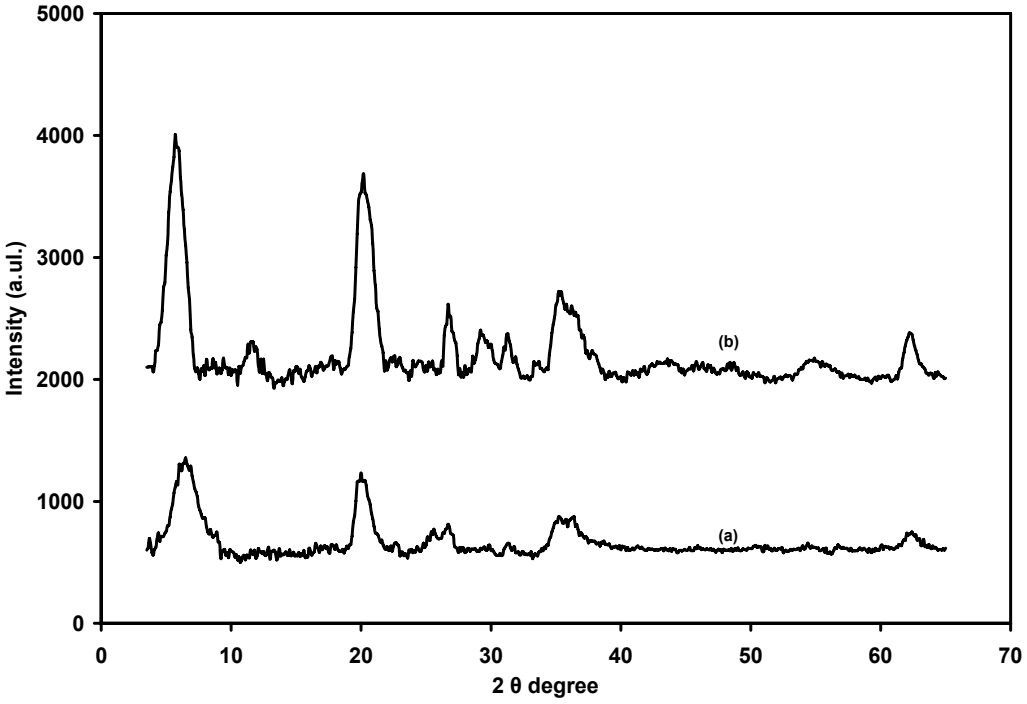


**Figure 1-15.** X-ray powder diffraction of (a) MMT, and (b) hydrated MMT.

**Table 1-1.** X-ray characteristic diffraction bands of raw and hydrated MMT (Harrane, et al., 2002)

| Samples | $d_{hkl}$ (Å) | 2θ | hkl | Nature of Sample |
|---|---|---|---|---|
| Raw-MMT | 13.4 | 6.6 | 001 | Montmorillonite |
| | 4.47 | 19.9 | 110 | Montmorillonite |
| | 4.16 | 21.4 | - | Quartz |
| | 3.35 | 26.6 | - | Quartz |
| | 3.21 | 27.8 | - | Feldspath |
| | 3.03 | 29.5 | - | Calcite |
| | 2.55 | 35.2 | 200 | Montmorillonite |
| | 1.68 | 54.6 | 009 | Montmorillonite |
| | 1.49 | 62.3 | 060 | Montmorillonite |
| Hydrated -MMT | 15.5 | 5.7 | 001 | Montmorillonite |
| | 4.47 | 19.9 | 110 | Montmorillonite |
| | 4.16 | 21.4 | - | Quartz |
| | 3.35 | 26.6 | - | Quartz |
| | 3.21 | 27.8 | - | Feldspath |
| | 3.03 | 29.5 | - | Calcite |
| | 2.55 | 35.2 | 200 | Montmorillonite |
| | 1.66 | 55.2 | 009 | Montmorillonite |
| | 1.49 | 62.3 | 060 | Montmorillonite |

The XRD analysis of polymer-clay nanocomposites becomes more complicated with the following factors. First, nanocomposites generally contain a fairly small amount of clay (typically less than 10 wt.-%). Therefore, the XRD analysis must be sensitive enough to detect the crystalline structure of the clay in the polymer. If this is not the case, no peaks appear in the diffraction pattern and a false conclusion that an exfoliated nanocomposite has been produced might be drawn. A simple method to verify the sensitivity of the analysis consists in finding if the crystallographic planes belonging to the clay layers themselves (hk0 bands) can be detected. If so, the analysis is sensitive enough to detect (001) reflections. Then, the analysis is performed at small angle ($2\theta$ degree $< 9^{o}$, i.e. $d > 9.8$Å) in order to detect the ($00\ell$) reflection and evaluate the d-spacing between the clay layers.

### 1.7.2. Transmission Electron Microscopy

Transmission electron microscopy (TEM) is a powerful technique used to study structures at and below the nanometer scale. It can be used to confirm results obtained by XRD about the organization of the clay layers in the nanocomposite. In addition, even though less than 10 wt-% of clay in polymer is not appropriate for XRD analysis, TEM analysis of these samples can still provide clear evidence of the distribution of clay particles in the nanoscale. Under appropriate conditions, TEM allows a precise observation of nanostructures with an exceptional resolution (the entire magnification range in TEM varies from 50X to 1,000,000X, with resolution down to about 0.2 nm). Therefore, TEM is widely used to characterize polymer nanocomposites. The description of the TEM in this section is restricted to only the bright field imaging system used for the structural characterization of polymer-clay nanocomposites, as shown in Figure 1-16. Figure 1-16 shows TEM images of polyurethane-clay nanocomposite with about 1 wt.-% of clay in the polymer. Nanocomposites with such low clay fraction cannot be analyzed by XRD (Tien, et al., 2001).

On the other hand, the main disadvantage of TEM is that only a small region can be observed at one time. This makes surveying sample morphology by TEM tedious and time-consuming. Another

disadvantage is the harsh process required for sample preparation. For instance, staining through toxic chemical deposition, embedding in epoxy resin, nano thickness slicing, and cryogenic conditioning of soft material, are sometimes involved. In addition, these harsh processes can cause serious damage to the original morphologies, which may lead to false data interpretations.

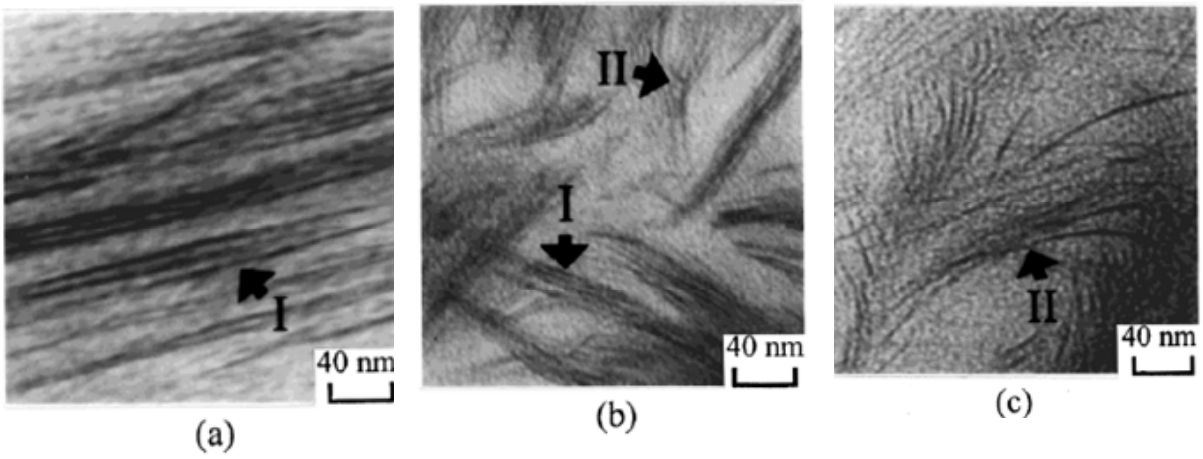


**Figure 1-16.** TEM micrographs of the cross-sectional views of polyurethane containing (a) 1 wt.-% monohydroxyl-montmorillonite, (b) 1 wt.-% dihydroxyl-montmorillonite, and (c) 1 wt.-% trihydroxyl-montmorillonite. (I) indicates intercalated structures and (II) indicates exfoliated structures (Tien, et al., 2001).

### 1.7.3. Scanning Electron Microscopy (SEM) and Energy-Dispersive X-Ray Analysis (EDX)

With the SEM/EDX analysis technique, materials can be imaged by SEM at high magnification (300,000 times) providing information on their physical properties including size, shape, and surface morphology. On the other hand, EDX provides information on the surface chemical composition. The morphology of clay particles in the polymer matrix is of great importance to understand its mechanical properties. SEM combined with EDX, through the detection of secondary electrons, is very well suited to morphological studies of polymer nanocomposites and clay particle distributions through the analysis of their surface elements. The surface characteristics may hold information about

nanoscale distribution in the polymer matrix. For instance, it can be useful for understanding mechanical failure in materials, providing information where cracks and failures are located.

### 1.7.4. Gel Permeation Chromatography (GPC) and Soxhlet Extraction

GPC works on the principle of size exclusion. A polymer solution is passed through a porous column made of cross-linked polymer (such as styrene divinylbenzene). Smaller chains can diffuse into pores of smaller sizes than larger chains, and consequently, smaller chains have a higher retention time in the GPC columns. A calibration curve relating retention time to molecular weight is used to calculate average molecular weights and molecular weight distribution (MWD) (Strying et al., 1989). For polyolefins, GPC is done at high temperatures (140 °C or higher) because of the difficulty in dissolving polyolefins at lower temperature.

Number and weight average molecular weights of extracted PE from PE-clay nanocomposite samples were determined using conventional GPC analysis and a universal calibration curve based on narrow polystyrene standards. Soxhlet extraction was used to extract the polymer from the clay particles. The extraction method consisted of continuously refluxing hot solvent over the sample.

### 1.7.5. Differential Scanning Calorimetry (DSC) and Thermal Gravimetric Analysis (TGA)

DSC measures the specific heat capacity and the enthalpic changes of a sample during cooling or heating. By monitoring the changes in the supplied energy as a function of temperature (or time), the thermal transitions of a polymer such as the glass transition and melting temperature, as well as the heat of fusion or crystallization, can be observed. For a semi-crystalline polymer, the shape of the DSC curve also indicates its crystallinity range. For polyethylene, the degree of crystallinity can be estimated by comparing the measured melting enthalpy ($\Delta H_f$) to that of a pure polyethylene crystal (Tudor et al., 1996). The $\Delta H_f$ for a pure polyethylene crystal is estimated to be approximately 289 J/mol (Tudor and O'Hare, 1996).

The melting transitions of polymers are very sensitive to their thermal history. Different crystalline structures are formed depending on the thermal treatment of the sample either by annealing or quenching the sample. To include the effect of the thermal history of the sample, DSC measurements can be obtained from the first temperature scan. A better estimate of the inherent properties of the polymer can be achieved by erasing the thermal history of the sample by melting it in the 1st scan and then using the 2nd scan to calculate the thermal properties. For PE-clay nanocomposites, DSC can be used to determine if the crystallinity and melting point of PE are affected by the presence of clay.

TGA measures weight change of a sample as function of temperature; the instrument is configured with a thermocouple assembly mounted on a balance, which allows monitoring the weight change and temperature differential simultaneously as a function of temperature. It is a precise quantitative method for determining combustibles, loss of volatiles, decomposition of hydrates and carbonates, and weight loss changes. In the standard analysis, sample weights from 5 to 10 mg are required, and heating rates are normally 10 °C/minute. Rates of weight loss or gain are easily obtained by the derivative of the weight loss curve, also called differential thermal gravimetry. Plotting the weight loss rate is useful for comparing different stages during thermal decomposition of the sample and therefore it is a valid method for understanding the mechanism of sample degradation.

Information obtained from TGA is used primarily for the calculation of clay content in the composite samples. The changes in thermal decomposition temperatures can also be used to understand the type of interaction that polymer chains have with the clay.

### 1.7.6. Fourier Transform Infrared Spectroscopy (FT-IR)

An IR spectrum is a unique molecular fingerprint that is easily distinguished from the absorption patterns of other molecules. This advantage enables IR to perform effective and rapid analysis of PE-clay composite samples. Analyses can be performed on relatively thin layers of sample, where generally the thickness does not exceed 0.5 mm.

On the other hand, its disadvantage is that factors such as differing molecular weights, its molecular weight distribution and side branches in polymer chains may be virtually indistinguishable.

Infrared spectra data provide useful information on the nature of the chemical bonds in PE-clay nanocomposite samples. PE-clay nanocomposite samples can be analyzed as films (about 0.1-0.3 mm in thickness using a hot plate press). As the size of clay is already in the nanometer scale, the IR beams (wavelength; 2.5 to ≈15 micrometers) can penetrate the film samples to give a spectrum with information on chemical bond formation between the clay surface and the polymer. The FT-IR analysis can also be used to obtain further insight about the conformation of chains in the galleries or on the vicinity of the surface. Vaia and co-workers have shown that alkyl chains inside clay galleries have well-defined stretching band shift when ammonium cation and amines were used for intercalations in clay (Vaia et al., 1994). According to those authors, FT-IR analyses directly probe the molecular conformation of the intercalated organic chains and the interlayer structure. The bands at ~ 2920 $cm^{-1}$ arise from the -$CH_2$ asymmetric stretching, $\nu_{as}(CH_2)$.

In general, the frequency and width of $\nu_{as}(CH_2)$, ranging form 2929 to 2918 $cm^{-1}$, are sensitive to the gauche/trans conformer ratio and packing density of methylene chains. The $\nu_{as}(CH_2)$ at higher frequencies (~2929 $cm^{-1}$) is known to be characteristic of gauche conformations along the hydrocarbon chain (chain disorder). Conversely, a band shifting to lower frequencies reveal the characteristic of highly ordered all-trans conformations, that is, highly ordered chains (Vaia et al., 1994).

### 1.8. Mechanical Properties

The mechanical properties of polymer-clay nanocomposites are very important for practical applications. When done properly, the combination of polymer and clay nanoparticles increases the tensile strength of the final nanocomposite. The lack of compatibility on the interface between the organic polymer phase and the inorganic clay phase is responsible for the inadequate impact

properties. In this study, we measured tensile properties to infer how well the clay platelets were distributed in the polyethylene matrix. An increase in tensile strength, for instance, would indicate that the clay was well dispersed in the clay-polyethylene nanocomposite and there was a strong interaction between the organic and inorganic phases.

In thermoplastics, Hookean initial elastic behavior is expected when the sample is loaded in the tensile mode until the sample draws and permanent deformation occurs. As the sample draws, the polymer chains may orient and may recrystallize to form fibrils and, eventually, the sample breaks. The initial yield stress is related to the onset of viscoelastic deformation. The ultimate yield stress and elongation represent the area underneath the stress-strain curve and relates to the toughness of the polymer. In turn, these parameters can be correlated to impact properties. The yielding behavior depends on the crystalline structure of the polymer (Bergman et al., 1999). These properties can be obtained from stress-strain measurements from film tested in tensile mode, as shown in Figure 1-17. The yield strength is the stress at intersection obtained by moving the line, with same slope of elastic deformation, by 0.2% in the strain scale.

In addition, the mechanical performance of nanocomposites is related to the degree of exfoliation of the clay in the polymer matrix. Exfoliation increases the surface area between the inorganic layers and the polymer, and this better interaction between the two phases may be responsible for the enhanced tensile strength of the nanocomposites. The dramatic improvements of tensile strength and modulus given by the exfoliated nanocomposite structure on polyamide 6-clay were first reported by Toyota researchers (Okada et al., 1990). The tensile strength of polyamide 6 increased by 55% and the modulus by 90% with the addition of only 4 wt.-% of exfoliated clay. Later, Lan and coworkers (Lan, et al., 1994) reported more than a ten-fold increase in strength and modulus in a rubbery epoxy matrix with only 15 wt.-% (7.5 vol%) of exfoliated organoclay. The tensile modulus increased by 30 wt.-% for partially exfoliated unsaturated polyester-clay nanocomposites. Alternatively, this can be achieved with 5 wt.-% of fully exfoliated clay. The

modulus of intercalated PMMA-clay nanocomposites with 20 wt.-% of clay was reported to be superior by 60% to the pure polymer (Lee et al., 1996).

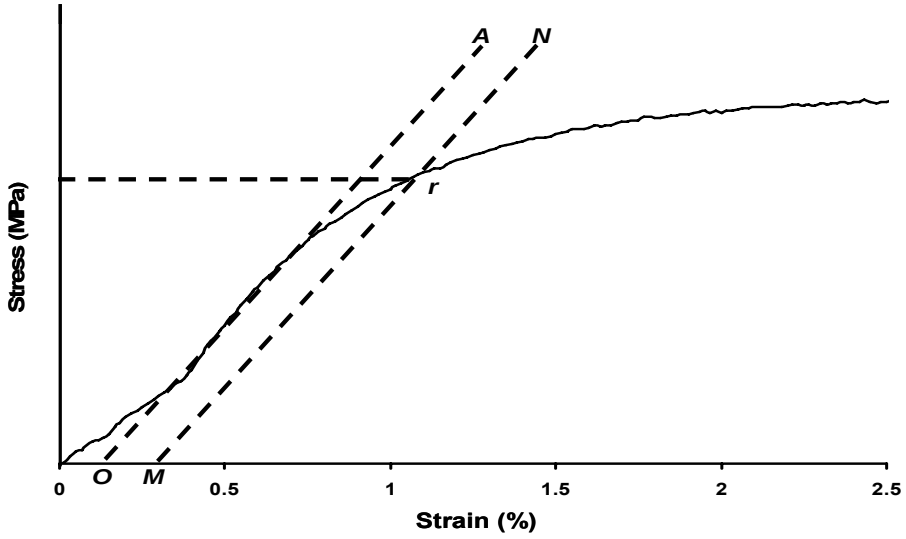


**Figure 1-17.** Definitions of Young's modulus and offset yield strength. Through *M* draw a line *MN* parallel to *OA* and locate the intersection of *MN* with the stress-strain curve. The stress at the point of intersection r is the "offset yield strength." The specified value of the offset must be stated as a percent of the original gage length in conjunction with the strength value. (ASTM D638 -03).

Several explanations have been given about the reinforcement properties of polymer-clay hybrids based on interfacial properties and restricted mobility of the polymer chains. Shi and coworkers (Shi et al., 1998) proposed that interfacial effects, caused by the direct binding (adsorption) of the polymer to the clay layers were the dominant factor. Shi and coworkers (Shi et al., 1998) have developed an interface model to predict the Young's modulus of elastomer-clay nanocomposites suggesting the important role of the interface. Usuki and coworkers (Usuki et al, 1995) suggested that the strong ionic interaction between polyamide-6 and clay layers could generate some crystallinity at the interface, therefore explaining part of the reinforcement effect. Another explanation, related also to interactions at the interface between the clay and the polymer, is the formation of a constrained

region in the vicinity of the clay layers. Kojima and coworkers (Kojima et al., 1993) proposed the concept whereby the improvement of tensile modulus of polyamide-6-clay nanocomposites was caused by the contribution of a constrained region in which the polymer chains had restricted mobility.

# Chapter 2
# PE-Clay Hybrid Nanocomposite by In-situ Polymerization in a Slurry Reactor

## 2.1. Introduction

Clays can be used to produce polymer nanocomposites by in situ polymerization. The clay has a double role: a) during the polymerization it can work as a catalyst support, and b) after polymerization it functions as functional nanofiller in the polymer matrix. Ideally, the type of organic modification on the clay should not decrease the catalyst activity.

If the organic modifier has two functional groups, one can react with the clay surface and the other is left available to react with the polymer being produced in situ. The approach of using bifunctional organic modifiers has been explored with great success with nylon-clay nanocomposites (Vaia et al., 1994; Wang et al., 1993; Kawai et al., 1985; Snyder et al., 1982). Coordination catalysts have been used to prepare polyolefin nanocomposites (Ko et al., 1996; Tudor et al., 1996; Tudor and O'Hare, 1997; Bergman et al., 1999; Heinemann et al., 1999). However, the use of coordination catalysts and bifunctional organic modifiers for the in-situ production of clay-polyolefin nanocomposites has never been reported in the open literature.

This chapter describes the use of bifunctional organic modifiers, such as 10-undecene-1ol, to intercalate montmorillonite (MMT) and its subsequent use in ethylene polymerization with a coordination catalyst (Shin et al., 2003). A novel method to synthesize polyethylene-clay (PE-clay) hybrid nanocomposites prepared by in-situ polymerization is proposed. This hybrid nanostructured material has polyethylene chains chemically linked to the clay surface, leading to excellent compatibility between the organic and inorganic phases.

## 2.2. Experiments

### 2.2.1 Materials

Commercial MMT, called KSF, was purchased from Sigma-Aldrich Co. Its cation exchange capacity (CEC) and surface area are reported to be 62 meq/100g and 20-40 $m^2/g$ respectively (Dias, et al., 2000). 10-undecene-1-ol, toluene, hexane, monochlorobenzene, trichlorobenzene, triisobutyl aluminum (TIBA, 1 M in hexane), and methyaluminoxane (MAO, 10 wt-% Al in toluene) were purchased from Sigma-Aldrich Co. Toluene, hexane, and monochlorobenzene were dried with molecular sieves (3A and 4A from Sigma-Aldrich). The molecular sieves were dried overnight in a muffle furnace at 400 °C before being used. Ethylene and nitrogen were dried through a column containing molecular sieves 3A and deoxygenated using a column containing copper catalyst. The Ni-diimine catalyst, (1,4-bis(2,6-diisopropylphenyl)-acenaphthenediimine) dichloro nickel, was prepared through a known procedure (van Koten et al., 1982), and dicyclopentadienyl zirconium dichloride ($Cp_2ZrCl_2$) was purchased from Sigma-Aldrich. Hydrochloric acid, nitric acid, and hydrofluoric acid were also purchased from Sigma-Aldrich. Standard solutions of Ni and Zr (Sigma-Aldrich Co.) were purchased for standard calibration.

### 2.2.2 Catalyst Supporting

The intercalation of MMT was done by an ion exchange reaction. MMT (10 g) was dispersed in 500 mL of HCl (0.1 N) and then washed with deionized water until no chlorine ion was detected with an $AgNO_3$ solution (0.1 N). The filter cake was vacuum-dried at 300°C for 24 hours. The dried and exchanged MMT (1 g) was transferred to a 250 mL Schlenk tube under nitrogen, dispersed in 50 mL toluene, treated with 1.7 mmol of TIBA for 2 hours, and dried again under vacuum for 3 hours.

The resulting solid (MMT/TIBA) was then treated with 1.7 mmol of 10-undecene-1-ol (UOH) dissolved in 20 mL of toluene. The resulting solid (MMT/TIBA/UOH) was then washed with 15 mL hexane three times and dried for 3 hours under vacuum. Finally, 1 g of the resulting solid was treated with 11 μmol of Ni-diimine or $Cp_2ZrCl_2$ in 20 mL of toluene solution, and washed with 20 mL

of toluene. Finally, the product was dried for 12 hours under vacuum to produce a catalyst supported on the organically-modified MMT (MMT/TIBA/UOH /CAT, where CAT is either Ni-diimine or $Cp_2ZrCl_2$).

### 2.2.3 Polymerization

The MMT-supported catalyst was tested for ethylene polymerizations first at atmospheric pressure using a glass reactor. Then, the catalytic activity was measured at different temperatures and ethylene pressures. Polymerizations at high pressure were carried out in a stainless-steel 1 L reactor. For the polymerization at atmospheric pressure, a 250 mL glass reactor equipped with a stirrer was purged with nitrogen 3 times. Subsequently, 20 mL monochlorobenzene, approximately 0.5-1.0 g of MAO, ethylene (at atmospheric pressure), and MMT/TIBA/UOH/CAT were introduced into the glass reactor. Ethylene was supplied on demand to keep the polymerization running at room temperature during the entire polymerization time (Figure 2-1.a).

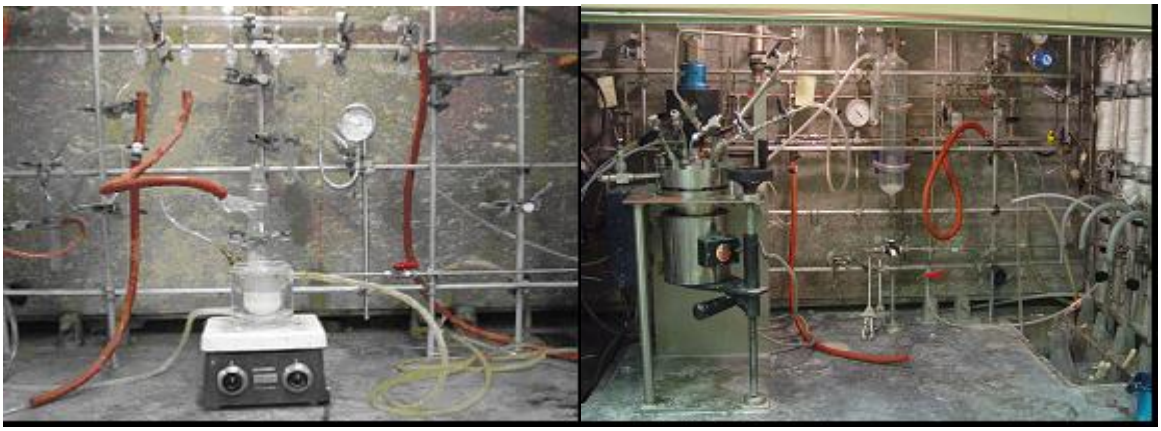

(a) (b)

**Figure 2-1.** Polymerization reactor systems: (a) 250 mL glass reactor for polymerization at atmospheric pressure, (b) 1 L autoclave reactor for high pressure polymerization.

For the high pressure ethylene polymerizations, the 1 L autoclave reactor was purged with dried nitrogen and vacuumed for 30 minutes three times to remove air and moisture. Subsequent

operations were done under nitrogen atmosphere at room temperature (Figure 2-1. b). All chemicals were injected using a cannular. 200 mL of diluent (monochlorobenzene) were transferred to the autoclave, followed by the cocatalyst, MAO. A suspension of MMT/TIBA/UOH/CAT in toluene was then transferred to the autoclave.

Polymerization of ethylene was carried out for one hour at ethylene partial pressures of 3 and 10 atm. After 1 hour, the polymerization was quenched by adding 5 mL of methanol. Then, the polymer slurry was dumped into ethanol (approximately 400 mL in a 1 L beaker), to which 10 mL of HCl solution (0.1N) was added. The suspension was stirred for 3 hours and the polymer slurry was filtered with filter paper and washed with 30 mL of ethanol twice. Finally, the polymer was dried in a vacuum oven at 70 $^{o}$C for 6 hours.

### 2.2.4. X-Ray Diffraction

The wide angle ($2\theta > 4^{o}$) X-ray diffraction pattern was obtained with a Siemens-500 diffractometer. The beam was Cu Kα radiation ($\lambda = 0.154$ nm), operated at 40 kV and 30 mA in transmission mode. This analysis was used to measure the basal spacing of the MMT before and after organic modification, and to quantify MMT intercalation from the position of the ($d_{100}$) peak in XRD. The small angle ($2\theta < 10^{o}$) X-ray diffraction was obtained with a D8-ADVANCE powder X-ray diffractometer (Bruker AXS) operating at 40 kV and 30 mA.

### 2.2.5 Transmission Electron Microscopy (TEM)

TEM was used to investigate the nanoscale morphology (the exfoliation of MMT and its dispersion within the polyethylene matrix). A Philips CM20 Super Twin microscope, operated at an acceleration voltage of 80 Kv, was used.

The nanocomposite samples were embedded in epoxy resin and cured for 24 hours before being cut with the ultramicrotome. The epoxy resin was prepared by mixing EPOFIX embedding (25 parts by weight) and EPOFIX hardener (3 parts by weight) and then cured with the nanocomposite

sample in room temperature for 24 hours. The embedded samples were first trimmed using a glass knife to prepare the block face in the size of approximately 300×1000 $\mu m^2$. Then, the block faces were further sectioned into slices of thicknesses in the range of 50-80 nm, using the LEICA EM UC6 cryo-ultramicrotome with a cold temperature chamber (-150 $^oC$) and diamond knives (DiAtome). The swing speed of the cutting arm was 1-0.3 mm/s, with 50-80 nm thickness feeding per each swing. These sections were then mounted on a copper grid (400 mesh), which had 3.05 mm diameter and a hole size of ~42 μm.

### 2.2.6. Scanning Electron Microscopy (SEM) and Energy Dispersive X-ray Spectroscopy (EDX) Analysis

The morphologies of MMT and polyethylene nanocomposites were observed using an ultrahigh resolution SEM (LEO 1530 FE-SEM) with a fully loaded EDX system (EDAX Pegasus 1200 integrated EDX). With a proven spatial resolution of 3 nm at 1 kV and 1.5 nm at 15 kV, this system can provide near-atomic-resolution imaging of a wide range of materials from metals, semiconductors, to polymers, biomaterials, and other soft materials. Because of the high magnification available (up to 300,000 times), it was possible to obtain images of the desired features in great detail (in the nanometer scale, < 100 nm) thus providing information on the size, shape, and surface details of the nanocomposites. The accelerating voltage was 15 to 20 keV in all cases. The samples were placed on the conductive tapes on the aluminum pan and were coated in 10 nm thick gold film using high vacuum sputter.

EDX analysis collects the X-rays, which are generated as the electron beam of the SEM is scanned across the sample surface. It provides information on the elemental composition (including C, Al and Si atoms) on the surfaces of MMT and nanocomposites. Most elements are detected at concentrations in the orders of 0.1%. Analysis of the element composition of PE-clay composites was made over fixed intervals (approximately 3 minutes) in order to collect sufficient counts.

### 2.2.7. Gel Permeation Chromatography (GPC)

GPC was used to measure the MWD of polyethylene using a Waters GPCV 150+ equipped with a Viscotek 150R viscometer, and using 1,2,4 trichlorobenzene (TCB) as the solvent at 140 $^{o}$C. Number average ($M_n$) and weight average ($M_w$) molecular weights were calculated using the universal calibration curve based on narrow MWD polystyrene standards.

### 2.2.8. Differential Scanning Calorimetry (DSC)

The melting point ($T_m$) was determined using a Thermal Analysis DSC 2920 differential scanning calorimeter (DSC) under argon atmosphere and a heating rate of 10$^{o}$C/min. The crystallinity of the polyethylene was calculated during the second heating scan and integrating the recorded signal using the known melt enthalpy for polyethylene ($\Delta H_{ideal}$ = 289 J/g) (Tudor and O'Hare, 1996). Polyethylene samples with weights from 5 to 10 mg were used.

### 2.2.9 Thermal Gravimetric Analysis (TGA)

TGA was used for the calculation of clay content and investigating changes in the thermal decomposition temperature of polymer in the nanocomposites. TGA was performed using the Thermal Analysis SDT 2960 instrument, with 10 $^{o}$C/min heating rate, under an oxygen and helium mixture (5% $O_2$, 95% He).

### 2.2.10 Fourier Transform Infrared Spectroscopy (FT-IR)

FT-IR spectra provided information on the nature of the chemical bonds in polymer materials and were useful for the characterization of their chemical composition. Polymer and nanocomposite samples were prepared as films, about 0.1 mm thick, using a hot plate press. When the clay particles are dispersed at the nanometer scale, FT-IR (with approximate wavelength range from 2.5 to 15 m□) can provide information on the chemical bonding between the clay surface and the polymer. Using a Bruker Tensor 27 (Bruker Co.) FT-IR system equipped with a computer for data analysis, the spectra

in transmission mode were recorded in the range from 400 to 4000 $cm^{-1}$, after 32 scans, with a resolution of 4 $cm^{-1}$. Calibration of the wavenumber was automatically done by the instrument using an internal polystyrene film. Spectra reported in this investigation were subtracted from a background spectrum obtained with no sample.

### 2.2.11. Direct Current Plasma-Atomic Emission (DCP) Spectrometry

Approximately 100 mg of catalyst-impregnated MMT was accurately weighed in a 15 mL Teflon vial using a OHAUS analytical balance, precise to ± 0.02 mg. Then, the powder was wetted with 1 mL of 14 M $HNO_3$ prior to the addition of 1 mL of 29 M HF. The vial was closed and placed on a hot plate at approximately 70 °C for 3 hours for sample dissolution. After opening, acids in excess were gently evaporated, along with $SiF_4$, at approximately 60°C. The sample was evaporated incompletely in order to be diluted with additional distilled water just before DCP analysis. Blank solutions for the baseline adjustment in the final calculation were prepared under the same conditions following the MMT sample preparation.

Measurements were made on emission peaks at 339.20 and 341.5 nm, for Zr and Ni respectively using an ARL Fisons SS-7, direct current plasma-atomic emission spectrometer (DCP-AES). Calibration curves were made from dissolved standards with concentrations from 0 to 50 ppm in the same distilled water. Standards and unknowns were analyzed 10 times each for 3 second counts. Instrument reproducibility, for concentrations greater than 100 times the detection limit, have < ±2% error.

### 2.2.12. Mechanical Properties

A uniaxial tensile tester (Minimat 2000, from Rheometrics) was used to obtain stress-strain curves of polymer nanocomposites. The maximum elongation of the materials was limited by the maximum span of the tensile tester of 80 mm. Tests were done at room temperature (23°C±2°C) and ambient moisture (55% ± 10% relative humidity). The data was used for calculation of Young's modulus and

yield stress. This small tensile tester is a very suitable instrument to measure the mechanical properties of relatively small samples (less than 1 g). Data measured with the Minimat 200 were compared to those obtained with an Instron tensile tester for the same samples. The crosshead speed was 10 mm $min^{-1}$. The reproducibility was in the 99 % range in tensile modulus and yield strength with Minimat 2000.

The specimens for tensile testing were prepared by the hot press method. A few grams of PE-clay nanocomposites were sandwiched in the steel mold (thickness of 0.5 mm), covered with two smooth transparent PET films, and then placed between two steel plates. The plates of the hydraulic press (P-215 C from Pasadena Hydraulics) were heated to about 180 to 200 $^{o}C$, thus higher than the melting point of the polymer samples. The steel plates with the sample mold in between were put in the hot hydraulic press. After melting the polymers (approximately 2 minutes), the samples were pressed using a pressure of 320 psi. After 3 minutes, the press was released to let the air bubbles in the polymers melt to escape. After 30 seconds, the samples were repressed for another 3 minutes. Finally, the molded polymer film was taken out and cooled in air. The test specimens were prepared by cutting the sheet samples with dog-bone shaped molds (Figure 2-2). The specimen size was scaled down from the suggested standard sizes form ASTM D638. The test specimens had dimensions of 15 to 30 mm length, 5 mm width and 0.5 mm thickness. The specimens for tensile testing were prepared by the same hot press method used in preparing the films for FT-IR investigation

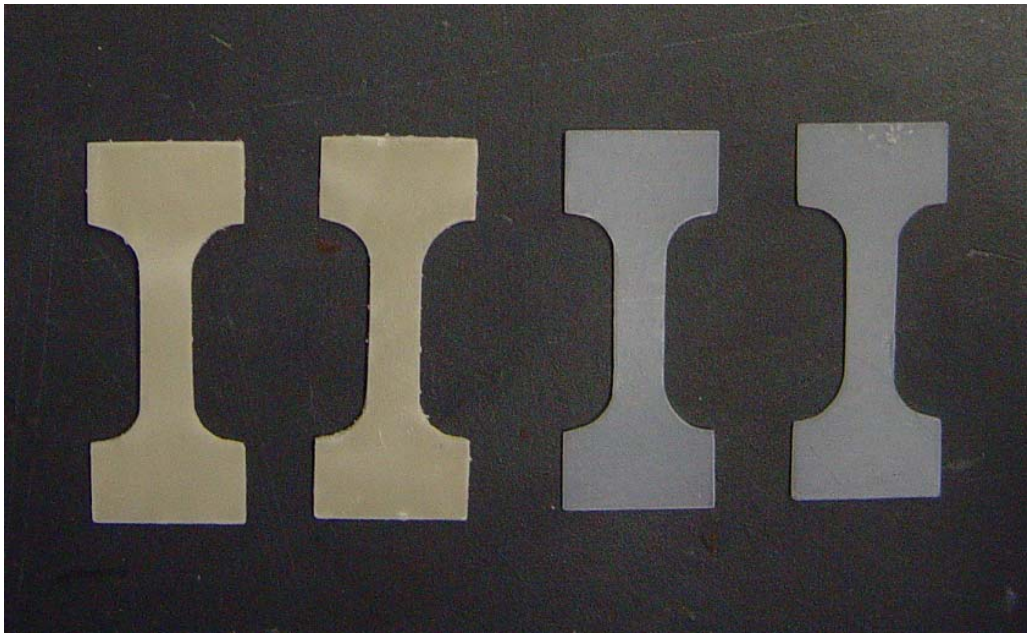

**Figure 2-2.** Dog-bone shaped specimens for tensile testing, prepared by cutting hot pressed polymer sheets with a dog-bone shape steel mold.

## 2.3 Results and Discussion

### 2.3.1. MMT Modification

The main objective of the approach proposed in this chapter is to develop a method to produce hybrid PE-clay nanocomposites by in situ polymerization. MMT was selected because of the high aspect ratio of the clay platelets after exfoliation (Grim, 1968; Pinnavaia, 1983).

To minimize catalyst activity losses found when olefins are copolymerized with polar comonomers (Imuta et al., 2001; Paavola et al., 2004), the intercalation process proposed here was carried out with a bifunctional organic modifier: one functionality (polar) reacts with the MMT surface, and the other functionality (vinyl) copolymerizes with ethylene. This permits the production of PE-clay nanocomposites where some PE chains have covalent bonds with the clay surface, thus avoiding additional expensive post-reactor polyethylene modification processes.

As shown in Figure 2-3, the synthesis process can be divided into 2 stages: the first stage is the modification of the MMT surface (intercalation), and the second stage is the in-situ polymerization (exfoliation).

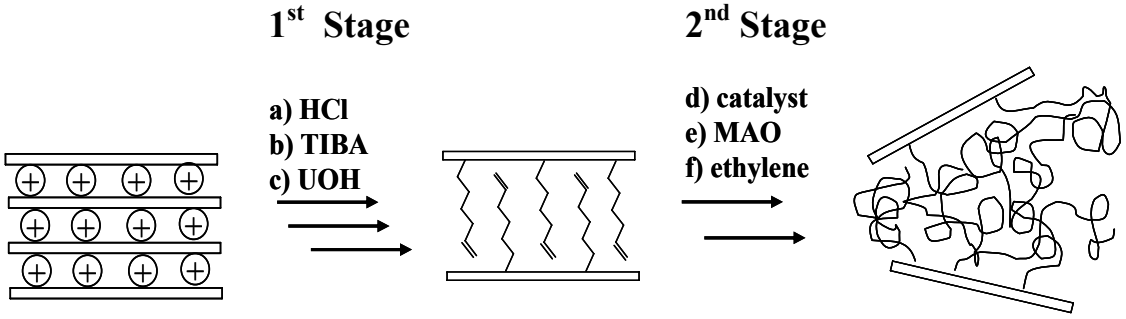


**Figure 2-3.** Synthesis approach using bifunctional organic modifiers to produce polyethylene chemically linked to exfoliated MMT layers by in-situ polymerization

The first stage involves the chemical modification of the clay. Initially, MMT was treated with hydrochloric acid to remove natural cations (mostly sodium), dried in vacuum at 300 °C overnight, and then treated with TIBA. TIBA reacts with silanol groups (>Si-OH) on the surface of MMT to form a product we call MMT/TIBA.

After washing out the excess TIBA and drying under vacuum, 10-undecene-1-ol (UOH) was contacted with MMT/TIBA to form MMT/TIBA/UOH. The polar OH groups react with the TIBA compounds on the surface of MMT. The vinyl groups of UOH can be used for ethylene and vinyl alcohol copolymerization (Marques et al., 1999). These two reaction steps enhance the intercalation and the organophilic character of the MMT layers. In addition, the pendant vinyl groups of UOH can be copolymerized with ethylene in the second stage, creating covalent bonds between the polyethylene chains and the MMT surface.

The second synthesis stage comprises catalyst impregnation and ethylene polymerization. The catalyst (in toluene solution) was added to dry MMT/TIBA/UOH. The suspension was left to soak in the catalyst solution with gentle stirring for 12 hours at 90 °C. Then, the solid was washed 3

times with 30 ml toluene solution. The catalyst slurry in toluene solution was allowed to settle for several hours and then the supernatant was removed through a cannular. The catalyst impregnated MMT (MMT/TIBA/UOH/CAT) was analyzed with DCP to determine the catalyst concentration.

### 2.3.2. Impregnation of Metallocene Catalytic Precursors

Ni-diimine and $Cp_2ZrCl_2$ were chosen as catalysts. Ni-diimine, as a late transition metal catalyst, is relatively less prone to contamination by polar impurities then $Cp_2ZrCl_2$. The Ni-diimine catalyst has the capacity to produce branched polyethylene without the addition of comonomers (Johnson, et. al., 1995) through a mechanism called chain walking. $Cp_2ZrCl_2$ was selected as the metallocene catalyst, because it is well known and easy to be compared with other systems.

DCP was used to determine the concentration of catalyst in MMT/TIBA/UOH/CAT (Fabio, 2005). The efficiency of the catalyst impregnation method was determined by the ratio of the initial catalyst concentration in solution used for immobilization reaction and the final catalyst concentration on MMT/TIBA/UOH/CAT, according to Equation (2-1):

$$E(\%) = \frac{M_f \times 100}{M_i} \qquad (2\text{-}1)$$

where,

E(%) = Catalyst impregnation efficiency

$M_f$ = Final number of moles of the transition metal on MMT/TIBA/UOH/CAT

$M_i$ = Initial number of moles of the transition metal in the catalyst solution

The initial concentration of catalyst used in the impregnation reactions was always approximately 11 μmol/ g-MMT/TIBA/UOH. By DCP analysis, it was observed that the concentrations of the transition metal on MMT/TIBA/UOH/CAT were, in the majority of cases,

between 10 and 10.8 μmol metal/ g MMT/TIBA/UOH, giving efficiencies of 90 % to 95%, as shown in Table 2-1.

**Table 2-1.** Data related to the impregnation reactions of the complexes on clay.

| No. | Metal Complexes | Impregnation [a] | |
|---|---|---|---|
| | | [Metal][b] | Efficiency (%) |
| **1** | $Cp_2ZrCl_2$ | 10.8 | 95 |
| **2** | Ni-diimine | 9.4 | 90 |

(a) Impregnation reaction: modified MMT suspension + catalyst solution in toluene, stirring for 12 hours at 90 $^{o}$C. (b) μmol metal/ g MMT, determined by DCP.

### 2.3.3. Intercalation and Exfoliation

In order to verify the intercalation of UOH between the MMT platelets, XRD analyses were carried out for MMT and MMT/TIBA/UOH/Ni-diimine (9.4 μmol-Ni/g-clay, analyzed by DCP, see Table 2-1). Figure 2-4 compares the X-ray diffraction patterns of MMT with those of MMT/TIBA/UOH/Ni-diimine. In Figure 2-4.a MMT shows the characteristic broad band for basal diffraction centered at 7.2$^{o}$, corresponding to a d spacing of 1.2 nm. The sharp band located at 8.9°, (0.9 nm) is attributed to the presence of illite group particles that are usual impurities in natural MMT, as discussed in Section 1.6.1.

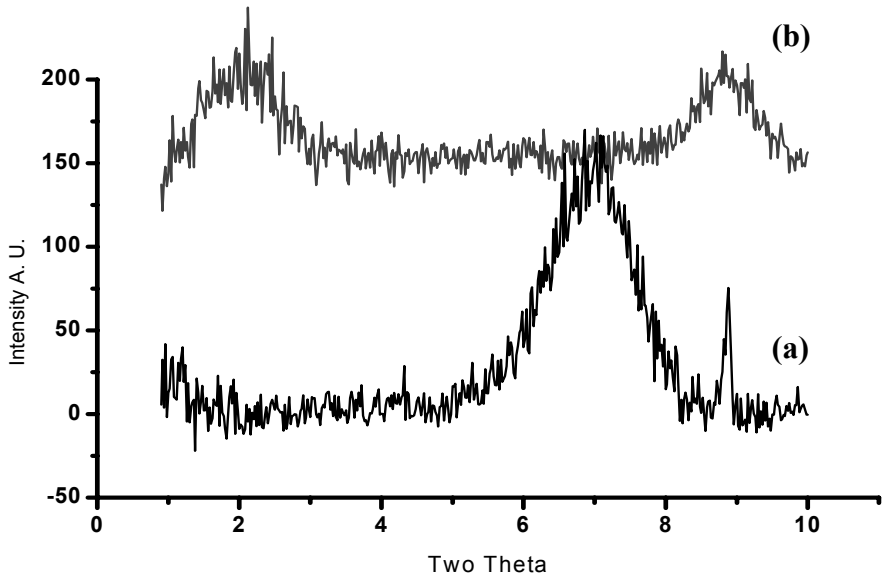


**Figure 2-4**. Small angle X-ray diffractograms for (a) MMT and (b) MMT/TIBA/UOH/Ni-diimine.

After treatment with UOH and supporting the catalyst, the basal band moved to 2.0°, which corresponds to a d spacing of 4.4 nm. This increase in the distance between the clay platelets implies that UOH and catalyst molecules were intercalated inside the MMT galleries.

After ethylene in-situ polymerization, the hybrid nanocomposite was microtomed and investigated by TEM. TEM images of nanocomposite particles, showing the morphology of intercalated and exfoliated MMT layers in the polyethylene matrix are depicted in Figure 2-5.a. The process of exfoliation is needed to separate the tactoid layers of MMT. Figures 2-5.b and 2-5.c show a few layers of MMT that were exfoliated during polymerization.

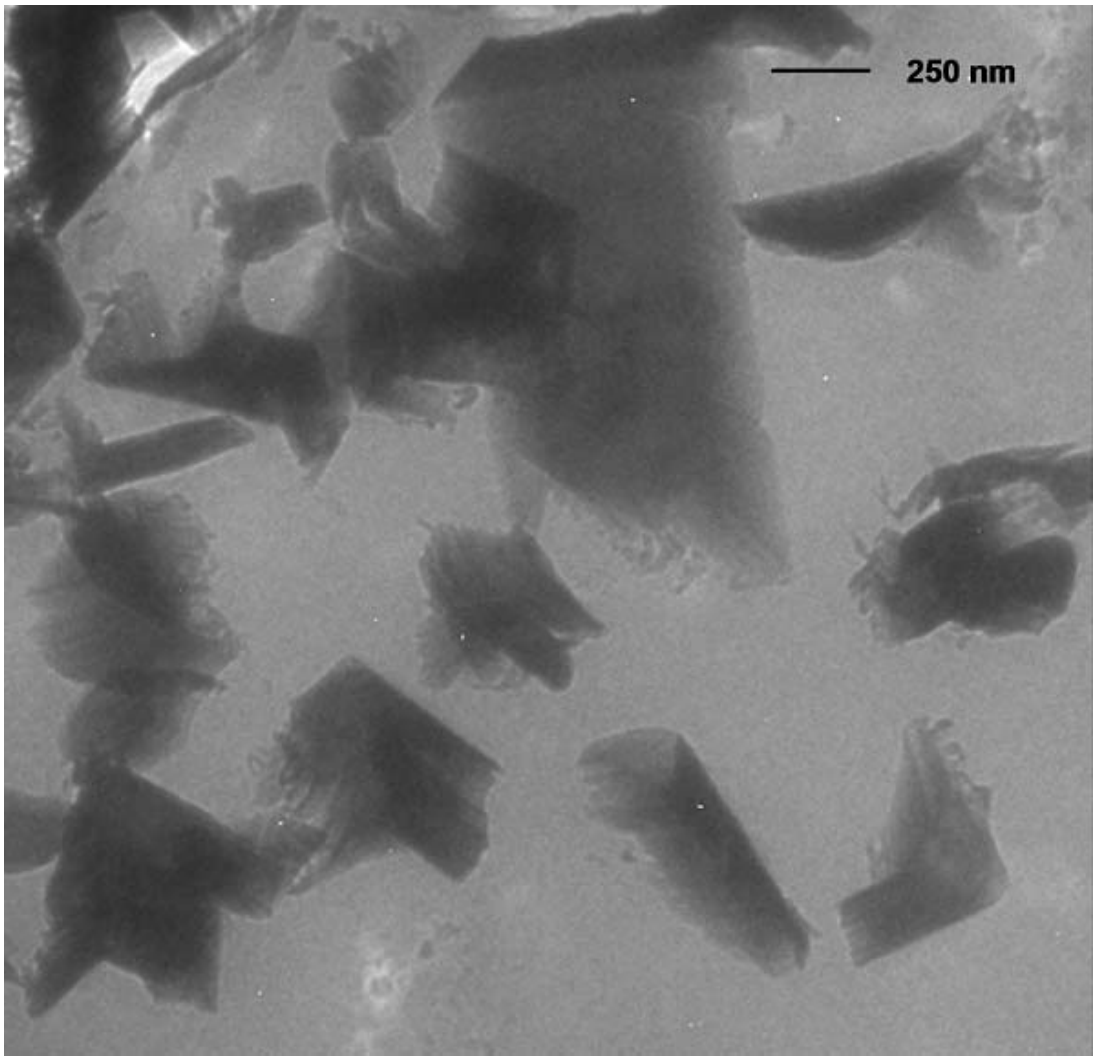


**(a)**

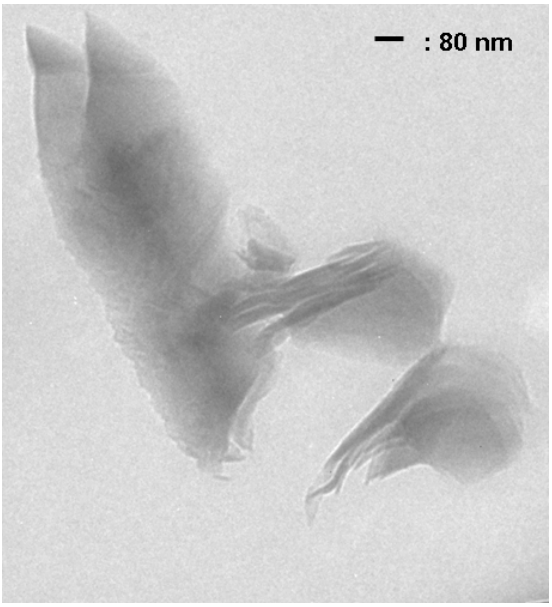


**(b)**

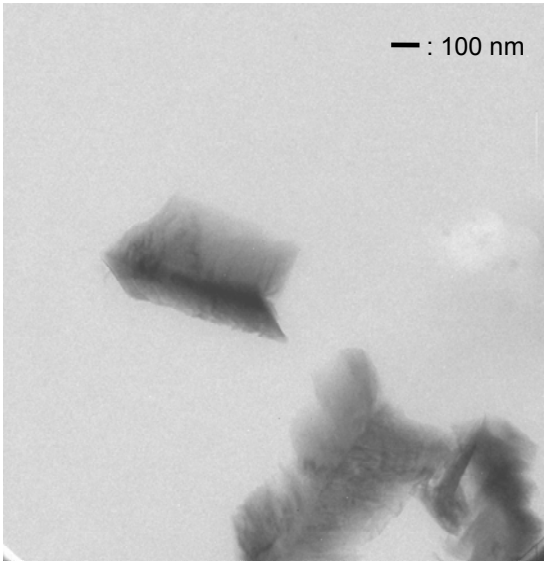


**(c)**

**Figure 2-5**. TEM images of PE-clay nanocomposites obtained by in-situ polymerization with MMT/TIBA/UOH/ MMT/TIBA/UOH/Ni-diimine and MAO catalyst system (sample 80 nm thick prepared by cryo-ultramicrotomy); (a) several types of MMT particles in a PE matrix, (b) different orientation of intercalated and exfoliated MMT layers, (c) opening edges of MMT layers (exfoliation).

The idealized model used to represent MMT assumes that the layers are flat, but in reality MMT layers have curved and irregular edges. Figure 2-5.a shows that several types of MMT layers were intercalated and some particles show broken pieces of a few nanometer scales at the edges during the exfoliation. Figure 2-5.b shows the different orientation of intercalated and exfoliated MMT layers. These layers are separated by several hundred nanometers. Figure 2-5.c suggests different types of exfoliation models. Based on the TEM images depicted in Figure 2-5, an intercalation and exfoliation model for MMT is suggested in Figure 2-6. During the polymerization, the growth of polymer chains inside the galleries forces the separation, or exfoliation, of the MMT layers.

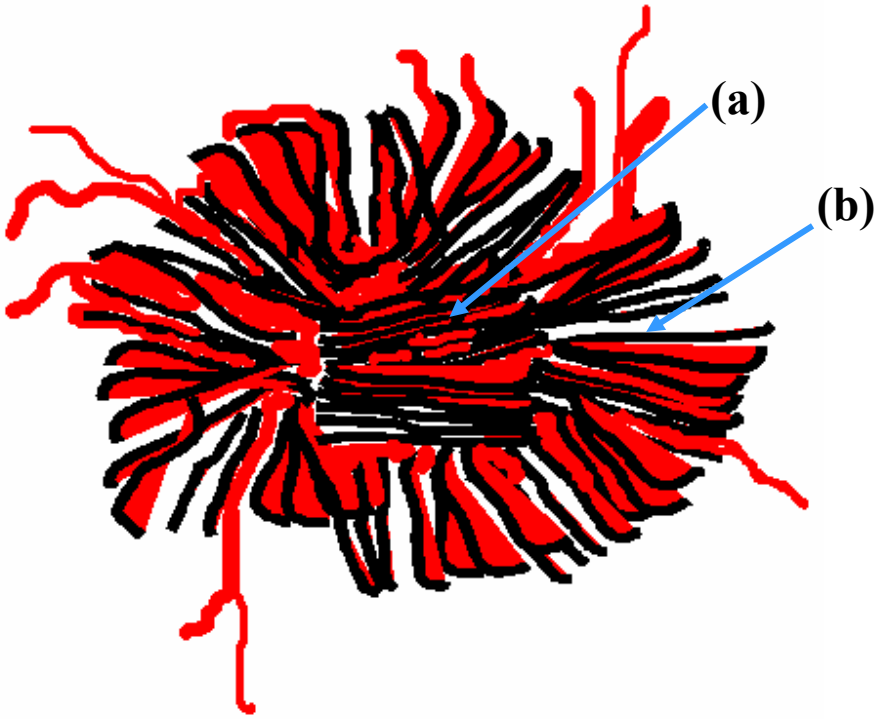


**Figure 2-6.** Model for intercalation and exfoliation by in-situ polymerization with MMT/TIBA/UOH/CAT and MAO showing several types of MMT platelets in the particle after the in-situ polymerization: (a) particle core showing different orientations of intercalated and exfoliated MMT layers; (b) opening edges of the MMT layers in the external surface of the particle.

### 2.3.4. Organic Modification of MMT and TGA Analysis

Figure 2-7 shows that MMT and MMT/TIBA/UOH particles have a different behaviour when suspended in deionized water. A mass of 0.5 mg of each sample was suspended in deionized water in 10 mL glass vials and shaken for 5 minutes. The vials were left for 24 hours to allow the free precipitation of MMT and MMT/TIBA/UOH particles in water.

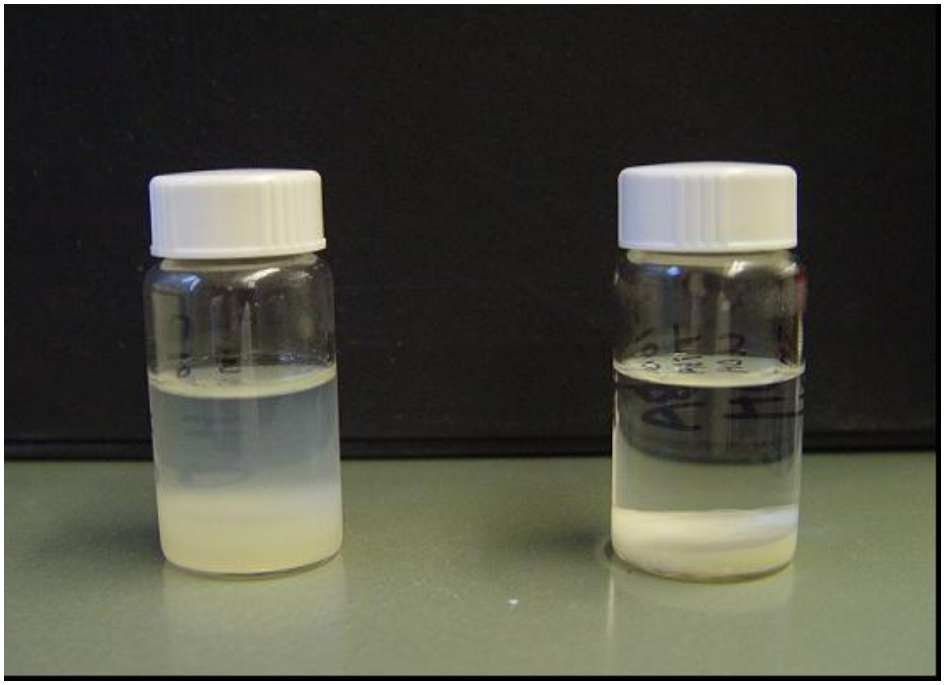

**(a)** **(b)**

**Figure 2-7.** MMT and MMT/TIBA/UOH were suspended in deionized water and shaken for 5 minutes. After free precipitation for 24 hours, images were captured with a Sony camera: (a) MMT, (b) MMT/TIBA/UOH.

After 24 hours, MMT (Figure 2-7.a) formed dispersion, whereas MMT/TIBA/UOH had settled to the bottom and showed a transparent supernatant. The MMT surface is hydrophilic and easy to be wetted, but MMT/TIBA/UOH showed clear phase separation from the aqueous phase (Figure 2-

7.b). This observation implies that MMT surface was changed by UOH from a hydrophilic to a lipophilic character. These results support the surface modification of MMT with UOH.

Thermogravimetric analysis (TGA) was conducted to confirm the presence of UOH on the MMT surface. Figure 2-8 shows the TGA thermographs of MMT, MMT/TIBA, MMT/TIBA/UOH and MMT/TIBA/UOH/CAT. MMT residues after removing part of the polymer chains by Soxhlet extraction (MMT/TIBA/UOH/CAT/PEex) were also analyzed.

MMT (curve (a) in Figure 2-8.a and b) shows first a 5 wt.-% loss at 100 °C due to loss of hydration water, then an additional 5 wt.-% weight loss around a higher temperature range (approximately from 400 to 700 °C), which is due to structural dehydroxylation of MMT (Iler, 1979; Kellum and Smith, 1967; de Farias and Airoldi, 1998; Jal et. al., 2004). The remaining 90 wt.-% represent the inorganic atoms that are still thermally stable at 1100°C, presumably sintered MMT plates.

The thermogram for MMT/TIBA (curve (b) in Figure 2-8.a and b) shows a 2 wt.-% loss in the interval 100 ~ 200 °C, which may be due to volatile molecules, such as water molecules and TIBA alkyl groups. A 3 wt.-% loss from 200 ~ 300 °C may be due to the vaporization of TIBA alkyl groups, while the last weight loss peak coincides with the weight loss due to the elimination of hydroxyl groups inside the MMT plates.

The thermogram for MMT/TIBA/UOH (curve (c) in Figure 2-8.a) also shows a 1.5 wt.-% loss of water (100 ~ 200 °C), a loss of about 4 wt.-% from 370 ~ 430°C, and finally a loss of 5 wt.-% from 430 °C to 1100 °C. The weight loss of volatile molecules, for MMT/TIBA/UOH (100 ~ 200 °C), is less than that for MMT and MMT/TIBA, probably because the UOH-modified surface of MMT makes it more difficult for the clay surface to adsorb water.

MMT/TIBA/UOH/CAT (curve (d) in Figure 2-8.a and b) shows a different weight loss trend. Its total weight loss is about 7.5 wt.-%, less than those of the previous MMT samples. We observe a smaller weight loss of hydrated water from 100 ~ 200 °C. On the other hand, there is a steady weight

loss, from ~ 270 °C to 600 °C. In this high temperature region, weight loss could be attributed to the decomposition of the organic groups of the catalyst, located between the MMT galleries.

Based on the TGA thermograms, the contents of TIBA and UOH in the MMT particles can be calculated. Assuming that hydrocarbon degradation of MMT/TIBA takes place from 140 to 350 °C, the number of moles of TIBA can be calculated as 8 μmoles/ g-clay. With the same method, the UOH concentration is calculated as12 μmoles/g-clay, assuming that the weight loss from 140 to 350 °C comes from hydrocarbons from UOH. After extraction of polyethylene from PE-clay nanocomposites, the residue left in the thimble has a higher weight loss, from 300 ~ 500 °C, probably due to the degradation of the remaining polymer chains on the clay surface (curve (e) in Figure 2-8.a and b)

The presence of polyethylene in the clay after Soxhlet extraction indicates that polyethylene is strongly bonded to the clay surface. Even after extraction with boiling TCB for 24 hours, polyethylene could not be completely removed from the clay. This provides strong evidence to our hypothesis that polyethylene is covalently bonded to the clay surface.

To achieve a more detailed analysis, the decomposition of MMT/TIBA/UOH was carried out in three different temperature-zones and its residues were palletized with KBR powder and analyzed with FT-IR (Figure 2.9). The FT-IR spectrum of the residue after a temperature scan up to 350°C shows a strong C-H stretching band at 2931 $cm^{-1}$, due to remaining hydrocarbon chains in MMT, whereas the residue after 650°C shows an attenuated band for C-H stretching. This observation implies that most of the hydrocarbon chains were decomposed from 350 to 650$^{o}$C, a higher temperature region than normally observed for organic materials, including UOH. It can be speculated that the UOH molecules intercalated in the clay galleries delayed the decomposition to higher temperatures. Small portions of hydrocarbon were still detected by FT-IR even after a temperature sweep from 650°C to 850C°. A fraction of the 6.4 wt% loss measured in this region could be attributed to hydrocarbon chains, likely UOH molecules intercalated in the clay galleries.

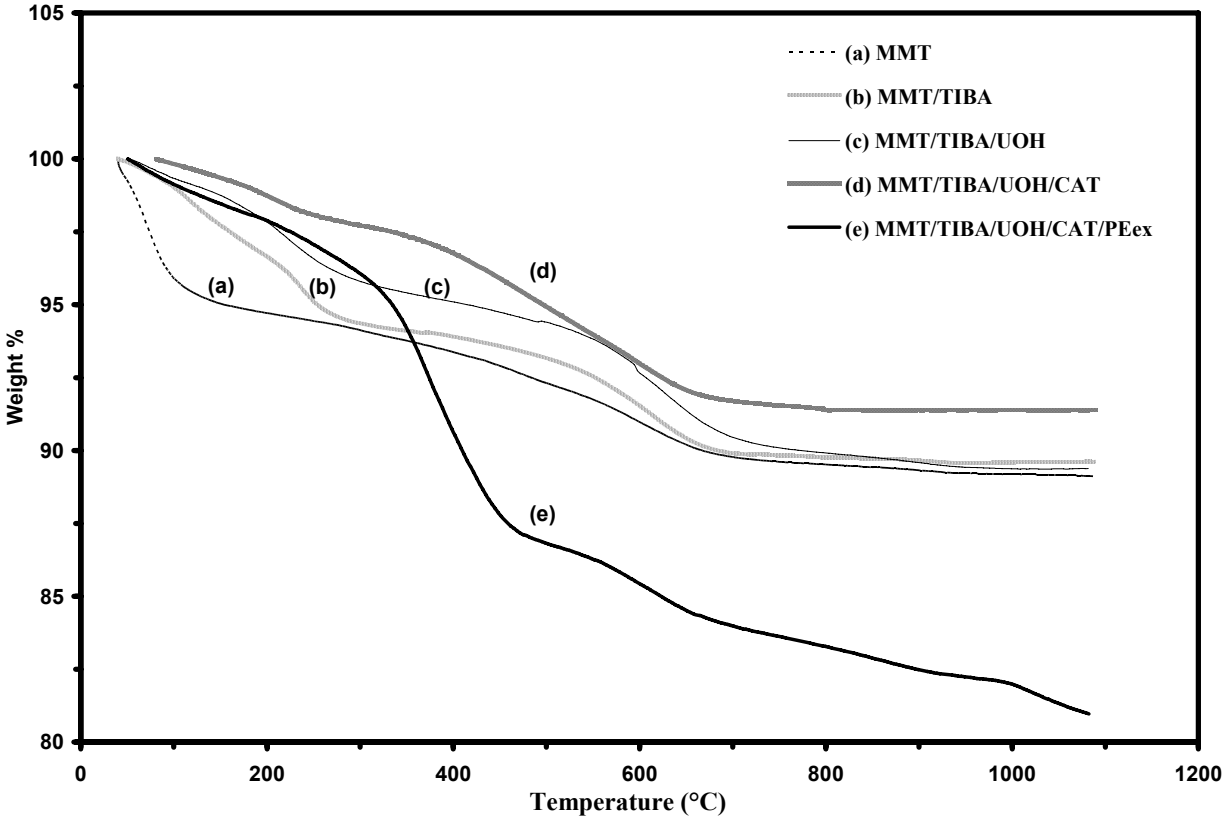
105
100
95
90
85
80
0
200
400
600
800
1000
1200
Weight %
Temperature (°C)
(a) MMT
(b) MMT/TIBA
(c) MMT/TIBA/UOH
(d) MMT/TIBA/UOH/CAT
(e) MMT/TIBA/UOH/CAT/PEex
(a)
(b)
(c)
(d)
(e)

**(a)**

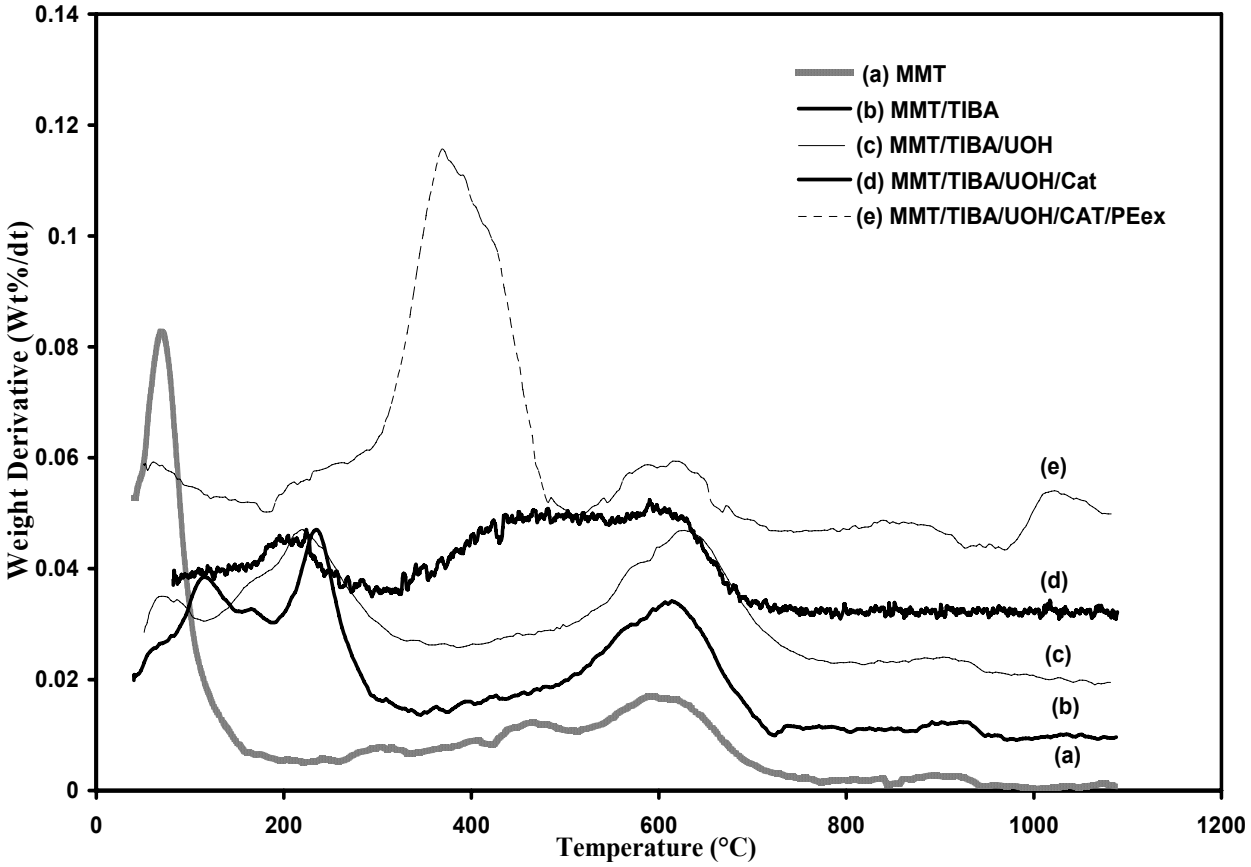


**(b)**

**Figure 2-8.** TGA thermographs for pristine MMT, MMT/TIBA, MMT/TIBA/UOH, MMT/TIBA/UOH/CAT and MMT residue after Soxhlet extraction with refluxing 1,2,4-trichlorobenzene for 24 hours; (a) Weight loss, (b) Weight loss derivative.

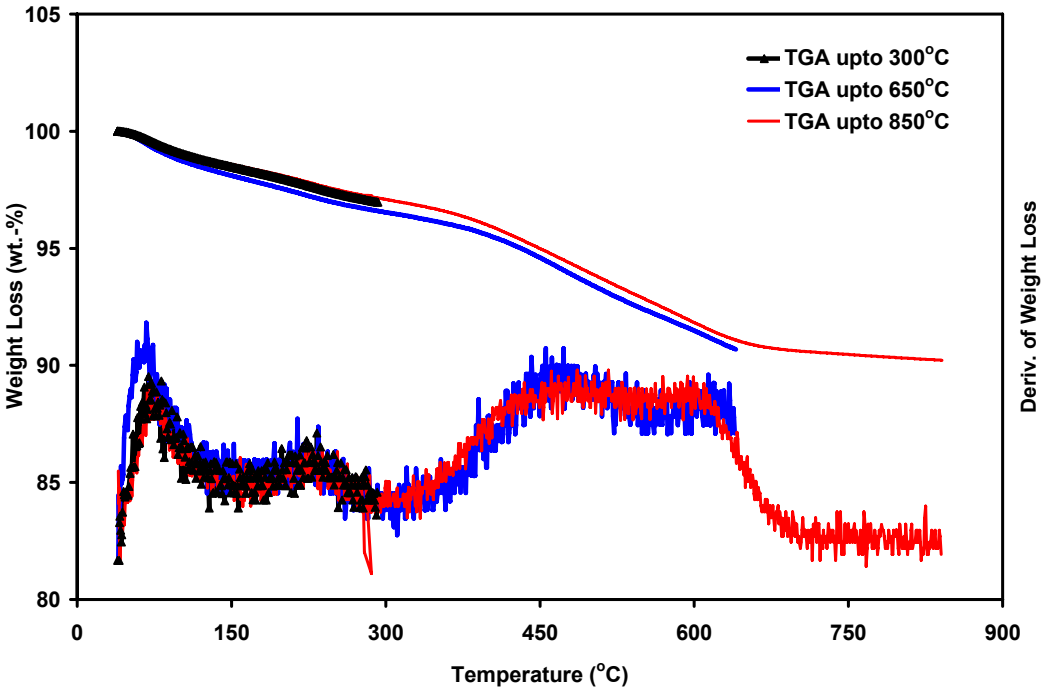


(a)

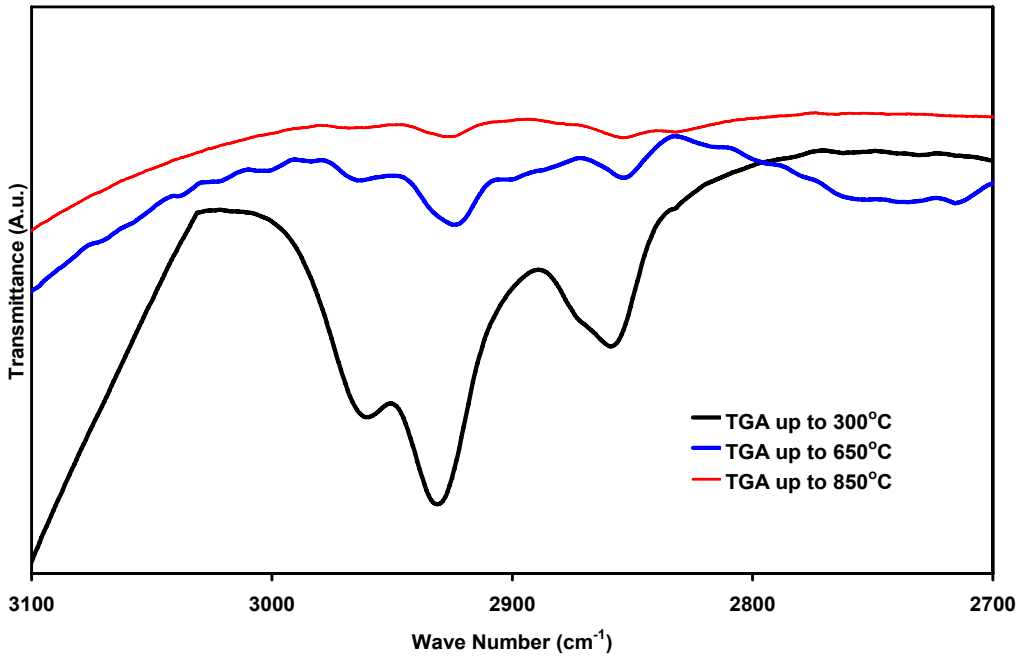


(b)

**Figure 2-9.** (a) TGA thermograph of MMT/TIBA/UOH and (b) FT-IR spectra of its residues in different temperature zones**.** (C-H stretching band at 2931 $cm^{-1}$)

### 2.3.5. In-Situ Polymerization (Low Pressure)

The catalyst-impregnated MMT (MMT/TIBA/UOH/CAT) was effective for ethylene polymerization, as indicated in Table 2-2. The approach proposed here produces polyethylene in good yield as compared with the yield obtained in the absence of MMT (entry 1 in Table 2-2). The clay wt.-% in the final polymer reported in Table 2-2 was determined by TGA or by using the initial clay loading and final polymer yield. Both methods agree well.

As shown in Table 2-2, it was possible to control the ratio between polyethylene and MMT by controlling the polymerization time or the initial MMT loading. Note that it is possible that only a fraction of the catalyst added to the MMT worked as active centers for polymerization. The quantification of active centers is still a theme of debate in the scientific literature and was not in the scope of this thesis.

For the same initial MMT/TIBA/UOH/CAT loading, increasing the polymerization time produces more polymer chains and decreases the weight percent (wt.-%) of MMT in the final product (see entries 2 and 3 in Table 2-2). This is important if such a system is chosen to prepare a master batch of PE-clay nanocomposites for subsequently blending with other polymers.

The polymerization temperature also affected the wt.-% of MMT in the final product in the range studied, most probably because decreasing the polymerization temperature decreases catalyst activity and the number of branches of the polyethylene chains (see entry 6 in Table 2-2); Ni-diimine produces polyethylene with fewer branches at lower polymerization temperatures (Simon et al., 2001).

The polyethylene-clay nanocomposites obtained from in-situ polymerization was submitted to extraction with TCB. The polyethylene fraction that was soluble in TCB was recovered by precipitation in ethanol, filtered, and dried in vacuum for 24 hours. The weight percentage that was extracted (Table 2-2) ranged from 58.7 % to 90.2 %.

The melting temperature ($T_m$) decreased as the MMT content increased. It has been reported that nanosize distributed MMT platelets may hinder the crystallization of some kinds of semi-crystalline polymer, resulting in a lower melting temperature (Fornes et al., 2003;Wendy et al., 2005). Another possible explanation is that the clay influences the branching mechanism by chain walking during polymerization (polyethylene with more short braches has a lower melting point).

The decomposition temperature ($T_D$) increased as the MMT content increased. It is well known that increasing the content of exfoliated MMT platelets decreases the rate of oxygen diffusion from the gas phase and of the thermo decomposition products produced between the clay galleries. According to Gilman et al. (1999), the diffusion of both volatile products produced by thermo oxidation in the clay galleries and oxygen from the gas-phase to the clay galleries could be hindered by the reassembly of the reticular distribution of the exfoliated clay plates on the surface.

PE-clay hybrid nanocomposites made by in-situ polymerization were analyzed with TGA. The weight loss versus temperature curves and their derivatives are shown in Figure 2-10. Figure 2-10 shows that the decomposition temperature increases as the MMT content increased. When the clay content changes from 6.3 wt.-% to 19.1 wt.-%, the onset of the decomposition temperature increased from 440 to 462 °C. There is a difference of 45 °C between the main decomposition temperature from pure polyethylene and a nanocomposite with 19.1 wt.-% of MMT. This significant difference in decomposition temperature, which depends on the clay content, could be due to a barrier/diffusion effect on mass transfer, oxygen from the atmosphere to the internal clay surface and decomposition products from inside of the clay galleries.

**Table 2-2**. Preparation of hybrid polyethylene-clay nanocomposites by in-situ polymerization with MMT/TIBA/UOH/Ni-diimine/MAO (1-6) and MMT/TIBA /UOH/ $Cp_2ZrCl_2$ /MAO (7-9).

| No. | Polymerization | | | | | Characterization | | |
|---|---|---|---|---|---|---|---|---|
| | Initial clay loading (mg) | Time (min) | Yield (pol+clay) (g) | Clay (wt.- %) [c] | Clay (wt.-%) [d] | Extract in TCB (wt.- %) | $T_m$ ($^oC$) | $T_D$ ($^oC$) |
| 1 | - | 90 | 1.6 [b] | 0 | 0 | 100 | 114 | 429 |
| 2 | 100 | 30 | 0.4 | 25.0 | 25.2 | 74.3 | 107 | 458 |
| 3 | 100 | 90 | 1.6 | 6.25 | 6.3 | 72.4 | 124 | 440 |
| 4 | 200 | 60 | 1.8 | 11.1 | 9.4 | 76.7 | 123 | 457 |
| 5 | 200 | 60 | 1.0 | 20.0 | 19.1 | 58.7 | 122 | 461 |
| 6 | 50 [e] | 30 | 0.2 | 25.0 | 28.5 | - | 100 | - |
| 7 | 200 | 60 | 0.92 | 21.7 | 19.0 | 90.2 | 128 | 460 |
| 8 | 100 | 60 | 1.5 | 6.0 | - | | 130 | 463 |
| 9 | 100 | 90 | 2.0 | 3.2 | 3.5 | - | 131 | 457 |

[a] Polymerization conditions: room temperature, atmospheric pressure of ethylene

[b] Homopolymerization of ethylene, no clay added, productivity 843 $kg_{pol}/mol_{Ni}.h$

[c] Determined using the initial clay loading and final polymer yield

[d] Determined by TGA

[e] Polymerization temperature 0 $^oC$

$T_m$ : temperature peak during melting measured by DSC

$T_D$: temperature peak during decomposition measured by TGA

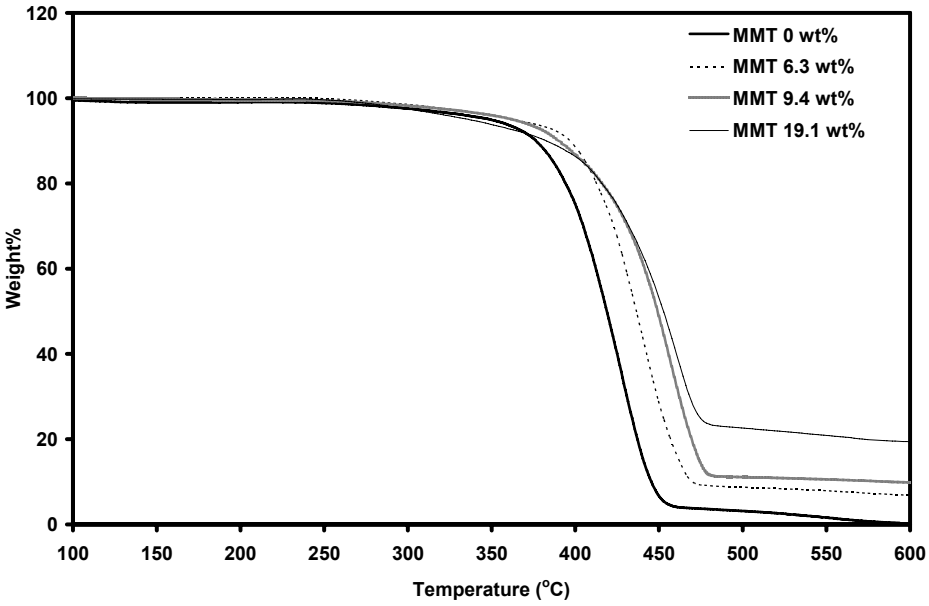


**(a)**

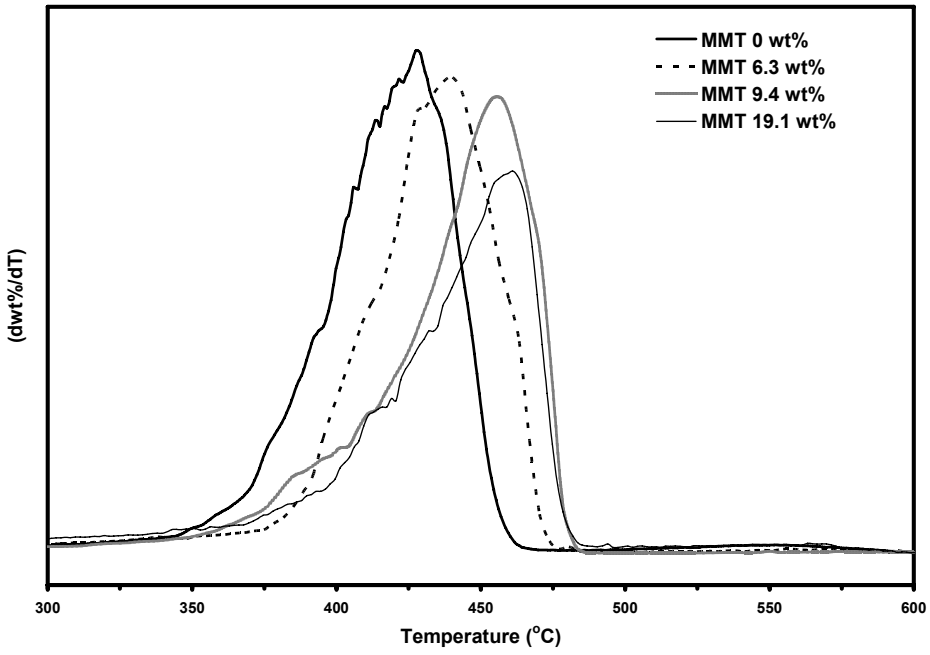


**(b)**

**Figure 2-10.** TGA thermographs for nanocomposites with different clay wt.-%: (a) Weight loss against temperature increase, (b) Derivative of weight loss against temperature increase.

### 2.3.6. Morphology of MMT and Organic-Modified MMT

The morphology of MMT was investigated with scanning electron microscopy (SEM) before and after organic modification. Figure 2-11 provides the overview and detail images of MMT from low (150×) to high (30,000×) magnification.

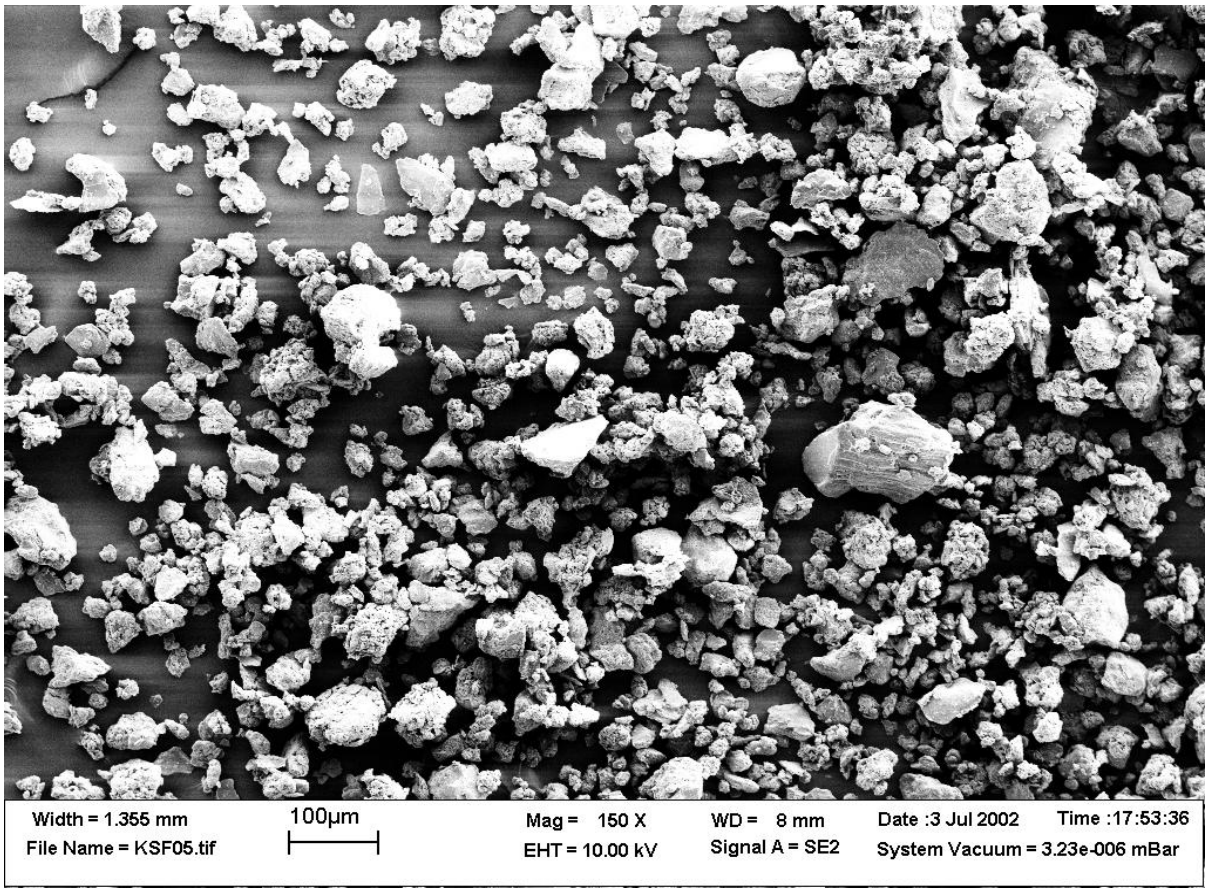


**(a)**

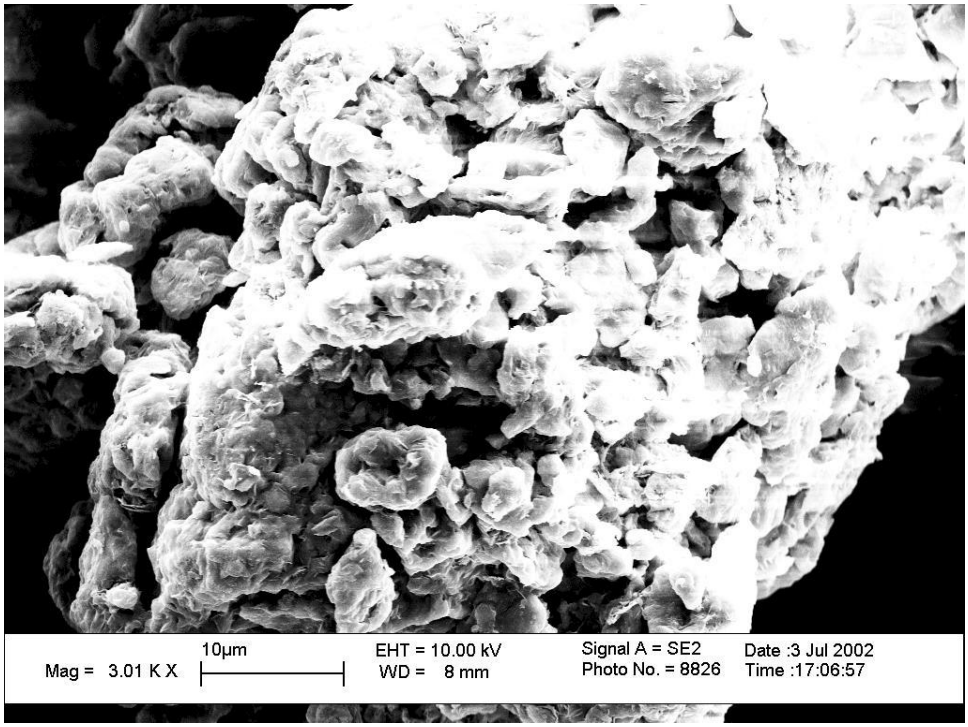
10µm
Mag = 3.01 K X
EHT = 10.00 kV
WD = 8 mm
Signal A = SE2
Photo No. = 8826
Date :3 Jul 2002
Time :17:06:57

**(b)**

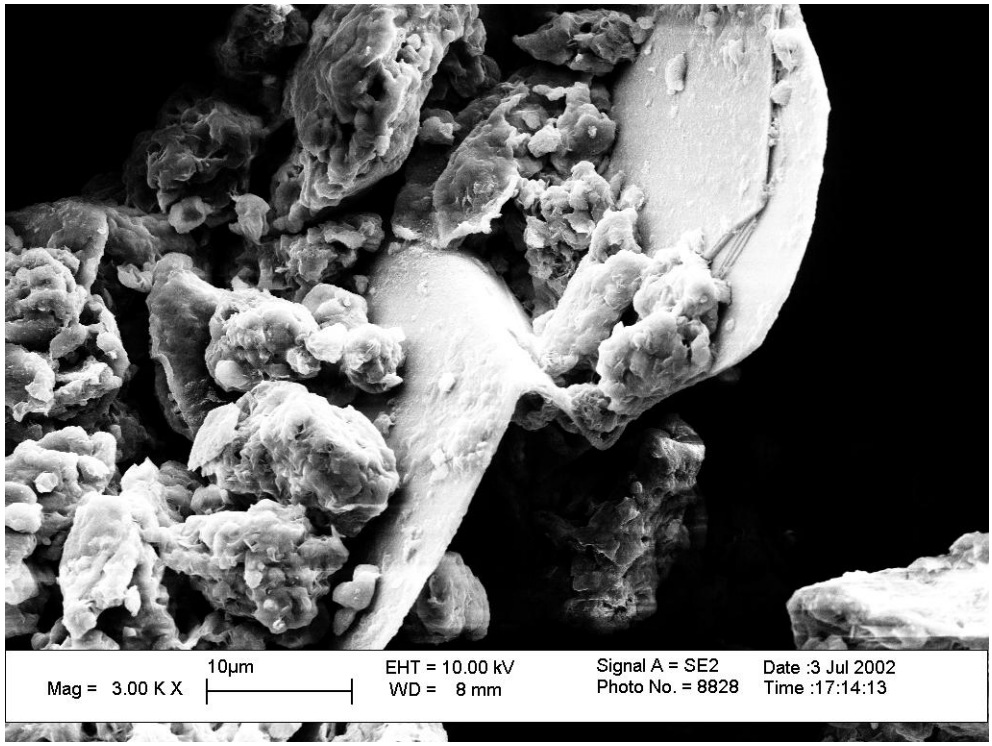
10µm
Mag = 3.00 K X
EHT = 10.00 kV
WD = 8 mm
Signal A = SE2
Photo No. = 8828
Date :3 Jul 2002
Time :17:14:13

**(c)**

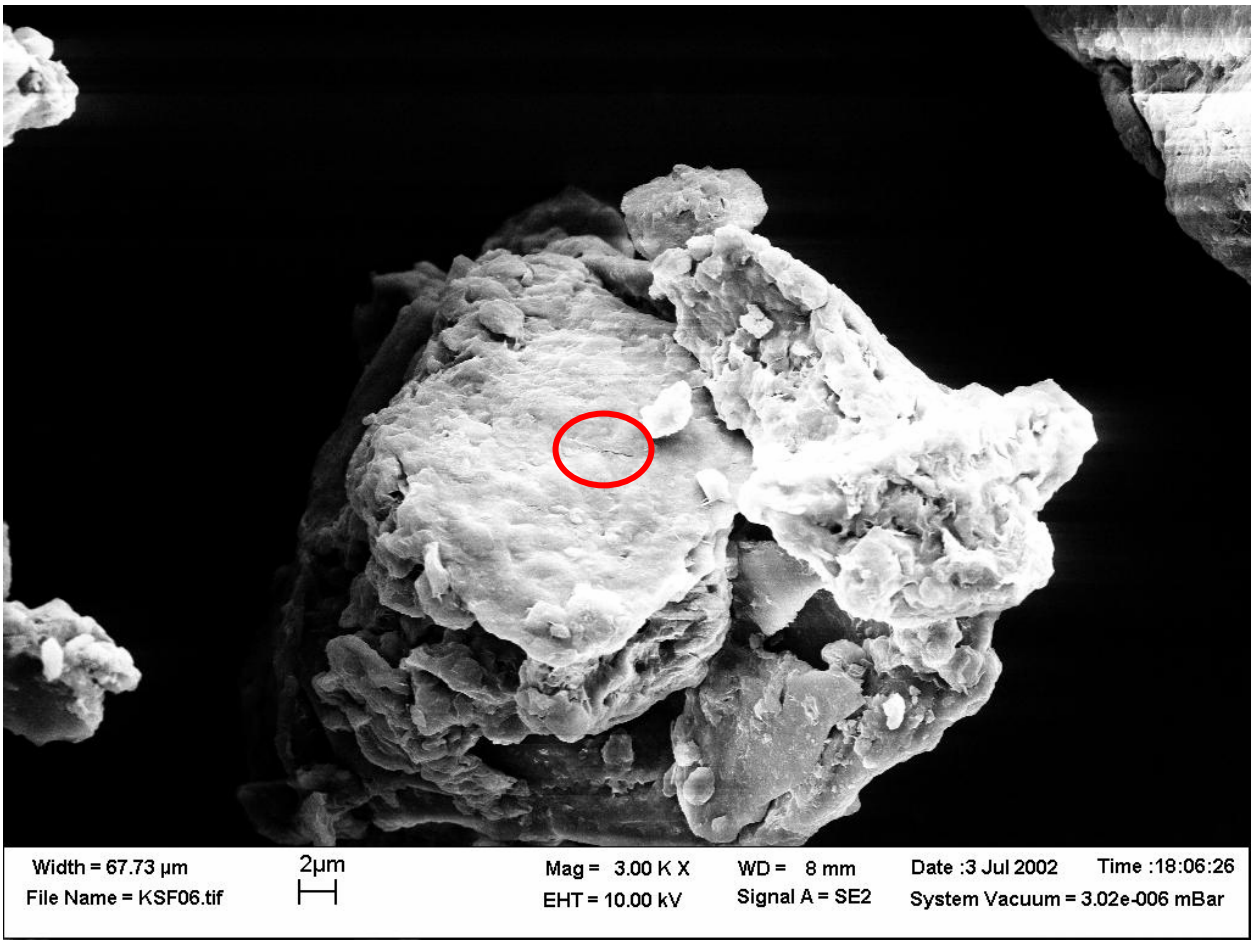
Width = 67.73 µm
File Name = KSF06.tif
2µm
Mag = 3.00 K X
EHT = 10.00 kV
WD = 8 mm
Signal A = SE2
Date :3 Jul 2002
Time :18:06:26
System Vacuum = 3.02e-006 mBar

**(d)**

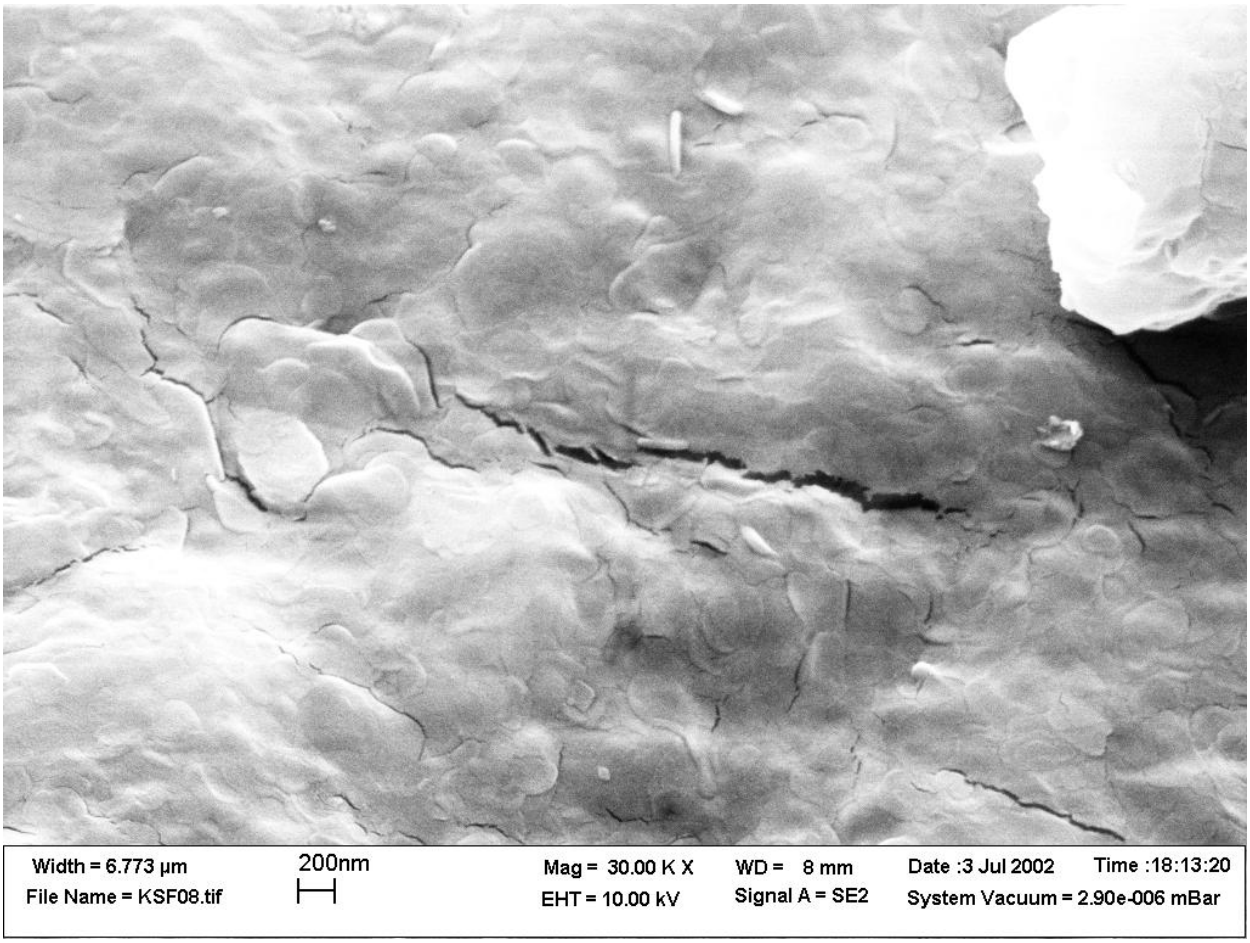


**(e)**

**Figure 2-11.** MMT particles: (a) Overall shapes of MMT particles, (b) MMT particles showing cabbage morphology, (c) MMT particles on the bare surface of illites, (d) Expanded cabbage shape of MMT, (e) Expanded surface of the highlighted area of the particle shown in Figure 2-11.d.

The SEM image in Figure 2-11.a shows different types of the MMT particles. The detailed image in Figure 2-11.b indicates that their surface is covered with irregular-shaped smaller particles (resembling the shape of a cabbage). As mentioned in Section 1.1.1, MMT particles contain some impurities, such as mica and quartz. Figure 2-11.c reveals that MMT particles are attached onto layered plates that may be illite group particles. Figure 2-11.d shows a typical MMT particle, made of aggregated MMT lamellae. The area marked with a red circle was expanded to confirm a 200 nm-sized MMT lamellae structure in Figure 2-11.e.

Figure 2-12 shows the morphology of MMT after treatment with TIBA (MMT/TIBA). At this magnification, the MMT/TIBA particles resemble the MMT particles shown in Figure 2-11. Figures 2-12.a and b expand these images, indicating that some MMT particles "sit" on the surface of the mica-type particles after the surface modification steps with TIBA.

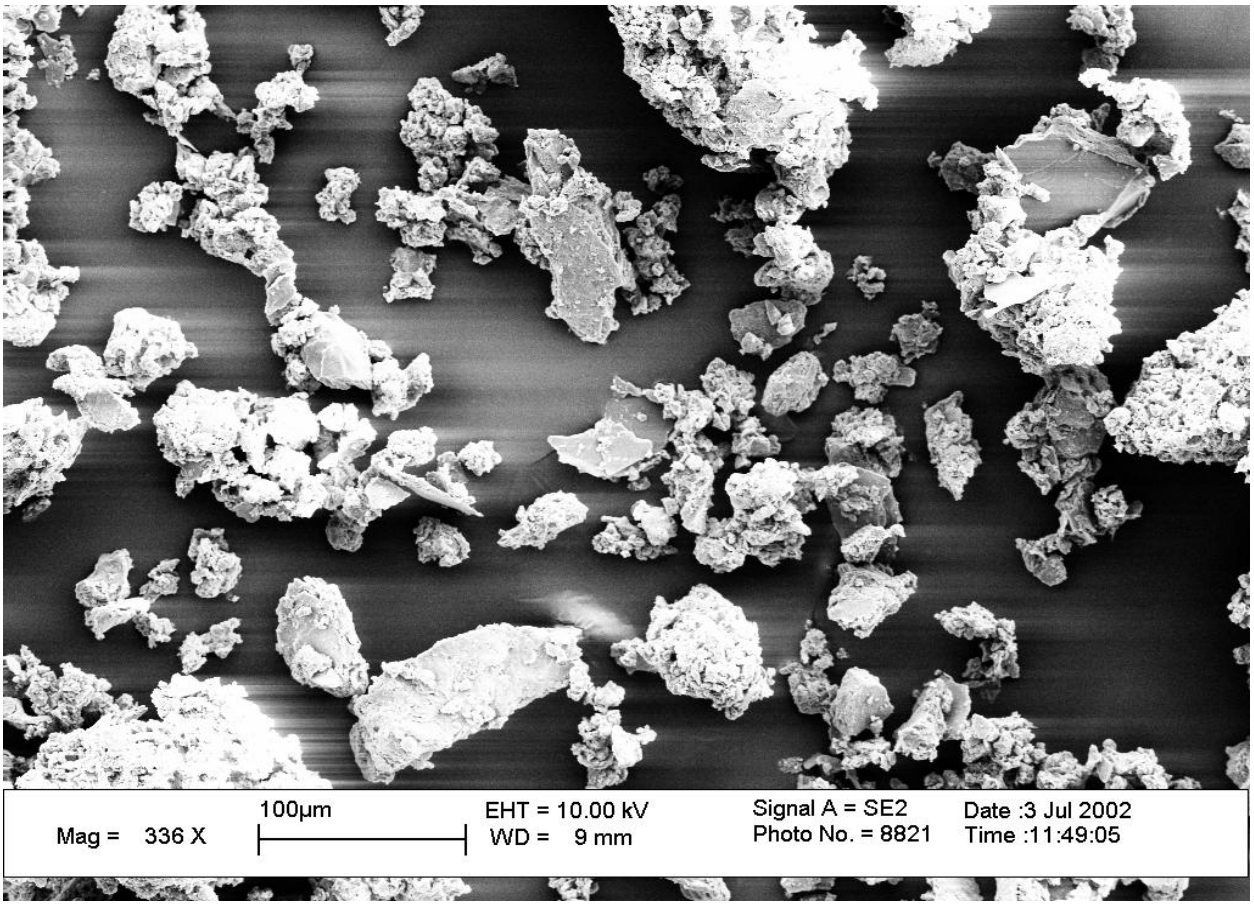


**(a)**

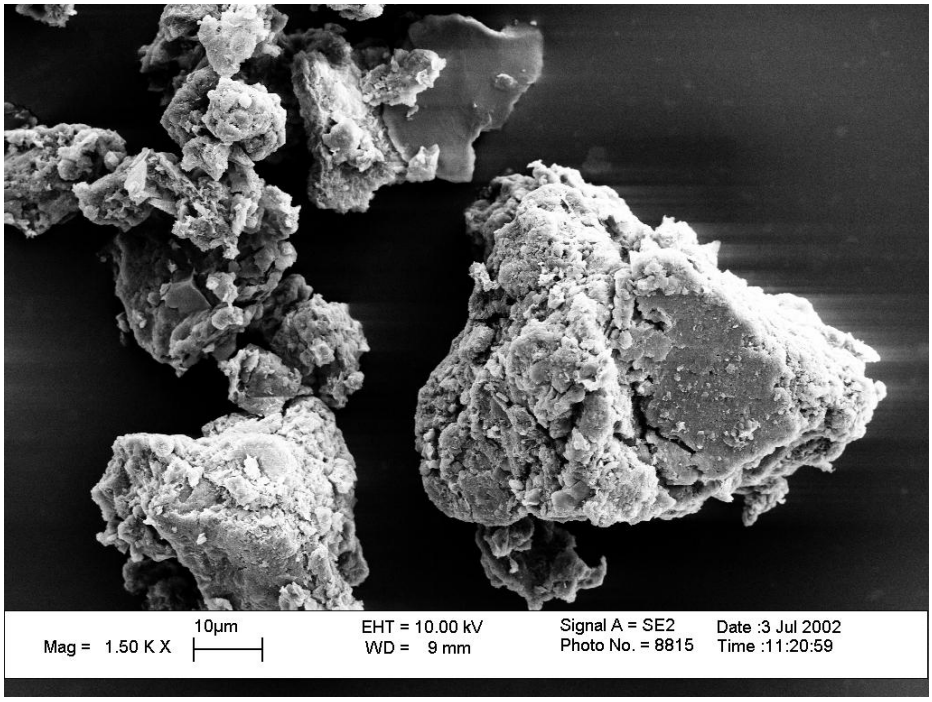


**(b)**

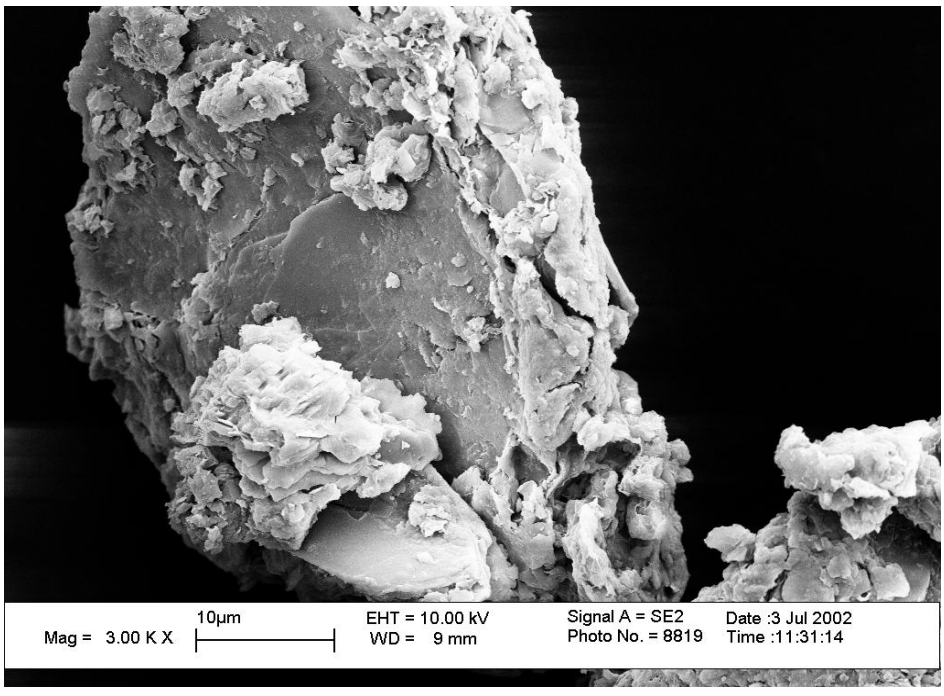


**(c)**

**Figure 2-12.** MMT/TIBA particles: (a) Overview of MMT/TIBA, (b) Expanded morphology of MMT/TIBA, (c) MMT/TIBA particle on mica-type particle.

After TIBA treatment, MMT was further treated with UOH (MMT/TIBA/UOH). In Figure 2-13.a, the overview image of MMT/TIBA/UOH is similar to those of MMT and MMT/TIBA. The image in Figure 2-13.b reveals that two types of particles are present: irregular-shaped (cabbage type) MMT particles and mica-type layered particles. These SEM images supported the XRD analysis which contains the sharp band at 8.9°, which implies no distance between the clay platelets, as discussed in Section 1.7.1.

.

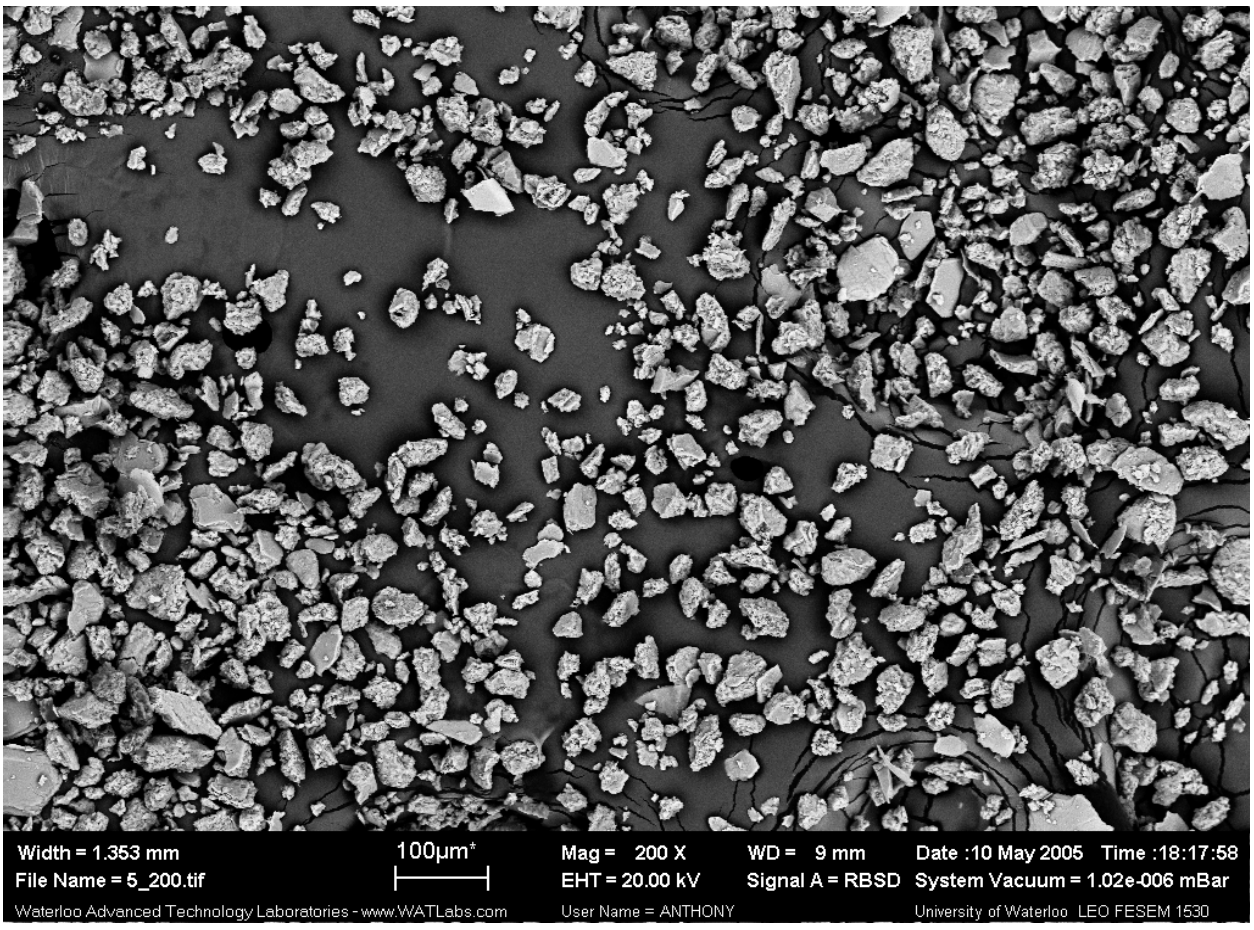


**(a)**

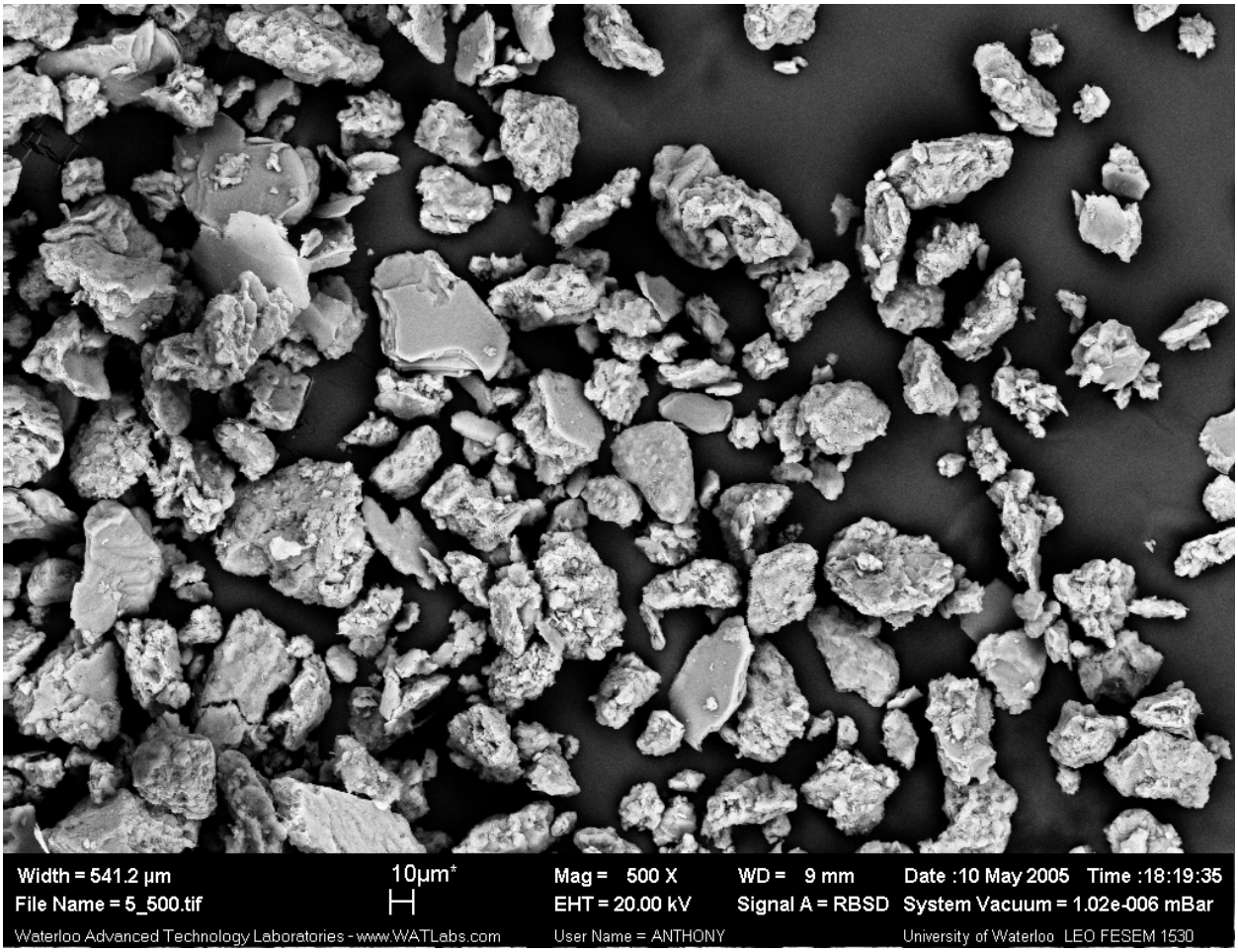


**(b)**

**Figure 2-13.** MMT/TIBA/UOH/Catalyst particles; (a) Overview of particles of MMT/TIBA /UOH, (b) Expanded morphology of MMT/TIBA/UOH.

### 2.3.7. Morphology of the PE-Clay Hybrid Nanocomposites

The degree of exfoliation obtained after the in-situ polymerization of ethylene was probed using TEM. Figure 2-14 shows the TEM micrograph of a film produced by scooping a nanocomposite solution after the polymerization with the grid for microscopy, and the TEM micrograph of a film (thickness of 50 nm) produced by melt pressing the nanocomposites directly onto the grid.

MMT has dimensions in the order of tens of micrometers, as shown in Figure 2-11. In the final nanocomposite, most of the MMT is homogeneously distributed over the polyethylene matrix and the dimensions are in the order of tens of nanometers (Figure 2-14). There were, however, some indications of partial exfoliation evidenced by the presence of MMT clusters. It can be speculated that, during the film formation, the polyethylene chains chemically bonded to the surface of the exfoliated MMT drag each individual layer as the polymer flows. If MMT had not been exfoliated during the in-situ polymerization, MMT clusters at the micrometer size range would have been present after film preparation.

Figure 2-14.a shows that the polymer fibers and the clay surfaces are intimately connected, likely by chemical bonds. In Figure 2-14.b, the TEM image indicates that the nanosized clay particles are well distributed in PE-clay hybrid nanocomposite with 6 wt.-% clay loading.

A plausible mechanism for PE-clay bonding is suggested in Figure 2-15. During the in-situ polymerization of ethylene, different polymer-clay morphologies are expected:

(a) Polyethylene chains formed during in-situ polymerization inside MMT galleries that do not copolymerize with the vinyl alcohol groups will not be chemically linked to the surface and could be removed by solubilization (excluding other mechanisms of chain transfer that could lead to bonding with the surface).

(b) Polyethylene chains that start with the vinyl alcohol group as the first monomer should be linked to the surface by the chain end. If a chain transfer step to alkylaluminum groups

bonded to the MMT surface takes place, the polyethylene chain would be also linked to the MMT surface by its chain end.

(c) If the polyethylene chain copolymerizes the vinyl alcohol group and then is transferred, it will be linked to the MMT surface by some point (or points) located between its chain ends.

(d) The active site could also copolymerize vinyl alcohol groups from opposite MMT surfaces, which would preclude complete exfoliation, since the layers would be connected via covalent bonds.

(e) Finally, different MMT layers after exfoliation could be connected by copolymerization of vinyl alcohol groups on distinct MMT layers.

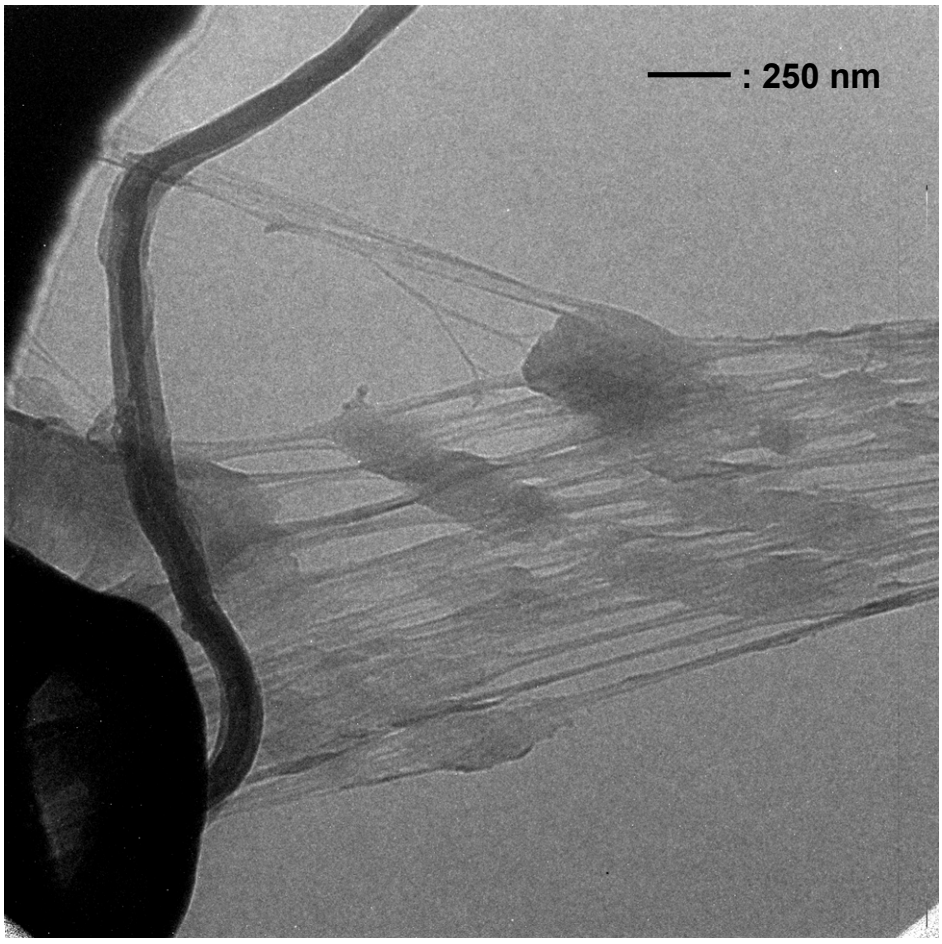


**(a)**

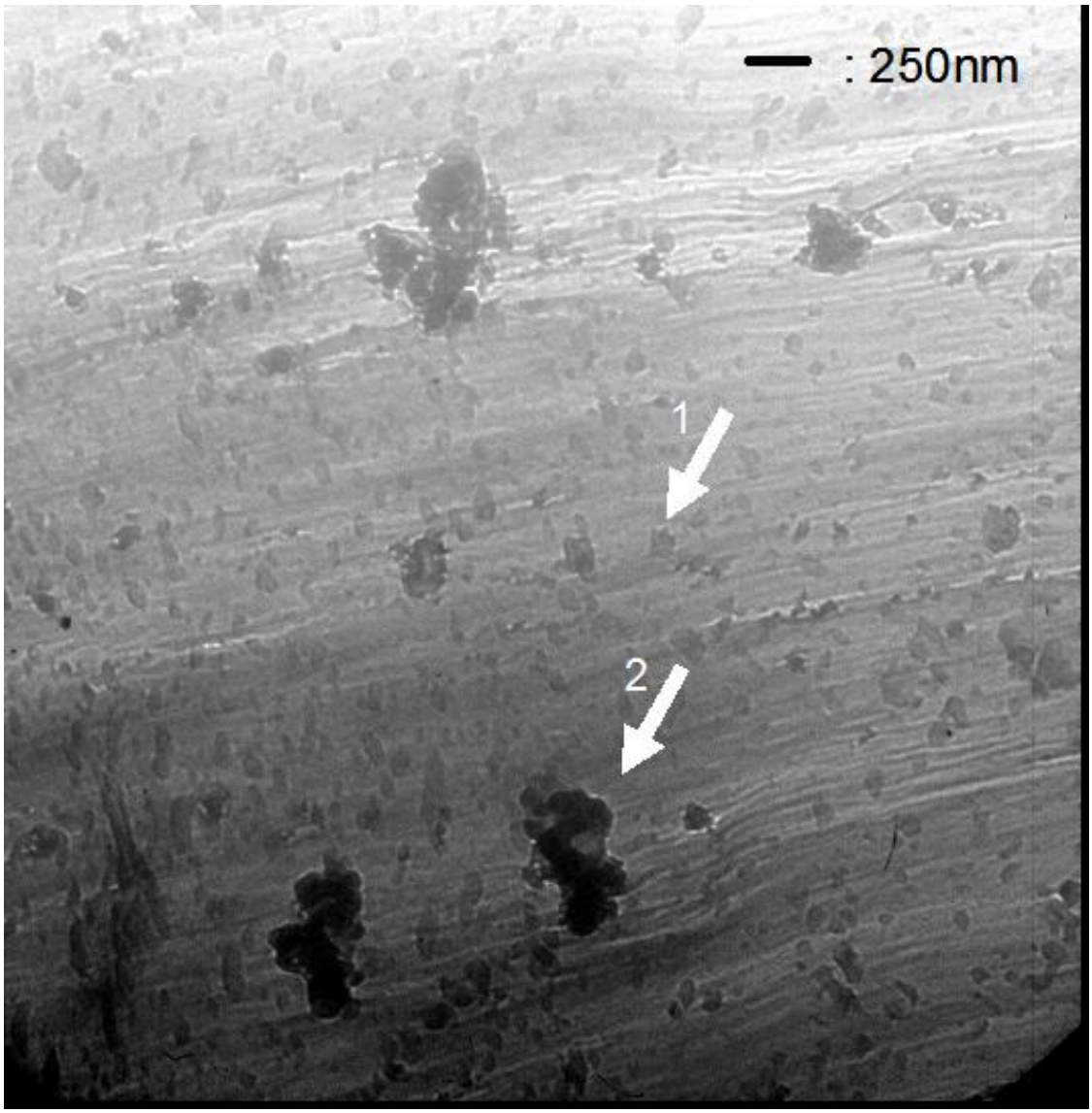


**(b)**

**Figure 2-14.** (a) Clay particle morphology obtained by scooping the dissolved sample in monochlorobenzene solution after the polymerization, (b) TEM micrograph of 50 nm-thick film indicating a homogeneous dispersion of clay layers: 1- on the polyethylene matrix, and 2-isolated clusters.

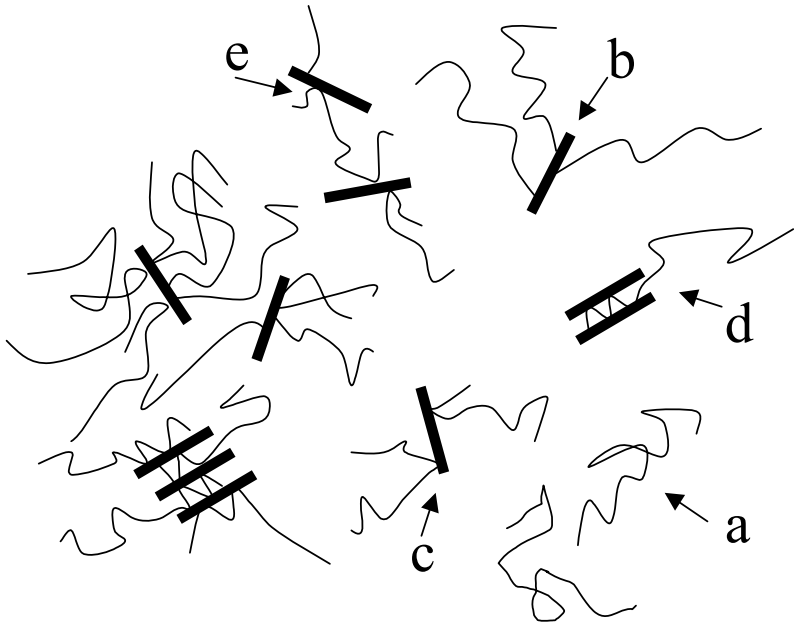


**Figure 2-15.** Proposed model for PE-clay hybrid nanocomposites: a) isolated polyethylene chain; b) polyethylene chain linked by its end to the organic modifier at the surface of an exfoliated MMT layer; c) polyethylene chain having the center part linked to the organic modifier at the surface of an isolated MMT layer; d) polyethylene chain linked a number of times to organic modifiers from opposite MMT layers, and the distance between the two silicate layers is close to that found in the intercalation; e) polyethylene chain linked to organic modifiers from distinct MMT layers, and the distance between the two silicate layers is much higher than that found during intercalation.

### 2.3.8. PE-Clay Hybrid Structure

Extraction of polyethylene chains from the hybrid PE-clay nanocomposite was carried out using hot TCB in a Soxhlet extractor. Results in Table 2-2 show that only part of the polyethylene could be extracted after 24 hours in reflux. Figure 2-16 shows SEM images of the residues after extraction and identifies distinct MMT and polyethylene phases. EDX also confirms that polyethylene was not totally removed from the PE-clay hybrid nanocomposites by TCB extraction, as will by discussed in Section 2.3.9.

The residue collected in the paper thimble was dried under vacuum oven at 70 °C for 24 hours and analyzed with SEM/EDX. Figure 2-16.a, (9 wt.-% MMT) indicates the presence of polyethylene directly connected on the surface of clay platelets after extraction. The expanded image, Figure 2-16.b, shows that the polymer fibrils with approximately 40 nm size are connected to the MMT surface. Given the size of these fibrils, they are likely composed of a bundle of several polyethylene chains. This image could be direct evidence of the interaction between polymer chains and MMT surface. Figure 2-16.c to 2-16.e are SEM images of a 19 wt.-% MMT sample. They show another morphology for PE-clay hybrid fibers, with thickness around 600 to 1000 nm.

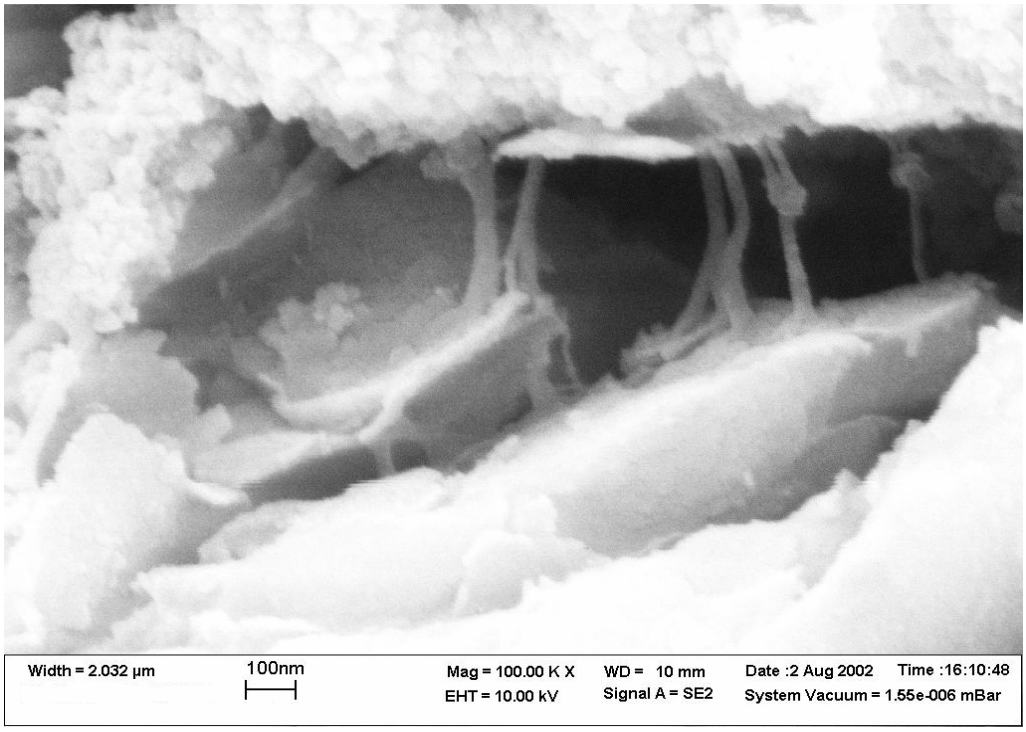
Width = 2.032 µm
100nm
Mag = 100.00 K X
EHT = 10.00 kV
WD = 10 mm
Signal A = SE2
Date :2 Aug 2002
Time :16:10:48
System Vacuum = 1.55e-006 mBar

**(a)**

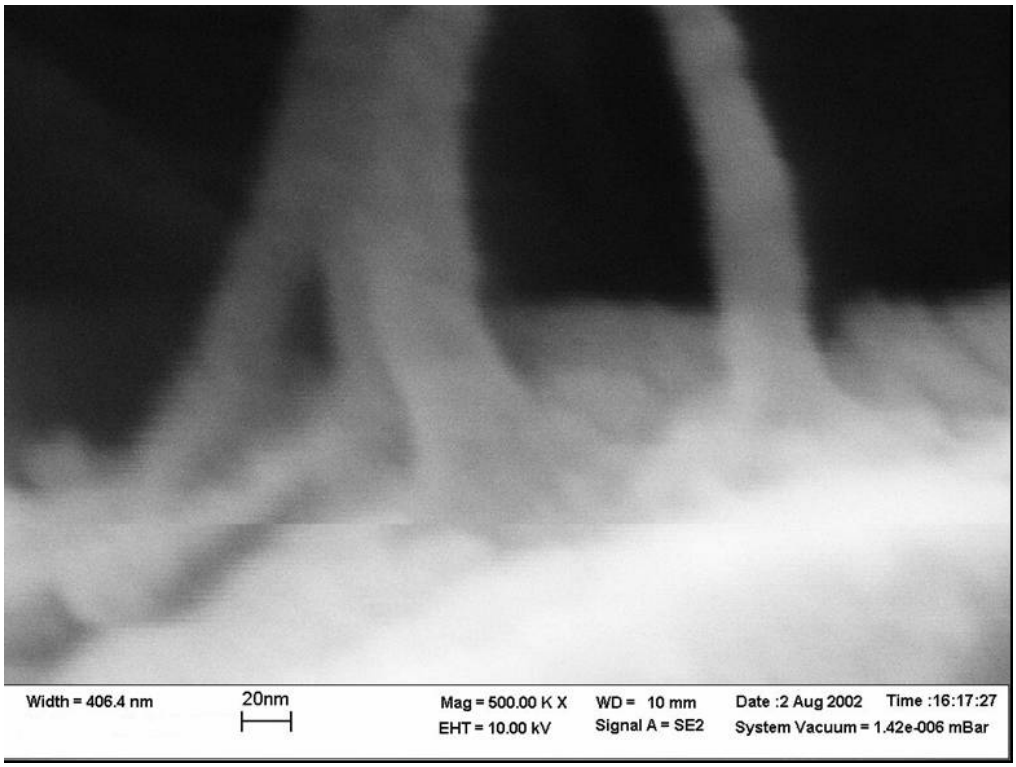
Width = 406.4 nm
20nm
Mag = 500.00 K X
EHT = 10.00 kV
WD = 10 mm
Signal A = SE2
Date :2 Aug 2002
Time :16:17:27
System Vacuum = 1.42e-006 mBar

**(b)**

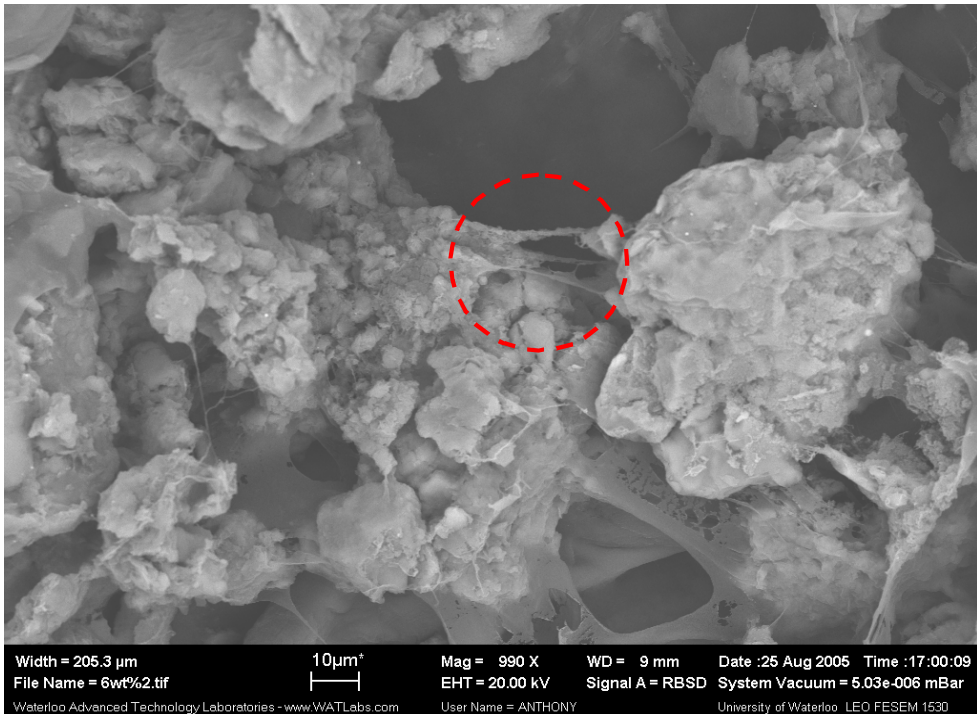
Width = 205.3 µm
File Name = 6wt%2.tif
10µm
Mag = 990 X
EHT = 20.00 kV
WD = 9 mm
Signal A = RBSD
Date :25 Aug 2005 Time :17:00:09
System Vacuum = 5.03e-006 mBar
Waterloo Advanced Technology Laboratories - www.WATLabs.com
User Name = ANTHONY
University of Waterloo LEO FESEM 1530

**(c)**

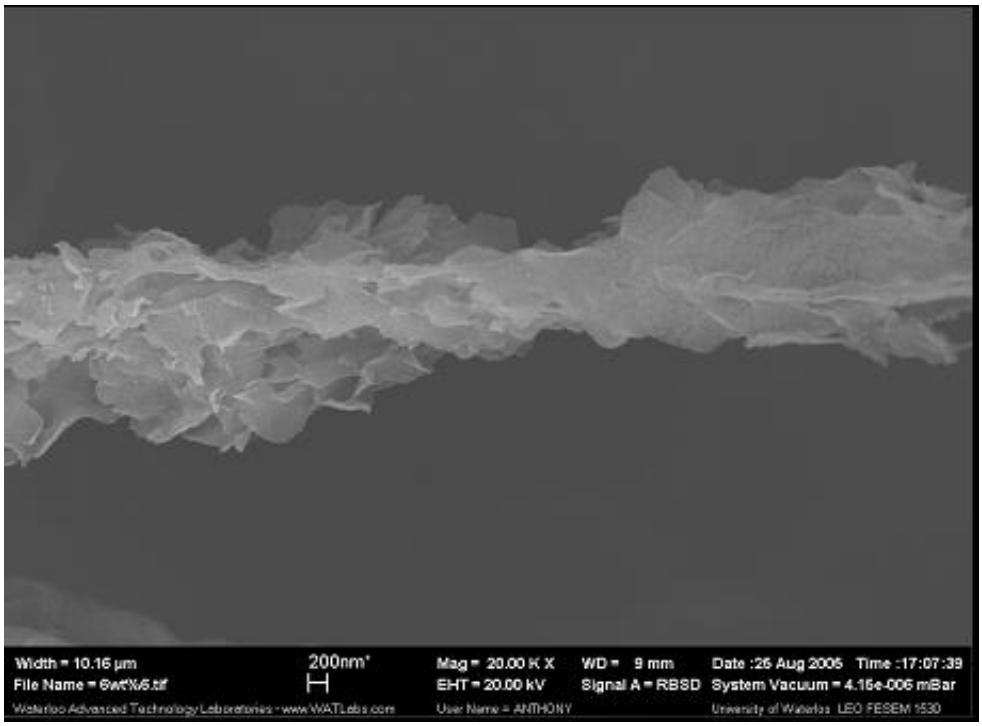
Width = 10.16 µm
File Name = 6wt%6.tif
200nm
Mag = 20.00 K X
EHT = 20.00 kV
WD = 9 mm
Signal A = RBSD
Date :25 Aug 2005 Time :17:07:39
System Vacuum = 4.16e-006 mBar
Waterloo Advanced Technology Laboratories - www.WATLabs.com
User Name = ANTHONY
University of Waterloo LEO FESEM 1530

**(d)**

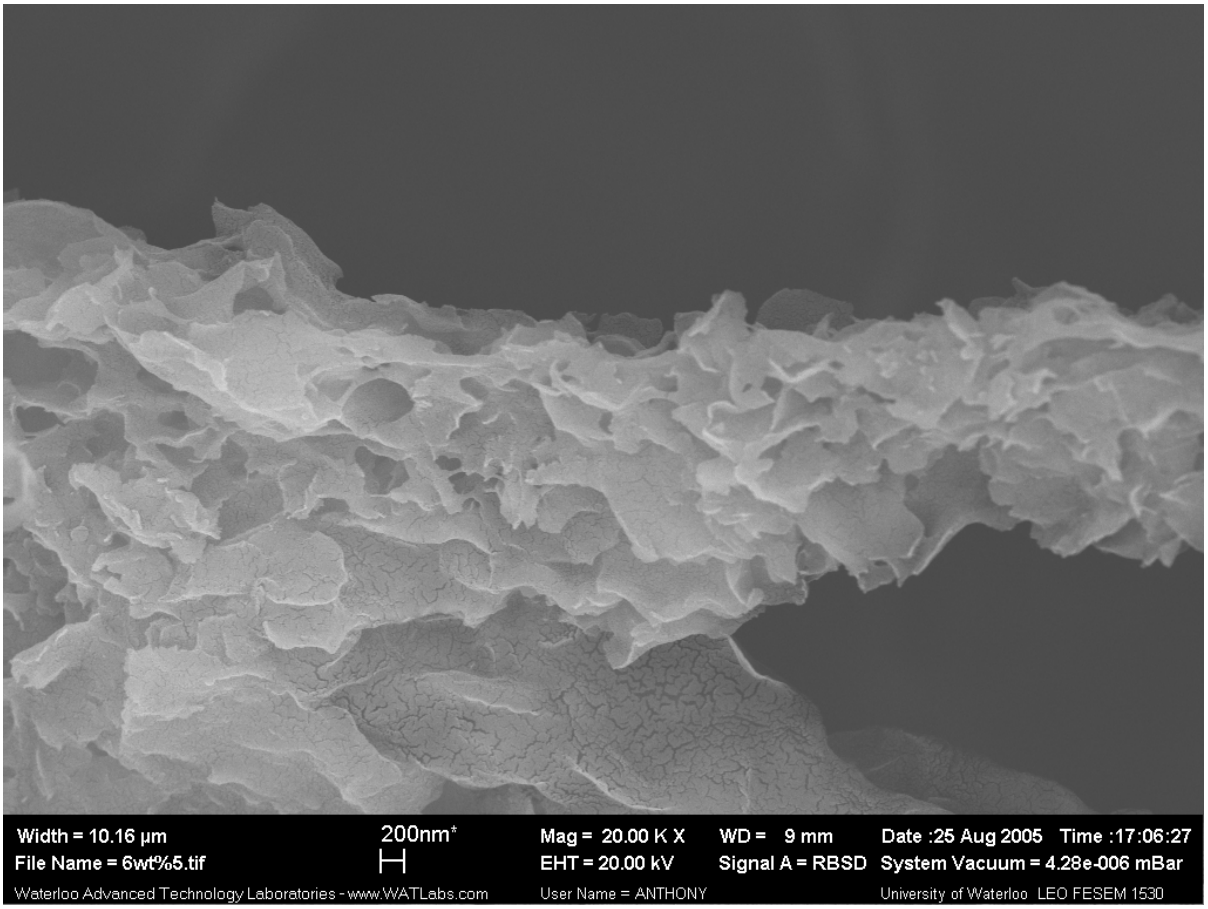


**(e)**

**Figure 2-16**. (a) SEM micrograph of polymer thread connected to the MMT surface in the residue after Soxhlet extraction (9 wt.-% MMT), (b) Expanded view of the polymer fiber structure, (c) SEM micrograph of polymer thread in the residue after Soxhlet extraction (19 wt.-% clay), (d) Expanded image of the area highlighted by the circle, shown in (c), (e) A second expanded image of the area highlighted by the circle, shown in (c).

### 2.3.9. Chemical Composition Analysis: MMT and PE-clay Hybrid Nanocomposites

The chemical composition of PE-clay hybrid nanocomposites was analyzed by EDX and FT-IR. Figure 2-17 provides EDX results of MMT, MMT/TIBA/UOH and MMT/TIBA/UOH/CAT/PEex. The same sample in Figure 2-16.d and 2-16.e was analyzed by EDX to identify elements in each SEM images.

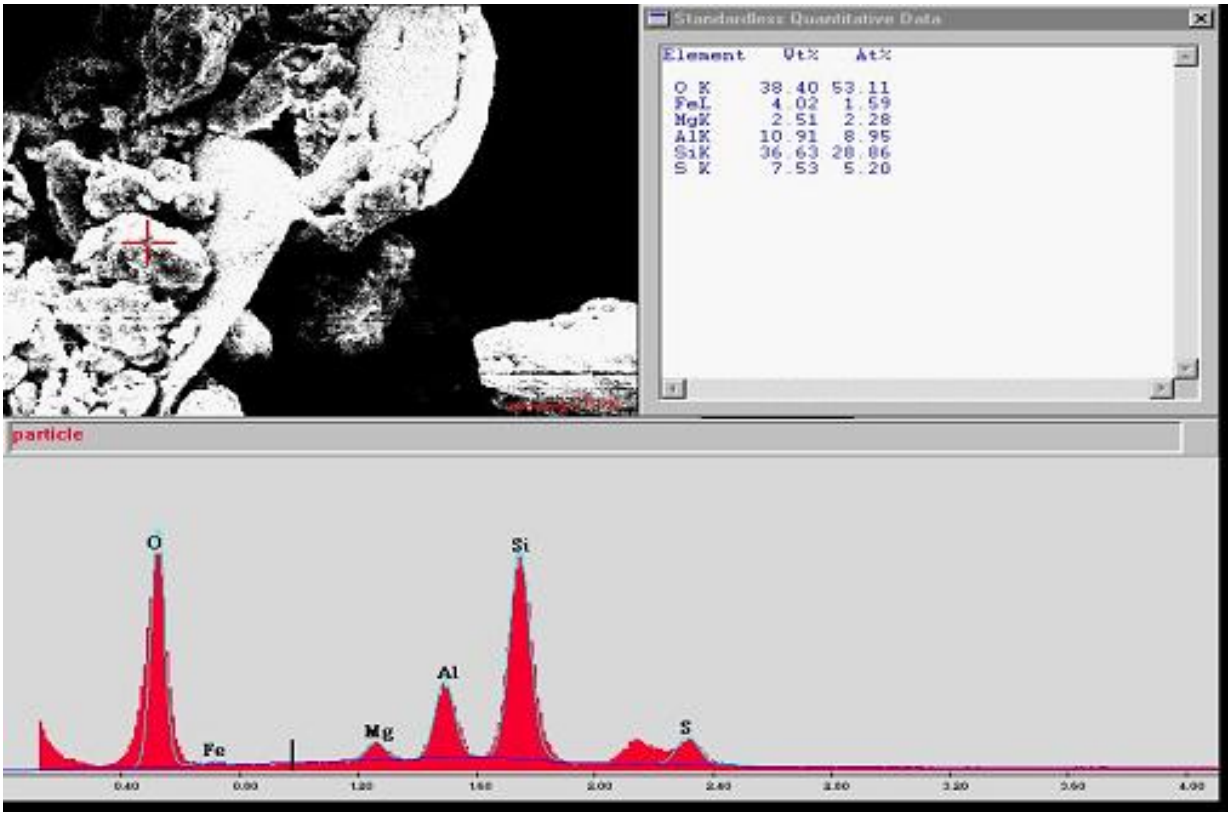


**(a)**

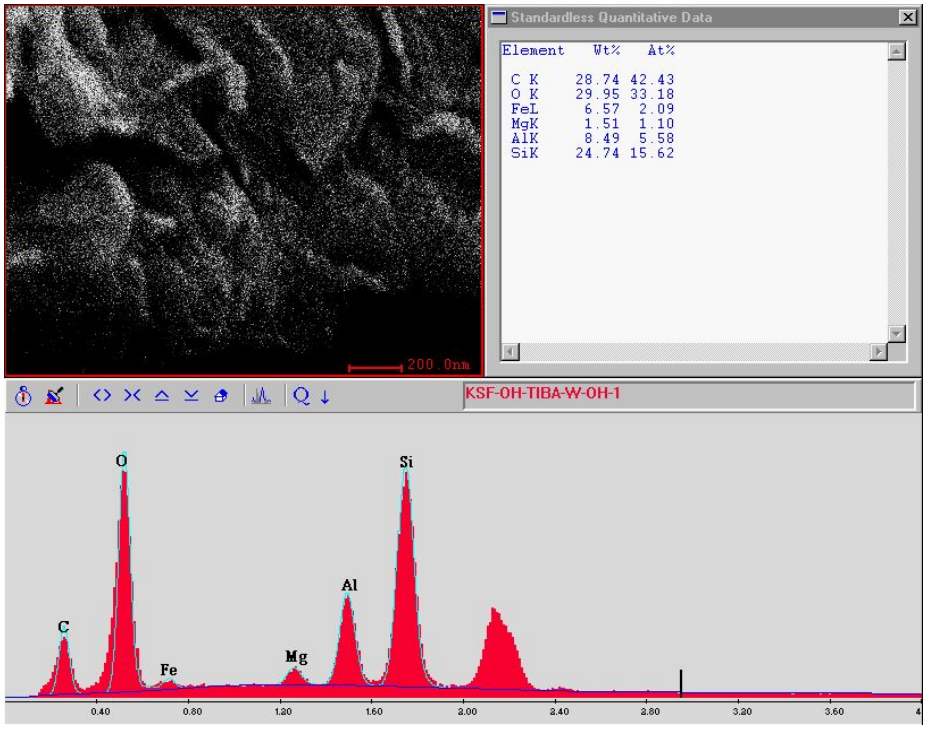


**(b)**

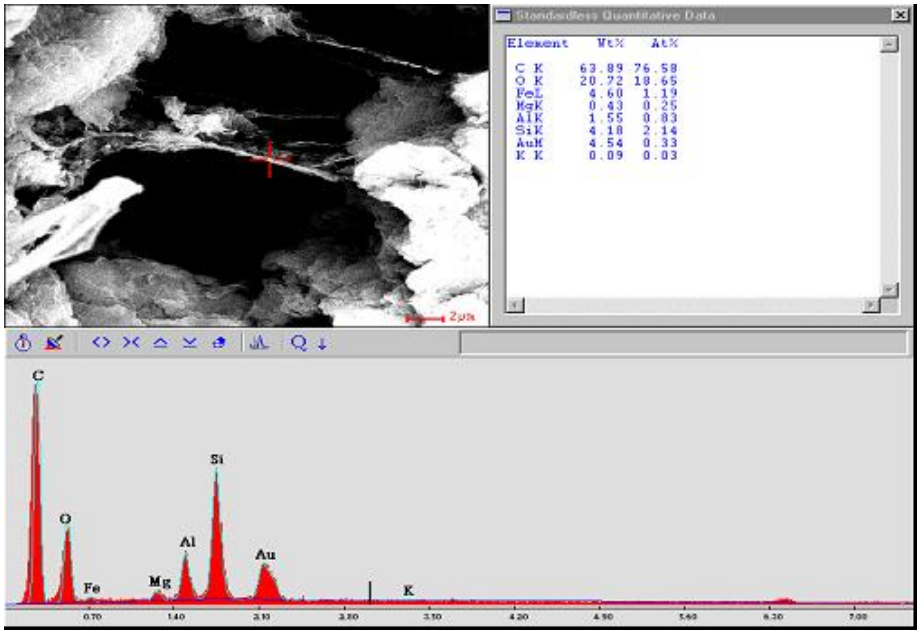


**(c)**

**Figure 2-17**. EDX analysis: (a) MMT, (b) MMT/TIBA/UOH and (c) MMT/TIBA/UOH/ PEex (19 wt.-% clay).

Figure 2-17.a shows that the MMT surface has no carbon atom band, whereas oxygen, silicon, aluminum and magnesium bands were observed; that is the regular chemical composition of MMT platelets. The analysis of MMT/TIBA/UOH (Figure 2-17.b) shows the presence of carbon atoms originating from UOH molecules. This implies that UOH molecules were attached to the MMT surface even after severe washing steps. The PE-clay hybrid threads, shown at previous SEM images (Figure 2-16.d and 2-16.e), were also analyzed by EDX (see Figure 2-17.c). EDX analysis clearly detected signals for carbon and silicone atoms, elucidating the composition of the hybrid structure of MMT lamellae and polyethylene fibers. Table 2-3 summarizes the chemical composition of these 3 samples. This observation confirms that the morphology observed with SEM (Figure 2-16. d and 2-16.e) was indeed a hybrid structure of PE and MMT layers.

**Table 2-3**. EDX, Elementary analysis of MMT, MMT/TIBA/UOH and MMT/TIBA/UOH/ CAT/PEex residues.

Unit: Atom %

| Samples | C | Si | Al |
|---|---|---|---|
| MMT | 0.0 | 28.9 | 9.0 |
| MMT/TIBA/UOH | 42.4 | 15.6 | 5.6 |
| MMT/TIBA/UOH/CAT/PEex[1] | 76.6 | 21.0 | 0.8 |

[1] residue fiber (PE-clay composite; 19wt.-% clay) after Soxhlet extraction with boiling TCB for 24 hours.

In Table 2-3, the carbon content increases in the following order: MMT, modified MMT and residue MMT. The relative small concentrations of aluminum atoms decreased from MMT, to

MMT/TIBA/UOH and to MMT/TIBA/UOH/CAT/PEex, likely because of the increase of carbon content in the samples.

The chemical composition of MMT, MMT/TIBA/UOH, and MMT/TIBA/UOH/ CAT/PEex was also investigated with FT-IR (Figure 2-18). Figure 2-18.b clearly shows the C-H stretching band at around 2931 $cm^{-1}$ and the C-H bending band at 1451 $cm^{-1}$ for MMT/TIBA/UOH. These bands are direct evidence of the existence of UOH on the surface of MMT. In the case of the MMT/TIBA/UOH/CAT/PEex, the C-H stretching band, the characteristic alkyl band, become sharper, due to the remaining polymer on the MMT. These results are in agreement with those of SEM/EDX, confirming that polyethylene chains are present on the surface of MMT after solvent extraction.

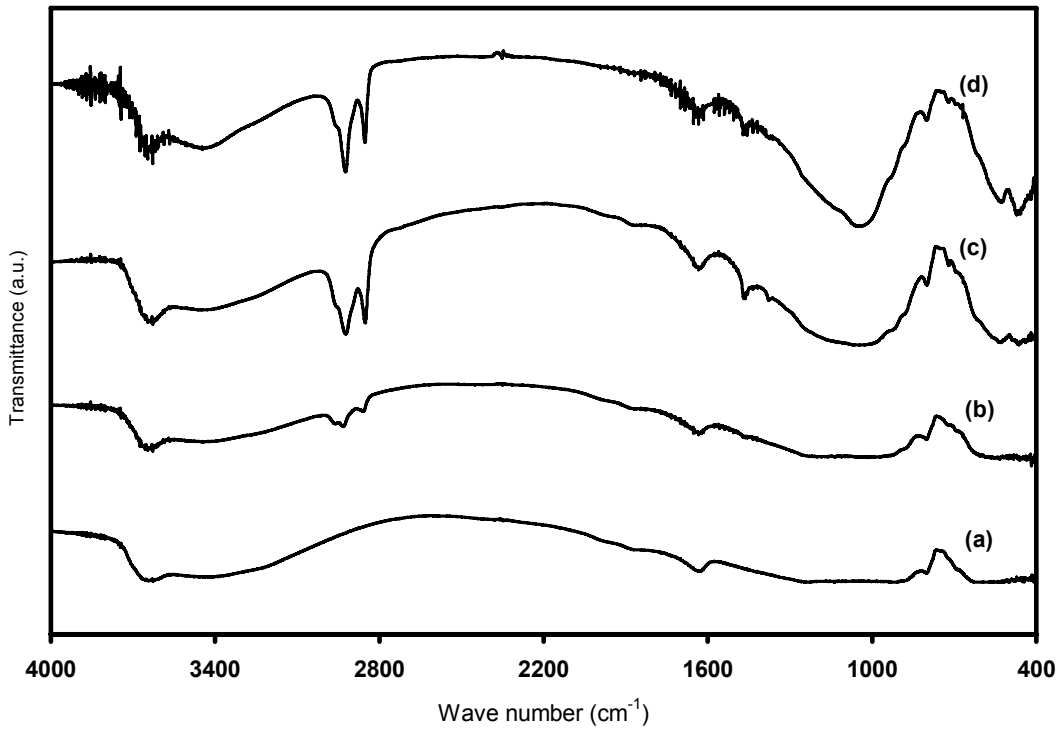


**Figure 2-18**. FT-IR spectra for (a) MMT, (b) MMT/TIBA/UOH, (c) 19 wt.-% MMT residue after Soxhlet extraction, (d) 25 wt.-% MMT residue after Soxhlet extraction.

The FT-IR analysis can also be used to obtain further insight on the conformation of chains in the galleries or close to the surface. Figures 2-18.a and 2-18.b show the difference between MMT and MMT/TIBA/UOH. Alkyl stretching bands in MMT/TIBA/UOH are observed in the range 2930-2910 $cm^{-1}$ and support the hypothesis that UOH molecules modify the MMT surface.

Vaia and co-workers have shown that alkyl chains inside clay galleries have a well defined stretching band shift when ammonium cations and amines were used for intercalation in clay (Vaia et al., 1994). According to those authors, the FT-IR analysis directly probes the molecular conformation of the intercalated organic chains and the interlayer structure. The bands at around 2920 $cm^{-1}$ arise from the $-CH_2$ asymmetric stretching, $\nu_{as}(CH_2)$. In general, the frequency and width of $\nu_{as}(CH_2)$, ranging from 2929 to 2918 $cm^{-1}$, are sensitive to the gauche/trans conformer ratio and packing density of methylene chains. The $\nu_{as}(CH_2)$ at higher frequencies (~2929 $cm^{-1}$) is known to be characteristic of gauche conformations along the hydrocarbon chain (chain disorder). Conversely, a band shifting to lower frequencies reveal the characteristic of highly ordered all-trans conformations, that is, highly ordered chains (Vaia et al., 1994).

In Figure 2-19.b, $\nu_{as}(CH_2)$ of MMT/TIBA/UOH was observed at 2932 $cm^{-1}$, close to the upper limit of 2928.9 $cm^{-1}$ reported in the literature (Vaia et al., 1994). This implies that the UOH molecules on the MMT surface/galleries are in a liquid-like gauche conformation, with a relatively low density of functional groups, compared to the trans conformation. On the other hand, the nanocomposites with 19 wt.-% and 25 wt.-% clay (Figures 2-19.c and 2-19.d) showed the $\nu_{as}(CH_2)$ band at 2921 and 2923 $cm^{-1}$, respectively, closer to the lower limit, 2918 $cm^{-1}$. Such results indicate that, in these nanocomposites, the organic chains are in highly ordered trans conformation and that there is a high density of functional groups per MMT surface area.

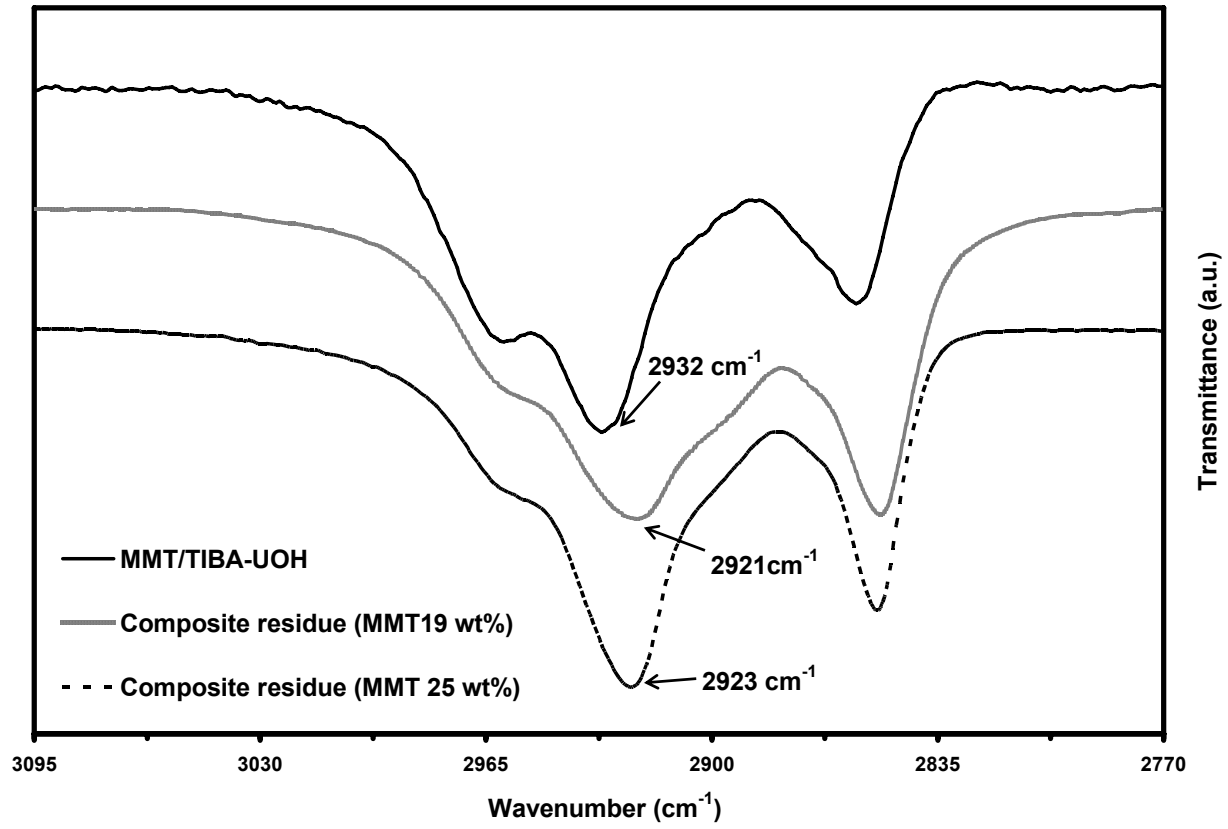


**Figure 2-19.** Selected regions of FT-IR transmittance spectra of MMT/TIBA/UOH, PE-clay hybrid nanocomposite (25 wt.-% clay) and PE-clay hybrid nanocomposite (19 wt.-% clay)

Based on these analyses, we can conclude that the concentration of UOH in MMT/TIBA/UOH is low (gauche conformation), whereas the alkyl chain concentration in the nanocomposite residues (MMT 19 wt.-% and MMT 25 wt.-%) is high (trans conformation). Therefore, it is reasonable to conclude that after in-situ polymerization the MMT layers are covered with alkyl chains (polyethylene) at high concentration and with trans conformation.

### 2.3.10 Thermal Analysis of PE-Clay Hybrid Nanocomposites

The melting temperature of the final hybrid polyethylene-clay nanocomposite was measured using DSC (Table 2-2). The low melting point of the polyethylene made with unsupported Ni-diimine catalyst is attributed to short chain branches, caused by chain walking during polymerization

(Johnson et al., 1995). However, for polymerizations carried out using the supported catalyst at the same temperature and pressure, polyethylene with higher melting points were obtained. It can be speculated that chain growth in the vicinity of the clay surface could have reduced the frequency of the chain walking, thus leading to polyethylene chains with fewer short branches. Similar behavior was observed before for Ni-diimine catalyst supported on silica (Simon et al., 2001). This clay surface effect on the frequency of chain walking (and, consequently, on $T_m$) supports the assumption that chain growth happened near the clay surface.

On the other hand, leaching of active sites from the clay surface would lead to homogenous polymerization and no surface influence on the chain walking mechanism would result. Silica-supported Ni-diimine catalyst produces polyethylene with two melting points due to homogeneous and heterogeneous phase polymerization (Simon et al., 2001). However, the polyethylene made with MMT/TIBA/UOH/Ni-diimine shows only one $T_m$. This result implies that most active centers in this catalyst system were likely located near the MMT surface.

Note that the method for supporting the catalyst used here does not anchor the Ni or Zr complex covalently to the clay surface. The rational is to have active sites near the clay surface in the beginning of the polymerization to allow copolymerization of ethylene and vinyl groups grafted onto the surface through UOH molecules. After exfoliation, active sites will continue to polymerize near the clay surface or will leach to the diluent and continue to polymerize away from the clay surface. If the polymer structure and polymerization conditions favor polymer precipitation, it is likely that it will trap the active site near the clay surface, avoiding undesirable catalyst leaching.

### 2.3.11. In-Situ Polymerization (High Pressure)

This novel method for preparation of hybrid polyethylene-clay nanocomposites was also tested in a 1-L high pressure autoclave reactor. Polymerizations were scaled up to different pressures and

temperatures, as shown in Table 2-4. Polymerization results can be divided into 3 groups, according to ethylene pressure and polymerization temperature (7-8, 9-10, and 11-13). In general, polymerizations with MMT/TIBA/UOH/Ni-diimine showed trends for temperature and monomer pressure similar to those for homogeneous polymerization reported in the literature (Simon et al., 2001).

The polymerization of ethylene with unsupported Ni-diimine catalyst was investigated as a reference. Runs 7 and 9 are reference polymerizations for the different polymerization temperatures (30 °C and 60 °C). The product obtained at the low polymerization temperature had a single melting point ($T_m$ = 66 $^oC$); this is typical of a polyethylene with narrow short chain branch distribution that can be obtained by a single-site catalyst. The product made at the high polymerization temperature had three melting points, probably because polyethylene chains with different short chain walking frequencies were produced. It is probable that active sites with different chain walking frequencies exist at 60°C. Similar results have been previously reported in the literature (AlObaidi et al., 2003).

For polymerizations at 30 °C, the activity of the unsupported catalyst (entry 7) was 5 times higher than that of the heterogeneous system (entry 8). This trend is also the same at 60°C (entries 9 and 10). The polymerization activity of the supported catalyst is always less than that of the homogeneous system, likely due to catalyst deactivation during supporting. One interesting characteristic of these systems is that runs 8 and 10 make polymer with a single high $T_m$ of approximately 115 °C, due to a lower short chain branch frequency in the polymer chains. It seems that the chain walking mechanism of the Ni-diimine catalyst system is influenced by the MMT surface, leading to lower polymerization activity and the higher $T_m$.

Polymerization with silica-supported Ni-diimine catalyst was reported to make polyethylene with two melting points, one in the range from 80 to 100 °C (polymerization by leached catalyst) and the other at approximately 115 °C (polymerization with supported catalyst) (AlObaidi et al., 2003). In the case of MMT/TIBA/UOH/Ni-diimine, samples 8, and 10 to 13 show only a single melting point

between 113 to 115°C, which is similar to that of polyethylene made with silica-supported Ni-catalysts. Polyethylene made with MMT/TIBA/UOH/Ni-diimine also has higher molecular weights and broader molecular weight distributions (larger PDIs), similarly to polyethylene made with silica-supported Ni-dmine catalysts (AlObaidi et al., 2003).

We have also studied the effect of ethylene pressure on the polymerization (Figure 2-20). Ethylene pressure was increased from 1 to 10 atm at 30 °C (Table 2-4, runs 11-13). As the pressure was increased, catalyst activity, $T_m$, and PE crystallinity increased, probably due to the attenuation of the chain walking frequency by the higher monomer concentration. $M_n$ and $M_w$ also increased, and PDI decreased.

**Table 2-4**. Properties of hybrid polyethylene-clay nanocomposites made by in situ-polymerization[(a)] in a high pressure reactor with MMT/TIBA/UOH/Ni-diimine.

| Exp. [(b)] | Temperature ($^o$C) | $P_{ethylene}$ (atm) | Prod.[(c)] | Clay (%) | $T_m$ ($^o$C) | Crystallinity | $M_n$ ($\times10^{-3}$) | $M_w$ ($\times10^{-3}$) | PDI |
|---|---|---|---|---|---|---|---|---|---|
| **7** | 30 | 10 | 5280 | 0 | 66 | 7.5 | 205 | 456 | 2.2 |
| **8** | 30 | 10 | 1082 | 2.5 | 115 | 22.3 | 317 | 900 | 2.8 |
| **9** | 60 | 10 | 2000 | 0 | 127, 135 | 7.3 | 109 | 244 | 2.7 |
| **10** | 60 | 10 | 891 | 2 | 113 | 9.2 | 147 | 456 | 3.1 |
| **11** | 30 | 10 | 737 | 6 | 123 | 28.3 | 237 | 741 | 3.1 |
| **12** | 30 | 3 | 570 | 8 | 116 | 9.5 | 214 | 677 | 3.7 |
| **13** | 30 | 1 | 355 | 12 | 110 | 7.2 | 142 | 645 | 4.5 |

(a) Catalyst precursor :Ni-diimine catalyst, Cocatalyst : MAO (2 g, 10 wt.-% Al in toluene)

(b) Catalyst loading per gram of clay: 9 μmol (7-10), 20 μmol (11-13)

Al/Ni molar ratio= 824 (7-10), 371 (11-13)

Polymerizations conditions: 500 mL toluene, $m_{MAO}$ = 2.0 g, 30 $^o$C, 30 min.

(c) Productivity (kg PE/ mol cat. h.)

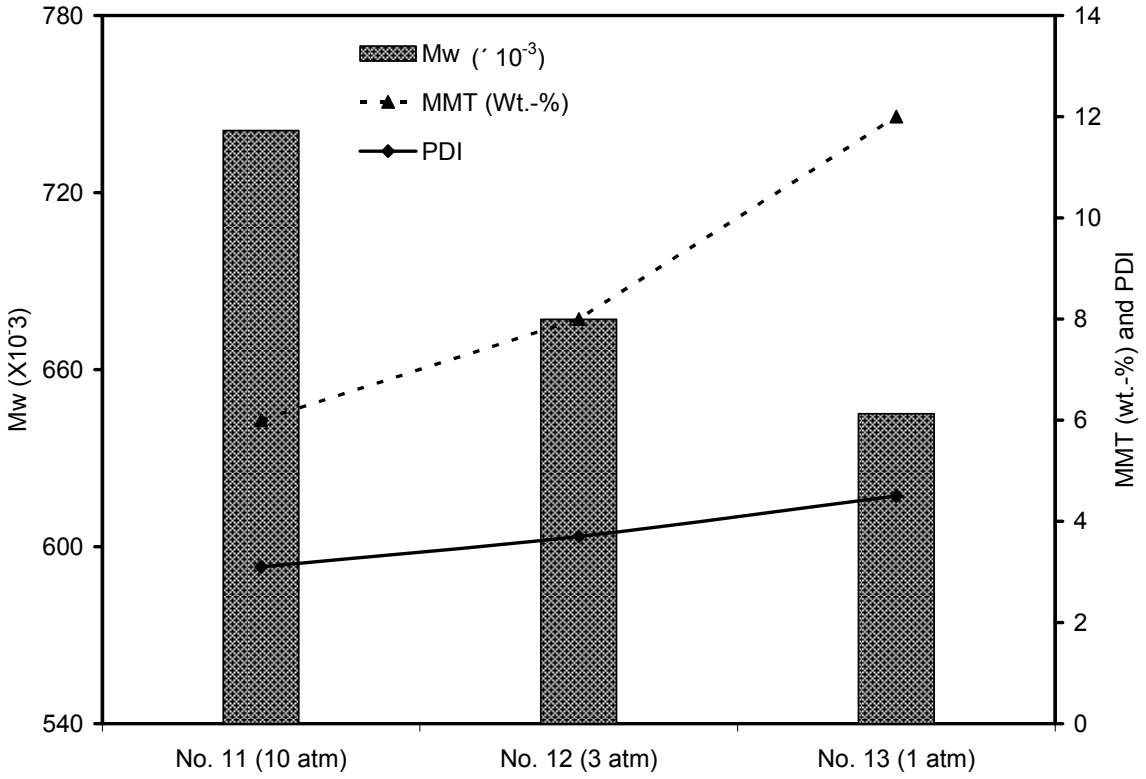


**Figure 2-20.** Dependence of molecular weight, PDI and MMT content of PE-clay nanocomposites on ethylene pressure.

## 2.4. Mechanical and Thermal Properties

*Crystallinity*

The mechanical properties of polyethylene are strongly influenced by the degree of crystallinity. Short chain branches in polyethylene are not included in the crystalline domains. As a consequence, the segment of the polyethylene chain containing the branching point is ejected into the amorphous phase. The crystallinity of the polyethylene samples was calculated from their enthalpies of fusion measured from differential scanning calorimetry, as shown in Figure 2-21 and reported in Table 2-5.

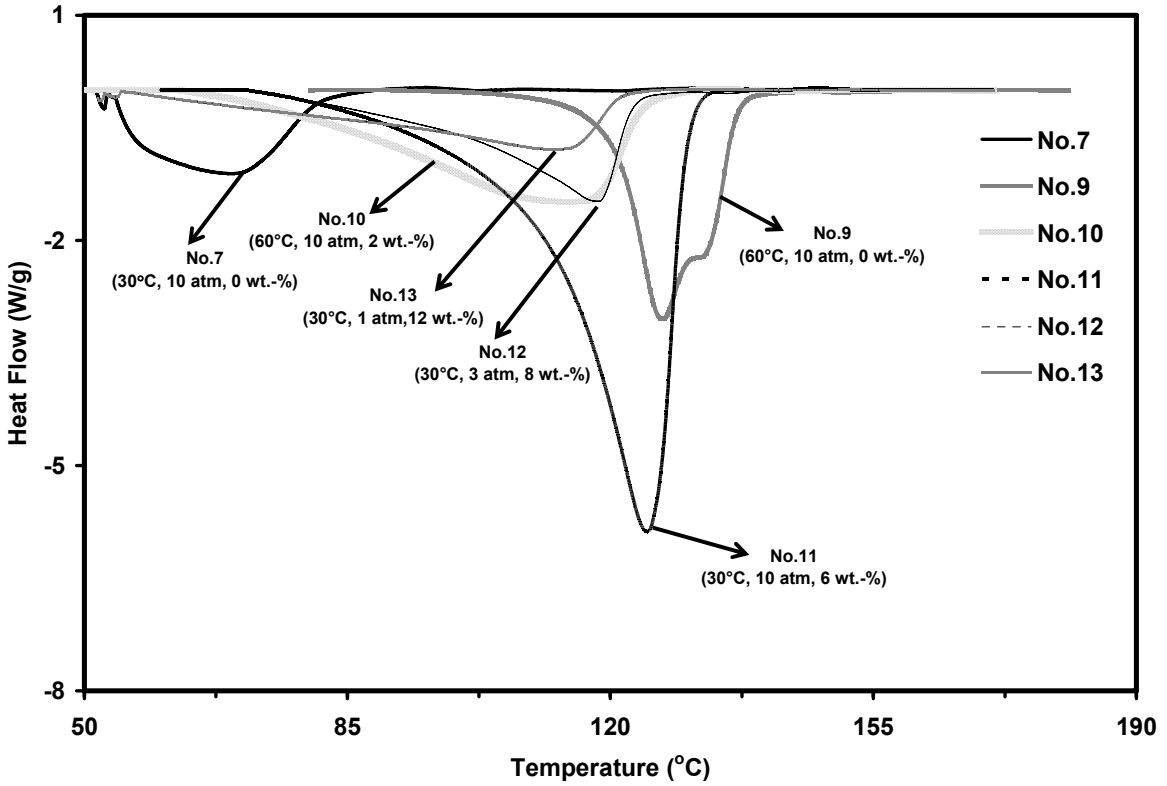


**Figure 2-21**. DSC analyses of PE-clay hybrid nanocomposites made by MMT/TIBA/ UOH/Ni-Diimine in a 1-L high pressure reactor. Polymerization conditions are written in the parentheses: polymerization temperatures, pressures and clay wt.-%.

*Tensile Testing*

Samples 8 and 11 (Table 2-4), which were polymerized at the same conditions, were chosen to help elucidate the effect of MMT wt.-% on mechanical properties. When the MMT content was increased from 2.5 (sample 8) to 6 wt.-% (sample 11), the tensile modulus increased 28%, even though sample 11 has lower $M_n$ and $M_w$, and higher PDI than sample 8. The comparison of samples 7 (no clay) and 10 (Table 2-4) is also illustrative of the clay effect. Even though the crystallinity increases by 1.7% from sample 7 to sample 10, the tensile modulus of sample 10, with only 2 wt.-% of MMT, is 9.5 times higher than that of sample 7.

This enhancement in mechanical properties may be attributed to the nanophase MMT distribution in the polyethylene matrix with a strong interaction between the two phases. It is likely that the introduction of the bifunctional modifier UOH between the MMT surface and polymer matrix is an important factor in this process.

The tensile mechanical properties of PE-clay hybrid nanocomposites were investigated using the samples shown in Table 2-4. The stress-strain curves, shown in Figure 2-22, provide insight on the deformation behavior. These curves were used to calculate the Young's modulus (E), yield strength, and elongation at break. A summary of results obtained by averaging the results of 3 specimens for each sample is reported in Table 2-5.

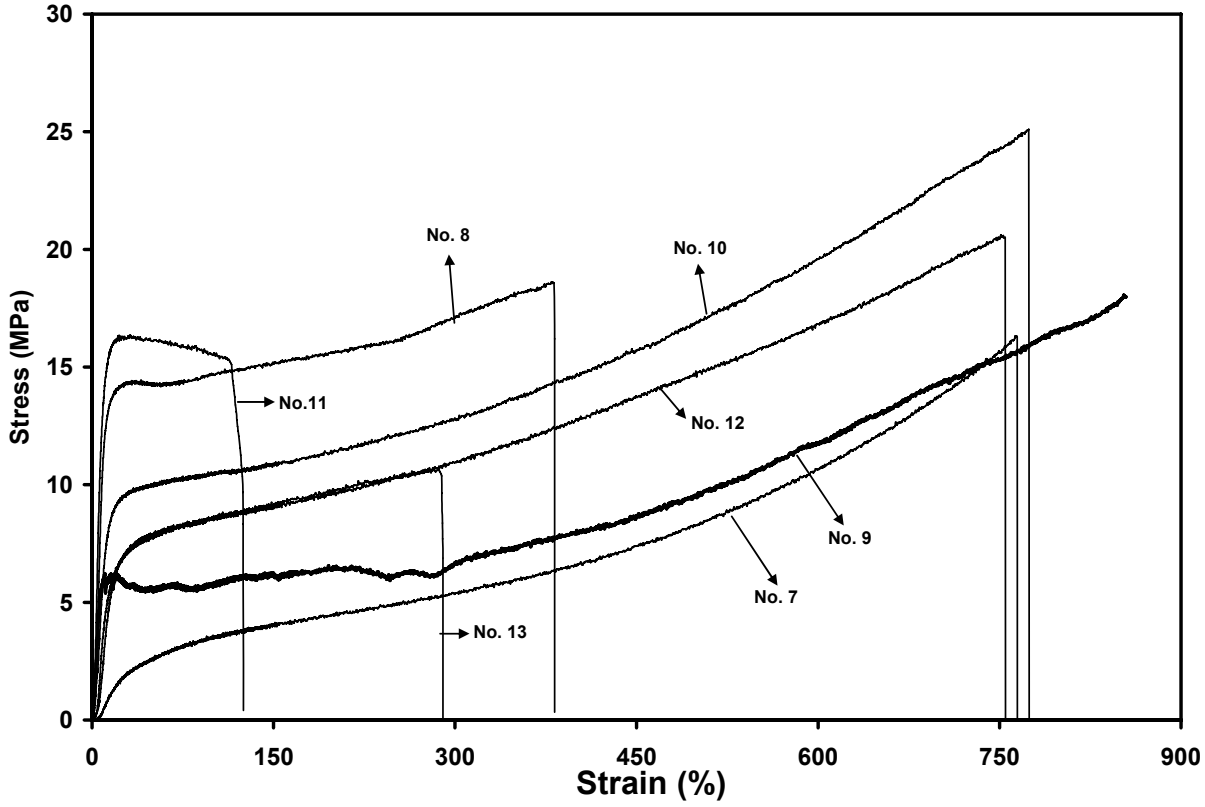


**Figure 2-22.** Stress-strain curves for PE-clay hybrid nanocomposites.

Samples 7 and 9 show the typical elongation curve of an amorphous polymer. As the MMT fraction increases from sample 7 to 12, the overall modulus increases, showing a linear relationship between the tensile modulus and MMT fraction.

**Table 2-5**. Tensile testing results with PE-clay hybrid nanocomposites made by MMT/TIBA-UOH/Ni-diimine in a 1-L high pressure reactor.

| No. | Tensile Modulus (MPa) | Polyethylene Crystallinity (%) | Clay (wt.-%) | Elongation at Break (%) |
|---|---|---|---|---|
| 7 | 0.1 | 7.5 | 0 | 765 |
| 8 | 1.8 | 22.3 | 2.5 | 382 |
| 9 | 0.93 | 7.3 | 0 | 854 |
| 10 | 0.95 | 9.2 | 2 | 774 |
| 11 | 2.3 | 28.3 | 6 | 125 |
| 12 | 0.6 | 9.5 | 8 | 754 |
| 13 | 0.9 | 7.2 | 12 | 290 |

## 2.5. Conclusion

A novel hybrid polyethylene-clay nanocomposite was prepared using in-situ polymerization with clay-supported transition metal catalysts. Initially, MMT was intercalated with triisobutylaluminum and 10-undecene-1-ol. The intercalation process allowed the transition metal catalyst and MAO to enter the MMT galleries and polymerize ethylene. The growth of polyethylene chains inside the clay galleries led to exfoliation of the clay platelets.

The coordination catalysts tested, Ni-diimine catalyst and $Cp_2ZrCl_2$, showed promising activity for implementation in in-situ polymerization. Under appropriate conditions, it was possible to control the morphology of the polymer particles produced with the catalyst supported on MMT.

The morphology of MMT layers dispersed in the polyethylene matrix was characterized with XRD, SEM and TEM. There is evidence that polyethylene chains were covalently bonded to the MMT surface. Undecylenyl alcohol acts as a bifunctional organic modifier by: a) intercalating the clay and making it organophilic, and b) by playing the role of a coupling agent, or comonomer, during polymerization with ethylene.

Higher decomposition temperatures and tensile modulus were observed as the MMT content of the nanocomposites was increased. Modification with TIBA/UOH showed relatively lower concentration of organic modifiers. The latter two phenomena are usually seen in ammonium modified MMT (Xie et. al., 2001) as a result of the severe conditions imposed during successive compounding and extruding.

The maximum tensile modulus was obtained at around 6 wt.-% of clay content in PE matrix. We observed an increase in tensile strength as the clay content increased without sacrificing the elongation properties. This result could be attributed to the strongly enhanced interfacial interaction between MMT surface and the polyethylene matrix.

# Chapter 3
# Gas-phase Polymerization with Transition Metal Catalysts Supported on Montmorillonite – A Particle Morphological Study

## 3.1. Introduction

When supported transition metal catalysts are used for polymerization, the final polymer particle replicates the shape of the support when the conditions are favorable. Investigations on particle morphology, particle growth and fragmentation have been approached experimentally and theoretically, as discussed in recent reviews (Soares et al., 1995; Hlatky, 2000; Mckenna et al., 2000).

Many different types of inorganic carriers have been tested as supports for metallocene catalysts (Janiak et al., 1994; Kitagawa et al., 1997; Fink et al., 1995; Hlatky, 2000; Houg et al., 1998). The most frequently investigated supports are spherical silica and polymeric particles (Cheng et al., 2004; Jongsomjit et al., 2004; Soga et al., 1995; Soga et al., 1995; Lee et al.,1997; Rieger et al., 1996; Kaninsky et al., 1993). Generally, spherical silica particles lead to good polymer particle morphology and have been widely employed.

One of the supporting techniques commonly described in literature is to impregnate the catalyst on a MAO-treated silica support (Kaminsky et al., 1993). Although this method has been used by a number of research groups in slurry or gas-phase polymerization reactors, MMT-supported catalysts for gas-phase polymerization have been seldom reported (Liu et. al, 2004). The use of MMT- supported catalysts in gas-phase processes is a very attractive procedure to produce PE-MMT hybrid nanocomposites.

In this chapter a novel approach to prepare in-situ polyolefin nanocomposites in gas-phase reactors using MMT- supported catalysts is described. The catalyst is supported inside the MMT galleries. In-situ polymerization allows the layered structure of MMT particles to be exfoliated directly in the reactor during the polymerization. Because polymerization is carried out in gas-

phase, there is no solvent in the system to extract the catalyst sites ($Cp_2ZrCl_2$ or Ni-diimine) from the MMT surface. The majority of this study focused on understanding the mechanism of particle morphology formation and particle growth using electron microscopy.

## 3.2. Experiments

### 3.2.1. Materials

All experimental materials are the same as described in Section 2.2.1.

### 3.2.2. Catalyst Preparation

The pre-contacting of MMT with $Cp_2ZrCl_2$ or Ni-diimine catalyst was carried out in a 250 mL glass reactor equipped with a stirrer at room temperature ($23 \pm 2$ $^{o}$C). Dried MMT (1 g) was first treated with TIBA and UOH in toluene solution, followed by addition of a solution containing the transition metal catalyst. The solvent was evaporated under vacuum for 3 hours at room temperature until a free flowing powder was obtained. The supported catalyst was transferred to a glass vial (5 mL) and soaked with 0.2 g of MAO (10 wt.-% MAO in toluene) at room temperature in a glove box before polymerization.

### 3.2.3. Pre-Polymerization

Pre-polymerizations were carried out under mild conditions (room temperature and atmospheric pressure) without stirring, using a 5-mL glass vial, located inside a 250-mL Schlenk tube, as shown in Figure 3-1. Before the pre-polymerization, the Schlenk tube was purged 3 times under vacuum with ethylene. Two polymerization times, 3 and 24 hours, were used for the study of MMT particle fragmentation in the early stages of polymerization.

**Figure 3-1.** Polymerization under atmospheric pressure using a Schlenk tube.

### 3.2.4. Gas-Phase Polymerization in a High Pressure Autoclave

For high pressure gas-phase polymerizations, a turbo-sphere reactor was used (Figure 3-2). Pre-polymerized catalyst particles were transferred to the 2.5 L-turbo-sphere reactor, equipped with gas purification, temperature control, and data acquisition devices. One hundred grams of NaCl was used as a seed bed and TMA was used to scavenge impurities. For all the polymerization runs, the residual TMA was removed from the reactor prior to catalyst injection by evacuation or successive dilution with ultra-high purified $N_2$ and venting after the impurity scavenging stage.

The polymerization of ethylene was carried out by pressurizing the reactor with ethylene and stirring the pre-polymerized catalyst particles. Polymerization activities were calculated from the ethylene flow rates measured with a mass flow meter. After 1 hour, the polymerization was quenched by adding methanol and stirred for additional 10 minutes. The polymer particles, with NaCl, were transfer to a 1-L beaker, filled with acid ethanol, and then filtered with a filter paper. After being

washed with 30 mL of acidic ethanol 3 times, the polymer particles were finally dried at 78 °C for 24 hours under vacuum to obtain the final PE-MMT hybrid nanocomposites.

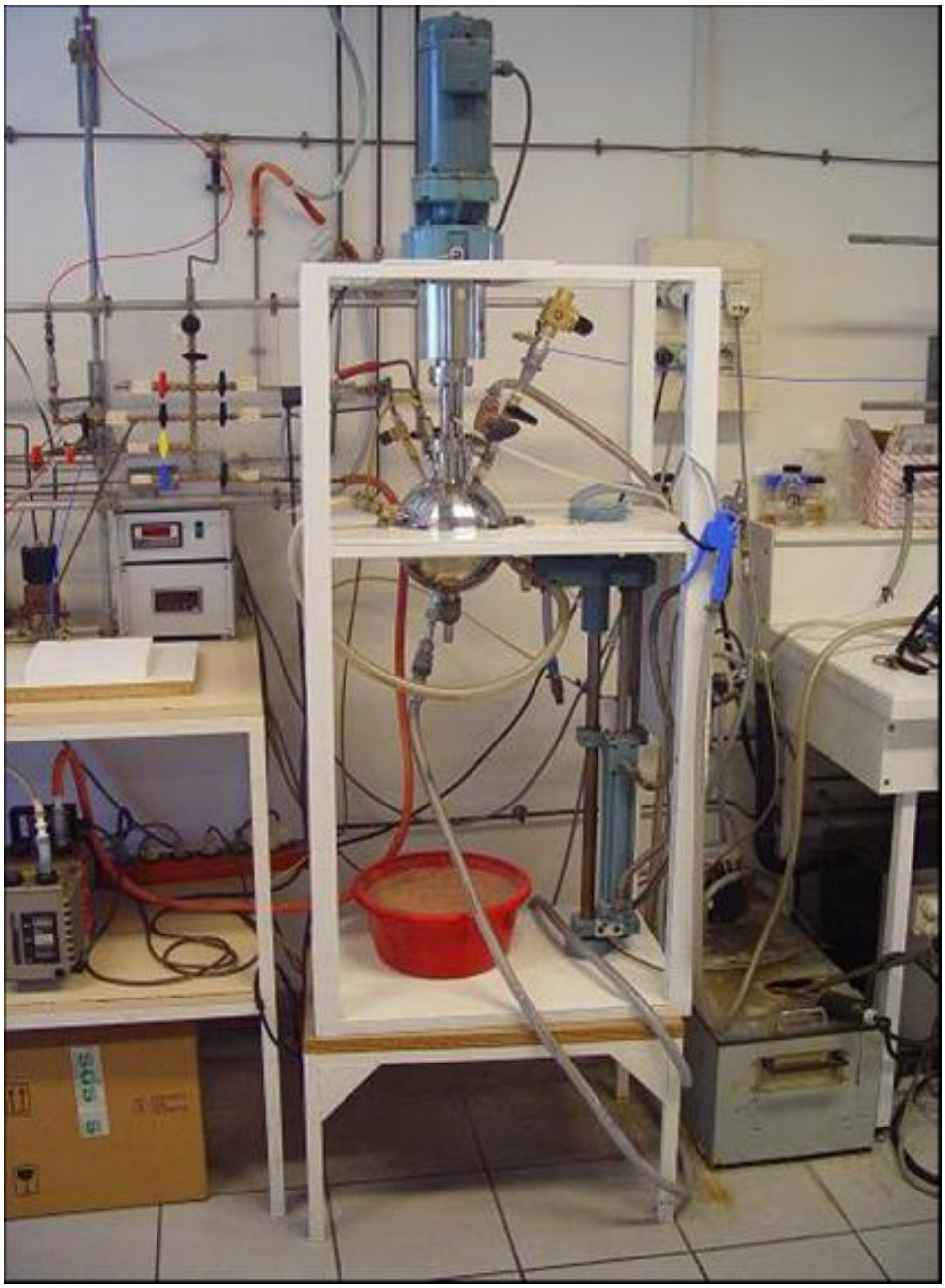

**Figure 3-2.** High pressure gas-phase turbo-sphere reactor in LCPP, in Lyon, France.

### 3.2.5. Characterization

Most particle morphological studies were performed by SEM, TEM and XRD. The analytical techniques used here were described in Chapter 2.

## 3.3. Results and Discussion

### 3.3.1. Morphology of Pre-Polymer Particles Made with MMT/TIBA/UOH/$Cp_2ZrCl_2$

Stirring was not used during pre-polymerization because we wanted to observe changes in particle morphology without the interference of outer mechanical forces. The particle morphology after 3 hours of polymerization is shown in Figure 3-3.a. Hereafter this sample will be called 3HP (3HP stands for 3 hours of pre-polymerization). Three different types (***A***, ***B*** and ***C***) of particles are observed in Figure 3-3.a:

- ***A*:** barely polymerized surface
- ***B*:** polymer on clay surface without cracks or fragmentations
- ***C*:** clay platelets fragmented into smaller particles

Figure 3-3.b shows a TEM image of intercalated MMT particles. The different contrast levels observed in Figure 3-3.b represent the MMT particles stacked one on top of the other (the darker regions representing higher staking levels). During in-situ polymerization, aggregates of MMT primary particles are first separated into smaller particles by the growing polymer (Figure 1-5). Each primary particle consists of several layers with a distance of 27 nm between the platelets, as can be inferred from Figure 3-3.b. Each intercalated plate has a thickness of approximately 5 nm, and appears to be bent at the edges.

In a second set of experiments, the pre-polymerization was allowed to proceed for 24 hours. These samples will be called 24HP. They are compared to the 3HP samples with the same degree of magnification (2K, 30K and 100K), in Figure 3-4. Inspection of the micrographs shows that the pre-polymerization induced the fragmentation of MMT particles after 3 hours (***A***, ***B*** and ***C***) and further encapsulated by polymer after 24 hours (***D, E*** and ***F***).

In micrograph ***B***, the MMT particles have been fragmented in particle of about 10 μm diameter and 100 nm polymer projections are observed on the surface of the MMT platelets, whereas in micrograph ***E***, the presence of 1 μm polymer threads are observed. It is likely that these polymer threads grew from inside the particles during polymerization. Other researchers have described the formation of polymer threads or fibrils on the catalyst support during early stages of polymerization with Ziegler-Natta catalysts (Boor, 1979). Polyethylene fibres were reported in the polymerization with a metallocene catalyst supported on MCM-41 particles at low temperature (Ye et al., 2003).

At the largest magnification (30K times, scale bar of 200 nm), the surface morphology of 3HP and 24HP particles are clearly different. The surface of 3HP particles shows polymer projections on the surface (see the circle in micrograph ***C***), whilst 24HP particles shows curved platelets on fragmented surfaces (see the small circle in micrograph ***F***) with polymer threads that are approximately 1 μm (see the large red circle in micrograph ***E***), probably coming from inside the clay particles. As the polymerization proceeds, it is reasonable to assume that the continuous production of polymer inside and around the clay particles leads to the accumulation of polymer and the further fragmentation of the clay particle. The polymer accumulation around the tactoids is responsible for fragmentation of the clay particles and the polymer accumulation inside the clay galleries could be responsible for the exfoliation of the MMT layers.

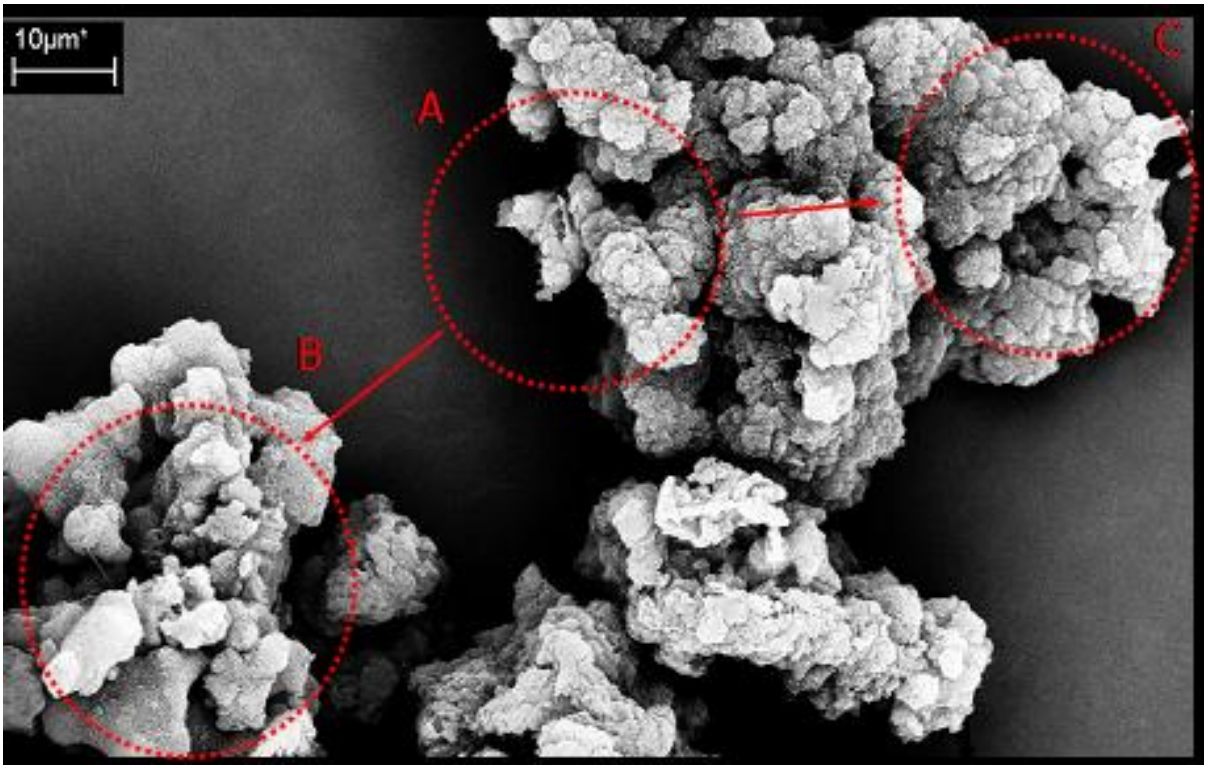


(a)

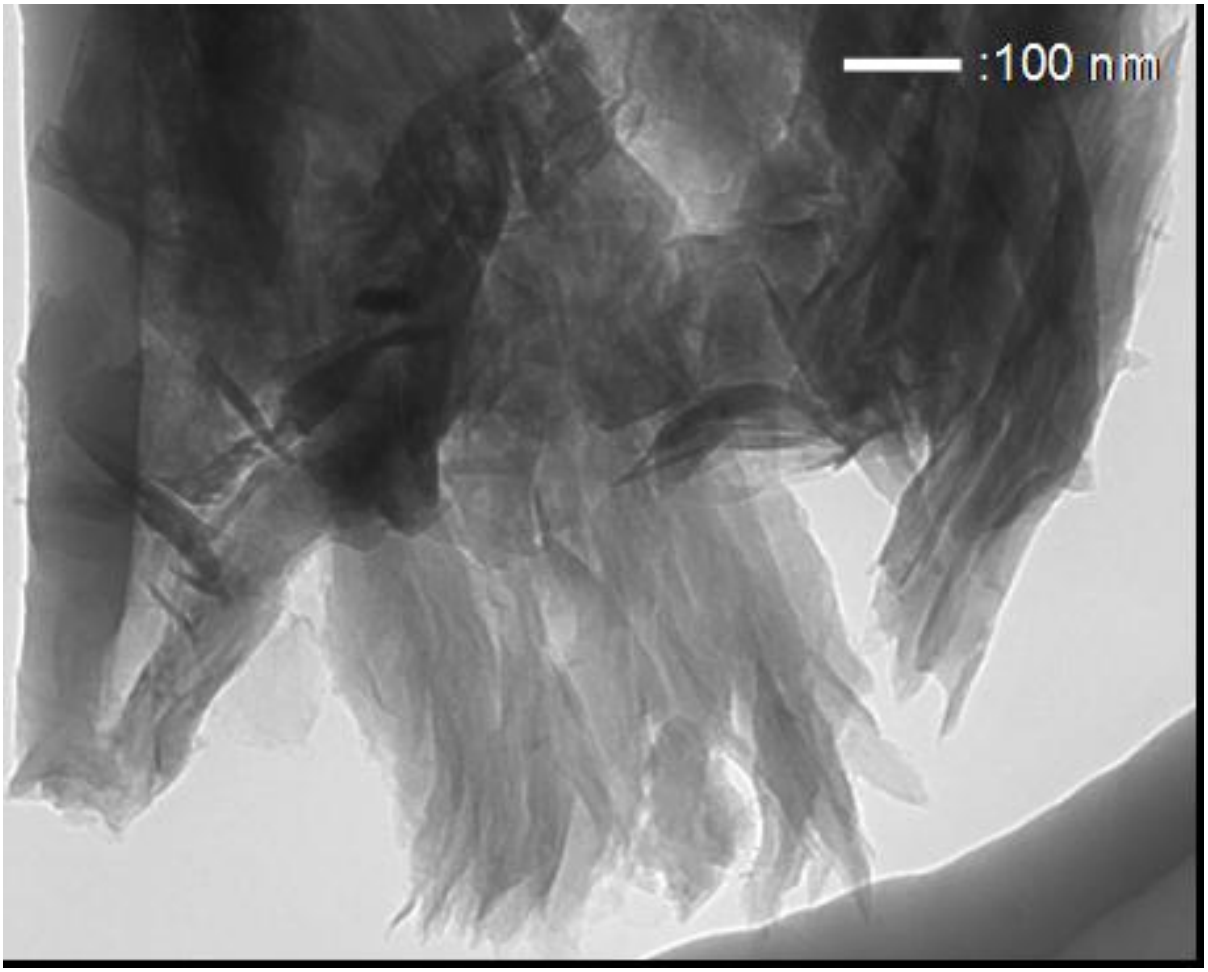


(b)

**Figure 3-3.** MMT particle morphology after 3 hours of pre-polymerization (3HP): (a) SEM image, (b) TEM image, 80 nm thin film, prepared with ultra microtoming under -160 °C in cryo-chamber.

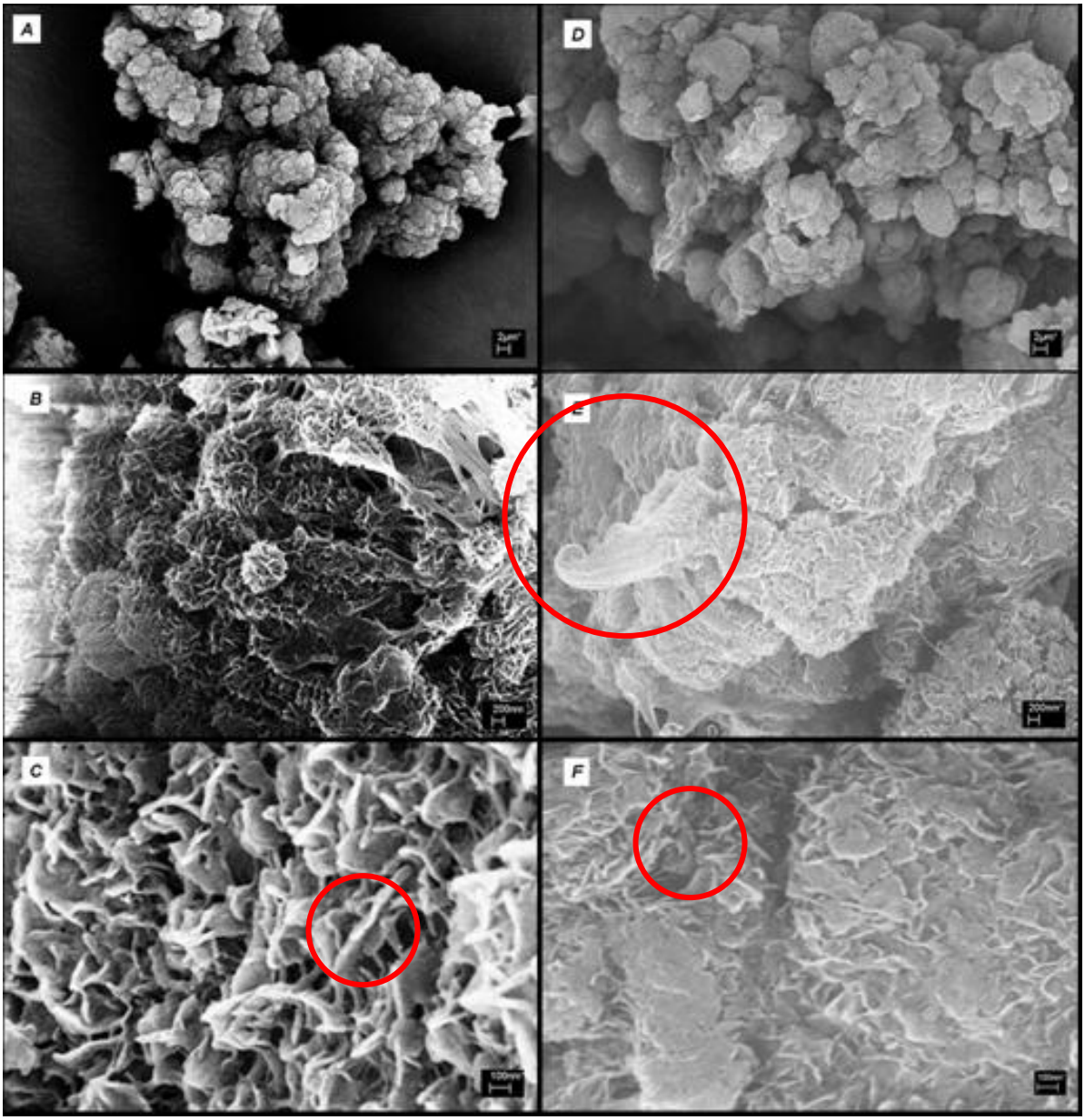


**Figure 3-4.** Comparison of particle morphologies after 3 hours (A, B, C) and 24 hours (D, E, F) of polymerization.

#### 3.3.1.1. Study of Exfoliation Mechanism with TEM and XRD

Selected polymer particles obtained in the pre-polymerization step were microtomed and studied with TEM and XRD to better understand the mechanism of particle growth and fragmentation. Figure 3-5.a shows the TEM image of a section of a pre-polymerized 24HP particle already shown in Figure 3-

4 (micrograph D to F). It seems that the exfoliation of the MMT sheets started from the edges of the clay layers, due to the growth and accumulation of polymer chains between the layers.

Figure 3-5.b shows that the clay platelets of the same sample are well aligned. The distance of 12.5 layers was measured to be 15.5 nm and the d-spacing was calculated as 12.4 Å, which is equivalent to a XRD peak at $2\theta = 7.2°$. This indicates that the structure of some MMT particles after the polymerization remains very close to that of the original MMT. The XRD for pristine MMT, and 3HP and 24HP particles, show a d-spacing peak at approximately $7.5^{o}$, corresponding to an interlayer distance of 12.3 Å. This XRD data matches well the calculation based on the TEM image shown in Figure 3-5.b. It seems that, during the gas-phase pre-polymerization, polymer intercalation or exfoliation starts from the edges of the MMT particles, but the core of some of the MMT particles are not substantially exfoliated during polymerization.

Figure 3-6 shows the diffractograms of pure MMT and 3HP and 24HP nanocomposites. The peaks located at around 21° and 24° correspond to the diffraction planes (110) and (200) of unit cell of polyethylene crystal. Their intensities increase as the polymer weight percent in the polymerized particles increase from MMT < 3HP < 24HP.

The combined evidence of SEM and TEM images, together with X-ray diffraction patterns, demonstrates that polymerization in the gas-phase starts on the surface of MMT particles, and further induces particle fragmentation.

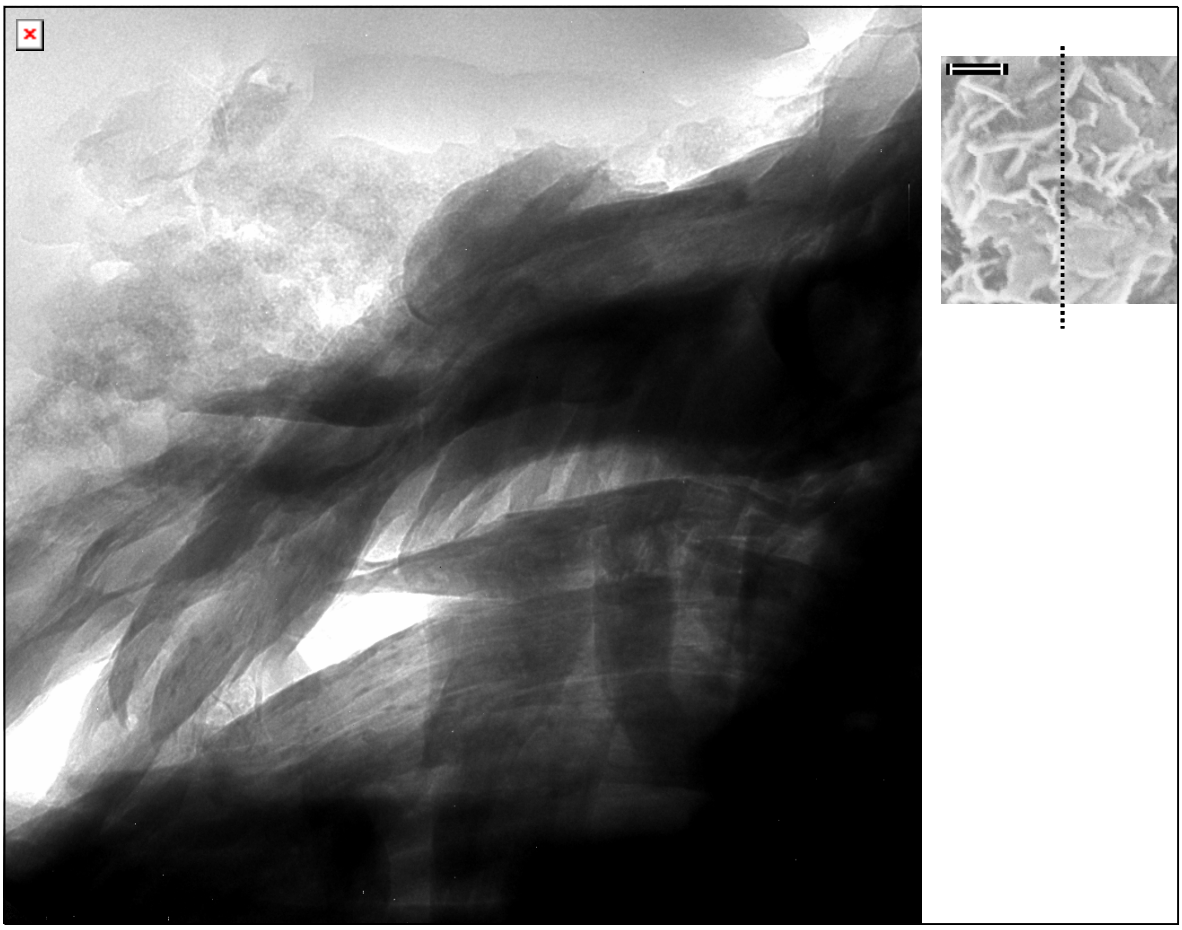

**(a)**

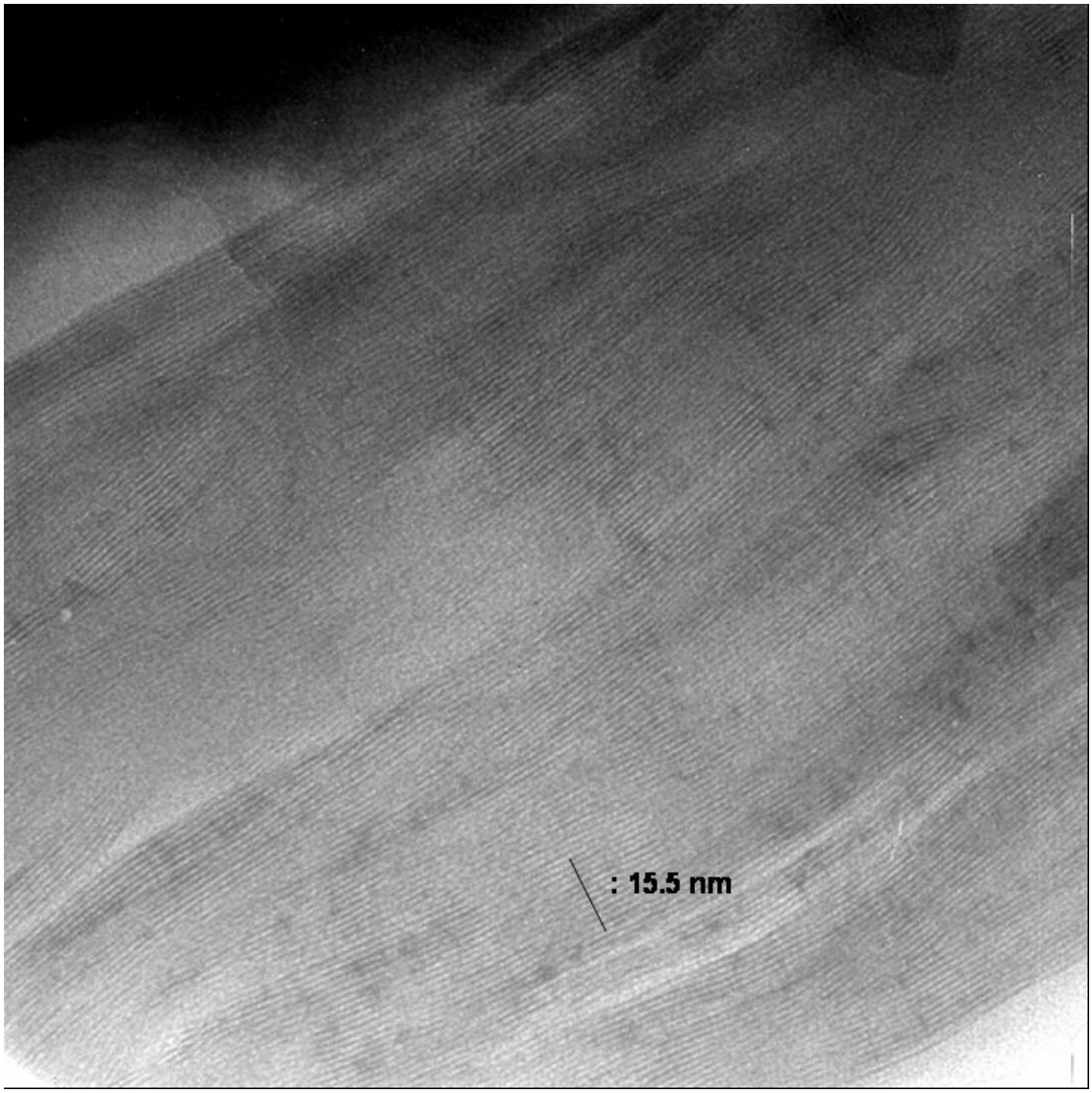


**(b)**

**Figure 3-5**. TEM pictures of a microtomed 24HP particle: (a) the inner edge of the particle after microtoming, showing that the MMT platelets were exfoliated and curved, (b) MMT layered platelets.

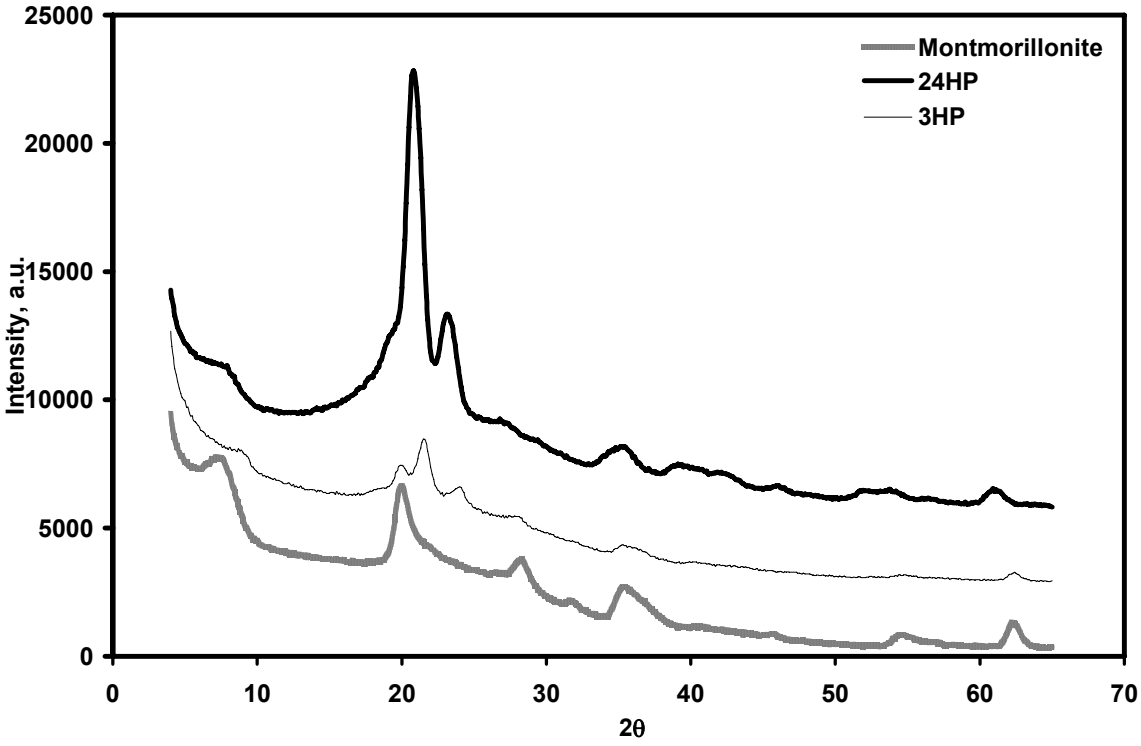


**Figure 3-6.** X-ray diffractograms of pure MMT, 3HP (45 wt.-% MMT) and 24HP (20 wt.-%) nanocomposites.

### 3.3.1.2. Gas-Phase Polymerization at High Pressure with MMT/TIBA/UOH/ $Cp_2ZrCl_2$

The morphology of polymer particles made in the high pressure gas-phase reactor was different from the morphology observed after the low pressure pre-polymerization. SEM images in Figure 3-7 show some spherical particles covered by a polymer outer shell and some particles with bare surfaces. The diameter of spherical particles varies from 20 μm to 300 μm (Figure 3-7.a to c).

Fragmented sub-particles were observed with dimension of a few micrometers in Figures 3-7.d to f. The particle fragmentation observed here seem to follow that proposed in the multigrain model, which has been developed to describe the fragmentation mechanism of magnesium-supported Ziegler-Natta catalysts (Soares, 1995). The projection, or fibril, morphology described above for pre-polymerization was not observed in polymer particles made under high pressure polymerization.

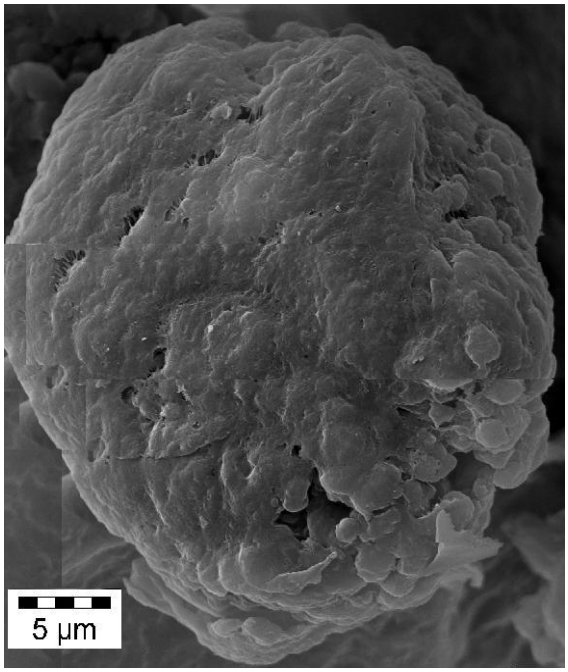


**(a)**

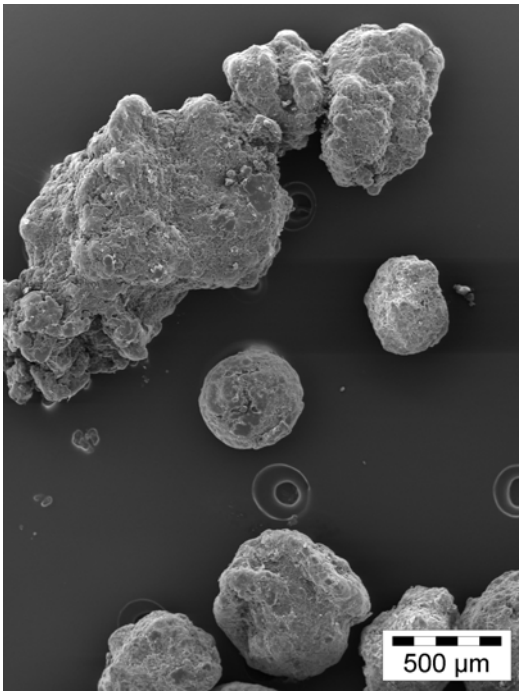


**(b)**

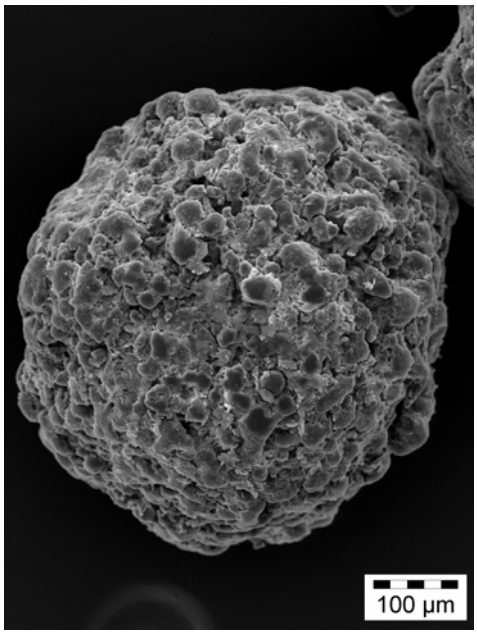


**(c)**

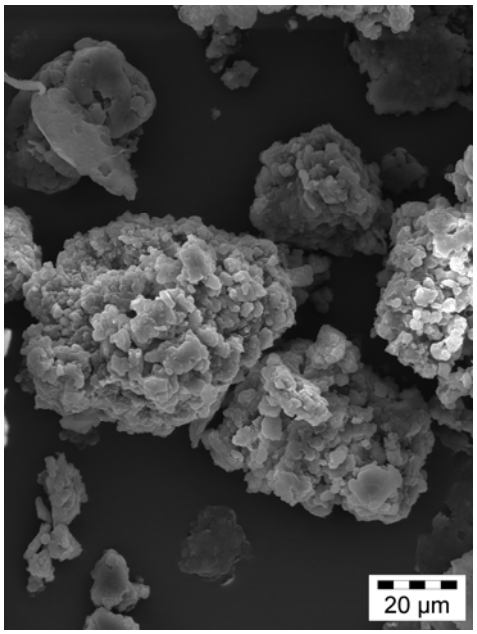


**(d)**

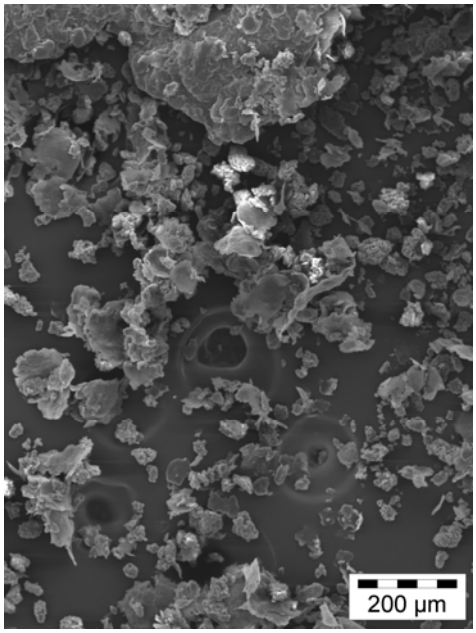


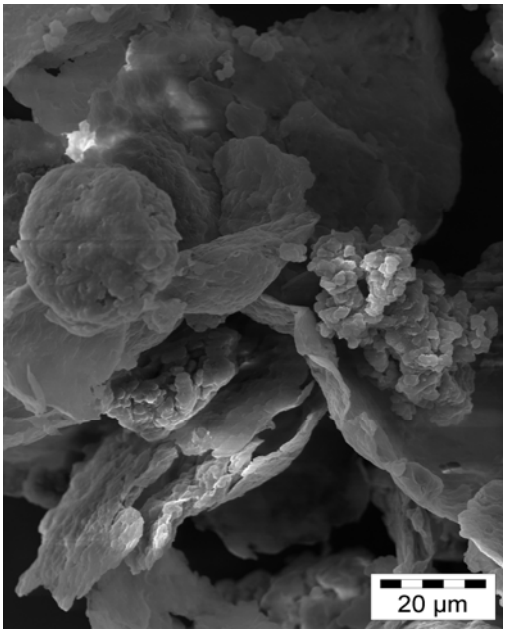


**(e)** **(f)**

**Figure 3-7.** Morphology of polymer particles after gas-phase polymerization: (a) Expanded image of a particle with polymer outer shell, (b) Several types of particle morphologies, (c) Expanded image of a spherical type particle, (d) Particles without polymer outer shell, (e) Overall morphology, (f) Particles with and without polymer outer shells.

Figure 3-8 shows the intraparticle morphology at higher magnifications. Figure 3-8.a shows particles that seem to be kept attached during the fragmentation, whereas Figure 3-8.b shows that some particles are linked by polymer threads.

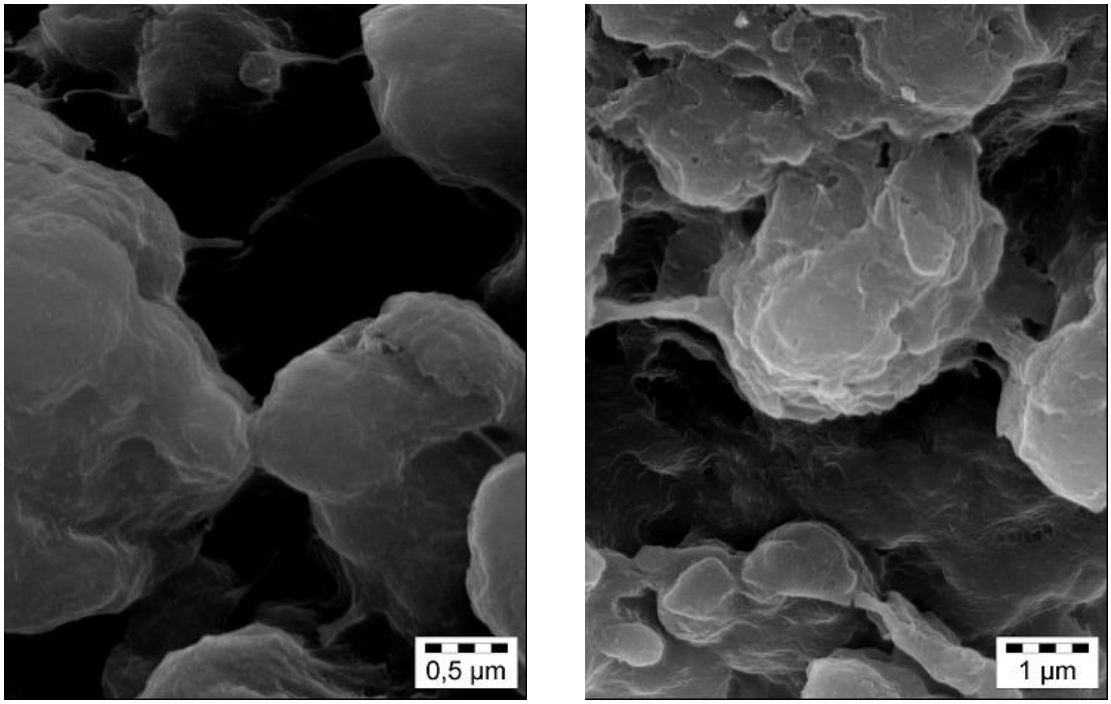


(a) (b)

**Figure 3-8.** Morphology of particles after gas-phase polymerization: (a) Attached particles just after fragmentation within particle clusters, (b) Divided particles after fragmentation continued within particle clusters.

Figure 3-9 shows the catalyst activity profile for the gas-phase polymerization (sample 24HP). An unexpected induction period was observed during the first 20 minutes of polymerization. The reason for this induction period is not totally clear. It may be caused by a reactor overpressure during catalyst injection or by side reactions between the supported catalyst and TMA used as impurity scavenger. It could also be related to mass transfer limitation during ethylene diffusion from the gas phase to the pre-polymerized catalyst. After the induction period, the polymerization rate increased steadily as the ethylene concentration between the MMT platelets increased during the polymerization. The fragmentation process of the particles could make monomer more accessible to

the active sites by increasing surface area and decreasing the characteristic monomer diffusion length. The induction period is followed by a steady growth in activity (acceleration-type kinetics).

According to the multigrain model mechanism, a mechanically strong catalyst support that does not fragment easily during polymerization will not favor an increase in surface area. Hence, there will be a mass transfer limitation for monomer diffusion to the active sites that will decrease the catalyst activity and lower the polymerization yield.

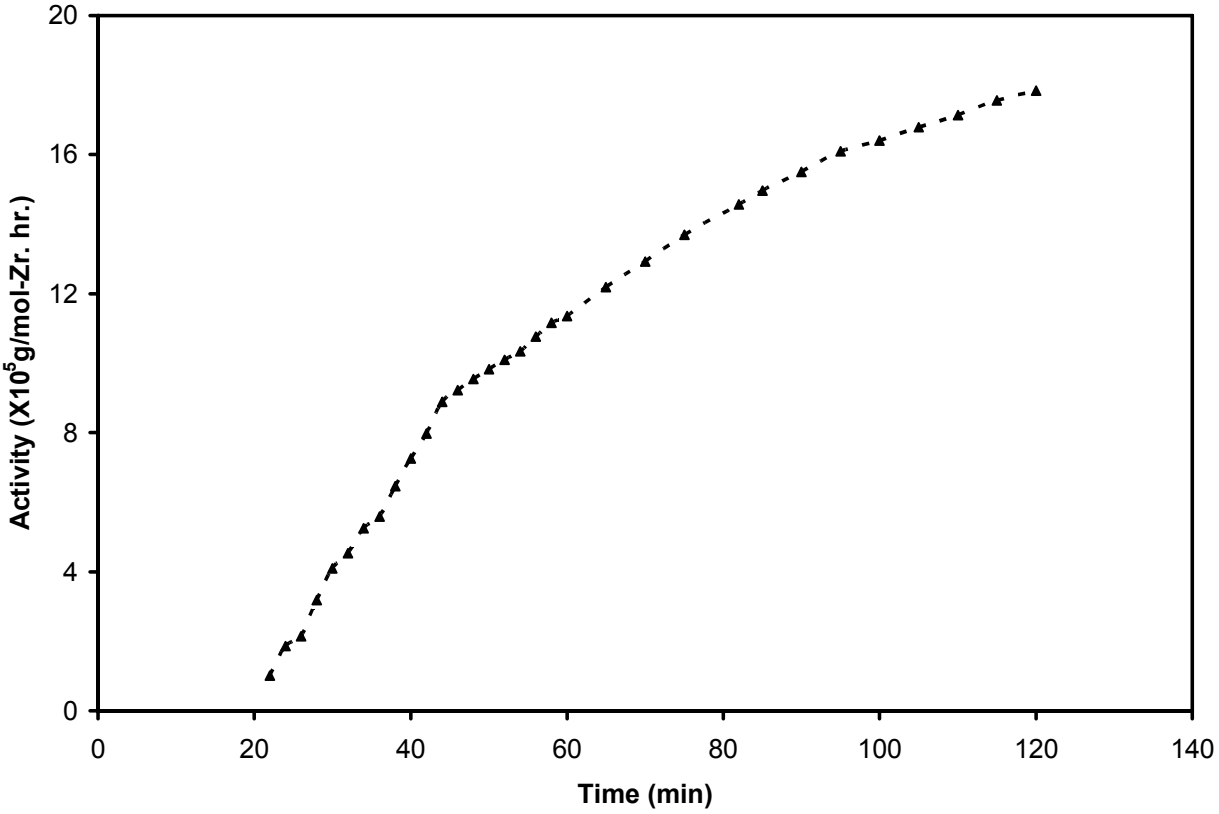


**Figure 3-9.** Activity profile of 24HP samples as a function of polymerization time. Ethylene pressure = 6 bar, polymerization temperature = 73 °C, Al/Zr = 2000.

### 3.3.1.3. Topology of Alkyl Chains Inside the MMT Galleries

The topological structure of alkyl chains inside MMT galleries were studied using transmission FT-IR and XRD (Vaia et al., 1994), as previously explained in Section 2.3.9. The polymer chains are thought to extend either parallel to the clay layers, forming lateral mono- or bi-layers, or radiate away from the surface, forming extended (paraffin-type) mono- or bimolecular arrangements (Lagaly, 1981; Lagaly, 1986; Weiss, 1963).

Figure 3-10 shows the FT-IR spectra (1400 $cm^{-1}$ - 1520 $cm^{-1}$) for 3HP and 24HP pre-polymers, and polyethylene. The $CH_2$ bending mode, $\delta(CH_2)$, is located, between 1460 and 1474 $cm^{-1}$. While the $\delta(CH_2)$ band for 3HP pre-polymer ranged between 1460 $cm^{-1}$ and 1474 $cm^{-1}$, the $\delta(CH_2)$ band for the pre-polymer 24HP was shifted to a lower frequency range (1457 $cm^{-1}$ - 1473 $cm^{-1}$) and became broader. In the case of polyethylene, the band is located in the lower frequency range (1467 $cm^{-1}$ - 1454 $cm^{-1}$). This type of change is normally associated with more disordered polymer chains (lower trans/gauche conformation ratio). This indicates that, as pre-polymerization proceeds from 3 to 24 hours, the polymer chains favor a more disordered configuration due to the tendency of the chains to maximize their conformational entropy.

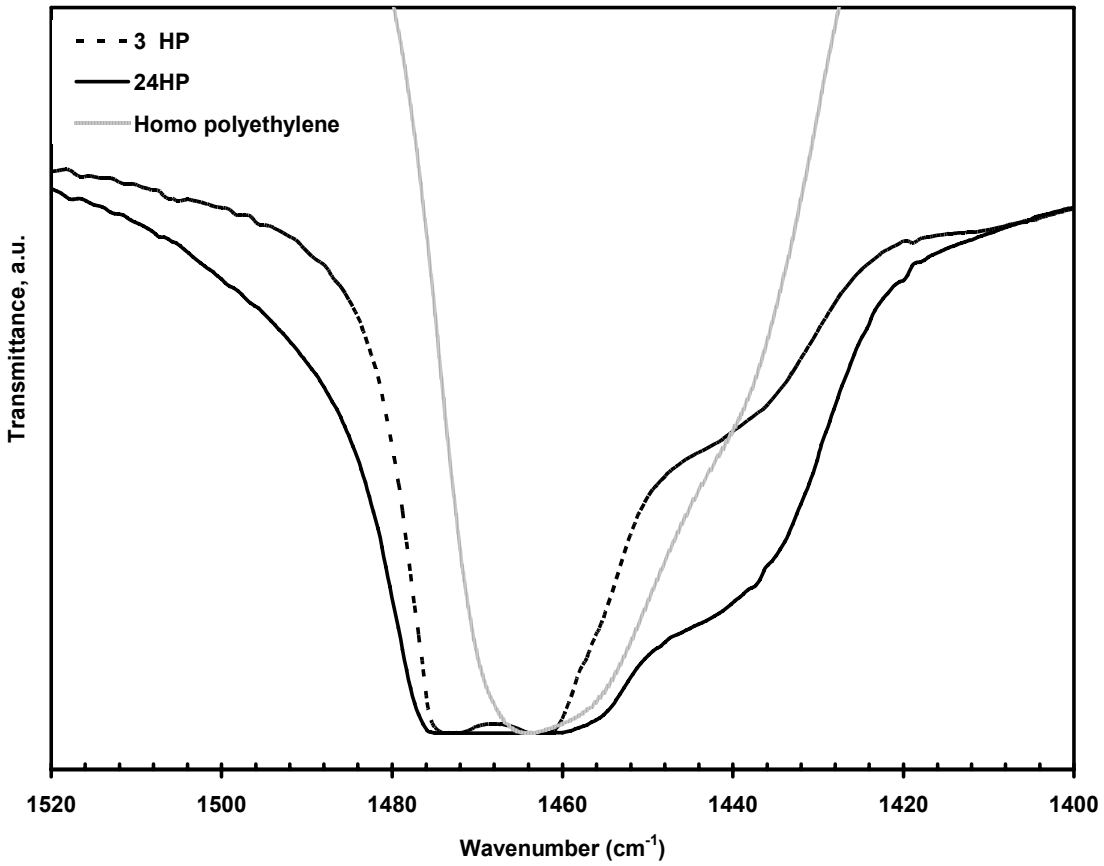


**Figure 3-10.** FT-IR transmittance spectra for 3HP and 24HP pre-polymers and polyethylene displaying different methylene modes. The spectra were obtained at room temperature.

Table 3-1 suggests the overall particle fragmentation mechanism for these supported catalysts. During the polymerization, polymer chains grow on the surface of MMT particles, around the tactoids, and inside the galleries, establishing the onset of intercalation and exfoliation. The MMT particles are also fragmented into the smaller particles, possibly into clusters of tactoids. Finally, polymer particles with good morphology (free flowing powder with spherical shape particles) are formed during the high-pressure polymerization stage. A high rate of polymerization was observed in this last stage.

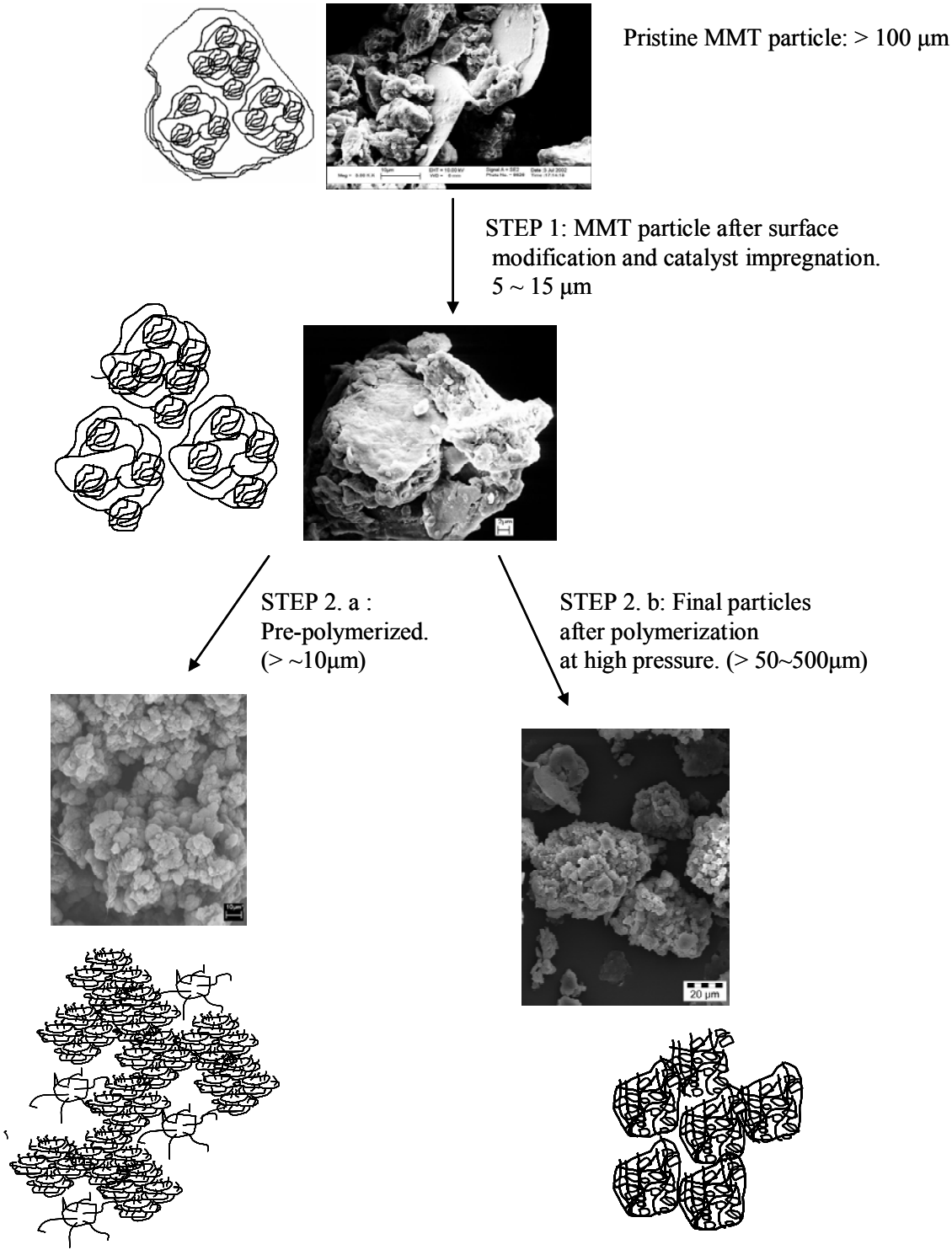


**Figure 3-11.** Proposed mechanism for particle fragmentation with MMT/TIBA/UOH/$Cp_2ZrCl_2$.

### 3.3.2. Morphology of Polymer Particles Made with MMT/TIBA/UOH/ Ni-diimine

The polymerization of ethylene was carried out with MMT/TIBA/UOH/Ni-diimine in a similar way described in Section 3.3.1 for MMT/TIBA/UOH/$Cp_2ZrCl_2$. The main objective of this investigation was to study the particle morphology development and mechanism of particle growth when a short chain branched polyethylene is produced. Fundamental differences are expected because this type of polyethylene is expected to be mostly amorphous. Because this type of polyethylene has rubber-like properties, the mechanism of particle growth and fragmentation will likely be different from when the polyethylene is semi-crystalline.

Figure 3-12.a shows the overall morphology of the pre-polymerized particles made with MMT/TIBA/UOH/Ni-diimine catalyst system after 1 hour polymerization. Figure 3-12.b shows different morphologies of the polymer film formed on the MMT particles. Figure 3-12.c shows a similar picture at a higher magnification. No polymer fibrils were observed in this case as opposed to the fibrils observed in the particles made with MMT/TIBA/UOH/$Cp_2ZrCl_2$. Instead, only a film of polyethylene covering the MMT particles was observed in the polymerization of ethylene catalyzed by Ni-diimine. These different morphologies in the early stage of polymerization are attributed to the low crystallinity of polyethylene made with the Ni-diimine catalyst.

The morphology of particles obtained after 24 hours of polymerization in gas-phase at atmospheric pressure is shown in Figure 3-13.a and b. The particle diameters increased to about 50 μm. Some particles show polymer threads (Figure 3-13.b), which seem to have grown from inside of the particles as polymerization continued, similarly what we observed for the $Cp_2ZrCl_2$ system.

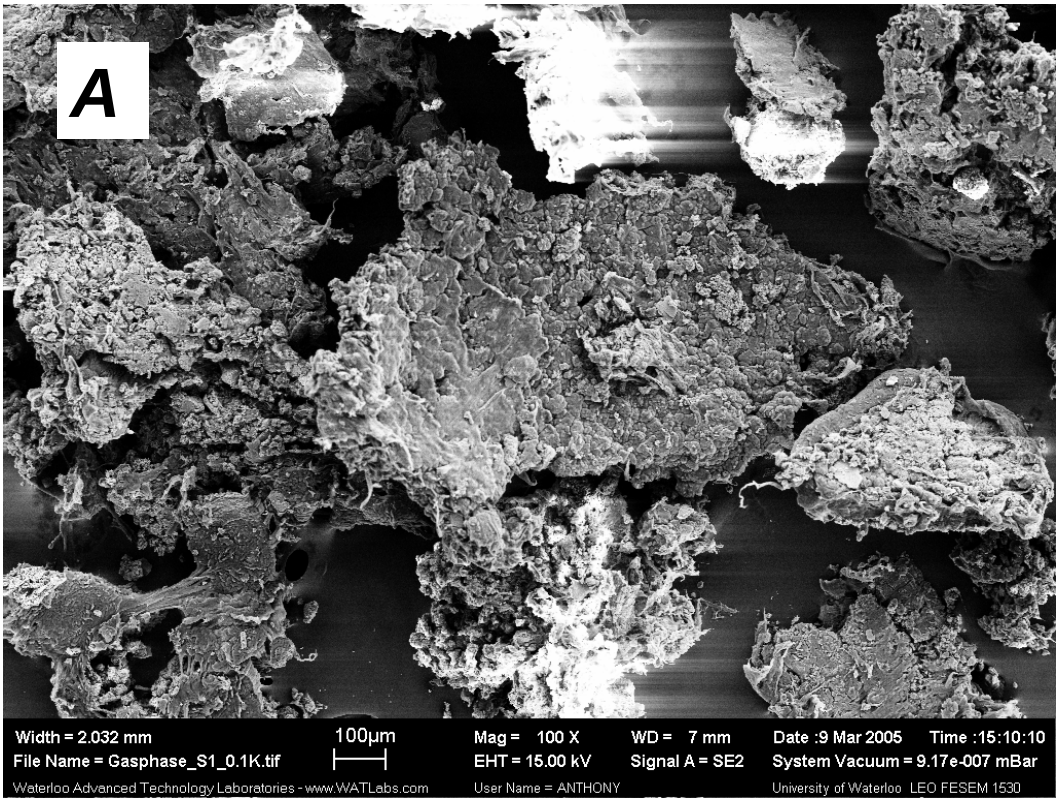
A
Width = 2.032 mm
File Name = Gasphase_S1_0.1K.tif
100µm
Mag = 100 X
EHT = 15.00 kV
WD = 7 mm
Signal A = SE2
Date :9 Mar 2005 Time :15:10:10
System Vacuum = 9.17e-007 mBar
Waterloo Advanced Technology Laboratories - www.WATLabs.com
User Name = ANTHONY
University of Waterloo LEO FESEM 1530

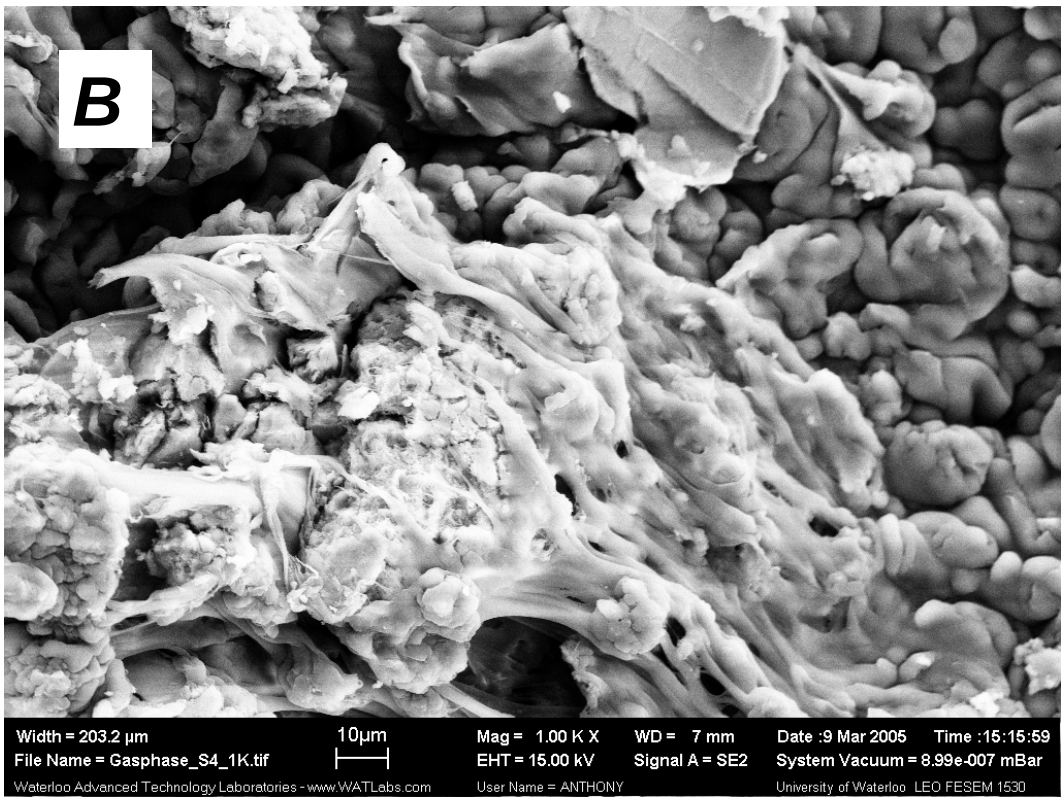
B
Width = 203.2 µm
File Name = Gasphase_S4_1K.tif
10µm
Mag = 1.00 K X
EHT = 15.00 kV
WD = 7 mm
Signal A = SE2
Date :9 Mar 2005 Time :15:15:59
System Vacuum = 8.99e-007 mBar
Waterloo Advanced Technology Laboratories - www.WATLabs.com
User Name = ANTHONY
University of Waterloo LEO FESEM 1530

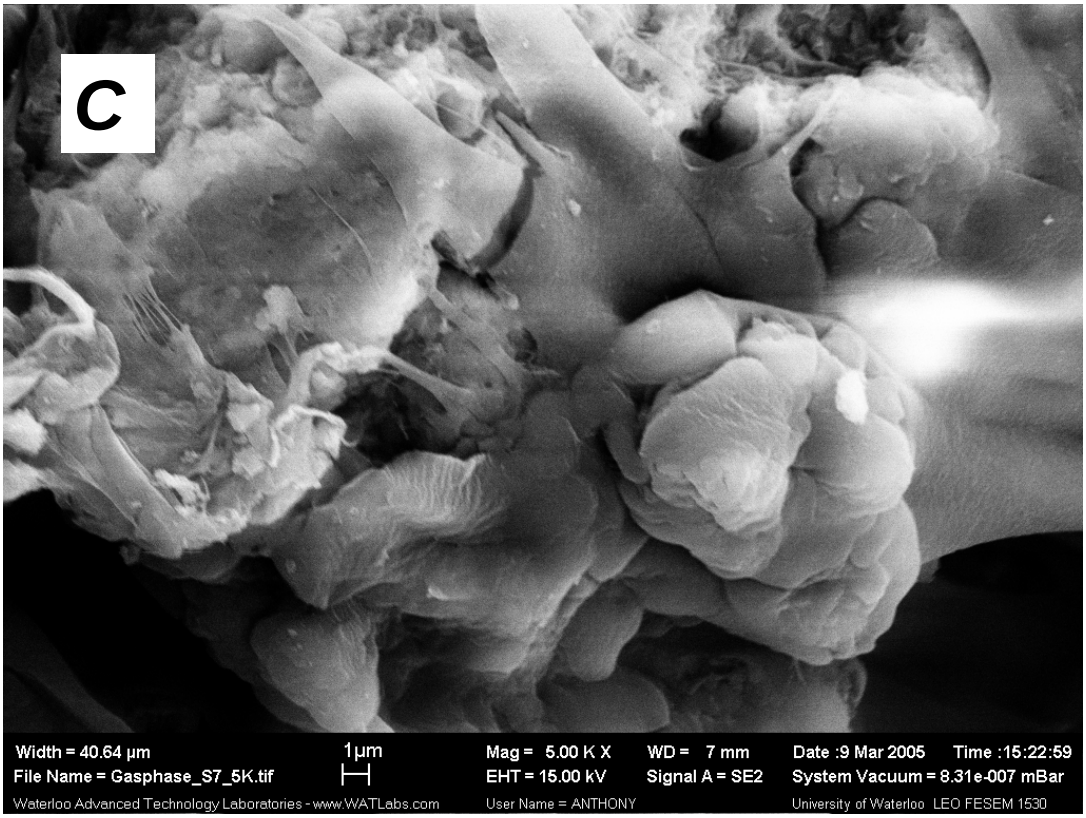


**Figure 3-12.** Morphology of pre-polymerized MMT/TIBA/UOH/Ni-diimine polyethylene particles after 1 hour in the glass reactor.

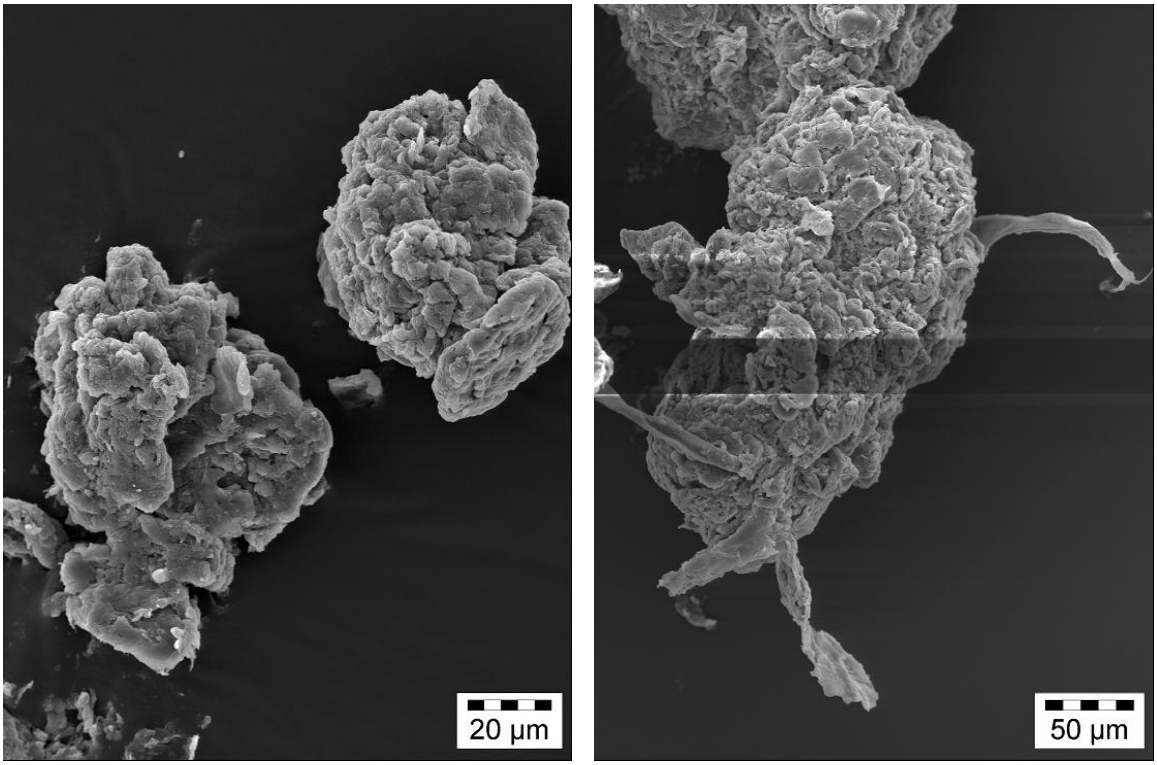


(a) (b)

**Figure 3-13.** Different particle morphologies of PE-MMT/TIBA/UOH/Ni-diimine polyethylene after 24 hours gas-phase pre-polymerization at atmospheric pressure.

#### 3.3.2.1. Gas-Phase Polymerization at High Pressure

MMT/TIBA/UOH/Ni-diimine was also used to polymerize ethylene in the high-pressure reactor. Figure 3-14 shows the morphology of the particles obtained under these conditions. Overall, the particle morphology shows clusters of PE-MMT composite spheres. The MMT particles are distributed in the PE-MMT (roughly) spherical particles, as shown in Figure 3-15. The molten appearance of the polymer surface in Figure 3-15 is probably caused by a combination of heat released during the polymerization, the poor gas-solid heat transfer properties of gas-phase reactors, and the lower melting point of short-chain branched polyethylene. Webb and co-workers showed that the temperature of polyethylene particles made in gas-phase polymerization, can increase up to 180°C

(Webb et al., 1991). A more detailed inspection of the polymer particle structures, shown in Figure 3-16, reveals layers of MMT covered with polyethylene.

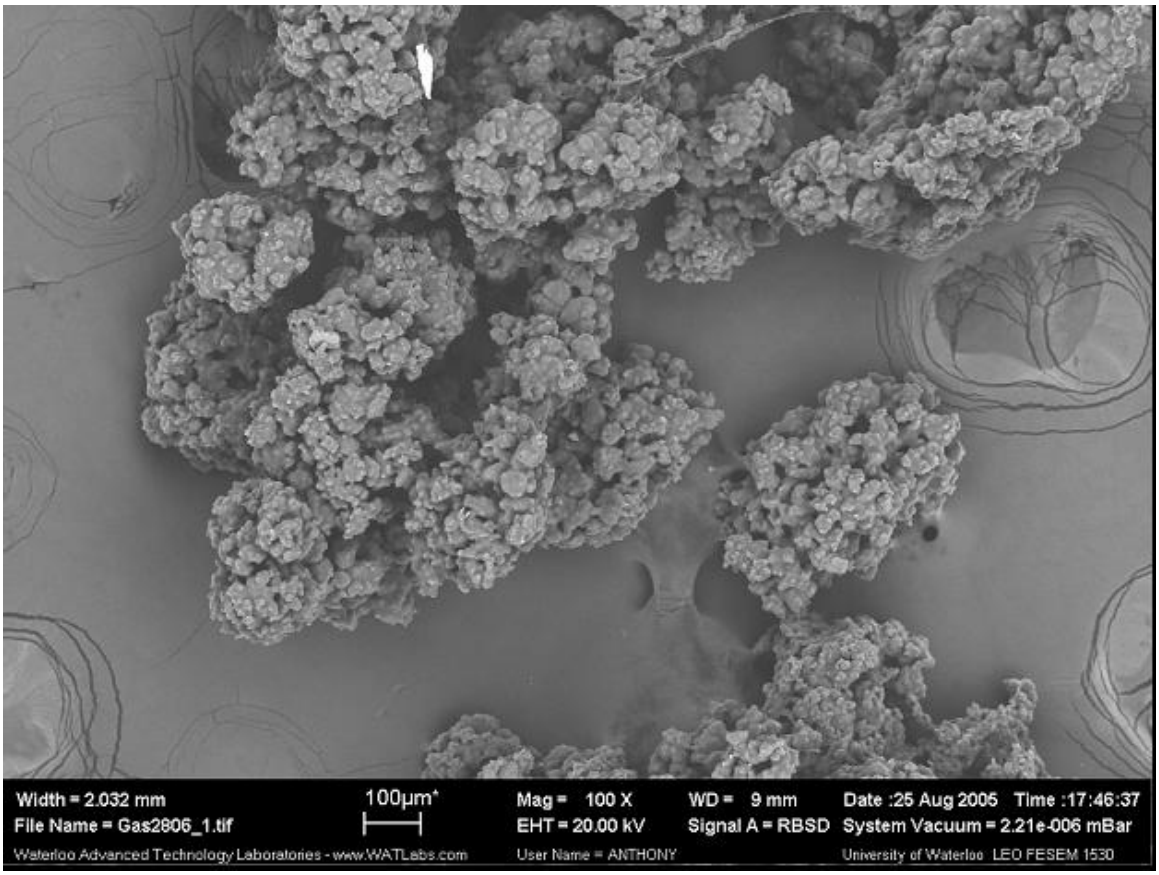


**Figure 3-14.** PE-MMT particle morphology after high pressure polymerization with MMT/TIBA/UOH/Ni-diimine.

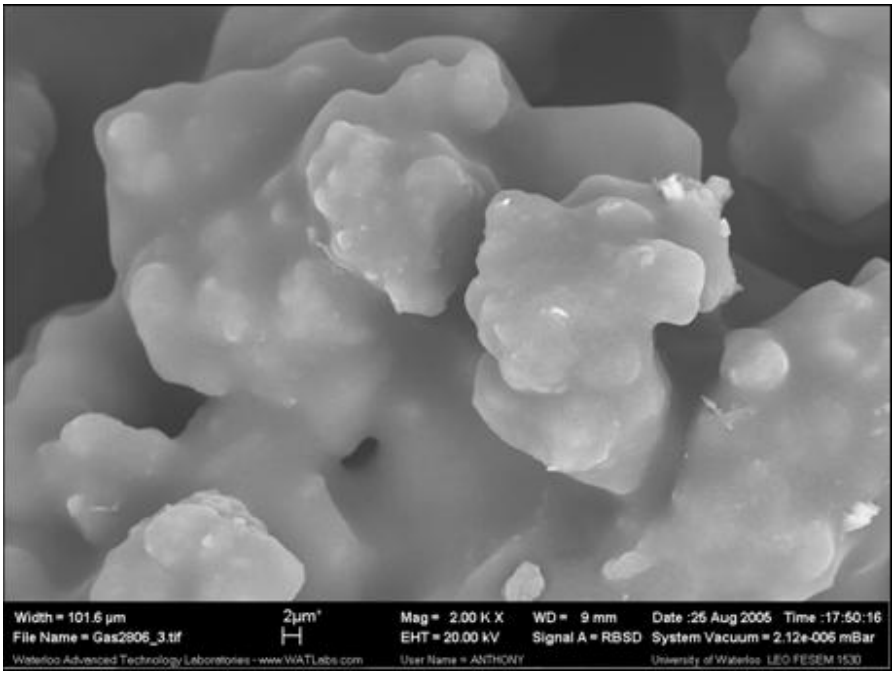


**Figure 3-15.** Detailed particle surface morphology after high pressure gas-phase polymerization with MMT/TIBA/UOH/Ni-diimine.

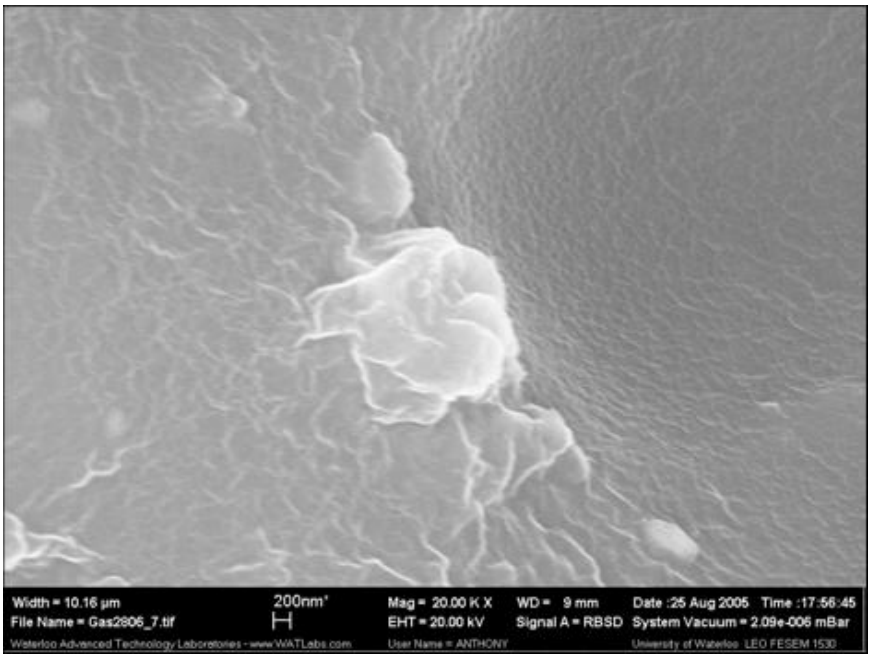


**Figure 3-16.** Nanoscale tactoid structure of MMT particles after gas-phase polymerization with MMT/TIBA/UOH/Ni-diimine.

The morphological changes of the MMT particles during polymerization are summarized in Figure 3-17. Three particle fragmentation steps, based on the previous SEM images, are suggested in Figure 3-17. Step 1 shows the typical morphology of MMT/TIBA/UOH/Ni-diimine particles before the polymerization. After 1-hour pre-polymerization at room temperature and atmospheric pressure, the average particle diameter increases from 5-15 μm to about 50 μm (Step 2). If the pre-polymerization is allowed to continue for 24 hours at these conditions, irregularly shaped particles, with protruding polymer fibrils, may be formed, as shown in Step 3.a. On the other hand, when the polymerization takes place at high ethylene pressure, particles with more regular morphology arise, as shown in Step 3.b.

Figure 3-18 shows the activity profile of MMT/TIBA/UOH/Ni-diimine during gas-phase polymerization. The polymerization rate rapidly increases to a maximum activity, followed by a continuous decline. This observation is consistent with the rate profiles of metallocene/MAO catalysts in ethylene gas-phase polymerization (Hammawa et al., 2006). The acceleration phase could be attributed to different induction times of individual catalyst particles caused by inhomogeneous MAO loading and different monomer diffusion rates in each active site. Gradual deactivation of the active sites by impurities leads to the activity decline phase (Hammawa et. al., 2006). The unexpected induction time is once more observed. We proposed a few tentative explanations for this induction time above when discussing polymerization with MMT/TIBA/UOH/$Cp_2ZrCl_2$. The induction time is shorter with MMT/TIBA/UOH/Ni-diimine than with MMT/TIBA/UOH/$Cp_2ZrCl_2$ (approximately 5 minutes and 20 minutes, respectively). Since the crystallinity of polyethylene made with Ni-diimine is much lower than the crystallinity of polyethylene made with $Cp_2ZrCl_2$, the effective diffusivity of ethylene in the polyethylene made with Ni-diimine is much higher than in polyethylene made with $Cp_2ZrCl_2$. Therefore, we may speculate that at least part of the induction time is caused by mass transfer limitation to ethylene diffusion from the gas phase to the active sites.

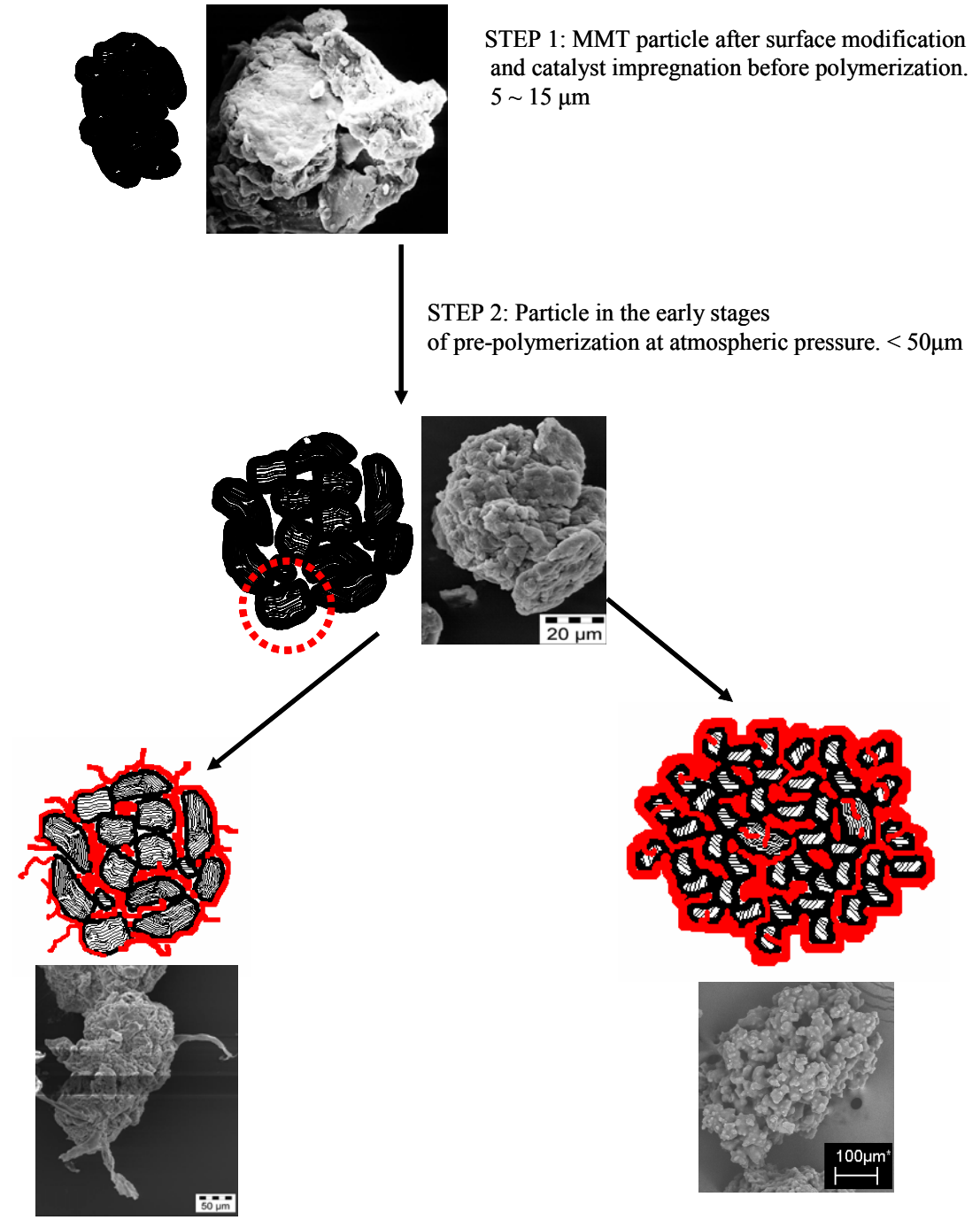


**Figure 3-17**. Particle fragmentation mechanism with MMT/TIBA/UOH/Ni-diimine-MAO system

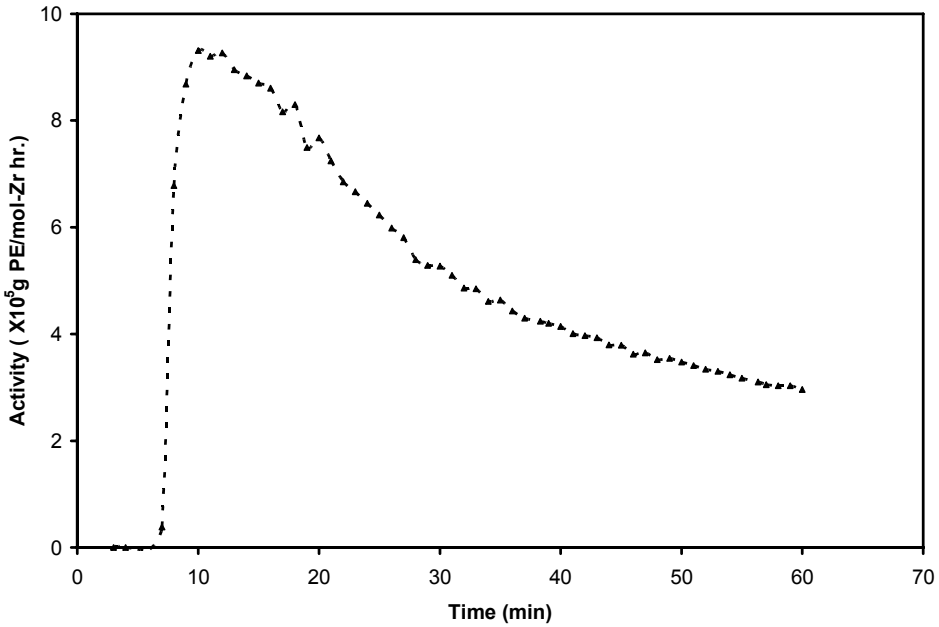


**Figure 3-18.** Polymerization with MMT/TIBA/UOH/Ni-diimine. Polymerization conditions: catalyst pre-polymerized at room temperature for 3 hours. Al/Ni = 2000, no scavenger added, pressure (ethylene) = 5 bar, temperature = 80 °C.

### 3.3.2.2. Analysis of Intercalation/Exfoliation of MMT Particles and its Influence on the Crystalline Polymer Phase

PE-MMT/TIBA/UOH/Ni-diimine particles were investigated to correlate XRD with DSC data and to study the influence of the MMT particles in the polymer crystalline structure. Based on the TGA thermogram, the MMT content was calculated as 62 wt.-% after gas-phase polymerization.

In Figure 3-19, the peak at 7.5$^o$ for MMT represents the individual layers before intercalation. This basal diffraction band disappeared after gas-phase ethylene polymerization. This observation implies that MMT exfoliated during gas-phase polymerization. The peaks located at around 21° and 24° are those from the crystal unit cell of polyethylene. The new band at 8.9$^o$ can be attributed to illite group impurities as explained in Section 2.3.3.

The SEM images shown in Figures 3-12 to 3-16 and the X-ray diffraction patterns in Figure 3-19 demonstrate that the MMT particles are fragmented into particles with smaller sizes during ethylene polymerization. These particles have a tactoid structure, undergoing a fragmentation mechanism similar to the one described by the multigrain model during polymerization with catalysts supported on non-layered supports.

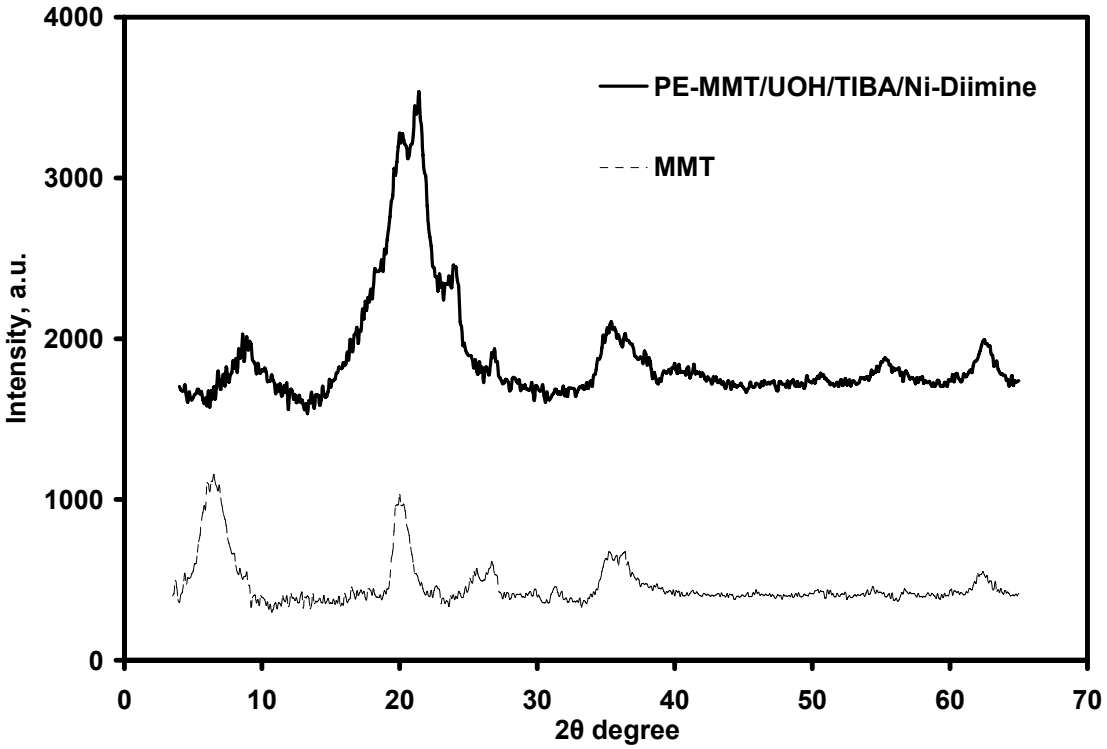


**Figure 3-19.** XRD analysis in early stages of polymerization with Ni-diimine in-situ polymerization: MMT and PE-MMT/TIBA/UOH/Ni-diimine (62 wt.-% MMT).

Previous investigations have indicated that exfoliated MMT added to a polymer matrix can change the degree of crystallinity of the polymer phase. For example, DSC analysis has shown that the degree of crystallinity of maleic anhydride-grafted polyethylene-MMT composite decreased because of the presence of exfoliated MMT platelets (Gopakumar et al., 2002). The authors suggested that this decrease might be attributed to the higher interfacial area and adhesion between the PE

matrix and the exfoliated MMT, which would act to reduce the mobility of crystallizable polymer segments.

DSC and XRD analysis were carried out to study the thermal behaviour of exfoliated MMT platelets in polyethylene synthesized in gas-phase polymerization. XRD analysis was applied before and after DSC scans, using the same sample.

Figure 3-20.a shows the DSC curves of PE-clay composite (6 wt.-%, MMT), prepared with MMT/TIBA/UOH/Ni-diimine in gas-phase polymerization under high pressure. In the 1$^{st}$ heating scan, the polyethylene crystallinity was 15 %, while in the 2$^{nd}$ heating scan the crystallinity was reduced to 9.3 %. The crystallinity measure in the 1$^{st}$ heating scan is that of the nascent polyethylene made during the gas-phase polymerization. The reduction in crystallinity in the 2$^{nd}$ scan implies that the recrystallization of polyethylene in the PE-clay nanocomposite was disturbed by the presence of MMT platelets. The XRD results shown in Figure 3-20.b also indicate that the polyethylene crystallinity was reduced after the 1$^{st}$ DSC scan.

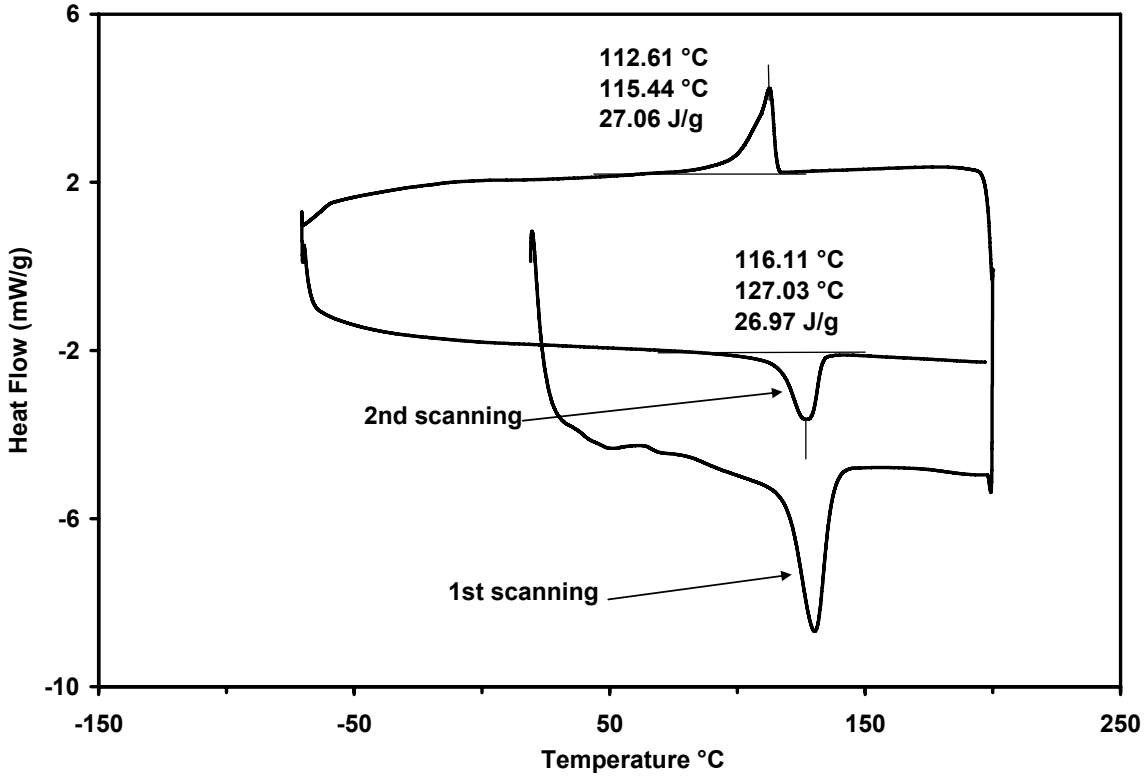
112.61 °C
115.44 °C
27.06 J/g
116.11 °C
127.03 °C
26.97 J/g
2nd scanning
1st scanning
Heat Flow (mW/g)
Temperature °C
6
2
-2
-6
-10
-150
-50
50
150
250

**(a)**

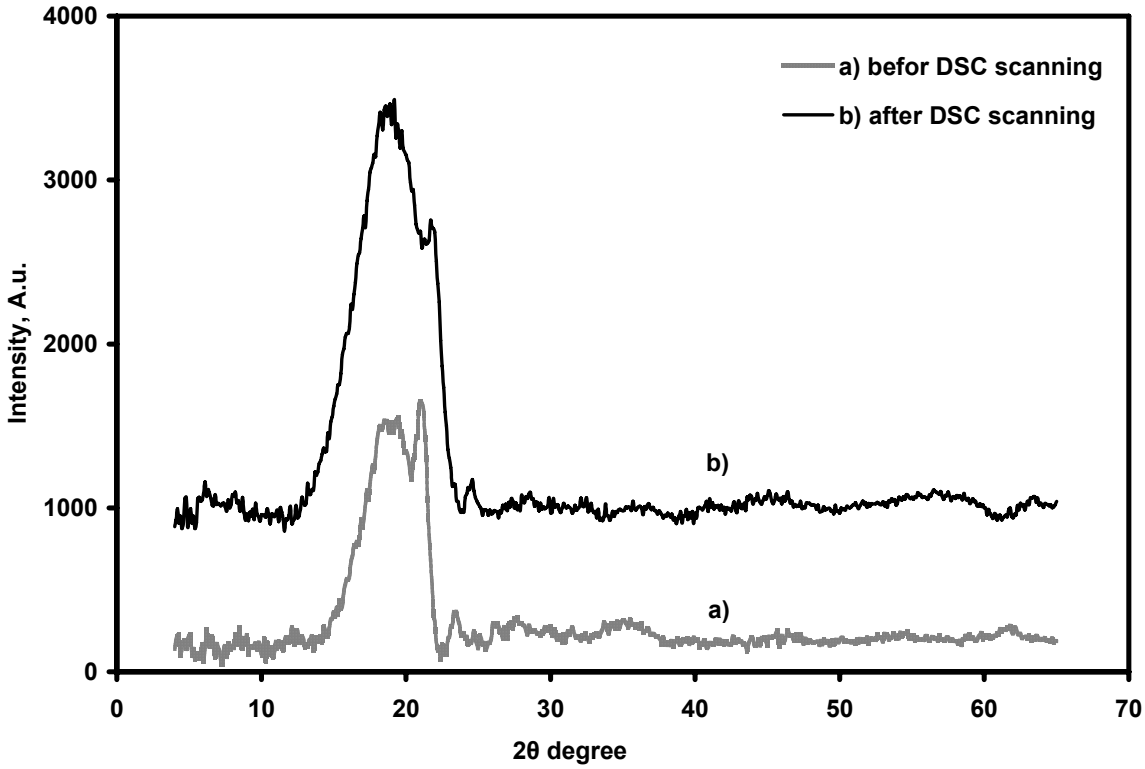


**(b)**

**Figure 3-20.** (a) DSC analysis of PE-MMT (6 wt.-% MMT) composite, synthesized under high pressure in gas-phase polymerization with MMT/TIBA/UOH/Ni-diimine-MAO catalyst (b) X-ray diffractograms before and after DSC scanning.

For a more detailed study of the effect of MMT layers on polyethylene crystallinity, the WAXS curves in the range from 10° to 25° were expanded and resolved into crystalline peaks and amorphous halo (Figure 3-21). The deconvolution of these peaks was carried out with Origin 7.0 following the procedure: a) curves were first normalized by a baseline setting; b) the baseline was subtracted; c) the deconvolution procedure was executed using Gaussian curves. The results of the deconvolutions are presented in Table 3-1.

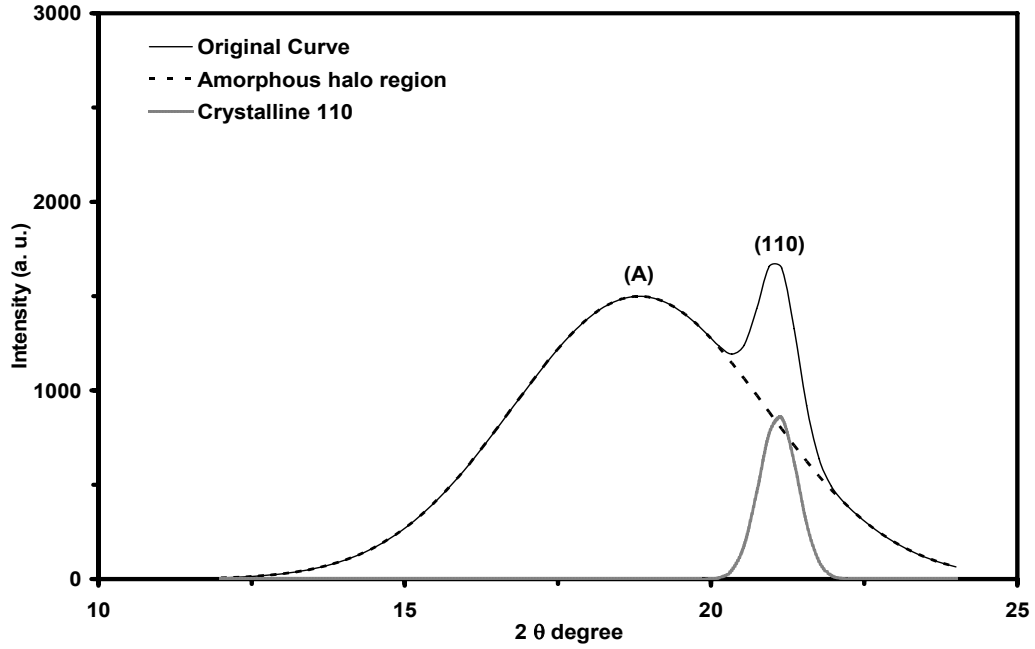


(a)

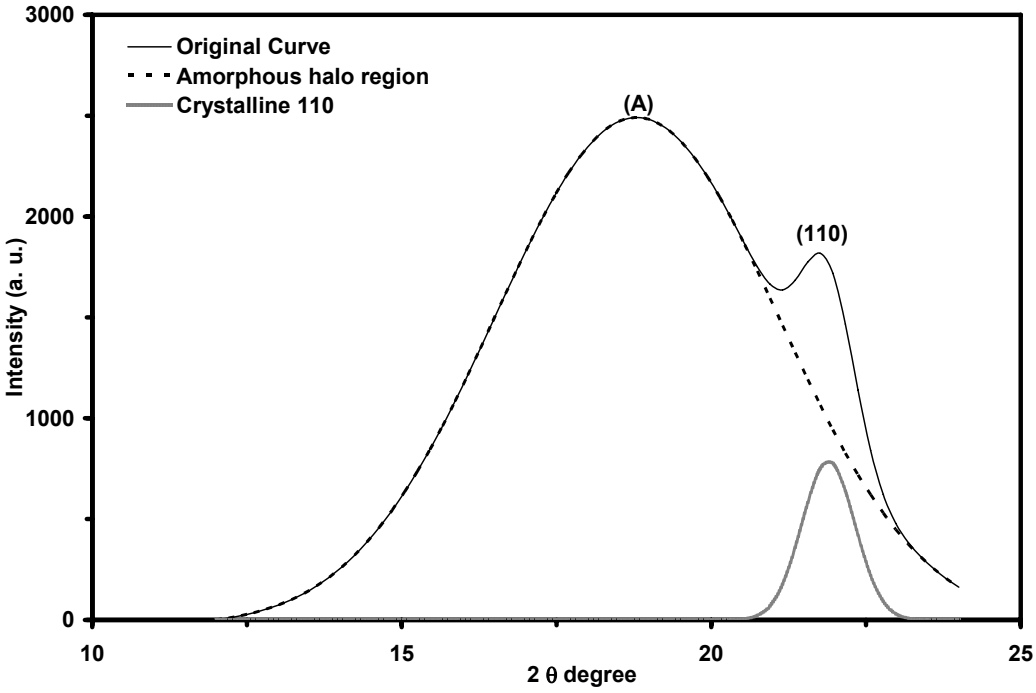


(b)

**Figure 3-21.** WAXS patterns, resolved into crystalline peaks (110) and amorphous halo using the diffractograms shown in Figure 3-20.b: (a) before DSC scanning, (b) after DSC scanning.

The percentages of the crystalline phase in X-ray diffractograms was calculated with Equation (3-1):

$$\text{Crystallinity (\%)} = \frac{I_{(110)}}{I_{normal}} \times 100 \qquad (3\text{-}1)$$

where $I_{(110)}$ is the integral of the deconvoluted crystalline (110) band and $I_{normal}$ is the integral of the normalized band.

**Table 3-1.** XRD data evaluation before and after DSC scanning.

| | Peak | Crystalline (%) | Area (Integrated) | Center (2θ°) | Width (2θ°) | Height (2θ°) |
|---|---|---|---|---|---|---|
| Before DSC Scanning | Normalized curve | 100 | 8393.77 | 20.95 | 5.08 | 1657.66 |
| | Amorphous halo. | 91.9 | 7712.25 | 18.92 | 4.88 | 1498.02 |
| | Crystalline (110) | 8.1 | 681.53 | 21.15 | 0.81 | 854.28 |
| After DSC Scanning | Normalized curve | 100 | 14797.04 | 18.71 | 6.10 | 2489.2 |
| | Amorphous halo. | 94.3 | 13951.56 | 18.71 | 5.28 | 2489.2 |
| | Crystalline (110) | 5.7 | 845.48 | 21.97 | 1.02 | 776.47 |

The location of the WAXS amorphous halo band depends on two components of the amorphous phase: one is liquid-like and the other is a higher molecular-ordered dense phase (Monar et al., 1999; Simanke et al., 2001; Bartczak et al., 1996). The position of the amorphous halo depends

on the degree of packing of molecules in the amorphous phase and the most frequently occurring intermolecular distance can be approximated by the equation (Alexander, 1969):

$$ra \approx 1.22 \frac{\lambda}{2 \sin \theta_\alpha} \tag{3-2}$$

where $ra$ is the intermolecular distance, $\theta_\alpha$ is the $2\theta$ degree of diffraction of the amorphous halo, and $\lambda$ is the X-ray wavelength. This is a reciprocal dependency, typical of all diffraction phenomena: the smaller the angle, the higher the intermolecular distance and, as a consequence, the smaller the density.

After the 1st DSC scan, the position of the amorphous halo changed from 18.92° to 18.71°. From Equation (3-2), the destructive influence of MMT particles is quite obvious on the intermolecular distance of partially ordered regions in the amorphous phase (see Table 3-1). After the heat treatment, MMT particles in the nanoscale distributed in the polyethylene matrix disrupt the regularity of the polymer chains and the close packing in the amorphous phase.

This trend was also observed in ethylene/1-octene homogeneous copolymers as the content of 1-octene in the polymer increased: 1-octene molecules introduced into the structure of polyethylene form short side branches which disrupt the regularity of the main chain and make closer packing of the chains impossible (Rabiej, 2005).

## 3.4. Conclusions

Through this morphological and kinetic study of ethylene gas phase polymerization with MMT-supported catalyst, it can be concluded that the MMT particle fragment due to polymer growth in the early stages of polymerization, and intercalation and exfoliation occur only to some extent. These conclusions are supported by X-ray diffraction patterns, SEM and TEM images.

In this study, ethylene polymerization with MMT/TIBA/UOH/$Cp_2ZrCl_2$ showed a longer induction time, low activity and acceleration-type kinetics. On the other hand, polymerizations with

MMT/TIBA/UOH/Ni-diimine displayed a shorter induction time followed by sharp acceleration to a maximum activity and a steady activity decline. Ethylene mass transfer resistances may explain, at least in part, the differences observed in induction time between the two catalysts.

We have also used DSC and XRD deconvolution to show that the presence of exfoliated MMT layers in the polyethylene matrix reduces the crystallinity of the polymer phase as compared to its nascent crystallinity.

A tentative mechanism for particle fragmentation during pre-polymerization and high pressure ethylene polymerization was also proposed.

# Chapter 4
# Ethylene/Acrylonitrile Copolymer with α-Dimine-[N,N] Nickel Dichloride/EASC System

## 4.1. Introduction

Olefins and polar monomers can be copolymerized to modify the structure and chemical composition of polyolefins in order to obtain resins with improved properties for food and chemical packing, and also to work as compatibilizing agents in polymer alloys (Boffa and Novak, 2000). Polar comonomers containing acrylate, alcohol, or ester groups have been copolymerized with ethylene using late transition metal catalysts based on Ni and Pd with bidentate chelate ligands (Johnson et al., 1995; Killian et al., 1996; Ittel et al., 2000; Brookhart et al., 1999; Brookhart et al., 1995). Some strategies that have been explored include protecting the nucleophilic groups of polar comonomers with Lewis acids, commonly alkyl aluminums or bulky alkyl groups, adding spacers between the terminal double bond and the polar groups, or designing new ligands (Marques et al., 1999).

The copolymerization of olefins and acrylonitrile by free radical or atom transfer radical polymerization was successfully achieved in both academia and industry (Kirk-Othmer, 2006), but not with transition metal catalysts (Yang et al., 2004; Szabo et al., 2004; Wu et al., 2005). Despite of its difficulties, the copolymerization of acrylonitrile and olefins with transition metal catalysts is very attractive (Yamamoto et al., 1971; Minagawa et al., 2001; Suh et al., 1987; Kwon et al., 1983; Lee et al., 1985) because it could produce new types of copolymers that could compete with engineering plastics (Schaper et. al., 2004; Boffa and Novak, 2000).

Hydrogenated nitrile rubber is one of the representative commercial products that could be made by the copolymerization of olefins and acrylonitrile. Nitrile rubber, produced by the copolymerization of butadiene and acrylonitrile, is chemically modified in a post-polymerization

hydrogenation step to make hydrogenated nitrile rubber. Due to its resistance to oils at elevated temperatures, hydrogenated nitrile rubbers, such as Therban®, have found excellent acceptance in the automotive industry (Wrana, et al., 2001).

In this chapter, the experiments for the copolymerization of ethylene and acrylonitrile using a Ni-diimine/EASC catalyst system will be described. Ethylaluminum sesquichloride (EASC) was chosen as a cocatalyst because it is suitable activator for Ni-diimine catalysts (Preishuber-Pflugl et al., 2002). Our main objective was to produce olefin thermoplastic elastomers containing nitrile groups in a single polymerization reactor using a transition metal catalyst. Furthermore, this new material would be very promising for the production of polyethylene-clay nanocomposites because it could be used as a compatibilizing agent in blending other ethylene and nitrile polymer nanocomposites.

### 4.1.1. Literature Review

In the early seventies, Yamamoto and coworkers reported π-bonding of acrylonitrile with a Ni complex, $R_2Ni(dipyridyl)(olefin)$ (Yamamoto et al., 1971). They suggested that $R_2Ni(dipyridyl)(olefin)$ changed to Ni(dipyridyl)(olefin) after elimination of σ-bonded alkyl groups (Figure 4-1) and became active for the polymerization of acrylonitrile. However, they reported later that the Ni(dipyridyl)(olefin) complex could initiate acrylonitrile polymerization only in the presence of traces of oxygen. Unfortunately, further details of the mechanism were not provided.

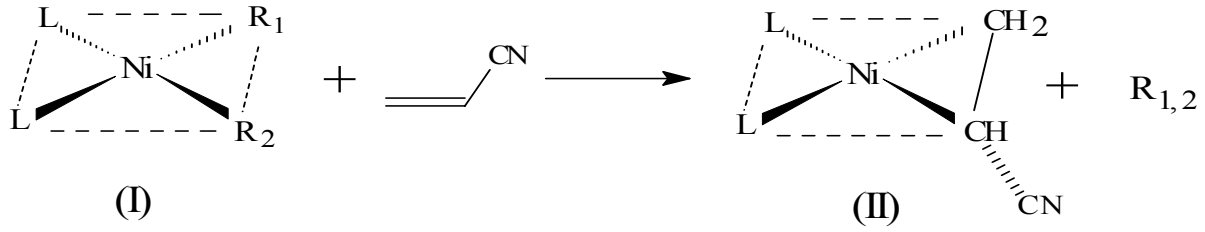


**Figure 4-1.** Ni catalyst and acrylonitrile π complex (Yamamoto et al., 1971). $R_1$ and $R_2$ are hydrocarbon chains. $R_{1,2}$ , a coupled chain is generated from (I) by reductive elimination mechanism.

Brookhart and coworkers successfully copolymerized ethylene and alkyl acrylate with a Pd-diimine catalyst (Johnson et al., 1996; Mecking et al., 1998), but addition of acrylonitrile to the system was reported to hinder further polymerization (Ittel et al., 2000).

Recent experimental and computational studies have revealed that cationic Pd(II) and Ni(II) diimine complexes exhibit a preference for σ-complexation with acrylonitrile, forming sites that are inactive for polymerization (Mikols et al., 2004). A σ-complex with acrylonitrile and a Rh catalyst was isolated and structurally verified, as shown in Figure 4-2 (Albietz et al., 2000; Lee et al., 1985).

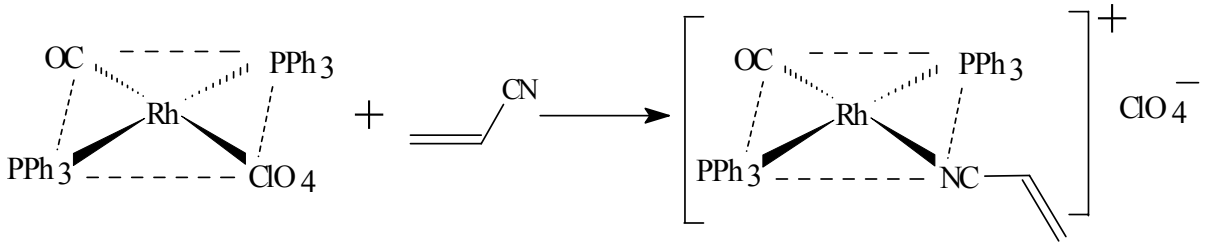


**Figure 4-2.** N isomer for a Rh complex with acrylonitrile (Lee, et. al., 1985).

It has been reported that the isomerization between vinyl and nitrile groups in acrylonitrile, called N/π isomerization (Figure 4-3) leads to complexes that are inactive for polymerization.

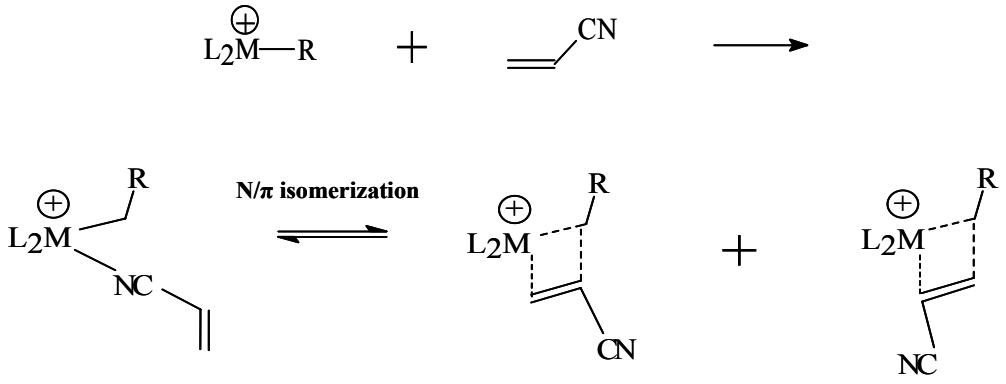


**Figure 4-3.** N/π isomerization mechanism for Fe metal catalyst with acrylonitrile (Rosenblum et. al., 1987).

Recently, Wu et al. (2005) suggested that when ethylene and acrylonitrile were copolymerized with $L_2PdMe_2$ ($L_2$: imidazol, pyridyl, bipyridine, or diimine ligands), the active species formed aggregates of the type $L_2Pd\{CH(CN)CH_2R\}(substrate)^+$, which competes with monomer coordination and resulted in low polymer yield (Wu et al., 2005).

Several metal catalysts (Cu, Fe and Pd) have been tested for ethylene and acrylonitrile copolymerization but could only homopolymerize acrylonitrile (Ittel et. al., 2000; Groux et al., 2005). However, even for acrylonitrile homopolymerization, the polymerization was started by the dissociation of ligands from $Cy_3PCuMe$ (Methyl(tricyclohexylphosphine) copper(I)) or the generation of metal hydrides from $(Bipy)_2FeEt_2$ (Diethyl(bis-bipyridyl) Iron(II)) (Schaper et al., 2004; Yang et al., 2004). This implies that, even if acrylonitrile is successfully coordinated to the metal catalyst, the actual acrylonitrile polymerization could take place through and anionic or free radical mechanism.

On the other hand, Hirooka et al. (1967) reported that Lewis acids such as $ZnCl_2 \cdot Et_2O$, $EtAlCl_2$ influenced the reactivity of ethylene and acrylonitrile copolymerization. When acrylonitrile is complexed with organoaluminum halides (ethyl aluminum sesquichloride and diethyl aluminum chloride) these Lewis acids can initiate the copolymerization of acrylonitrile and olefins in the absence of a catalyst (Figure 4-4).

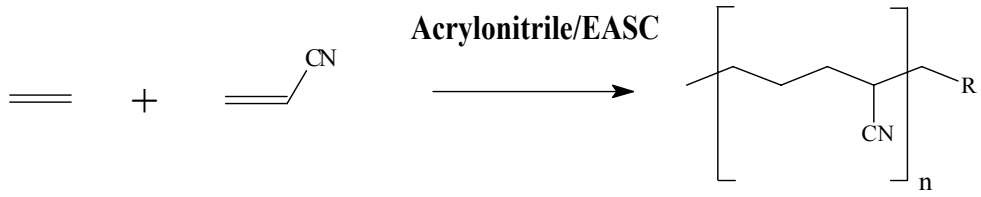


**Figure 4-4.** Plausible copolymerization between ethylene and acrylonitrile in the presence of EASC (R= ethylene and acrylonitrile alternating polymer chain).

Based on these previous investigations, we can speculate that the Ni-diimine/EASC catalyst could promote ethylene and acrylonitrile polymerization by several mechanisms. Considering the high stability of Ni-diimine catalyst, two feasible mechanisms can be suggested in this study. First, successive polymerizations could happen. After ethylene polymerization, alkyl group coupling (reductive elimination) could happen by the addition of acrylonitrile (Figure 4-1) (Inaba et al., 1984). Then, acrylonitrile could be polymerized, plausibly in the presence of traces of $O_2$. Secondly, the cocatalyst EASC alone can activate acrylonitrile polymerization (Figure 4-4), while Ni-diimine polymerizes ethylene. This chapter reports the successful copolymerization of ethylene and acrylonitrile with Ni-diimine/EASC catalyst system and the physical properties of the final product.

## 4.2. Experiments

### 4.2.1. Materials

All reactions were performed under inert nitrogen atmosphere using standard Schlenk techniques or inside a glove-box. Ethylene (CP, Praxair) and nitrogen (UHP, Praxair) were purified by passing them through molecular sieves (4 Å, 8-12 mesh, Aldrich) and copper oxide beds (13 wt.-% on alumina, Aldrich). Acrylonitrile, monochlorobenzene, trichlorobenzene, toluene and triisobutyl aluminum (1 M in hexane), and ethylaluminum sesquichloride (97 wt.-% Al) were all purchased from Aldrich. Ethylaluminum sesquichloride was diluted to 25wt-% in toluene. Toluene and monochlorobenzene were dried with molecular sieves prior to use. The catalyst (1,4-bis2,6-diisopropylphenyl)-acenaphthene diimine nickel(II)) dichloride (Ni-diimine) was prepared following a procedure reported in the literature (Koten, 1982). Triisobutyl aluminum (TIBA), ($Al(C_3H_7)_3$, 1.9 mol/L solution in toluene), methylaluminoxane (MAO) and toluene were purchased from Aldrich. In most polymerizations, acrylonitrile was purified by vacuum distillation to eliminate organic stabilizers. The purified acrylonitrile was stored in Schlenk tubes with molecular sieves 4 Å and kept in a refrigerator at -5°C.

### 4.2.2. Sample Preparation

**Ethylene and acrylonitrile polymerization**

All polymerizations were carried out in a Schlenk tube under purified ethylene. The dried Schlenk tube was purged with nitrogen and vacuumed successively for several times. Then, 30 mL of monochlorobenzene was transferred to the Schlenk tube. EASC (0.5 g) and Ni-diimine catalyst (20 μmol in toluene) were also transferred to the Schlenk tube. The Ni-diimine catalyst was activated with EASC. Degassing of the solvent containing the catalyst was achieved via cycles of freezing (with liquid nitrogen) and vacuum followed by thawing. Then, the solvent was saturated with ethylene and acrylonitrile was pre-contacted with TIBA in 1:1 molar ratio. The objective was to shield the polar nitrile group for five minutes prior to polymerization. The polymerization apparatus, polymerization procedures and polymer work up were described in Section 2.2.3.

**Fractionation of ethylene/acrylonitrile copolymers**

The ethylene/acrylonitrile copolymers were fractionated by solvent extraction. The extractions were done with hot xylene inside a thimble, following the standard procedure described in ASTM D2765-01. All extractions were run for 24 hours. The extracted fraction was poured into ethanol for precipitation, followed by filtering and washing with ethanol repeated times over a paper filter. All fractions were dried in the oven at approximately 80$^{o}$C. The dried extracted and non-extracted fractions were weighted on a digital scale balance to calculate the extraction ratios. Films of these fractions were prepared by melt pressing for investigation with FT-IR spectroscopy.

**Hot pressed ethylene/acrylonitrile copolymers film**

A few grams of the copolymers were sandwiched between two smooth transparent PET films and placed between two steel plates. The plates of the hydraulic press (P-215 C from Pasadena Hydraulics Inc.) were heated to 180 - 200$^{o}$C. The steel plates, with the samples in between, were put in the hot

hydraulic press. After melting the polymers (approximately 2 minutes), the samples were pressed at 320 psi. After 3 minutes, the press was released to let the air bubbles in the polymers melt to escape. After 30 seconds, the samples were pressed again for another 3 minutes. Finally, the polymer film was taken out and cooled in air to obtain the film specimens for further testing.

**Curing test**

Ethylene/acrylonitrile copolymer films were placed in a heatable sample holder (#A 729-T, Bruker) for transmission mode with a Bruker Optics FT-IR (Tensor 27). The FT-IR spectra monitored the progress of the curing reactions in 5-minute time intervals at 160$^{o}$C ($\pm$1°C). The spectra were analyzed by OMNIC software. In the case of PAN, the xylene-insoluble part of ethylene/acrylonitrile copolymer was grinded with KBr powder in a mortar. The powder samples were pressed into pellets of 13 mm diameter, with Aldrich micro KBr pellet die, under a pressure of 3000 psi using a hydraulic press (Carver Laboratory Press, Model 3912, Fred S. Carver). After heating on a hot plate for 1 minute at 300°C, the FT-IR spectrum was acquired with Bruker Optics FT-IR (Bruker, Tensor 27).

**Surface modification of ethylene/acrylonitrile films with sulfuric acid**

The aqueous sulfuric acid solution is a mixture of concentrated $H_2SO_4$ and deionized water that has reached a concentration of 50 % in volume ratio. The pressed ethylene/acrylonitrile copolymer films were cut into strips 0.1 mm thick, 10 mm long and 5 mm wide, and transferred into 5 mL of aqueous sulfuric acid solution in a 10 mL vial and hydrolyzed at room temperature for 12 hours while vigorously stirring on a shaker. After stirring, the film samples were filtered and washed with deionized-water several times, and finally dried at 60 °C under high vacuum for 12 hours.

### 4.2.3. POLYMER ANALYSIS

**Elementary analysis**

The amount of acrylonitrile in the copolymer was estimated from elementary analysis using an EA 1108 analyzer, in Guelph Chemical Laboratories LTD.

**Nuclear magnetic resonance (NMR)**

Ethylene/acrylonitrile copolymers and its fractions were characterized by $^{1}$H-NMR and $^{13}$C-NMR (Bruker AMX 500). The samples were placed in a 5 mm sample tube and dissolved in 1,1,2,2-tetrachloroethane (TCE) at 120 $^{o}$C. The spectra were referenced internally using TCE ($^{1}$H $\delta$ 5.95 ppm). The spectra were taken with a 70° pulse, flip angle, an acquisition time of 1.500 s pulse repetition time and 32 scans. The standard pulse sequence for $^{1}$H NMR was used and a total 32 scans were accumulated with a relaxation delay of 2 s. For $^{13}$C NMR, typical pulse conditions were as follows: 45° pulse, 5.000 s pulse repetition time, and 13 K data points.

**Fourier-transform infrared (FT-IR) spectroscopy**

The FT-IR spectra in transmission mode were recorded in the range from 400 to 4000 cm$^{-1}$, after 32 scans, with a resolution of 4 cm$^{-1}$. Calibration of the wavenumber was automatically done by the instrument using an internal polystyrene film. Spectra reported in this investigation were subtracted from a background spectrum obtained with no sample. The film samples were prepared as described above. The film specimens were analyzed by FT-IR in transmission mode. For the surface analysis, reflectance mode was used with the attenuated total reflectance (ATR) technique. The spectra in the ATR mode were recorded with similar parameters.

Isothermal cure reaction data with pressed film samples were monitored at 200 $^{o}$C with 5-minute time intervals with a Bruker Tensor 27, FT-IR system equipped with a computer to data analysis. The xylene-insoluble fraction was grinded together with KBr powder in a mortar and made into thin pellets with a press. The pellets were analyzed by FTIR in transmission mode and recorded

in the same way as mentioned above. Finally, the pellets were cured on a hot plate at approximately 250$^{o}$C for 5 minutes and measured again by FT-IR in transmission mode to study the effect of curing on the polymer structure.

**Contact-angle measurements**

Contact-angle measurements were carried out with a surface tension meter (Model 2500XE, made by AST Products, Billerica, Massachusetts). The surface tensions of the pressed films, polyethylene and polyethylene/acrylonitrile copolymer, were calculated with sessile drop method and compared for changed hydrophobicity before and after sulfuric acid treatments. Deionized water was used as a test liquid because of its polarity. Each reported contact angle measurement represented an average value of at least four separate drops on different areas of a given pressed sample on the flat glass. The size and volume of the drops were kept constant (within a fraction of a millimeter) since it is known that variations in the volume of the drops can lead to inconsistent contact angle measurements. Final contact angle measurements were recorded (usually within 10-15 seconds after the drop was formed) once their values did not change after drop placement. The above approach was followed to minimize transient droplet shape variations due to droplet relaxation and spreading. Prior to each set of contact angle measurements, the films were cleaned with ethanol and water according to the following sequence: three rinses with ethanol, two with water, one with ethanol, and three with water. The films were subsequently oven-dried under vacuum for 10 minutes at 120 °C and immediately placed in sealed containers (Fadeev et al., 1999; Marmur et al., 1994, 1998:Chan et al., 1994). This is a very effective method of evaluating surface energy and hydrophobicity for grafted polymers with polar monomers and thermoplastic composites.

**Gel permeation chromatography (GPC)**

Gel permeation chromatography (GPC) data were obtained using a Waters GPCV 150+ equipped with a Viscotek 150R viscometer, using 1,2,4 trichlorobenzene (TCB) as a solvent at 140 $^{o}$C. Number

($M_n$) and weight ($M_w$) average molecular weights were calculated using conventional GPC analysis and the universal calibration curve based on narrow polystyrene standards.

**Differential scanning calorimetry (DSC) and thermo gravimetric analysis (TGA)**

Copolymer melting point ($T_m$) was determined using a Thermal Analysis DSC 2920 differential scanning calorimeter (DSC), with a heating rate of 10$^o$C/min under argon atmosphere. The copolymer decomposition temperature, determined by thermogravimetric analysis (TGA), was performed using Thermal Analysis SDT 2960 instrument, with a heating rate of 10$^o$C/min under oxygen atmosphere (5% $O_2$, 95% He).

**Transmission Electron Microscope (TEM)**

The morphology of ethylene/acrylonitrile copolymers was measured with a transmission electron microscope (TEM), Philips CM20 Super Twin, operating at an acceleration voltage of 80 KV. The specimens were sliced at -140 °C in a liquid nitrogen chamber with a diamond knife, LEICA EM UC6. The thickness of the slices was between 50 and 80 nm.

**Tensile tests**

The stress-strain curves of ethylene/acrylonitrile copolymer films were obtained in tension mode. This analysis was done according to the testing conditions described in Section 2.2.12.

## 4.3. Results and Discussion

### 4.3.1. Polymerization Results

Table 4-1 compares catalyst activities for ethylene/acrylonitrile (1 to 6) and 1-hexene/acrylonitrile (or acetonitrile) (7 to 11) copolymerizations with different acrylonitrile concentrations. Sample 1 (ethylene homopolymer) is the reference for ethylene/acrylonitrile copolymerizations. At low acrylonitrile concentrations, polymer yields were comparable to those of the homopolymerization

runs, approximately 2.0 grams in one hour for ethylene and 0.66 grams in 3 hours for 1-hexene. As the concentration of acrylonitrile increased in the ethylene/acrylonitrile copolymerizations, the polymer yield decreased and reached a plateau value of approximately 0.32 g after 1 hour of polymerization. An increase in acrylonitrile concentration also seems to increase the molecular weight and decrease the polydispersity of the polymer. This effect is more noticeable for polydispersity than for $M_w$. While the $M_w$ for the ethylene homopolymer is 233 kg/mol, the $M_w$ of the ethylene/acrylonitrile copolymers varies from 250 to 364 kg/mol; however PDI decreased from 3.2 for the homopolymer to 2.8 to 2.2 for the copolymers (except for sample 2 that has PDI = 3.4). It seems that, for low concentrations of acrylonitrile (sample 2), the polymerization active sites were not significantly influenced by acrylonitrile, yielding 2.0 g of polymer with PDI = 3.4. However, for concentrations of acrylonitrile over 0.36 mol/L, polymerization activities were reduced to much lower values.

Copolymerizations of 1-hexene and acrylonitrile or acetonitrile (samples 8 to 11) were done differently from ethylene/acrylonitrile copolymerizations. Initially, only 1-hexene was added to the reactor and allowed to polymerize for a certain time. Then, the nitrile comonomer was added and the polymerization was allowed to continue for a given amount of time shown in Table 3-1 as (+ hours).

Samples 7 and 8 show that the addition of a small amount of acrylonitrile to the reactor has very little effect on polymer yield, $M_w$ and PDI, even when the copolymerization time for 1-hexene and acrylonitrile is 24 hours. However, when the concentration of acrylonitrile was increased to 0.73 mol/L (samples 9 and 11), $M_w$ practically doubled, even for a short polymerization time of 0.5 hours, without significantly affecting polymer yield. This increase in $M_w$ may be due to the coupling of alkyl chains, as reported by Minagawa and coworkers (Minagawa et. al., 1994; 1995; 2001).

When acetonitrile was used (sample 10) instead of acrylonitrile, no increase in molecular weight was observed. Since acetonitrile does not have vinyl functional groups, this observation seems to support the hypothesis that acrylonitrile-terminated poly (1-hexene) chains are coupled through the

reaction of terminal vinyl groups. Therefore, we can speculate that the acrylonitrile functions not only as a killing agent for 1-hexene polymerization but also behaves as a coupling agent between two polymer chains as described in Figure 4-1.

**Table 4-1.** Ethylene/acrylonitrile copolymerizations catalyzed by Ni-diimine/EASC

| No. | M[1] | C[2] | [C] (mol/L) | Time (h) | Yield (g) | Mw (kg/mol) | PDI |
|---|---|---|---|---|---|---|---|
| 1 | $C_2H_4$ | - | - | 1 | 2.1 | 233 | 3.2 |
| 2 | $C_2H_4$ | $C_2H_3CN$ | 0.06 | 1 | 2.0 | 247 | 3.4 |
| 3 | $C_2H_4$ | $C_2H_3CN$ | 0.36 | 1 | 0.32 | 364 | 2.8 |
| 4 | $C_2H_4$ | $C_2H_3CN$ | 0.48 | 1 | 0.30 | 295 | 2.4 |
| 5 | $C_2H_4$ | $C_2H_3CN$ | 0.60 | 1 | 0.32 | 249 | 2.2 |
| 6 | $C_2H_4$ | $C_2H_3CN$ | 0.73 | 1 | 0.32 | 277 | 2.2 |
| 7 | $C_6H_{12}$ | - | - | 3 | 0.66 | 420 | 2.3 |
| 8[3] | $C_6H_{12}$ | $C_2H_3CN$ | 0.06 | 3 (+24) | 0.67 | 444 | 2.3 |
| 9[3] | $C_6H_{12}$ | $C_2H_3CN$ | 0.73 | 12 (+0.5) | 0.58 | 761 | 4.7 |
| 10[3] | $C_6H_{12}$ | AcetoN | 0.73 | 12 (+0.5) | 0.62 | 418 | 3.5 |
| 11[3] | $C_6H_{12}$ | $C_2H_3CN$[4] | 0.73 | 12 (+0.5) | 0.66 | 790 | 3.4 |

Experimental conditions: solvent volume: 25 mL monochlorobenzene; [Ni-diimine] = 4.25μmol/L, [Al]/[Ni-diimine] = 43, temperature = 25°C ; $P_{ethylene}$ = atmospheric.

1. No. 1 - 6 for ethylene/acrylonitrile copolymer

   No. 7 - 11 for 1-hexene/acrylonitrile polymerization

   No.10 for 1-hexene/acetonitrile polymerization

2. C: comonomer (nitrile comonomers treated with triisobutylaluminum)

3. No.8 - 11 runs with 1-hexene initially, then nitrile comonomer was added.

   Polymerizations were continued for the additional time indicated as (+hours).

4. No.11; acrylonitrile without triisobutylaluminum

All samples were dried in the oven at 80°C for 24 hours.

### 4.3.2. FI-IR Analysis of Ethylene/Acrylonitrile Copolymers

Some of the ethylene/acrylonitrile copolymer samples were fractionated by Soxhlet extraction using boiling xylene. Ninety four wt.-% of sample 3 was soluble in xylene. Figure 4-5 compares the IR spectra of sample 3 with those of its xylene-soluble and xylene-insoluble fractions. In Figure 4-5, the band at 2245 $cm^{-1}$ can be assigned to the stretching band of isolated nitrile groups (–C≡N) in the polymer chain and the band at 2214 $cm^{-1}$ to its isomer, shifted due to the conjugation of the diene groups or the π-bonding with metals. Both bands indicate that nitrile groups have been incorporated in the polymer chains (Wu and Liedberg, 1988).

After Soxhlet extraction with boiling xylene, the xylene-insoluble fraction (Figure 4-5.b) shows the characteristic polyacrylonitrile bands at 1250 and 1230 $cm^{-1}$ (Minagawa et. al., 1994; 1995; 2001). The intensity of these two absorptions (D1230/D1250) is proportional to the content of the isotactic triads determined by $^{13}C$ NMR spectroscopy. Therefore, Figure 4-5. b shows that isotactic polyacrylonitrile sequences are present sample 3. This observation agrees with $^{1}H$ and $^{13}C$ NMR results that will be discussed later in Section 4.3.3.

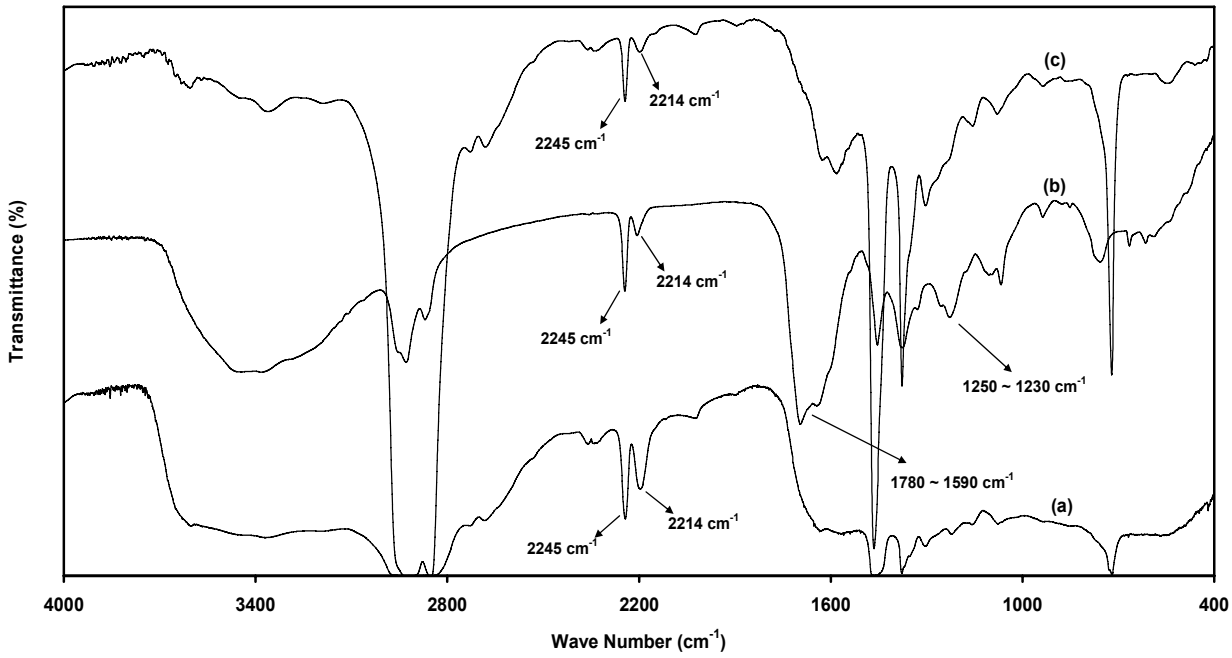


**Figure 4-5.** FT-IR spectra of ethylene/acrylonitrile copolymer sample 3: (a) Ethylene/ acrylonitrile copolymer; (b) Xylene-insoluble fraction; (c) Xylene-soluble fraction.

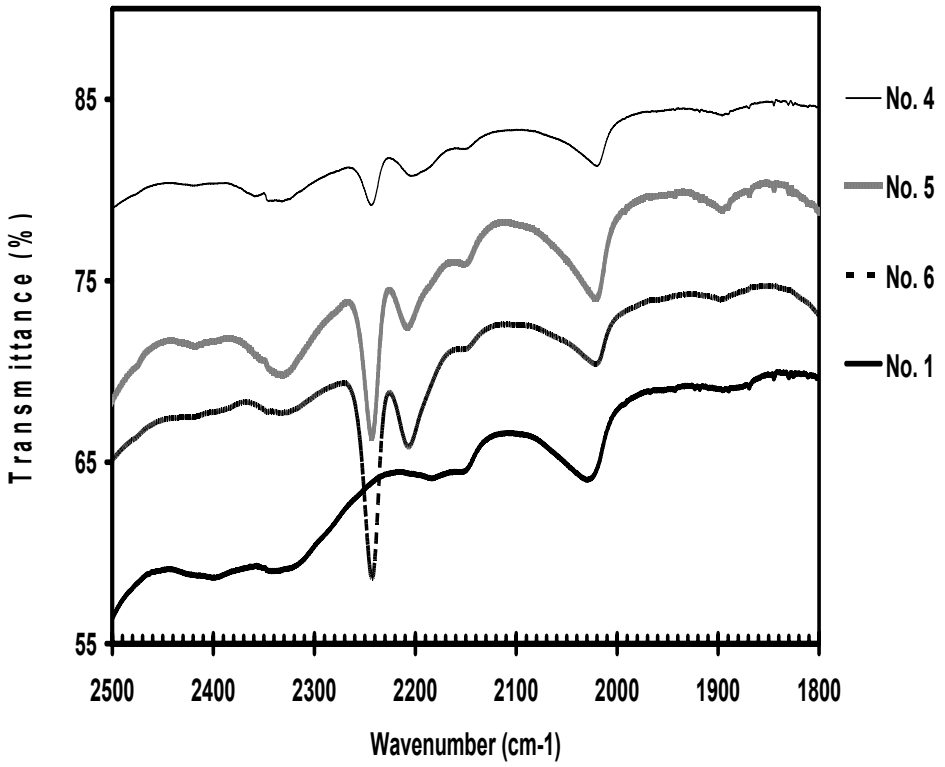


**Figure 4-6.** FTIR spectra of ethylene/acrylonitrile copolymer samples expanded in the frequency range 1800-2500 $cm^{-1}$.

The strong band at 1590-1780 $cm^{-1}$ in Figure 4-5.b can be assigned to several types of double bonds such as cyclic imines, carbonyl groups generated after oxidation of nitriles, and terminal vinyl groups (Coates, 2000 and Devasia et al., 2005). It is possible that the isotactic polyacrylonitrile segments of the xylene-insoluble fractions are cyclized, since the nitrile groups of isotactic polyacrylonitrile can react with inter- or intramolecular adjacent nitrile groups (Jung, 2002). The xylene-soluble fraction in Figure 4-5.c shows a stronger nitrile band at 2245 $cm^{-1}$ and a relatively weaker band at 1590-1780 $cm^{-1}$ than the ones in the insoluble fraction. This indicates that the xylene-soluble fraction has nitrile functional groups, but fewer cyclized isotactic polyacrylonitrile sequences.

Figure 4-6 shows that the intensity of the nitrile bands differ among samples 4, 5 and 6, accordingly to the concentration of acrylonitrile used in the polymerization. As expected, copolymer samples made with higher acrylonitrile concentration have a more pronounced 2245 $cm^{-1}$ band.

### 4.3.3. NMR Analysis of Ethylene/Acrylonitrile Copolymer and PAN

**Ethylene/Acrylonitrile copolymer before Soxhlet extraction**

The $^{1}H$ NMR spectrum of sample 6 is shown in Figure 4-7.a. The peaks at δ 2.1 and δ 2.3 ppm suggest the presence of methylene protons having chemical bonds with polar functional groups, such as nitrile (R–C**H₂**–C≡N) and imido (R–C**H₂**CO–NH) groups. The hydrogen of the imido group (R–$CH_2$CO–N**H**) (Table 4-2) at δ 8.2 presumably could be formed during the work-up with hydrochloric ethanol solution. The nitrile groups that have been protected with TIBA react with water molecules in acidic solution and can be easily changed into imido groups through a mechanism known as acid-catalyzed hydration. Unfortunately, the $^{13}C$ NMR spectrum in Figure 4-7.b does not show the characteristic bands for the nitrile functional groups. Since the polymer samples are dissolved in TCE, we can speculate that the solubility of the xylene-insoluble fraction in TCE is very low and could become NMR-inactive in solution (Pham and Petiaud 1980).

**Xylene-insoluble fraction (Polyacrylonitrile, PAN)**

The $^{1}H$ NMR spectrum of the xylene-insoluble fraction shows strong evidence for the presence of polyacrylonitrile blocks (PAN) and hydrocarbon chains. In Figure 4-8.a, the bands at 2.1 ppm are assigned to methylene protons adjacent to the nitrile group and the bands at 3.1 ppm to methine protons on carbons which are also bonded to the nitrile group (Table 4-3). The signal at δ 0.90 has not been reported in the spectra of PAN made by anionic and radical polymerizations. This signal is a doublet with a separation of $\Delta\delta = 0.001$ at 120 $^{o}C$. This presumably arises from the polymer chain ends ($CH_3$–CH(C=N)–), considering its chemical shift and doublet coupling.

Several small peaks are present in the $^{13}C$ NMR spectrum of PAN, as shown in Fig. 4-8.b. The methine (–CH) carbon gives rise to three well-resolved peaks centered at approximately 27.5 ppm due to triad chemical shift sensitivity. The isotactic triad appears at a lower magnetic field, followed by atactic and syndiotactic signals (White, 1960).

**Table 4-2**. $^{1}H$ NMR assignment for ethylene/acrylonitrile copolymers (sample 6, Table 4-1)

| No. | Assignment[c] | Reference (ppm) | Origin sample (ppm) |
|---|---|---|---|
| 1 | R–C**H$_2$**–C≡N | 2.0 | 2.1 |
| 2 | R–C**H$_2$**CO–O– | 4.1 | 4.1 |
| 3 | R–C**H$_2$**NH– | 8.31 | 8.2 |

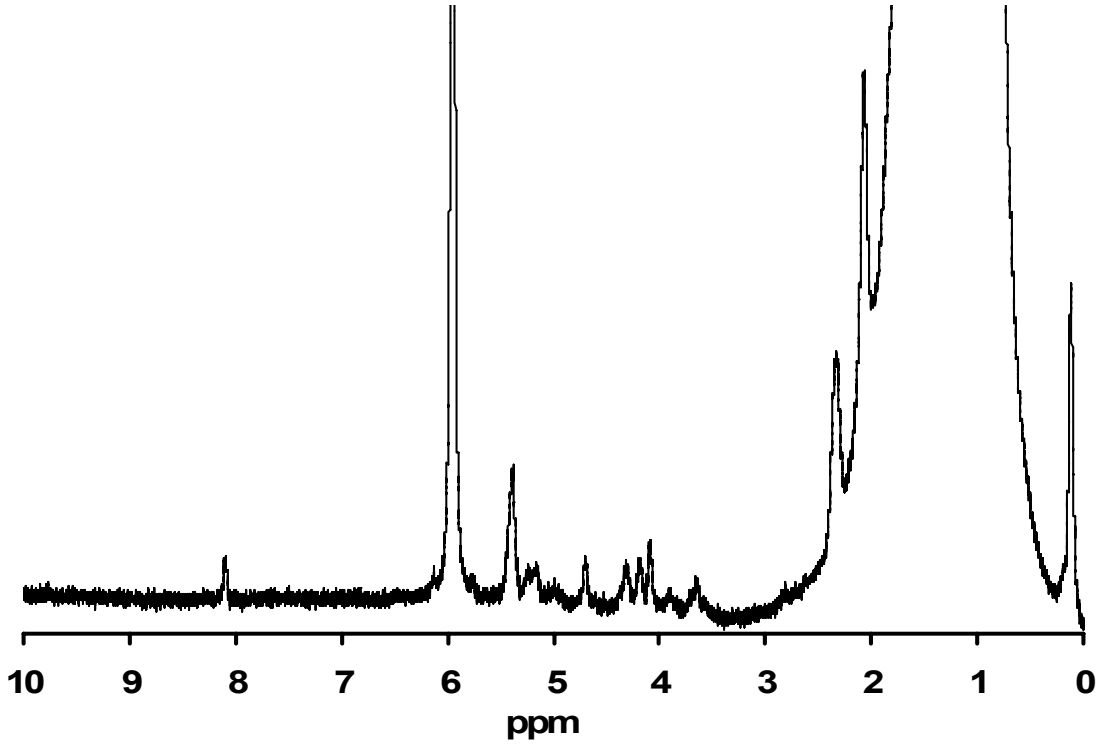


(a)

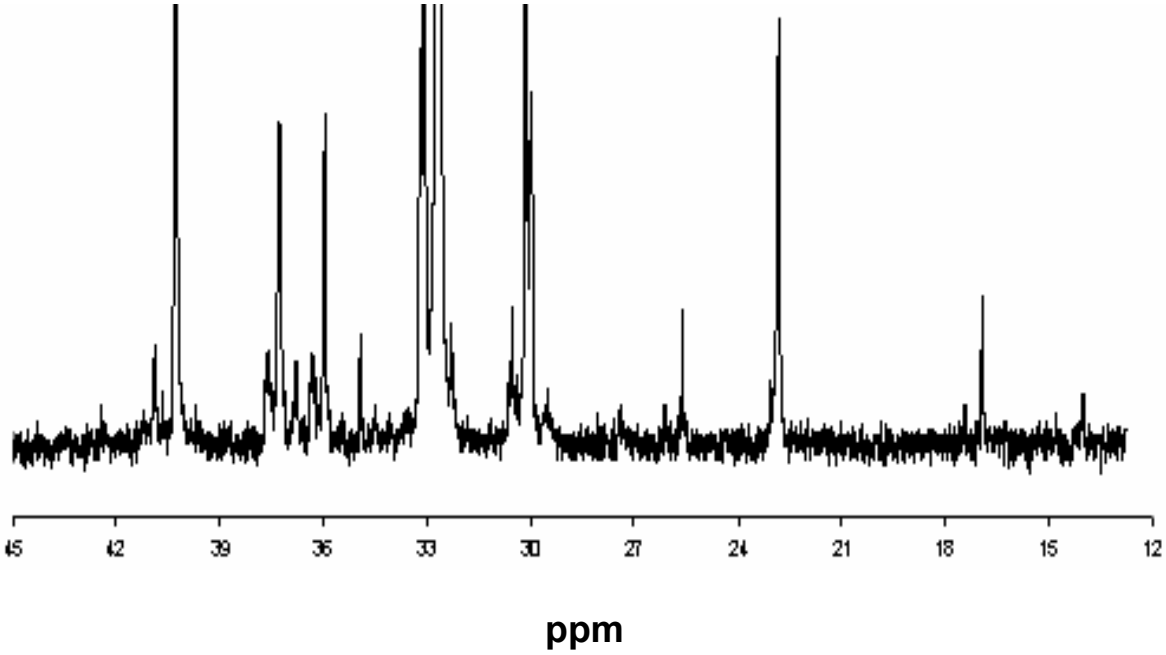


(b)

**Figure 4-7.** NMR spectra of ethylene/acrylonitrile copolymer (sample 6, Table 4-1): (a) $^{1}H$ NMR spectrum; (b) $^{13}C$ NMR spectrum.

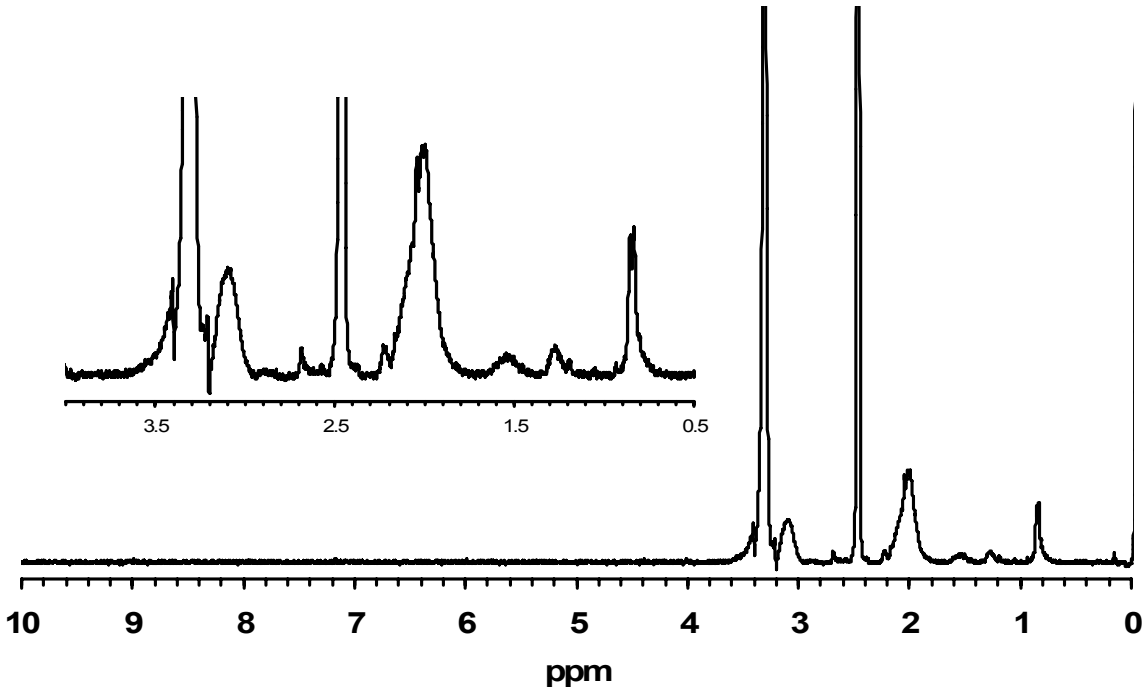


(a)

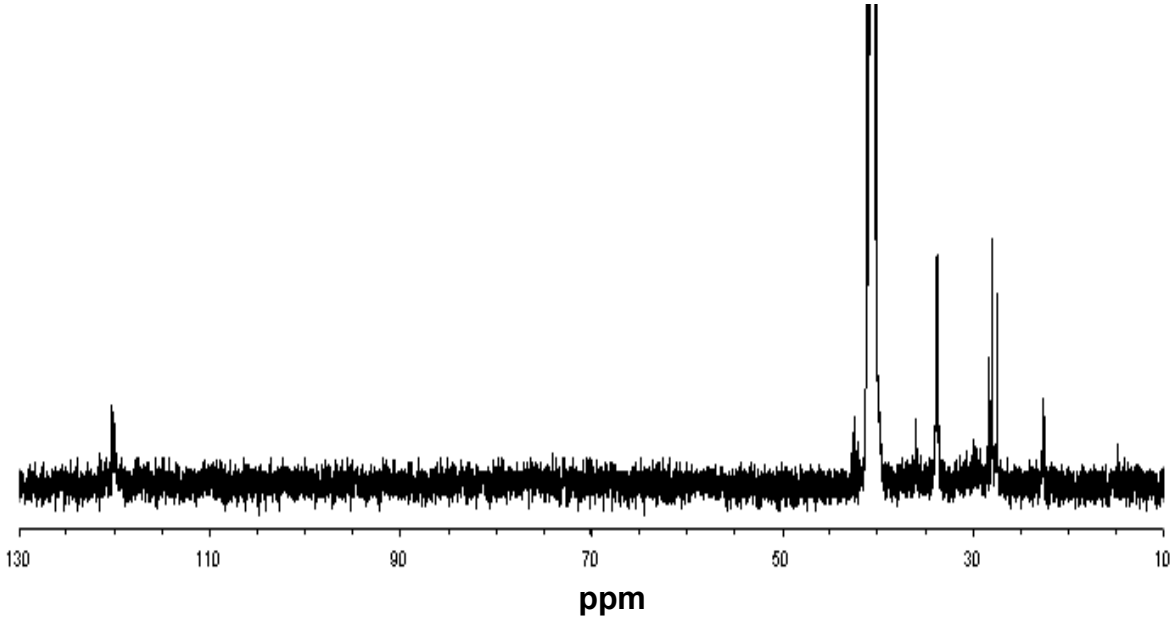


(b)

**Figure 4-8.** NMR spectra of xylene-insoluble fraction (PAN): (a) $^{1}H$ NMR spectrum; (b) $^{13}C$ NMR spectrum.

**Table 4-3**. $^{1}$H NMR band assignments of Polyacrylonitrile.

| No. | Assignment[c] | Reference (ppm) | Origin sample (ppm) |
|---|---|---|---|
| 3 | C**H**$_{3}$-CH(R)–C≡N | 1.23 | 1.3 (br) |
| 4 | ***C***H$_{3}$–CH(C=N)–), | 0.9 | 0.9 |
| 1 | R–C**H**$_{2}$–C≡N | 2.1 | 2.1 (br) |
| 2 | R$_{2}$–C**H**–C≡N | 3.1 | 3.05~3.25 (br) |

### 4.3.4. TEM Analysis of Ethylene/Acrylonitrile Copolymerization

Figure 4-9 shows the morphology of an ethylene/acrylonitrile copolymer sample (sample 6, Table 4-1) measured by TEM. Evenly distributed nanosized PAN domains are observed in the polyethylene matrix. Some of these spherical domains are connected to adjacent ones, presumably forming interpenetrating structures in the polyethylene matrix. The darker core in each PAN domain may have a higher concentration of nitrile groups. After Soxhlet extraction with boiling xylene, the TEM image of the xylene-soluble fraction shows nanosized spheres in the polymer matrix, but no PAN domains (Figure 4-10).

From this morphological study, we can conclude that these ethylene/acrylonitrile copolymers have PAN-rich domains that are distributed in a polyethylene-rich matrix, in agreement with FT-IR and NMR results depicted in Figures 4-5 to 4-8. The adhesion force between these two phases will be discussed in Section 4.3.10.

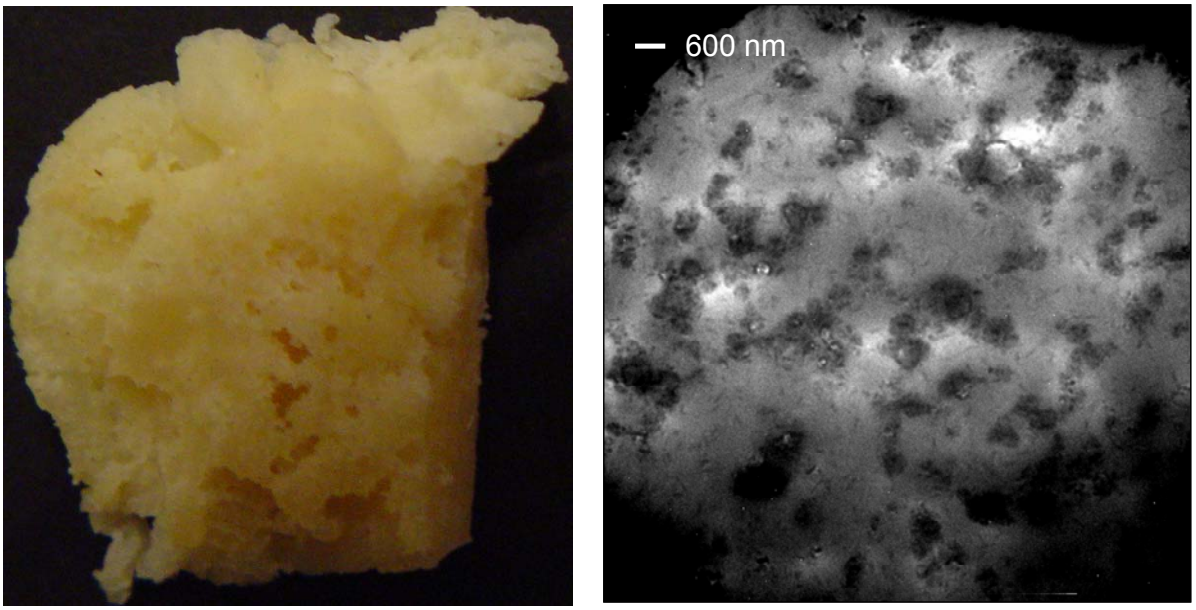


(a) (b)

**Figure 4-9.** Sample 6 (Table 3-1): (a) picture of resin by Sony Cyber-Shot DSC-F717 digital camera; (b) TEM of microtomed 80 nm thick section of the sample 6.

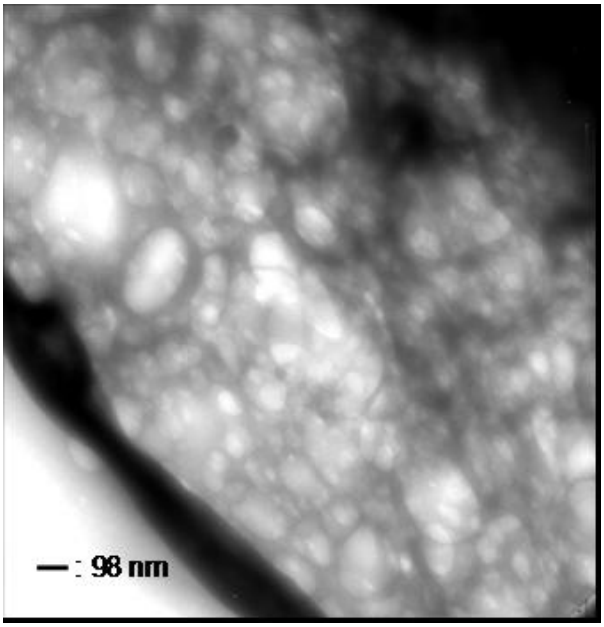


**Figure 4-10.** TEM of a microtomed section (80 nm thickness) of the heptane-soluble fraction (sample 6) after 12 hours Soxhlet extraction.

### 4.3.5. FT-IR Analysis of the Curing Reaction of Ethylene/Acrylonitrile Copolymers

In Figure 4-11, the curing reaction at 160 °C of an ethylene/acrylonitrile copolymer (sample 5 in Table 3-1) was monitored by FT-IR. New bands appeared at 1600 $cm^{-1}$ and 1635 $cm^{-1}$ and intensified as heating continued. The band at 1600 $cm^{-1}$ can be assigned to the stretching mode of imine functional groups (>C=N) and the band at 1635 $cm^{-1}$ to vinyl groups (>C=C<) (Coates, 2000). The band at 1680 $cm^{-1}$ can be assigned to the conjugated imine which continued to be aromatized.

Figure 4-12 shows the FT-IR spectra of the xylene-insoluble fraction (PAN) of an ethylene/acrylonitrile copolymer before and after thermal treatment at 300°C on a hot plate. Two peaks emerged at 1610 $cm^{-1}$ and 1667 $cm^{-1}$ and the intensity of the nitrile group peak at 2242 $cm^{-1}$ decreased. These two new peaks can be assigned to the conjugated imine and vinyl structures, formed by inter or intrachain reactions of the nitrile groups (Calberg et al., 1998). These peaks may demonstrate the onset of the extended conjugation of the cyclized structure, supported by the disappearance of the 1460 $cm^{-1}$ absorption band, the characteristic band of the bending vibration of the ($–CH_2$) group. The increase in the intensity of the peak at 1380 $cm^{-1}$ (C=N stretching) (Choi et al., 2002) is another indication of the formation of cyclic conjugation leading to a tetrahydropyridine-type ladder structure.

Cyclization and aromatization were suggested as feasible mechanisms for the changes of functional groups in the FT-IR spectra before and after pyrolysis of PAN (Table 4-4). A mechanism for thermal-treatment induced changes in polyethylene/acrylonitrile copolymers will be proposed later in Figure 4-16.

**Table 4-4**. Infrared frequencies of polyacrylonitrile before and after curing[a] (Bellamy, 1974)

| No. | Assignment[b] | Reference ($cm^{-1}$) | Before curing ($cm^{-1}$) | After curing ($cm^{-1}$) |
|---|---|---|---|---|
| 1 | $\nu$(NH), $\nu(NH_2)$ | 3350 | - | 3375 |
| 2 | $\nu_{as}(CH_2)$ | 2935~2915 | 2937 | 2933 |
| | $\nu_{ss}(CH_2)$ | 2865~2845 | 2877 | 2887 |
| 3 | $\nu$(C≡N) | 2243 | 2243 | 2243 |
| 4 | $\nu$(C≡N)[c] | 2190 | 2210 | 2214 |
| 5 | $\nu$(>C=O) | 1700 | 1780 ~1725 | 1700 |
| 6 | $\nu$(C=N) | 1720~1380 | - | 1635~1680<br>1380 |
| 6 | $\nu$(C=C)[d], $\delta$(N-H) | 1600 | - | 1600 |
| 7 | $\delta(CH_2)$ | 1454 | 1458 | - |
| | | 1362 | 1382 | 1404 |
| 8 | $\nu_s$(C-C) | 1063 | 1063 | 1063 |
| 9 | $\omega$(C-H) 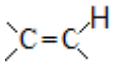 | 806 | 806 | 806 |
| 10 | $\nu$ (C-CN) | 785 | 775 | 775 |

a. Curing conditions are described in the experimental section.

b. $\nu$ : stretching; $\delta$ : in-plane bending; $\omega$ : out-of-plane bending.

c. Downward shift in frequency for isomorphic structures of nitrile groups in the polymer chain.

d. Conjugated vinyl group (Coates, 2000).

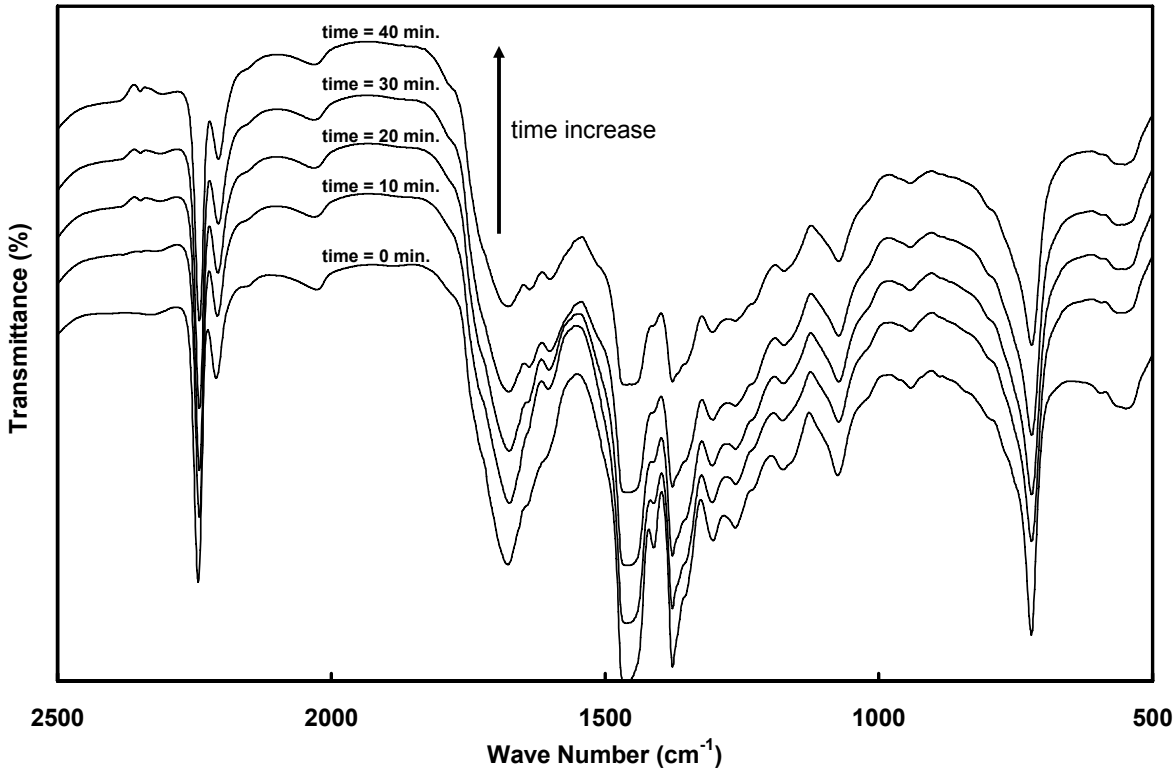


**Figure 4-11.** FT-IR analysis during heating at 160°C**.** The ethylene/acrylonitrile copolymer film (sample 5 in Table 3-1) was loaded in the heating block and FT-IR measurements were taken at 10 minute intervals.

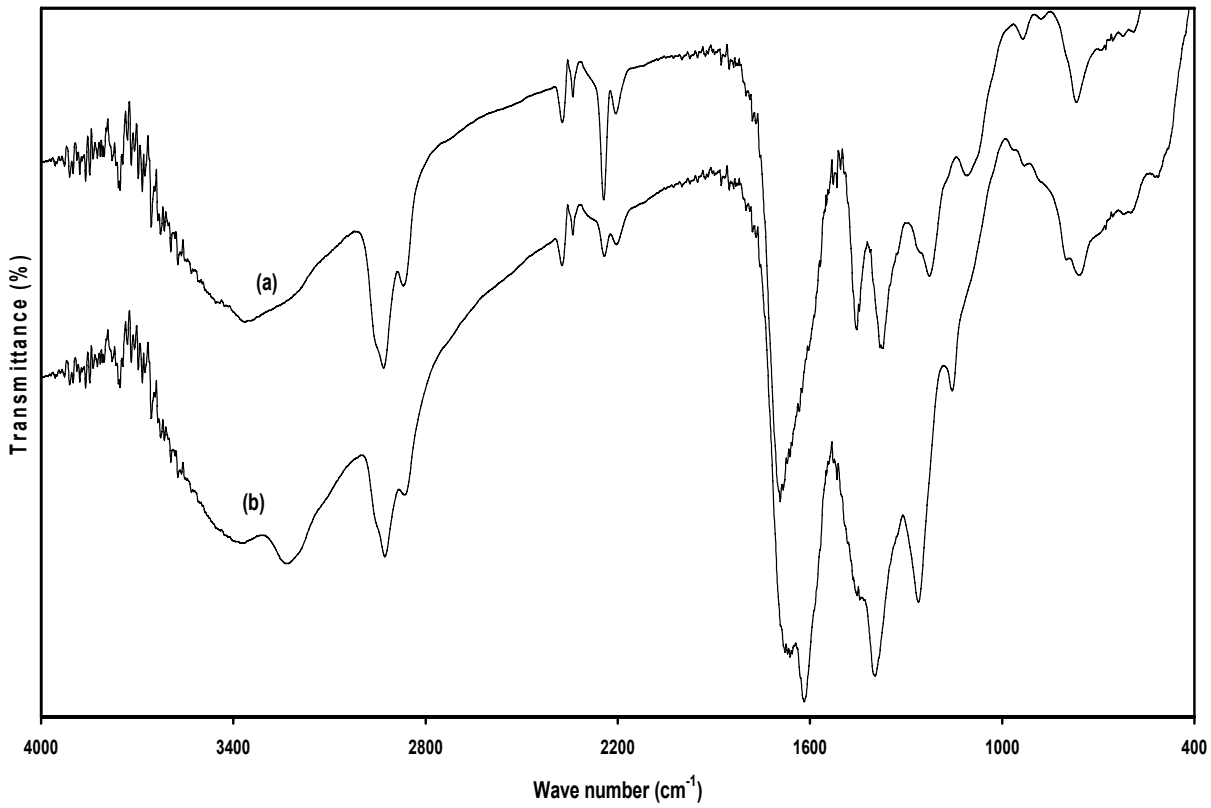


**Figure 4-12.** FT-IR spectra of Xylene insoluble fraction from sample 5 (Table 3-1) (PAN rich group); (a) before and (b) after the thermal treatment. The sample was heated to 300°C for 5 minutes on the hot plate.

### 4.3.6. DSC and XRD Analyses after DSC Thermal Treatment

Figure 4-13 shows DSC curves of ethylene/acrylonitrile polymer, and its xylene-soluble and xylene-insoluble fractions. The ethylene/acrylonitrile copolymer and its xylene-insoluble fraction showed characteristic exothermal peaks in the high temperature range from 180°C to 380°C. These exothermal peaks can be attributed to inter or intramolecular reactions between nitrile groups in the polymer chains (Mathur, 1992; Jung et al., 2002). These peaks were absent from the DSC of the xylene-soluble fraction.

The two exothermal peaks shown in Figure 4-13.a are in a similar temperature range to the peaks measured for PAN at approximately 267.8°C and 309.9, attributed to intermolecular crosslinking and aromatization reactions (Mathur, 1992).

The DSC data for the ethylene/acrylonitrile copolymer and its xylene-insoluble fraction are compared to that of PAN in Table 4-5. The onset temperature of the exothermal peak for PAN is much higher than for the other two samples. This difference could be due to a different configuration of acrylonitrile in the ethylene/acrylonitrile copolymer chains. The FT-IR spectrum shown in Figure 4-12.b, (xylene-insoluble fraction) showed bands from 1500 $cm^{-1}$ to 1700 $cm^{-1}$, which are characteristic bands for cyclization and intermolecular crosslinking. Soxhlet extraction provides enough heat to the xylene-insoluble fraction for intermolecular crosslinking and cyclization to take place, which could lower its solubility in the xylene. In Figure 4-13.b, the xylene-insoluble fraction shows only one broad band for cyclization and aromatization.

**Table 4-5.** Parameters obtained from DSC exotherms of PAN, Ethylene/acrylonitrile copolymer and its xylene-insoluble fraction.

| | PAN | Ethylene/acrylonitrile | Xylene-insoluble fraction |
|---|---|---|---|
| $T_i$ (°C) | 226.2 | 175 | 210 |
| $T_f$ (°C) | 379.2 | 380 | 340 |
| $\Delta T$ (°C) | 153.0 | 205 | 130 |
| $T_{pk}$ (°C) | 267.8<br>309.9 | 235.3<br>298.3 | 282.2 |
| $\Delta H$(J/g) | -1093 | -213.1 | -111.2 |

$T_i$: onset temperature for exotherm; $T_{pk}$: peak temperature; $T_f$: extinction temperature for exotherm; $\Delta$H: heat evolved; $\Delta T$: $T_i - T_f$

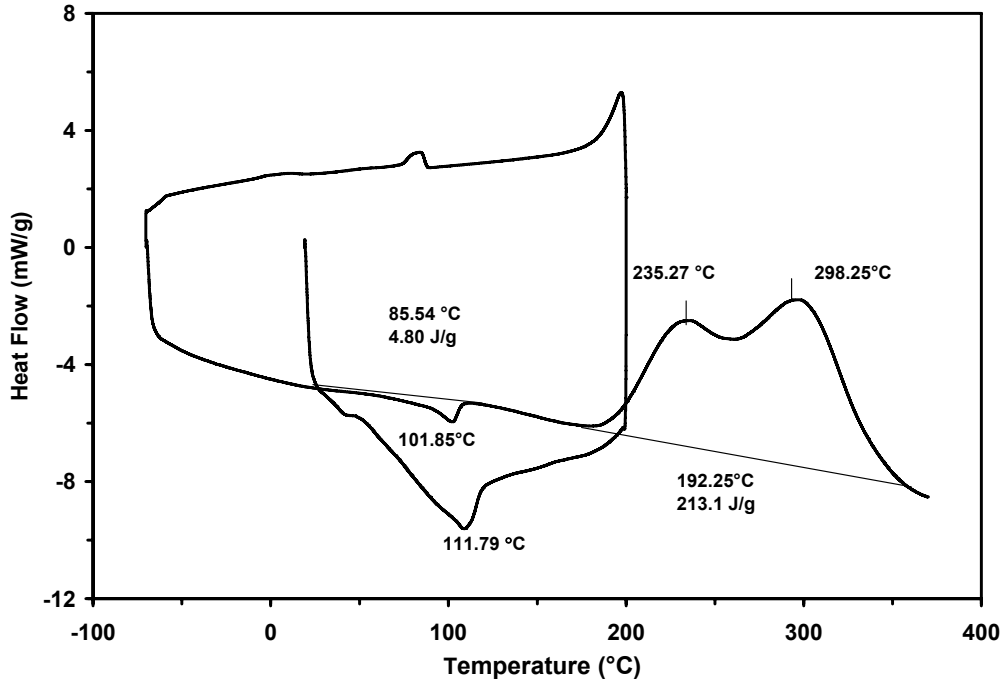
Heat Flow (mW/g)
Temperature (°C)
85.54 °C
4.80 J/g
235.27 °C
298.25°C
101.85°C
192.25°C
213.1 J/g
111.79 °C

(a)

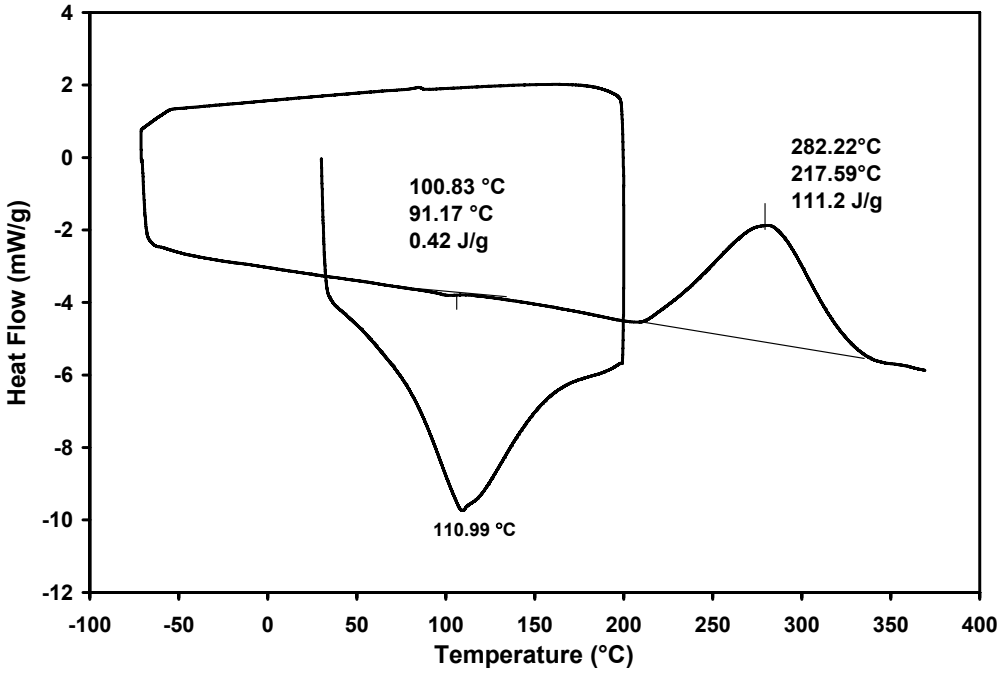
Heat Flow (mW/g)
Temperature (°C)
100.83 °C
91.17 °C
0.42 J/g
282.22°C
217.59°C
111.2 J/g
110.99 °C

(b)

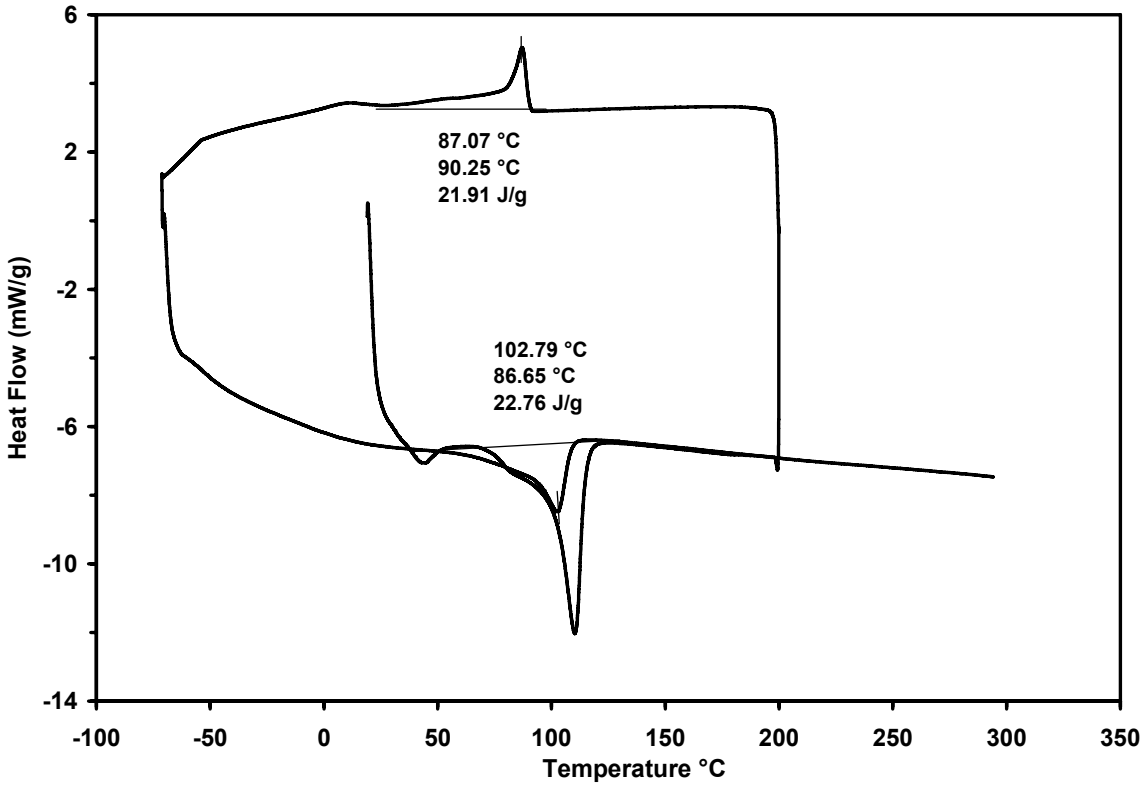


(c)

**Figure 4-13**. DSC curves (a) pristine polymer (sample 6 in Table 3-1), (b) xylene-insoluble fraction (from sample 6 in Table 3-1), and (c) xylene-soluble fraction (from sample 6 in Table 3-1).

Cyclization and aromatization reactions of ethylene/acrylonitrile copolymers were reported to form meso lamellar structures, which were active in X-ray diffraction (Thunemann 2000; Jung 2002). This aromatized chain fiber forms planar structures (lamellar mesophases) that can scatter X-rays.

Figure 4-14 shows the X-ray diffractograms of sample 6 before and after DSC scanning up to 370 °C. Figure 4-14.b clearly shows a new shoulder at $17^{o}$ for the β phase, which results from the aromatization reaction after DSC scanning (Thunemann, 2000). This new peak was reported due to the generation of lamellar structure by the further reactions after aromatization of PAN (Thunemann, 2000).

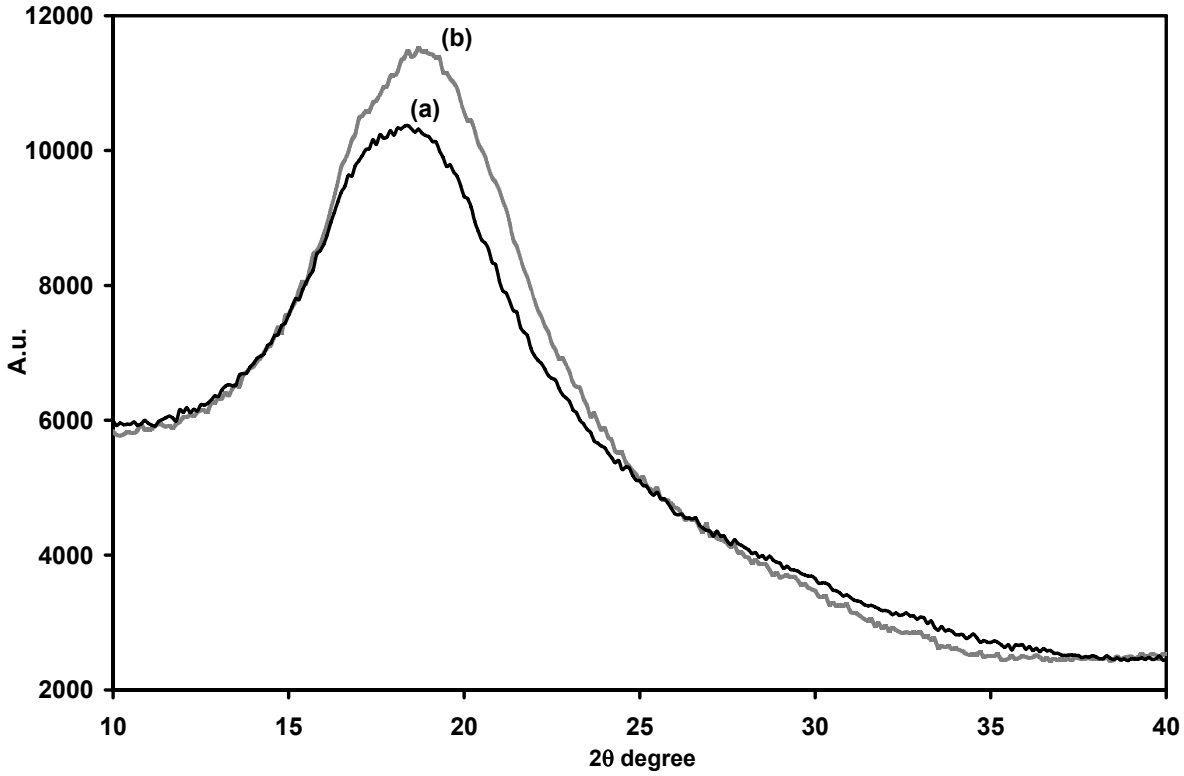


**Figure 4-14.** X-Ray diffractograms of ethylene/acrylonitrile copolymer (sample 6): (a) before DSC scanning, (b) after DSC scanning.

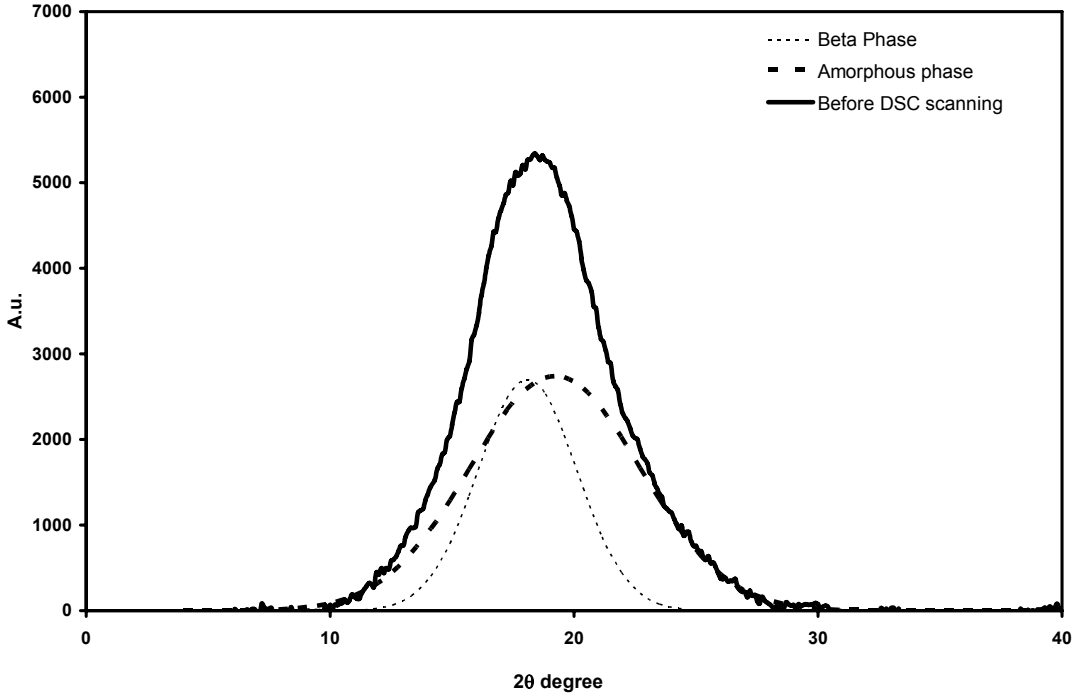


(a)

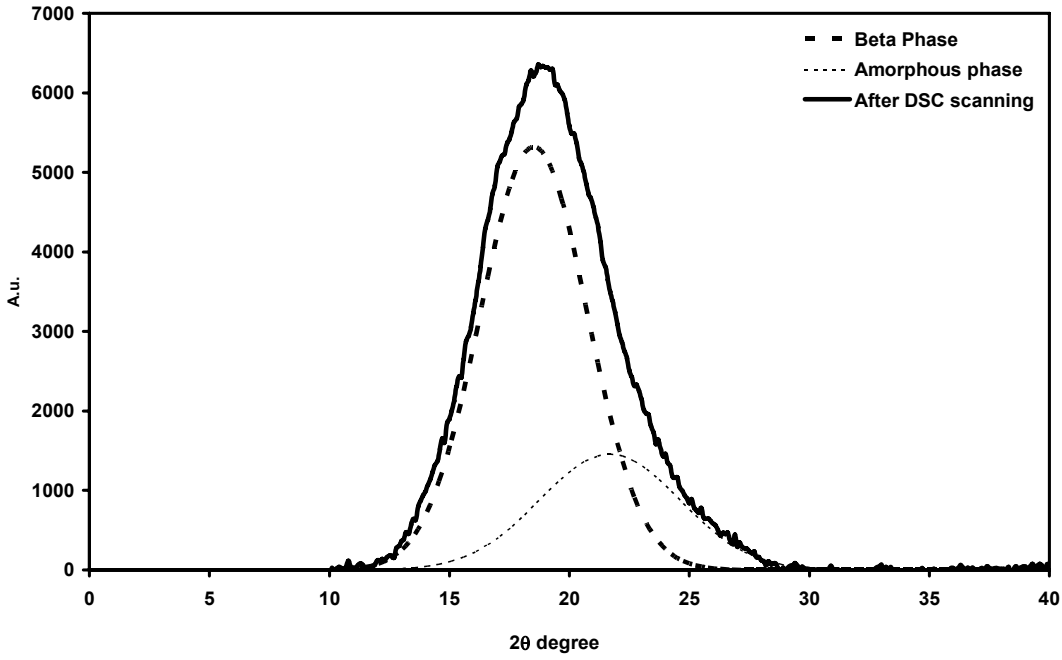


(b)

**Figure 4-15.** Deconvoluted X-ray diffractograms of ethylene/acrylonitrile copolymer (sample 6 in Table 3-1): (a) before DSC scanning, (b) after DSC scanning.

The XRD diffractograms in Figure 4-15 were normalized and deconvoluted by the method described in Section 3.3.2.2. (Figure 3-21). The ethylene/acrylonitrile copolymer obtained after the DSC scanning, shown in Figure 4-15.b, also had the peak for the β phase at 17°. This peak was more clearly observed after the DSC run. The deconvolution of the curve shown in Figure 4-15a was attempted, however such result does not seem to be reliable because of the similarity of the resulting peaks in such deconvolution. This observation supports our hypothesis that the exothermic peak from 235 - 300 °C is related to cyclization and aromatization of the nitrile groups in the polymer chains to form lamellar structures that become active in the X-ray analysis.

A mechanism for the cyclization and aromatization of the nitrile groups is proposed in Figure 4-16. Some of the nitrile groups could have been changed to acid groups when HCl solution was added to the reactor to stop the polymerization. A detailed mechanism of the acid hydrolysis of nitrile groups will be discussed in Section 4.3.7.

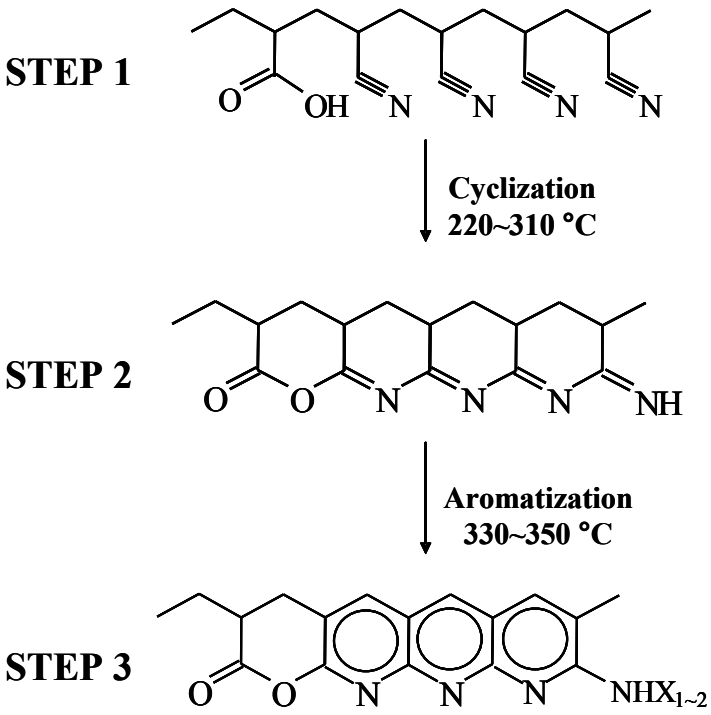


**Figure 4-16.** Proposed mechanism for cyclization and aromatization of nitrile and acid groups during thermal treatment of ethylene/acrylonitrile copolymers.

### 4.3.7. Functional Group Modification with Sulfuric Acid Solution

The transmittance FT-IR spectrum of an ethylene/acrylonitrile copolymer shows the typical bands of nitrile group at 2240 $cm^{-1}$ (Figure 4-17.a). After acid treatment with $H_2SO_4$ solution (1/1 volume ratio) for 24 hours, the characteristic band of carbonyl groups appeared at 1700 $cm^{-1}$.

The surface of the sample was analyzed with FT-IR using the attenuated total reflectance (ATR) method (Figure 4-17.b). The film before acid treatment did not show any absorption band for nitrile groups. This observation indicates that the nitrile functional groups are located underneath the film surface and can not be detected by a surface analysis method. After surface modification with the acid solution for 24 hours, a strong carbonyl absorption band appeared at 1700$cm^{-1}$. The carbonyl functional group (>C=O) is assumed to be the result of the oxidation of imino or nitrile groups by the sulfuric acid solution, as proposed in Figure 4-18.

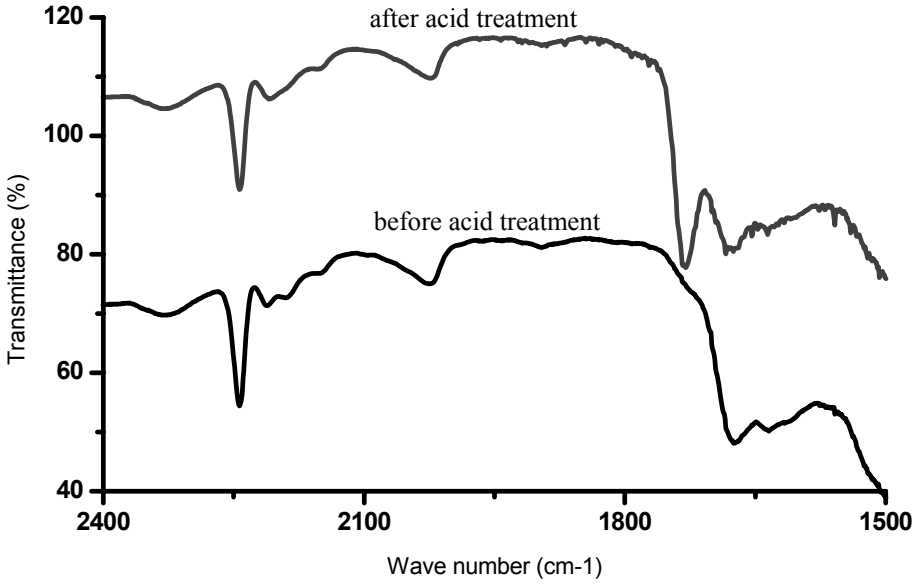


(a)

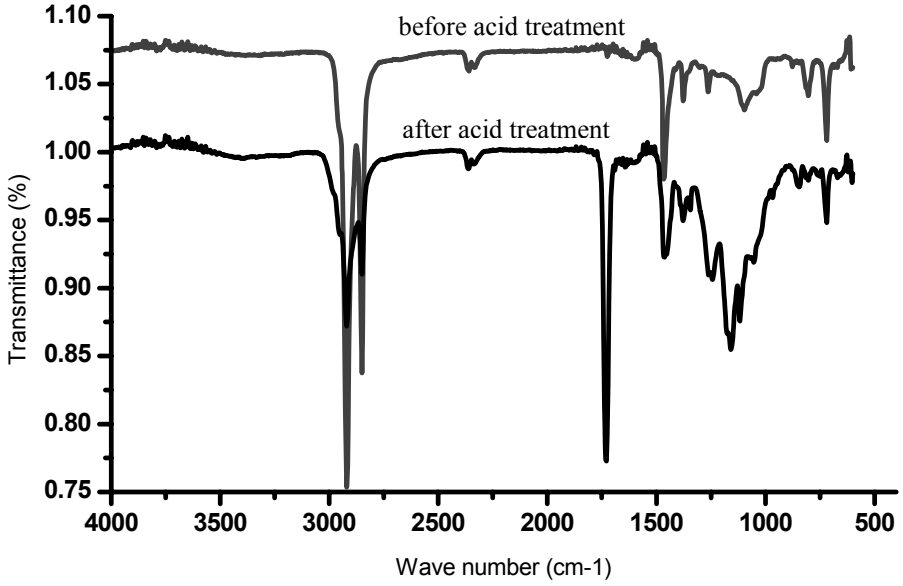


(b)

**Figure 4-17.** FT-IR and ATR spectra of ethylene/acrylonitrile copolymer (sample 5 in Table 3-1) before and after treatment with sulfuric acid solution ($H_2SO_4$:$H_2O$ = 1:1 volume ratio) (a) Transmittance spectra, (b) ATR spectra.

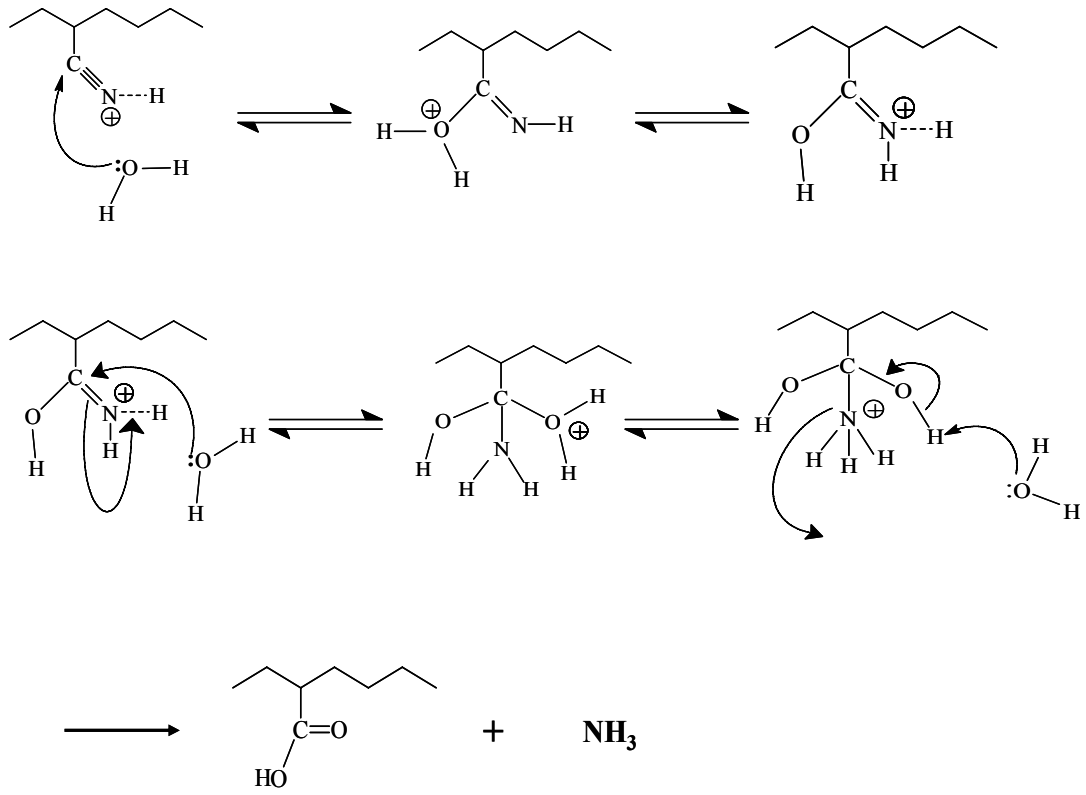


**Figure 4-18.** Mechanism for acid-catalyzed hydration of nitrile groups during treatment with sulfuric acid.

### 4.3.8. Contact Angle Measurements

Water contact angles with surfaces have been used as a measure of their wettability or surface tension. Low water contact angles indicate high surface tensions (high wettability) and vice-versa.

Ethylene homopolymer and ethylene/acrylonitrile copolymer films were prepared by molting the polymer samples on the surface of glass slides. Water contact angles were measured before and after sulfuric acid treatment (Figure 4-19). The ethylene/acrylonitrile copolymer had a much higher wettability than polyethylene after the sulfuric acid treatment. When water droplets (1 μl) were applied to the polyethylene film, they stretched out as shown in Figure 4-19.a. Here, large contact

angles are observed on the pristine polyethylene surface and slightly lower angles on the oxidized film surface.

On the other hand, after sulfuric acid treatment, the large water contact angle observed on the ethylene/acrylonitrile polymer, changed to much lower angles (Figure 4-19.b). In this case, we propose that chemical bonds between the polar PAN segments and polyethylene chains determine the contact angle after sulfuric acid treatments.

This observation agrees with FT-IR and ATR spectra (Figure 4-17) and the morphologies shown in the previous TEM images (Figure 4-9). It seems that the polar nitrile groups and the PAN chains form evenly distributed aggregates with diameter of approximately 500 nm in the polyethylene matrix.

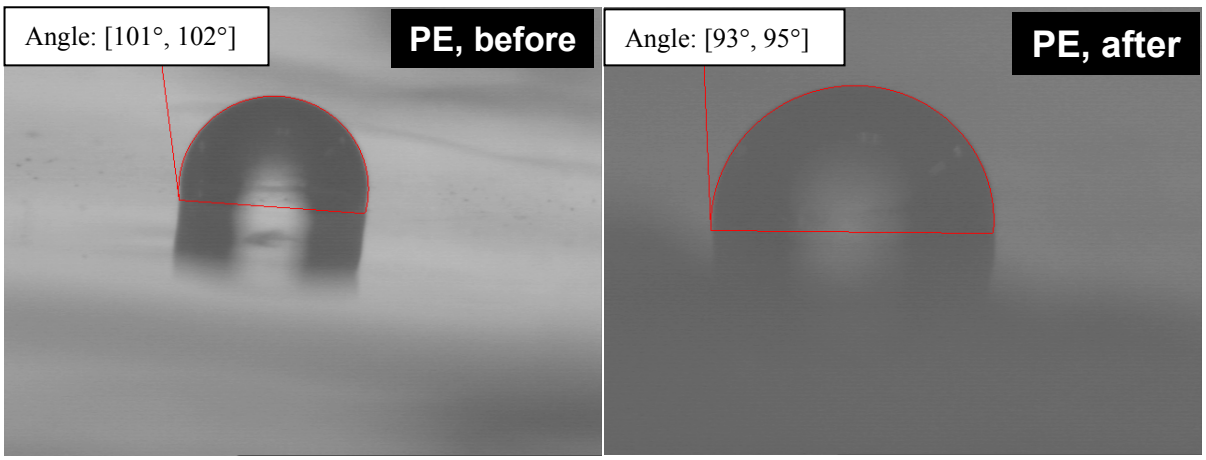


(a)

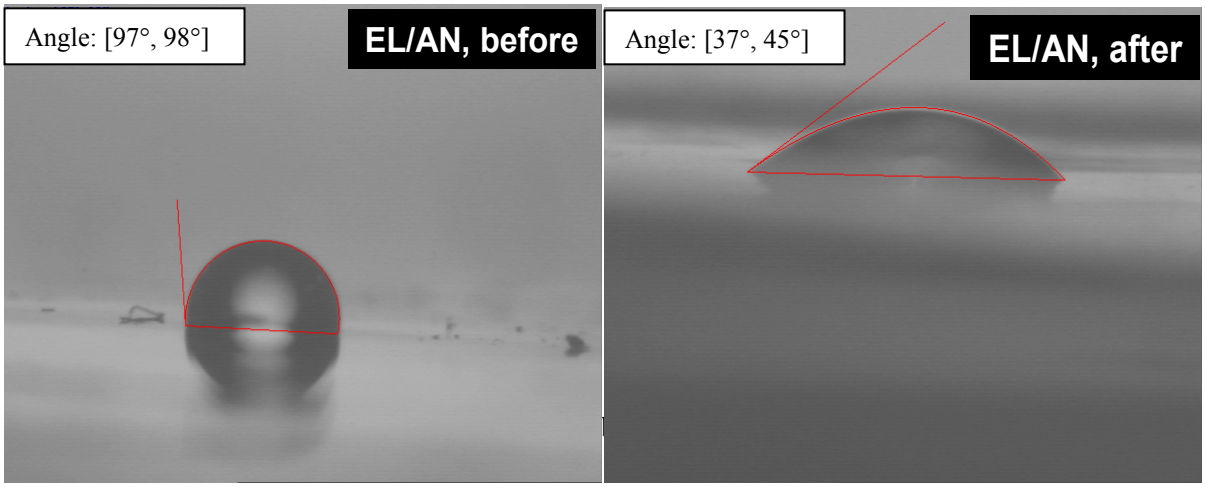


**Figure 4-19.** Photographs showing water droplets on polyethylene (sample 4) and ethylene/acrylonitrile copolymer (sample 6) films. (a) polyethylene, (b) ethylene/acrylonitrile copolymer.

### 4.3.9. Thermal Analysis

TGA was used to study the thermal properties of these copolymers (Figure 4-20). The ethylene/acrylonitrile polymers (samples 3, 4, and 6) start degrading at higher temperatures than the polyethylene sample (sample 1). As shown in Table 4-6, the ethylene/acrylonitrile copolymers have higher $T_{onset}$ and $T_{max}$ than polyethylene (sample No. 1). These higher degradation temperatures may be attributed to the nitrile groups and/or to the relatively high thermal stability of cyclized and aromatized ring structures in the PAN domains of the ethylene/acrylonitrile copolymers (Choi et al., 2002).

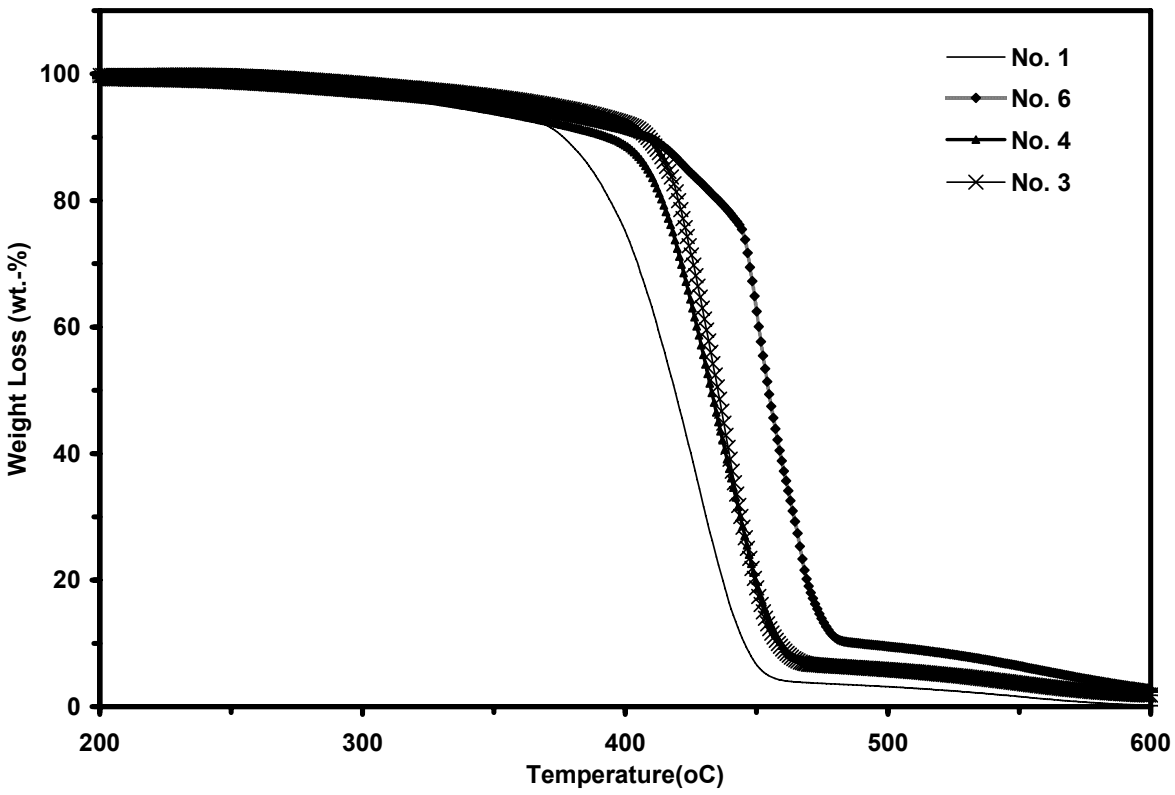


**Figure 4-20.** TGA curves of ethylene/acrylonitrile copolymers (samples 3, 4 and 6) and polyethylene (sample 1) (helium-oxygen 5%).

**Table 4-6**. TGA analysis of ethylene/acrylonitrile copolymers (samples 3, 4, 6) and polyethylene (sample 1) (helium-oxygen 5%)

| Sample No. | $T_{onset}$ (°C) | $T_{max}$ (°C) |
|---|---|---|
| 1 | 379 | 418 |
| 3 | 406 | 435 |
| 4 | 406 | 436 |
| 6 | 430 | 455 |

Temperature scanning rate: 10 °C/min., from 80 °C to 850 °C, under a gas mixture (5% $O_2$, 95% He).

### 4.3.10. Tensile Testing

Young's modulus and yield strength were obtained from stress-strain curves, as shown in Figure 4-21. All ethylene/acrylonitrile copolymers had higher Young's moduli and yield strengths than the pure polyethylene sample. Tensile properties are summarized in Figures 4-22 and 4-23. The mechanical properties were slightly increased as the acrylonitrile concentration increased (Table 4-7). Assuming nitrile concentrations have a linear relationship with FT-IR intensity at 2243 $cm^{-1}$, as explained in Section 4.3.2 (Figure 4-6), we can speculate that increased tensile properties may be due to the increased concentration of nitrile functional groups in the copolymer samples. In addition, the incorporation of acrylonitrile produced copolymers with higher tensile modulus and higher tensile strength than polyethylene without compromising elongation. These results confirm that strong adhesion forces exist between the polyethylene matrix and nanophase PAN domains.

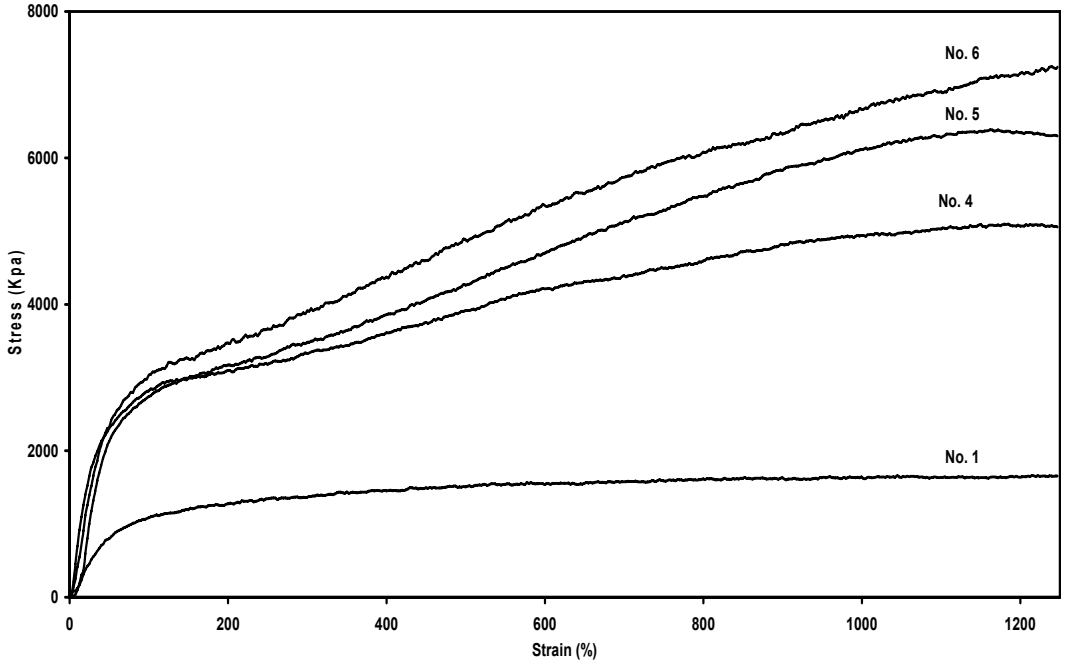


**Figure 4-21.** Stress-Strain curves for ethylene/acrylonitrile copolymer and polyethylene samples**.** See Table 4-1 for the description of each sample.

**Table 4-7**. Young's modulus and yield strength of the samples (see Table 4-1 for sample details)

| **Sample** | **Name** | **Acrylonitrile concentration** | **Young's Modulus** | **Yield Strength** |
|---|---|---|---|---|
| **No.** | | **mol/L** | **MPa** | **MPa** |
| 1 | PE(Pure) | 0 | 3.1 | 0.9 |
| | | | | |
| 4 | PE-AN | 0.48 | 7.0 | 2.3 |
| | | | 7.0[a)] | |
| | | | | |
| 5 | PE-AN | 0.60 | 7.3 | 2.4 |
| | | | 7.1[a)] | |
| | | | | |
| 6 | PE-AN | 0.73 | 7.5 | 2.5 |
| | | | 7.3[a)] | |
| | | | | |

a) Replicate runs

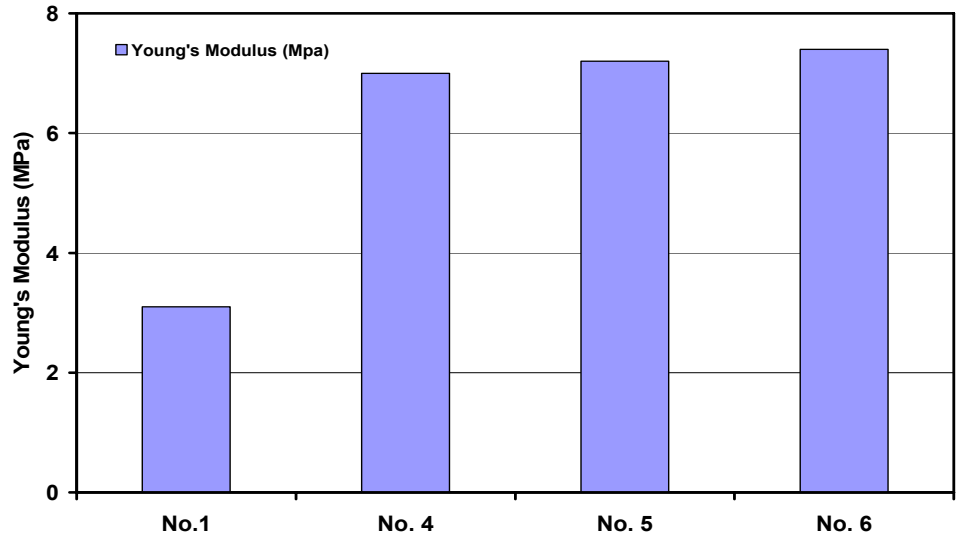


**Figure 4-22.** Young's modulus of polyethylene and ethylene/acrylonitrile copolymers.

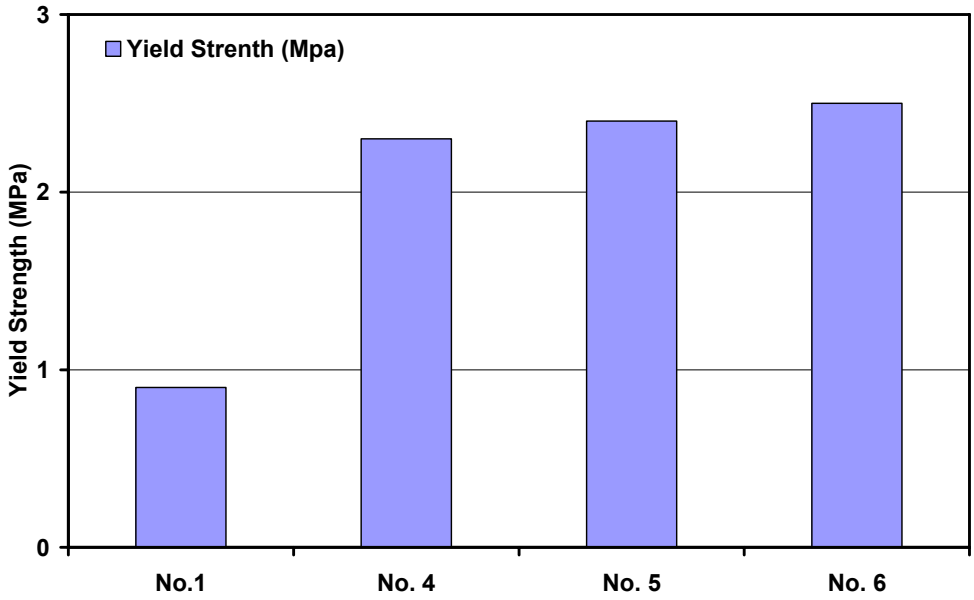


**Figure 4-23.** Yield strength of polyethylene and ethylene/acrylonitrile copolymers.

### 4.3.11. Polymerization and Curing Mechanism for Ethylene/Acrylonitrile Copolymers

Figure 4-24 illustrates a possible structure for the PAN domains within the polyethylene matrix (the dotted circle represents the nitrile domain). The domains diameter is approximately a few hundred nanometers and they are evenly distributed in the polymer matrix, as seen in the TEM image shown in Figure 4-11. In such domains, the nitrile groups can easily react with each other. This intra- or inter-chain reaction may lead to crosslinking between the polymer chains.

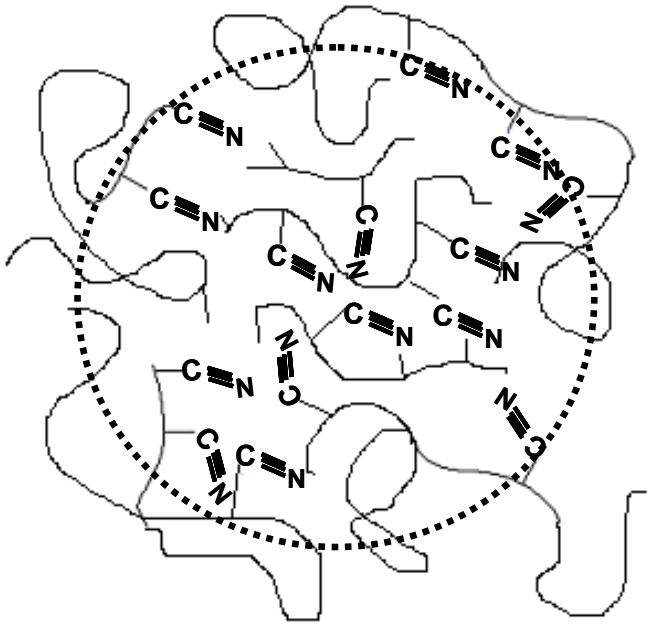

**Figure 4-24.** Possible morphology for the PAN domains in the polyethylene matrix.

## 4.4. Conclusion

The copolymerization of ethylene and acrylonitrile with the Ni-diimine/EASC catalyst system produced a rather complex product that contain polyacrylonitrile (or acrylonitrile-rich copolymer phase) spherical domains dispersed in a polyethylene (or acrylonitrile-poor copolymer phase) matrix. The PAN-rich phase can be crosslinked during Soxhlet extraction or DSC thermal treatment to form an xylene-insoluble fraction.

The xylene-insoluble fraction seems to be composed mainly by PAN, as shown by FT-IR and NMR analyses. TEM images show that this PAN-rich phase is distributed as nanosize domains in the polyethylene matrix. The PAN sequence has an isotactic structure and can form lamellae through cyclization and aromatization of nitrile groups in the polymer chains, as confirmed by FT-IR, DSC and XRD. Through the formation of the lamellar phase, crosslinking of the polyethylene matrix and PAN-rich domains may take place, which explains the better tensile properties of these novel ethylene/acrylonitrile copolymers.

When a low concentration of acrylonitrile is added to the reactor, the activity of ethylene and acrylonitrile copolymerization is comparable to that of ethylene polymerization. For higher concentrations of acrylonitrile, however, the catalyst activity decreases, the weight average molecular weight increases, and the polydispersity decreases.

On the other hand, acrylonitrile acts as a terminating and coupling agent when copolymerized with 1-hexene. Polymer yield does not increase upon addition of acrylonitrile to a reactor were 1-hexene polymerization is taking place, but the molecular weight average practically double its value.

# Chapter 5
# Ethylene in-situ Polymerization with a Catalyst Supported on Clay Modified with Acrylonitrile

## 5.1. Introduction

Since nylon-6/silicate nanocomposites were reported by Toyota company, many research groups have studied polar polymers as base materials for silicate nanocomposites (Kojima et al., 1993): polystyrene (Vaia et al., 1993), poly(ethylene oxide) (Vaia et. al., 1995), poly(n-isopropyl acrylamide) (Liang et. al., 2000), polycarbonate (Juang et. al., 2000), polyurethane (Wang and Pinnavaia, 1998), polyepoxy (Wang and Pnnavaia, 1994) polyimide (Tyan et. al., 2001), polyphenol (Choi et. al., 2000), poly(methyl methacrylate) (Biasci et al., 1994). The synthesis of polyacrylonitrile/silicate composites by in-situ polymerization, however, has been seldom reported. (Carrado et. al, 1998; Bastow et. al., 1991; Bergaya et. al., 1992)

The synthesis of ethylene/acrylonitrile copolymers was described in Chapter 4. These copolymers have a hybrid structure, combining a polyethylene matrix with nanophase polyacrylonitrile domains. We showed that these nanocomposites have increased tensile properties because of the strong interfacial interaction between the polyethylene matrix and the polyacrylonitrile domains, plausibly because of cyclization, aromatization, and crosslinking of the nitrile groups in the polymer chains.

In this chapter we discuss the synthesis of ethylene/acrylonitrile copolymer/clay nanocomposites. Clays are good host galleries for polar comonomer and the resulting nanocomposites may combine the advantages of ethylene/acrylonitrile copolymers to those of polyethylene/clay nanocomposites.

## 5.2. Experimental

Experimental materials and methods are used in the same ways as described in Section 2.2. Only changed parted from Section 2.2 are described in this section.

### 5.2.1. Materials

Acrylonitrile was purchased from Aldrich and was purified by vacuum distillation to eliminate organic stabilizers, stored in a Schlenk tube with dried molecular sieve 4 Å, and kept in the refrigerator at -5°C.

### 5.2.2. Treatment of MMT with Acrylonitrile

MMT was pretreated with TIBA solution as described in Chapter 2. One gram of MMT/TIBA (MMT modified with TIBA) was transferred into a 250 ml 2-neck Schlenk tube reactor in a glove box. Then, the reactor was connected to the Schlenk line in the fumehood and 5 ml of acrylonitrile solution was added. The clay particles were dispersed in acrylonitrile solution under $N_2$ and stirred at about 200 rpm in room temperature for 12 hours. After stirring, the particles were allowed to precipitate for 30 minutes and the supernatant solution was removed through a cannularr. The precipitate was carefully dried under vacuum for about 1 hour until the particles were free-flowing. MMT modified with TIBA and acrylonitrile will be called MMT/TIBA/AN.

### 5.2.3. In Situ Polymerization with MMT/TIBA/AN

A 250 ml glass Schlenk tube reactor equipped with a stirrer was purged with nitrogen three times before the introduction of the reagents. Subsequently, 25 ml monochlorobenzene, MMT/TIBA/AN, MAO, catalyst precursors (Ni-diimine or $Cp_2ZrCl_2$) and ethylene (at atmospheric pressure) were introduced into the glass reactor in this sequence. Ethylene was supplied under atmospheric pressure for about an hour. Before starting the polymerization, the MMT/TIBA/AN slurry was pre-contacted with MAO for 5 minutes and the catalyst precursor solution was injected. The resulting slurry

solution was degassed under vacuum. After degassing, the reactor temperature was allowed to reach room temperature. The polymerization of ethylene was then carried out through stirring the MMT/TIBA/AN and catalyst precursor. After 1 hour, the polymerization was quenched by adding 10 ml of methanol. The final nanocomposites were dried in the vacuum oven for 6 hours.

### 5.2.4. Hot-Pressed Ethylene/Acrylonitrile Copolymer Films

Film samples for IR and tensile testing analysis were prepared by the following method: A few milligrams of the polymers were sandwiched between steel plates and placed between the two steel plates of the press. The sample was previously covered with PET film to obtain a smooth film surface. The plates of the hydraulic press (P-215 C from Pasadena Hydraulics) were heated to about 180 - 200$^{o}$C. After melting the polymers for approximately 2 minutes, the samples were pressed to 320 psi. After 3 minutes, the press was released to let the air bubbles in the polymer melt to move out. After 30 seconds, the samples were pressed again for another 3 minutes. Finally, the polymer films were taken out and cooled in air to obtain the film specimens. For the curing test, after the polymer degassing step, the samples were pressed again for additional 20 minutes at 200°C.

### 5.2.5. Analysis and Testing

**Differential Scanning Calorimeter (DSC) and Thermal Gravimetry Analysis (TGA)**

The melting point ($T_m$) was determined using a Thermal Analysis DSC 2920 differential scanning calorimeter (DSC), with a heating rate of 10$^{o}$C/min under argon atmosphere. DSC analysis was done by two series of tests with the same sample. Each test consisted of 3 scans: 1) heating and melting from 25$^{o}$C to 200$^{o}$C, 2) cooling from 200$^{o}$C to -70$^{o}$C, 3) heating and melting from -70$^{o}$C to 375$^{o}$C. The 3$^{rd}$ scan is for the exothermic reaction between of the inter- or intramolecular nitrile groups. The decomposition temperature determined by thermogravimetric analysis (TGA) was performed using Thermal Analysis SDT 2960 instrument, with a heating rate of 10$^{o}$C/min under an atmosphere of 5% $O_2$ and 95% $H_e$. The temperature ranged from 80°C to 800°C, with a heating rate of 10$^{o}$C/min.

**Tensile Test**

The stress-strain curves of ethylene/acrylonitrile copolymer films were obtained in tension mode. The instrument used was the MiniMat 2000, manufactured by Rheometrics. The methods are used as explained in Section 2.2.

## 5.3. Results and Discussion

### 5.3.1. In-Situ Polymerization with MMT/TIBA/AN

Ethylene was polymerized in the absence of MMT/TIBA/AN and the catalyst activity was compared to polymerizations with MMT/TIBA/AN in Table 5-1.

**Table 5-1.** In-situ polymerization with clay modified with acrylonitrile (MMT/TIBA/AN) and Ni-diimine catalyst.

| No. | MMT/TIBA/AN (g) | CAT (μ mol) | MAO (g) | Yield (g) | Productivity ($kg/mol_{cat}$-hr) | Clay[b] (wt%) |
|---|---|---|---|---|---|---|
| 1 | 0 | 2.3 | 0.25 | 0.92 | 400 | - |
| 2 | 0.05 | 2.3 | 0.25 | 0.86 | 374 | 5.8 (6.4) |
| 3[a] | 0.05 | 2.3 | 0.25 | 0.32 | 130 | 16.5 (13.4) |
| 4 | 0.025 | 2.3 | 0.25 | 0.74 | 322 | 3.3 |
| 5 | 0.2 | 2.3 | 1 | 0.94 | 408 | 17.5 |
| 6[c] | 0.27 | 4.9 | 0.5 | 1.71 | 346 | 13.6 (4.2) |

Experimental conditions: solvent: 25 ml of monochlorobenzene; polymerization time: 1hour. [Ni-diimine Cat] = 92 μmol/L; [Al]/[Ni-diimine Cat] = 403, 1612 (sample 5); Temperature = 25°C ; $P_{ethylene}$ = atmospheric.

a. Polymerization started without pre-contact of MMT/TIBA/AN with MAO.

b. Clay residue calculated by amount of MMT/TIBA/AN and its activities.

(Clay residue measured by TGA analysis, the weight contains acrylonitrile monomers)

c. Catalyst = $Cp_2ZrCl_2$; solvent: 25 ml, monochloro benzene; [$Cp_2ZrCl_2$] = 196 μmol/L;

[Al]/[ $Cp_2ZrCl_2$] = 378; Temperature = 25$^oC$ ; $P_{ethylene}$ = atmospheric

Comparing samples 1 and 2, made with the same catalyst concentration, we notice that the catalyst activity for sample 2 was comparable to that of sample 1. In the preparation of sample 3, there was no pre-contact step between MMT/TIBA/AN and MAO. Polymerization was started shortly after adding MAO and catalyst precursor. The catalyst activity for sample 3 is much lower than for sample 1. On the other hand, with a pre-contact time of 5 minutes and an increase in the Al/Ni ratio in sample 5, the activity was almost same as that of sample 1. This may be due to pre-contact effect of the polar monomer with alkyl aluminum in polymerization as previously described (Marques et al., 1999). The acrylonitrile effect was also observed for the unsupported ethylene/acrylonitrile copolymerizations discussed in Chapter 4. We can speculate that during copolymerization of ethylene and MMT/TIBA/AN, the latter behaves as a polar monomer "supported" on clay.

Sample 6 shows that $Cp_2ZrCl_2$ is also active for this copolymerization. Its activity was comparable to that of Ni-diimine but cannot be compared directly because of its different concentration.

### 5.3.2. FT-IR Analysis

Figure 5-1 shows that the PE-MMT/TIBA/AN nanocomposite shows absorbance bands at 2244 $cm^{-1}$ that are characteristic of aliphatic nitrile group, C≡N (Coates, 2000 and Devasia et al., 2005). It is known that *v* (C≡N) of free acrylonitrile at 2230 $cm^{-1}$ is shifted to higher frequencies at 2279 $cm^{-1}$ upon coordination to metals through the nitrogen atom (Lee et al., 1985). This observation supports the idea that after clay modification, most acrylonitrile molecules exist in the clay galleries without

any coordination to metals and were polymerized to the aliphatic nitrile polymer through in-situ polymerization. A polymerization mechanism of ethylene and acrylonitrile with Ni-diimine catalysts has been proposed in Chapter 4.

After Soxhlet extraction, PE-MMT/TIBA/AN residue left in the thimble does not have the nitrile band at 2244 $cm^{-1}$. Three new absorbance bands are detected at about 1690 -1590 $cm^{-1}$ (imino group, C=N– stretching or vinyl group, C=C) (Figure 5-2) (Coates, 2000 and Devasia et al., 2003). These bands indicate typical characteristics of pyridinoid structures after Soxhlet extraction. They support our hypothesis that the acrylonitrile molecules in the polymer chains were cyclized and aromatized during heating and pressing.

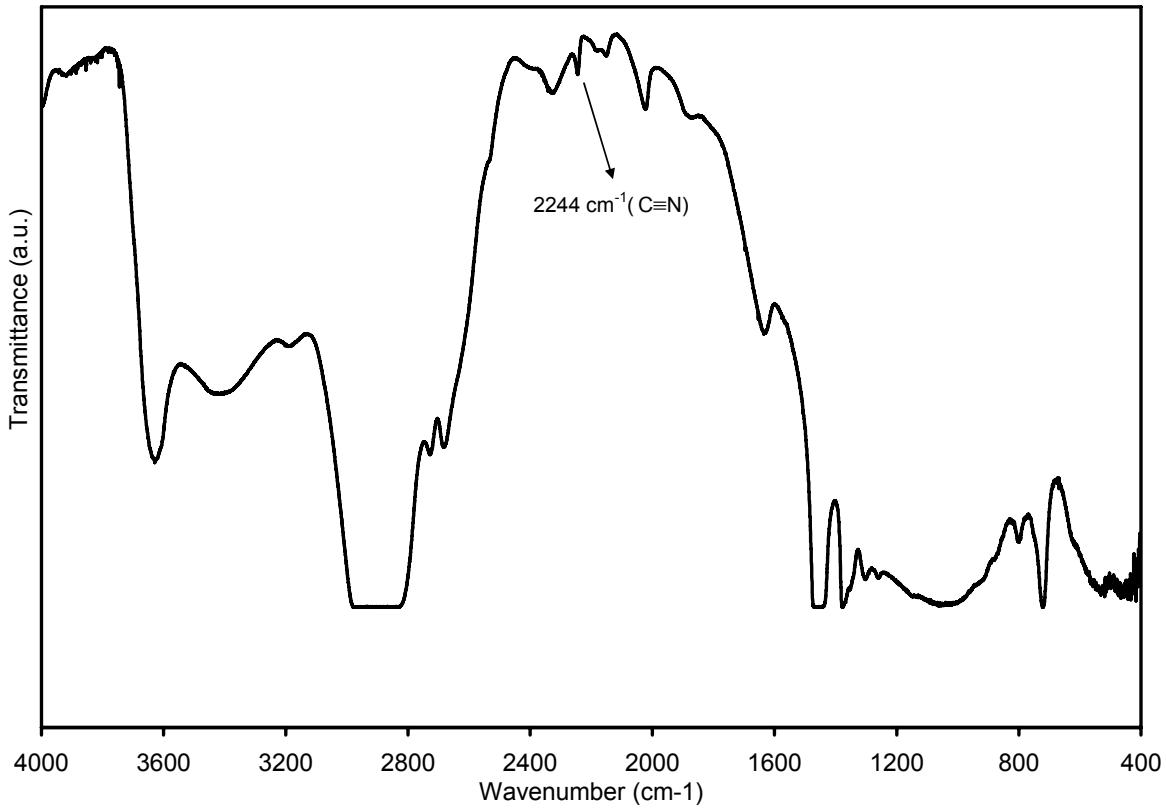


**Figure 5-1.** FT-IR spectrum of PE-MMT/TIBA/AN made with Ni-diimine catalyst (sample 2, Table 5-1).

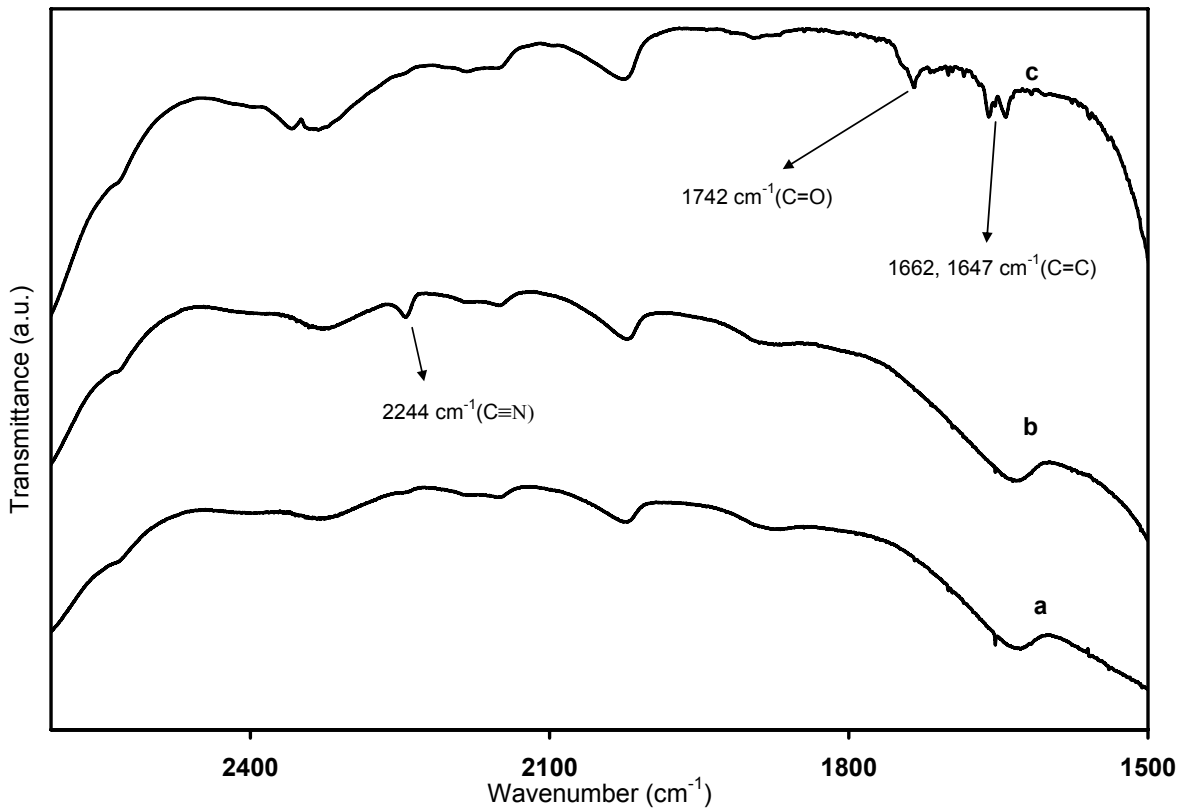


**Figure 5-2.** FT-IR spectra for the comparison of functional groups between 1500 $cm^{-1}$ and 2700 $cm^{-1}$: (a):Polyethylene (sample 1), (b) PE-MMT/TIBA/AN nanocomposite (sample 2), (c) PE-MMT/TIBA/AN residue after Soxhlet extraction for 24 hours with boiling xylene.

### 5.3.3. XRD Analysis

Figure 5-3 shows XRD diffraction patterns of MMT/TIBA/AN. The diffraction pattern of the (001) plane occurs at 3.6°, shifted by about 4° from its original position at 7.2° (basal spacing of 1.23 nm); its equivalent d spacing is 2.39 nm. Therefore, TIBA and acrylonitrile enlarge the basal space of pristine MMT. Some acrylonitrile molecules may be attached to the external surface of the clay, but most of them might be within the clay galleries. Figure 5-4 shows the wide-angle XRD patterns of the PE-MMT/TIBA/AN residue (71 wt.-% of clay) after xylene extraction for 24 hours. The basal diffraction band was not observed even at this high clay content and only the broad band at 8.86° was left. As explained in Section 1.7.1, this band is due to the presence of illite groups in the MMT.

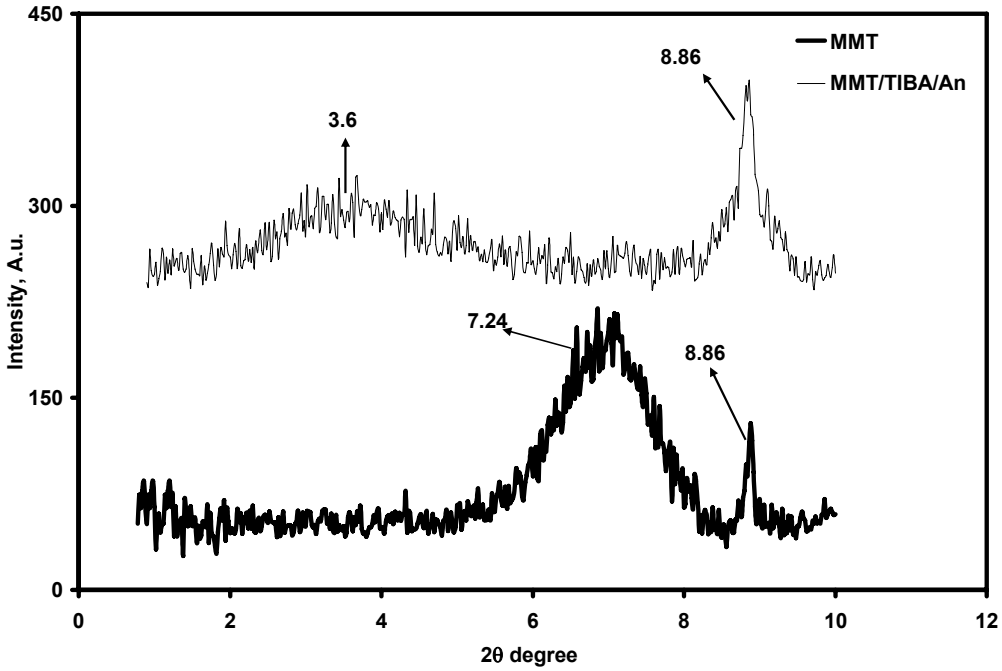


**Figure 5-3.** Small angle X-ray diffraction patterns for MMT and MMT/TIBA/AN.

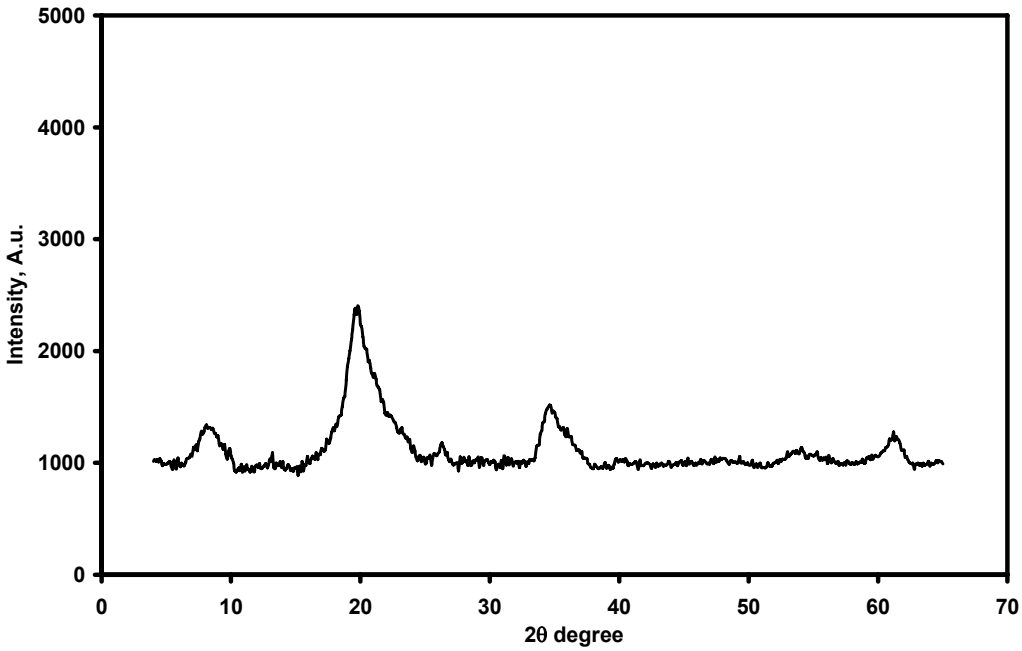


**Figure 5-4.** Wide angle X-ray diffraction patterns of PE-MMT/TIBA/AN residue (71 wt.-% of clay) after xylene extraction for 24 hours.

From these plots, it can be inferred that the MMT layers were totally exfoliated by the growing polymer and formed a PE-clay hybrid nanocomposite. This infers that clay platelets are very well distributed in the PE matrix in nano phases, and very well matched with the next XRD spectra.

### 5.3.5. DSC Analysis

Figures 5-5.a and 5-5.b show two sequential DSC thermograms of the same PE/MMT/TIBA/AN nanocomposite. Each test consisted of 3 scans. The 3$^{rd}$ scan in each test was extended to 375°C. In the thermogram (Figure 5-5.a), an exothermic peak was observed from 260°C to 375°C. The second thermogram (Figure 5-5.b) detected a new glass-transition temperature ($T_g$) at 15.25°C, but further scanning to 375 °C did not reveal any exothermic peak. These results imply that the high-temperature exothermic peak in the DSC thermogram, which might be related to chemical reaction of the nitrile groups in the polymer chains, was directly related to the appearance of the new $T_g$ in the subsequent DSC thermogram. This type of exothermic band in the DSC curves was also investigated for polyacrylonitrile and attributed to cyclization and aromatization of the pyridinoid structure in the polymer chains (Jung et al., 2002).

Cross-linking reactions between polyethylene chains and PAN domains was explained in Chapter 4. Such a result demonstrates that direct incorporation of the rigid clay platelets onto polyethylene chains may retard polymer chain movements and alter amorphous chain dynamics due to its large clay plate mass. The melting temperature ($T_m$) measured in the second scan of the second thermogram (after reaction of the nitrile groups) was 133.6°C, 2.6°C lower than 136.2°C, the $T_m$ measured in the second scan of the first thermogram. Usually, $T_m$s investigated by DSC for both macrophase-separated and nanophase-exfoliated systems, show effectively no difference within the experimental errors. The micro size particles and exfoliated nano clay plates both behave like a nucleating agent in the polymer matrix, but it was reported that nanosize silicate in polyethylene matrix influences the different crystalline rates. This DSC observation shows a new $T_g$ band after the

exothermic band. It supports the strong interactions between polyethylene chains and exfoliated clay platelets.

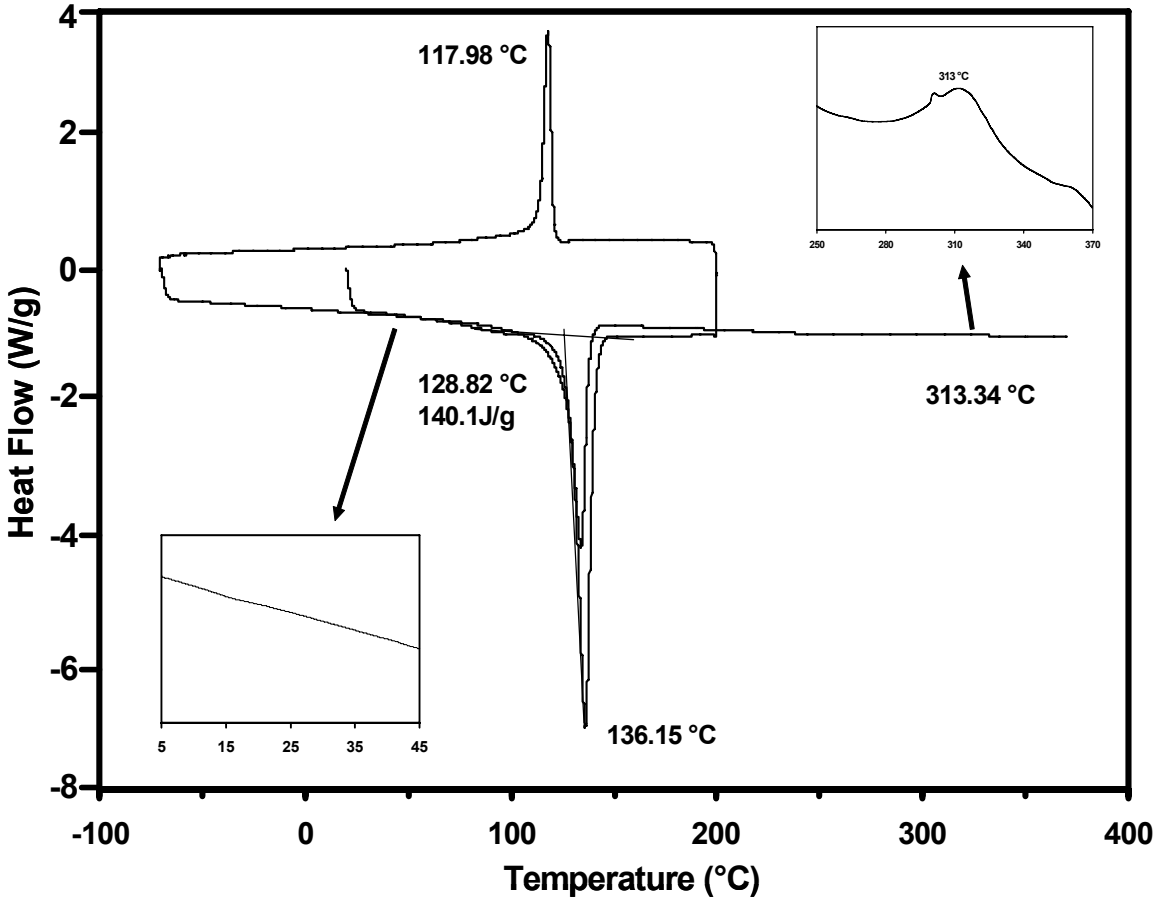


**(a)**

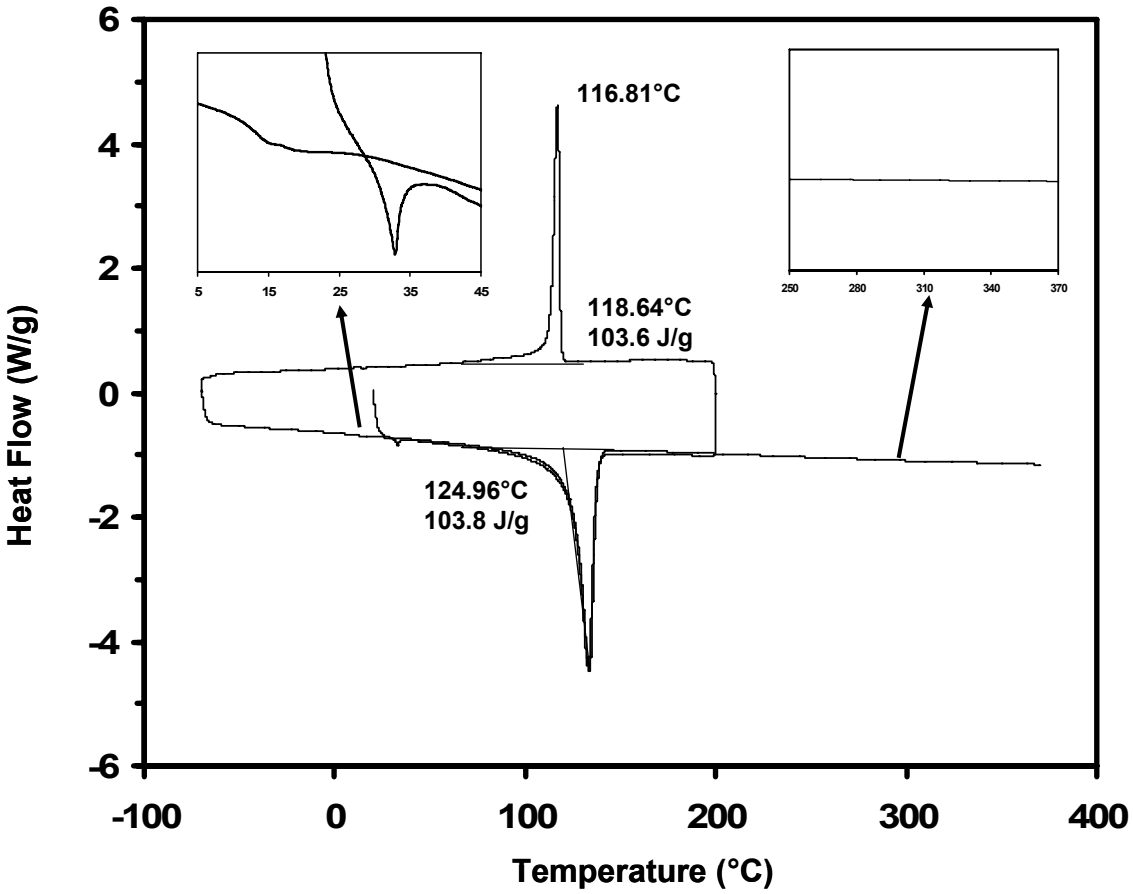


**(b)**

**Figure 5-5.** DSC curves for PE-MMT/TIBA/AN (sample 6): (a) 1st DSC thermogram, (b) 2nd DSC thermogram.

### 5.3.4. TGA Analysis

Figure 5-6 shows the TGA analysis results of MMT, MMT/TIBA and MMT/TIBA/AN. The thermal decomposition of MMT/TIBA/AN shows different behavior, compared with MMT and MMT/TIBA. It shows the relatively slower decomposition from 100 °C to 300 °C. In this region, hydrated water molecules or light weight molecules are vaporized, which is observed in MMT and MMT/TIBA. Additional decomposition was observed from 400 °C to 500 °C, which is similar

behavior of MMT/TIBA/UOH, discussed in Section 2.3.4. Slower decomposition in this temperature range could imply that acrylonitrile molecules could be located inside of clay platelets.

In Figure 5-7, PE-MMT/TIBA/AN, nanocomposites (Sample 2 and 3 in Table 5-1) show a different mass-loss behavior from that of polyethylene. They decompose over a broader temperature range, suggesting that the polymer is a mixture of several chain structures.

In Figure 5-8, the derivative weight loss curves of PE-MMT/TIBA/AN nanocomposites and polyethylene were compared. While the polyethylene sample exhibits a one-step decomposition behavior, the nanocomposites decompose in three-steps in the range of 360°C-395°C, 395°C-437°C and 440°C-460°C. The first weight-loss region, centered at 378°C, may be due to the decomposition of short-chain branched polyethylene that has a lower decomposition temperature than non-branched polyethylene. The second weight-loss region, centered at 416°C, is essentially identical to the decomposition peak temperature for polyethylene. The third weight-loss region, centered at 450°C, was only observed for PE-MMT/TIBA/AN. This temperature range from 440°C-460°C may be related to the degradation of chain containing nitrogen atoms.

In summary, these analyses show the broader decomposition temperature range with PE-MMT/TIBA/AN. The different decomposition behaviors of the PE-MMT/TIBA/AN nanocomposites are probably related to the presence of nitrogen groups and nanophase clay platelets in polyethylene matrix.

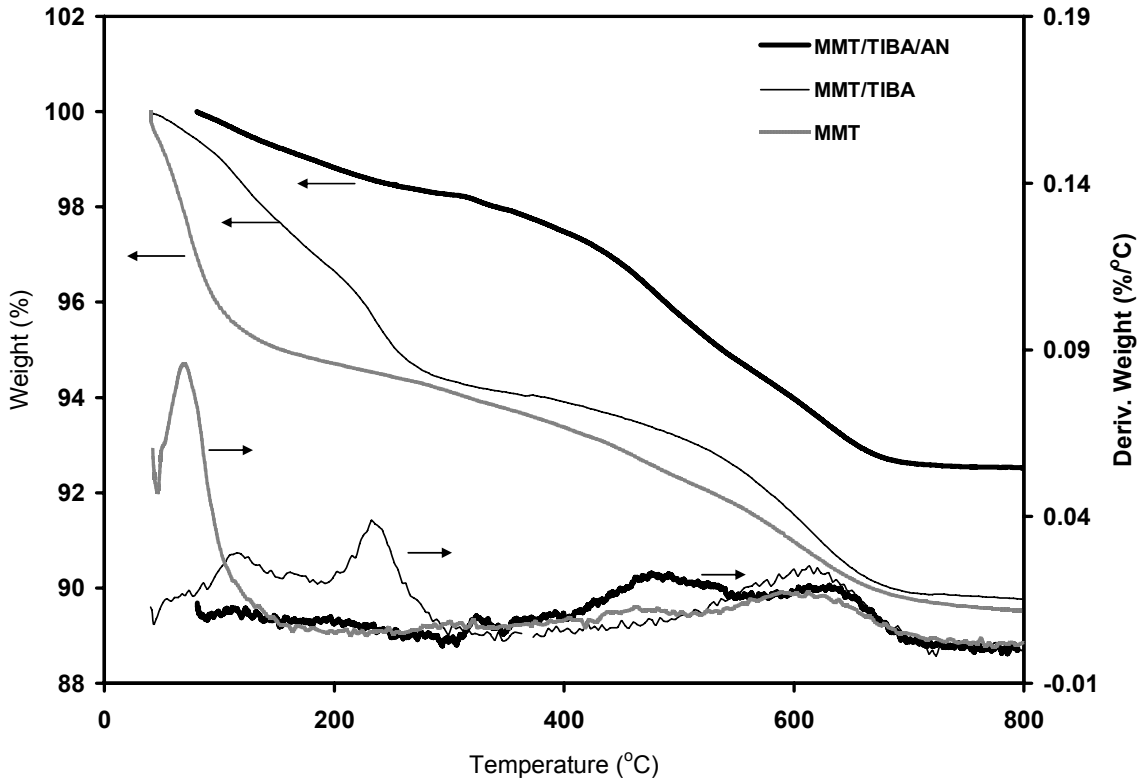


**Figure 5-6.** TGA and DTG (derivative weight loss) curves of MMT, MMT/TIBA and MMT/TIBA/AN samples.

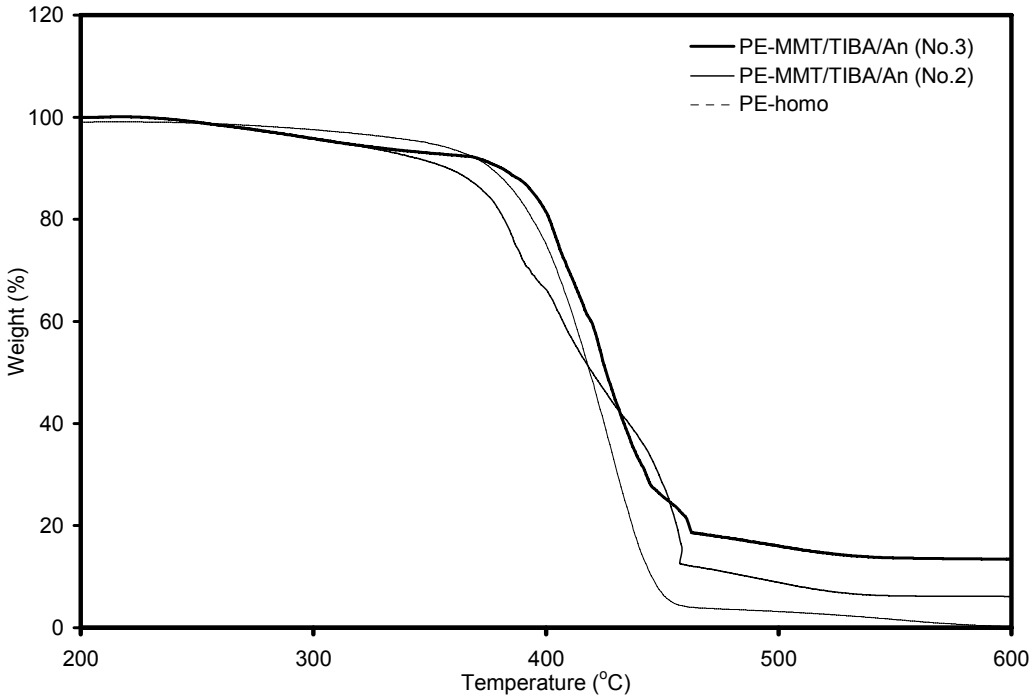


**Figure 5-7.** TGA curves of polyethylene and two PE-MMT/TIBA/AN samples.

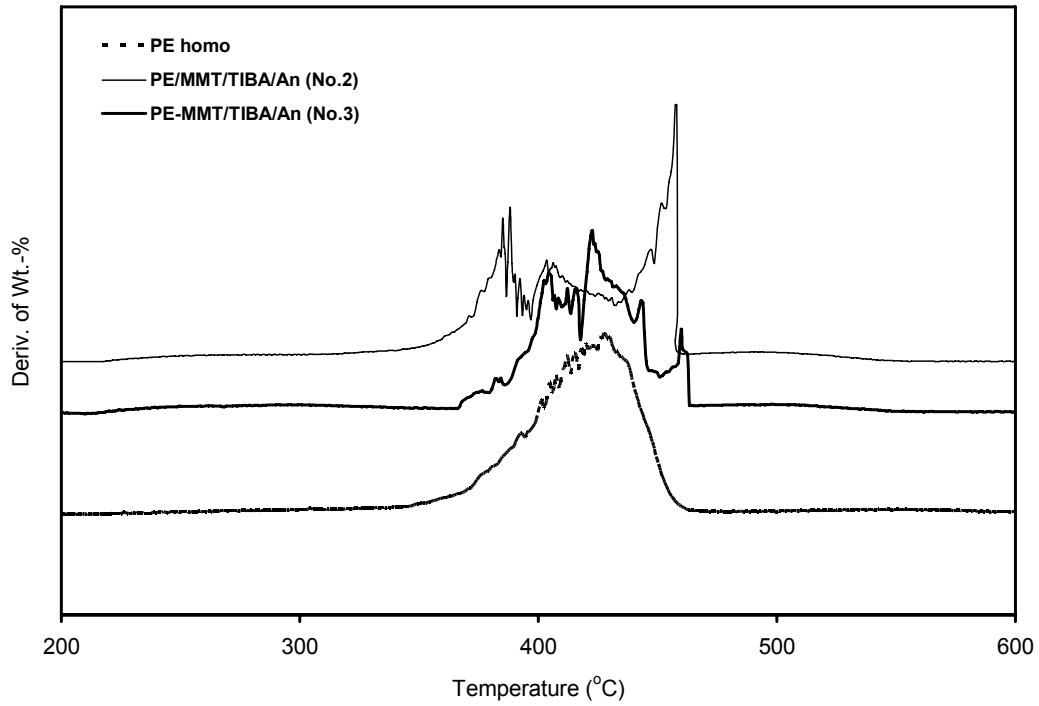


**Figure 5-8.** DTG (derivative weight loss) curves from TGA comparing polyethylene and PE-MMT/TIBA/AN.

**Mechanical Properties**

Figure 5-10 shows stress-strain curves for a polyethylene and three PE-MMT/TIBA/AN nanocomposites. It was found that two nanocomposites (samples 3 and 4, Table 5-2) have higher Young's modulus and yield strengths than polyethylene and the dry-blended PE-clay composite (samples 1 and 2, Table 5-2). Samples 1 and 2 have the same mechanical properties, thus showing that adding unmodified MMT to polyethylene does not enhance mechanical properties. The better mechanical properties of samples 3 and 4 depend on the concentration of the acrylonitrile used to make the PE-MMT/TIBA/AN nanocomposites. Both tensile modulus and tensile strength increase significantly as the wt.-% of MMT/TIBA/AN increases.

Krasnogorov (1978) showed that when acrylonitrile molecules were polymerized in contact with polyethylene by free radical polymerization, the resulting product contained PE/PAN grafted chains that exhibited excellent tensile properties.

PE-MMT/TIBA/AN nanocomposites allow high tensile modulus, high tensile strength without compromising high elongation (Figures 5-11 and 5-12). Actually, no breaks were shown until 450% elongation. These results indicate the strong adhesion forces between the polymer matrix and the modified clay surfaces. This may indicate that the polyethylene and the acrylonitrile-modified clay platelets were well mixed, forming a hybrid nanocomposite. Although impact properties were not tested, based on the area below the stress-strain curves, it is expected that these nanocomposites would have a impact strength higher than polyethylene.

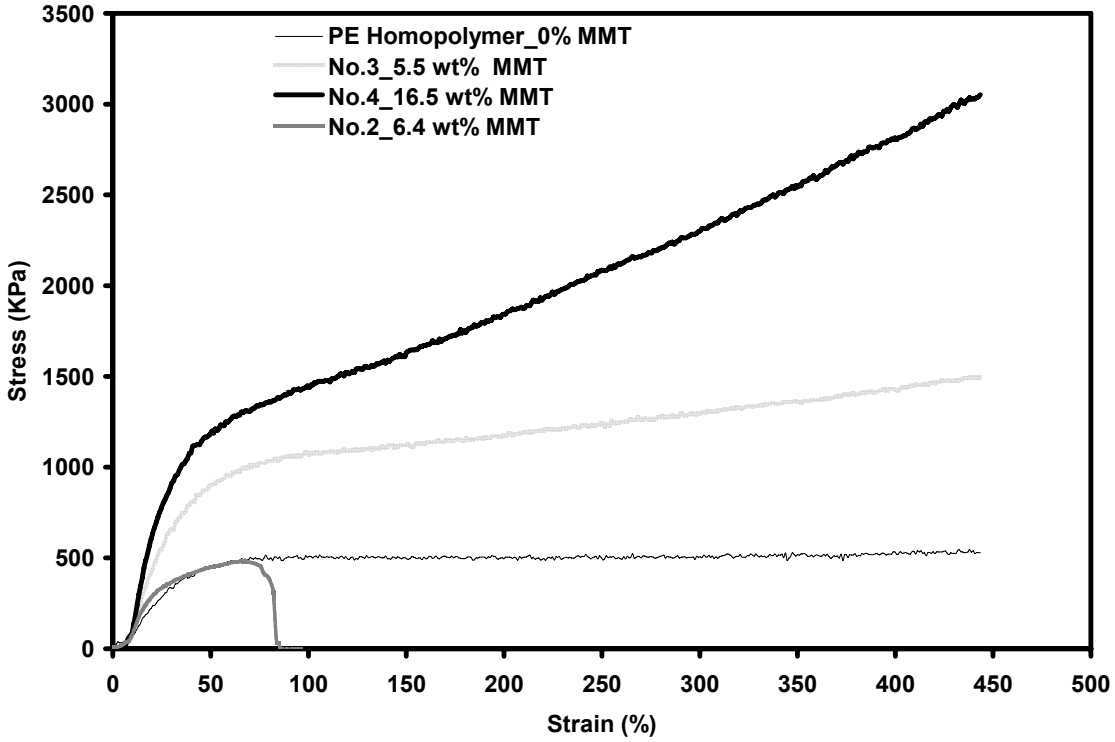


**Figure 5-10.** Stress-strain curves for polyethylene (0 wt.-% MMT), sample 2 (6.4 wt.-% MMT, dry-blended), sample 3 (5.5 wt.-% MMT) and sample 4 (16.5 wt.-% MMT).

**Table 5-2**. Young's modulus and yield strength of nanocomposite samples. [a]

| No. | Name | MMT Content (Wt.-%) | Young's Modulus (MPa) | Yield Strength (MPa) | Elongation at Break (%) |
|---|---|---|---|---|---|
| 1 | PE | 0 | 1.4 | 0.4 | NB[c] |
| 2[b] | PE/MMT | 6.4 | 1.6 | 0.4 | 80 |
| 3 | PE/MMT/TIBA/AN | 5.5 | 3.1 | 0.8 | NB |
| 4 | PE/MMT/TIBA/AN | 16.5 | 7.6 | 1.6 | NB |

[a] The same samples in Table 5-1 were used for tensile testing.

[b] Dry blending PE homopolymer with pristine MMT.

[c] NB: none broken.

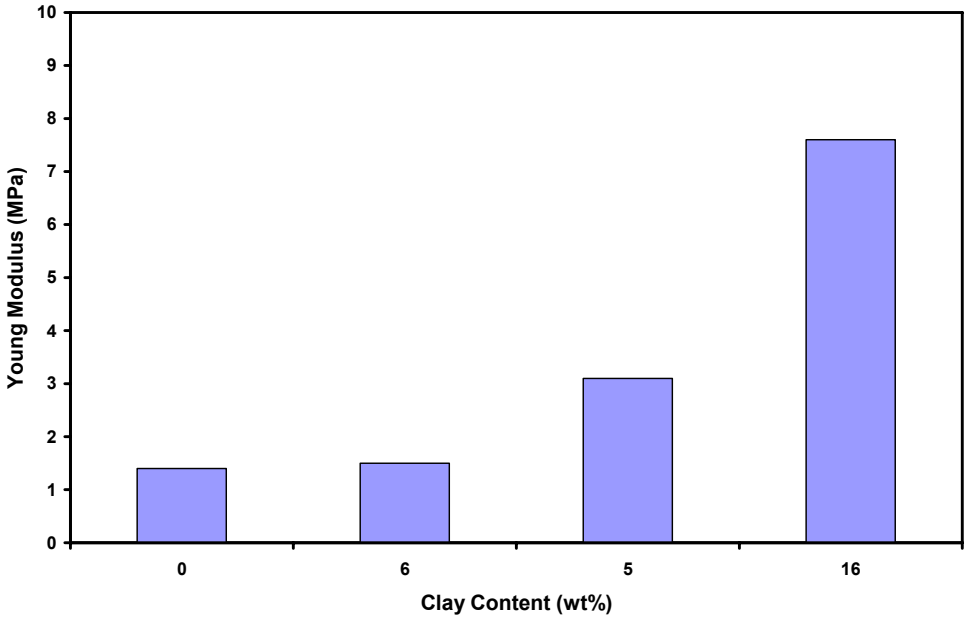


**Figure 5-11.** Young's modulus of polyethylene and PE-MMT/TIBA/AN.

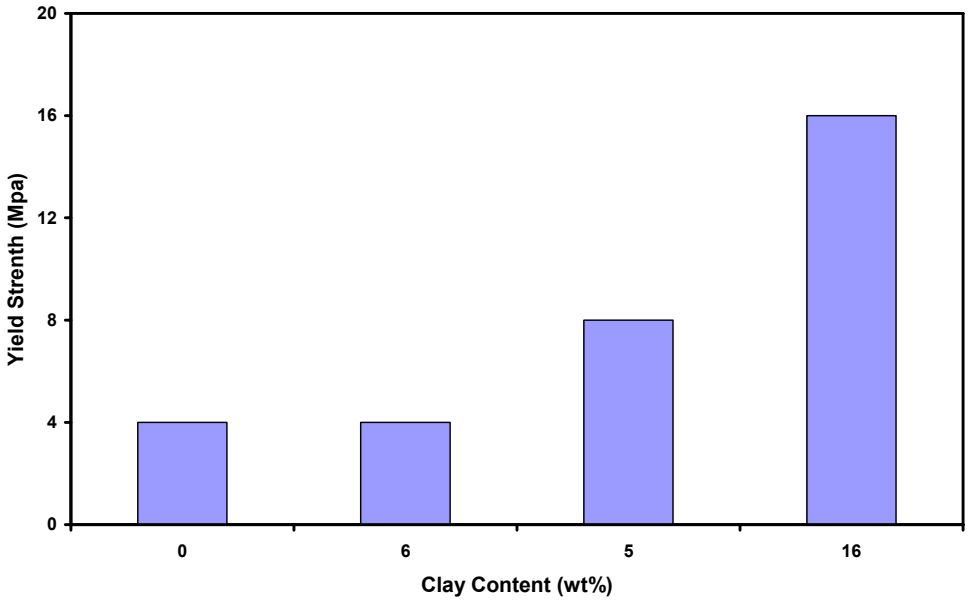


**Figure 5-12.** Yield strength of polyethylene and PE-MMT/TIBA/AN.

## 5.4. Conclusion

A novel method has been proposed to copolymerize ethylene in the presence of acrylonitrile-modified clay. Before polymerization, TIBA and acrylonitrile were contacted with MMT (MMT/TIBA/AN). Ni-diimine and $Cp_2ZrCl_2$ activated with MAO were used as catalysts. The copolymerization product is rather complex, containing polyethylene and ethylene/acrylonitrile copolymers with long sequences of acrylonitrile. The polymerization productivity depended on the pre-contact step between MAO and MMT/TIBA/AN.

The thermal properties of the PE-MME/TIBA/AN composited proved that strong interactions existed between the polymer chains and the exfoliated clay platelets. The new $T_g$ found after the first DSC analysis that may be due to the cross-linking reactions of the nitrile groups in the polymer chains, creating strong interactions between polymer chains and clay platelets that disturb the mobility of the polymer chains.

FT-IR spectra of the original sample as well as of the fractionated sample were used to determine the existence of nitrile and other functional groups in the nanocomposite. Soxhlet extraction proved the presence of crosslinked structures in xylene-insoluble fraction of the polymer nanocomposite.

We also observed that the dispersion of MMT in the polymer matrix took place in the nanoscale, as measured by XRD and TGA. XRD analysis did not detect a basal diffraction band for PE-MMT/TIBA/AN residues after Soxhlet extraction containing 44 wt.-% of MMT. Since these bands, if present, can be detected by XRD when the MMT content in the polymer is lower than 10 wt.-%, the MMT in the nanocomposite is likely completely exfoliated.

The PE-MMT/TIBA/AN have tensile properties that are better than pure polyethylene or a dry-blended mixture of polyethylene and MMT, which shows again that the MMT particles interact very strongly with the polymer matrix. The testing results showed that by making a nanocomposite with excellent interaction between the polymer and clay phases both Young's modulus and yield

strength could be improved in comparison to pure polyethylene. The Young's modulus of some PE-MMT/TIBA/AN samples reached up to 3.1~7.6 MPa, almost double of that of pure polyethylene (1.4 MPa) synthesized under the same conditions.

# Chapter 6
# Contributions to Research

This thesis proposes a new synthetic method of the polyethylene-clay hybrid nanocomposites through in-situ polymerization. The bifunctional surface modification was first investigated as a modifier for MMT during the ethylene polymerization. The intercalation of UOH into MMT galleries, its bonding to the gallery surfaces and consequent incorporation in polyethylene chains are key contributions of this thesis.

Intercalation of transition metal catalysts and cocatalyst allows ethylene polymerization in the galleries, thus leading to the exfoliation of clay in nanosize platelets within the polyethylene matrix, which was verified through electronic optical microscopes. This process also allows covalent chemical bonding between clay and polyethylene. For the physical properties of these hybrid nanomaterials, higher decomposition temperatures and tensile properties were observed. The maximum tensile property was obtained at around 6 wt.-% of clay content in PE matrices. More importantly, it shows an increase in tensile strength without sacrificing the elongation properties. This result could be attributed to the strongly enhanced interfacial interaction between MMT surface and PE polymer matrices.

In gas phase polymerization (high pressure) it was possible to obtain polymer particles with good morphology, a feature that is much needed for an industrial reactor. Experiments carried out at atmospheric pressure provided insight on the mechanism of particle growth and fragmentation; which are necessary for determining the importance of pre-polymerization in industrial scale. Moreover, microscopy study (TEM) on cross sections of the polymer particles obtained in the early stages provided evidence of intercalation and exfoliation of the clay structure in the growing polymer particle. This is the first time experimental data is provided to understand the mechanism of particle growth and fragmentation when the catalyst support is a layered silicate.

A novel method was proposed to prepare ethylene/acrylonitrile copolymerizations. Ethylene/acrylonitrile copolymers were successfully tested prior to the application to PE-Clay nanocomposites. Ni-diimine/EASC catalyst system shows comparable activities by the addition of low concentration of acrylonitrile. Xylene insoluble part of ethylene/acrylonitrile copolymer shows the PAN rich structure, confirmed with FT-IR, $^{1}H$ and $^{13}C$ NMR spectra. DSC curves of Xylene insoluble parts show the characteristic exothermic bands, which have been observed for the cyclization and aromatization of PAN structure. XRD analysis of ethylene/acrylonitrile copolymer after DSC scan shows the appearance of a new band, which was reported by the lamellar structure induced by cyclization and aromatization of PAN structure. TEM images of ethylene/acrylonitrile copolymer shows the domains of PAN distributed in nano size in polyethylene matrix. The physical properties of the ethylene/acrylonitrile copolymers were tested for tensile properties. The yield strength and elongation was both increased more than two times than that of ethylene homopolymer. Thermal property, degradation temperature is also increased more than 50°. Acrylonitrile was used as organic modification of MMT and subsequently applied to the in situ polymerization of ethylene. The thermal property obtained by DSC proved that strong interaction between polyethylene chains with exfoliated clay platelets. FT-IR spectroscopes of the PE-MMT/TIBA/AN samples show the existence of nitrile groups with clay nanoparticles in the polyethylene matrix.

For the morphological comparison between slurry and gas phase, slurry polymerization was focused on the verification of intercalation and exfoliation of clays in the slurry phase during the polymerization. Its chemical bonds between the clay platelets and polymer matrix could be confirmed by further Soxhlet extraction and SEM and TEM analysis. On the other hand, the gas phase polymerization provided us the evidence of the particle fragmentation through the intercalation and exfoliation mechanism.

Soxhlet extraction proved the presence of cross-linked structure in certain polymer nanocomposites and that covalent chemical bonding or other very strong interactions between the

organic and inorganic phases was present in these hybrid materials. Overall comparison for the tensile properties, the enhanced properties can be achieved as a following order; Polyethylene/Acrylonitrile Copolymer**>>**PE-MMT/TIBA/AN **≥** PE-MMT/TIBA/UOH **>>** Homo-Polyethylene.

# Chapter 7
# Suggestions for Future Works

From a technology point of view, PE-Clay nanocomposites in-situ polymerizations are attractive materials, but the manufacturing procedure needs improvement and development.

For PE-Clay hybrid nanocomposites further investigation could go in the following aspects:

- Further studies for the side reactions between clay platelets and catalyst to reduce the deactivation of transition metal active center during polymerization, as well as the characterization of how homogeneous the catalyst dispersion is in the clay particles.

- Other bifunctional molecules should be investigated for the future applications. MMT can be used for the host galleries for polar monomers for the copolymerization with ethylene.

- Molecular weight and molecular weight distribution, based on GPC analysis need to be studied as changing MMT content in the reactor. It will explain that the influence of MMT platelets for the polymerization kinetics.

- The impact properties should be studied for the PE-Clay hybrid nanocomposites.

For the ethylene-acrylonitrile further investigation could go in the following aspects:

- $^{1}H$ and $^{13}C$ NMR studies are needed for the copolymerization mechanism of ethylene/acrylonitrile with Ni-diimine/EASC catalyst system. It will be helpful for development of the catalyst recipe.

- For the enhancement of ethylene/acrylonitrile copolymers, the content of acrylonitrile in ethylene polymer matrix should be investigated, by controlling the PAN domain size and its distributions.

- The mechanical and thermal properties should be studied for the full inspection of ethylene/acrylonitrile copolymers. This investigation leads to the application field in the commercial market of ethylene/acrylonitrile copolymers

# References


Akelah, A.; Salahuddin, N.; Hiltner, A.; Baer, E.; Moet, A.; Morphological hierarchy of butadieneacrylonitrile/montmorillonite nanocomposite, *Nanostructured Materials*, **1994**, 4, 965.

Albietz, P. J. Jr.; Yang, K.; Lachicotte, R. J.; Eisenberg, R.; Cationic Unsymmetrical 1,4-Diazabutadiene Complexes of Platinum(II), *Organometallics*, **2000**, 19, 3543.

Alexander, L. E.; *X-Ray Diffraction Methods in Polymer Science*, Wiley-Interscience, New York 1**969** p.381.

AlObaidi, F.; Ye, Z.; Zhu, S.; Ethylene Polymerization with Silica-Supported Nickel-Diimine Catalyst: Effect of Support and Polymerization Conditions on Catalyst Activity and Polymer Properties, *Macromolecules Chem. Phys.*, **2003**, 204, 1653.

Annual Book of ASTM standards, D 638-03, Standard Test Method for Tensile Properties of Plastics, **2004**.

Bang, Y. H.; Lee, S.; Cho, H. H.; Effect of Methyl Acrylate Composition on the Microstructure Changes of High Molecular Weight Polyacrylonitrile for Heat Treatment, *J. Appl. Polym. Sci.*, **1998**, 68, 2205.

Bartczak, Z.; Galeski, A.; Argon, A.S.; Cohen, R.E.; On the plastic deformation of the amorphous component in semicrystalline polymers, *Polymer*, **1996**, 37, 2113.

Bastow, T.; Hardin, S. G.; Turney, T. W.; The formation of β′-sialon from a montmorillonite-polyacrylonitrile composite by carbothermal reduction: an NMR, TGA, XRD and EM study, *J. Mater. Sci.*, **1991**, 26, 1443.

Bellamy, L. J.; The Infrared Spectra of Complex Molecules, Chapman and Hall, London, **1974**, 1, 295.

Bergaya, F.; Kooli, f.; Alcover, F.; Alcover, F. J.; Synthesis of "SiMON" ceramics from various clays and different sources of carbon, *J. Mater. Sci.*, **1992**, 27, 2180.

Bergman J. S.; Chen, H.; Giannelis, E .P.; Tomas, M. G.; Coates, G. W.; Synthesis and characterization of polyolefin–silicate nanocomposites: a catalyst intercalation and in situ polymerization approach, *Chem. Comm.*, **1999**, 2179.

Biasci, L.; Aglietto, M.; Ruggeri, G.; Ciardelli, F.; Functionalization of montmorillonite by methyl methacrylate polymers containing side-chain ammonium cations. *Polymer*, **1994**, 35, 3296.

Boffa, L. S.; Novak, B. M.; Copolymerization of Polar Monomers with Olefins Using Transition-Metal Complexes, *Chem. Rev.*, **2000**, 100, 1479-1493.

Boor, J.; Ziegler-Natta Catalysts and Polymerizations, Academic Press, New York, **1979**, p 202.

Bousmina, M.; Study of Intercalation and Exfoliation Process in Polymer Nanocomposites, *Macromolecules*, **2006**, 39, 4259.

Brandrup, J.; On the Chromophore of Polyacrylonitrile. V. The Oxidation of Isobutyronitrile, *Macromolecules*, **1968**, 1, 72.

Brindley, G. W.; Brouwn, G.; Crystal structures of clay minerals and their X-ray identification, *Mineralogical Society*, **1980**, p 170.

Brookhart, M. S.; Johnson, L.K.; Killian, C. M.; Arthur, S. D.; Feldman, J.; McCord, E. F.; Mclain, S. J.; Kreutzer, K. A.; Bennett, A. M. A.; Coughlin, E. B.; Ittel, S. D.; Parthasarathy, A.; Tempel, D. J.; WO Patent Application 9623010 to DuPont, April 3, **1995**.

Brookhart, M. S.; Johnson, L.K.; Killian, C. M.; Arthur, S. D.; Feldman, J.; McCord, E. F.; Tempel, D. J.; Patent Application 5880241 May 3, **1999** to DuPont (Polymer compositions).

Busenberg, E.; Clemency, C. V.; Determination of the cation-exchange capacity of clays and soil using ammonia electrode, *Clays clay miner.*, **1973**, 21, 213.

Calberg, C.; Mertens, M.; Baute, N.; Jerome, R.; Carlier, V.; Sclvons, M.; Legras, R.; Dynamic Mechanical Thermal and Infrared Analyses of Polyacrylonitrile "Electrografted" onto a Metal, J. Polym. Sci. B; *Polym. Phys.*, **1998**, 36, 554.

Carrado, K. A.; Xu, L.; In Situ Synthesis of Polymer-Clay Nanocomposites from Silicate Gels, *Chem. Mater.*, **1998**, 10, 1440.

Chan, C.-M.; Polymer Surface Modification and Characterization, **1994**, (New York: Hanser).

Cheng, X.; Lofthus, O. W.; Deck, P. A.; Ethylene polymerization using silica-supported zirconocene dibromide/methylalumoxane catalysts, *J. Mol. Catal. A: Chemical*, **2004**, 212, 121.

Chien, J. C. W.; He, D.; Determination of molecular weights and Mark-Houwink constants for soluble electronically conducting polymers, *J. Polym. Sci. Part A.*, **1991**, 29(13), 1585.

Choi, M. H.; Chung, I. J.; Lee, J. D.; Morphology and Curing Behaviors of Phenolic Resin-Layered Silicate Nanocomposites Prepared by Melt Intercalation, *Chem. Mater.*, **2000**, 12, 2977.

Choi. Y. S.; Wang, K. H.; Xu, M.; Chung, I.; J. Synthesis of Exfoliated Polyacrylonitrile/Na-MMT Nanocomposites via Emulsion Polymerization, *Chem. Mater.*, **2002**, 14, 2936.

Chow, W.S.; Mohd Ishak, Z.A.; Karger-Kocsisb, J.; apostolovc, A.A.; Ishiaku, U.S.; Compatibilizing effect of maleated polypropylene on the mechanical properties and morphology of injection molded polyamide6/polpropylene/organoclay nanocomposites, *Polymer*, **2003**, 44, 7427.

Coates, G. W.; Precise Control of Polyolefin Stereochemistry Using Single-Site Metal Catalysts *Chem. Rev.*, **2000**, 100, 1223.

Coates, J.; Interpretation of Infrared Spectra, A Practical Approach, Encyclopaedia of analytical Chemistry, R. A. Meyer (Ed.) Copyright © John Wiley &Sons Ltd., **2000**, 1.

de Farias, R. F.; Airoldi, C. J.; Thermogravimetry as a Reliable tool to Estimate the Density of Silanols on a Silica Gel Surface, *J. Thermal. Anal. Cal.*, **1998**, 53(3). 751.

Devasia, R.; Reghunadhan, C. P.; Sivadasan, N. P.; Katherine, B. K.; Ninan, K. N.; Cyclization Reaction in Poly(acrylonitrile/Itaconic Acid) Copolymer: An Isothermal Differential Scanning Calorimetry Kinetic Study, *Journal of Applied Polymer Science*, **2003**, 88, 915.

Dias, P. M.; De Faria, D. L. A.; Constantino, V. R. L.; Spectroscopic Studies on the Interaction of Tetramethylpyridylporphyrins and Cationic Clays, *Journal of Inclusion Phenomena and Macrocyclic Chemistry*, **2000**, 38, 251.

Earley, J. W.; Osthaus, B. B.; Milne, I. H.; Purification and properties of montmorillonite, *Am. Miner.*, **1953**, 38, 707.

Fabio, M.; *Thesis, Produção de blendas poliméricas e nanocompósitos utilizando sistemas catalíticos binários (Production of blends and nanocomposites using binary catalytic systems)*, Universidade federal do Rio Grande do Sul, **2005**, June.

Fadeev, A. Y.; McCarthy, T. J.; Trialkylsilane Monolayers Covalently Attached to Silicon Surfaces: Wettability Studies Indicating that Molecular Topography Contributes to Contact Angle Hysteresis, *Langmuir*, **1999**, 15, 3759.

Ferreira, M. L.; Belelli, P. G.; Damiani, D. E.; Theoretical and experimental study of the interaction of methylaluminoxane (MAO)-low temperature treated silica: Role of trimethylaluminium (TMA), *Macromolecules Chem. Phys.*, **2000**, 201, 1334.

Fink, G.; Mulhaupt, R.; Brintzinger, H. H.; *Ziegler Catalyst*; Springer Verlag: Berlin, **1995**.

Fornes, T. D.; Paul, D. R.; Crystallization behavior of nylon 6 nanocomposites, *Polymer*, **2003**, 44, 3945.

Frisch, H. L.; Mark, J.; Nanocomposites prepared by threading polymer chains through zeolites, mesoporous silica, or silica nanotubes, *Chem. Mater.*, **1996**, 8, 1735.

Giannelis, E. P.; Polymer Layered Silicate Nanocomposites, *Adv. Mater.*, **1996**, 8, 29.

Gibson, V. C.; Spitzmesser, S. K.; Advances in Non-Metallocene Olefin polymerization Catalysis, *Chem. Rev.*, **2003**, 103, 283.

Gilman J. W.; Ksahiwagi, T.; Giannelis, E. P.; Manias, E.; Lomakin, S.; Lichtenhan, J. D.; Jones, P.; Flammability properties of polymer-layered silicate nanocomposites. In: Al-Makaika S, Golovey A. Wilkie C. A., editors, *Chemistry and technology of polymer additives*. Oxford: Blackwell Science; **1999**, Chapter 14.

Gopakumar, T.G.; Lee, J. A.; Kontopoulou, M.; Parent, J. S.; Influence of clay exfoliation on the physical properties of montmorillonite/polyethylene composites, *Polymer*, **2002**, 43, 5483.

Gridnev, A. A.; Ittel, S. D.; Catalytic Chain Transfer in Free-Radical Polymerizations, *Chem. Rev.*, **2001**, 101, 3611.

Grim, R. E.; *Clay Mineralogy*, New York: McGraw-Hill, **1968**.

Groux, L. F.; Weiss, T.; Reddy, D. N.; Chase, P. A.; Piers, W. E.; Zigler, T.; Parvez, M.; Benet-Buchholz, J.; Insertion of Acrylonitrile into Palladium Methyl Bonds in Neutral and Anionic Pd(II) Complexes, *J. Am. Chem. Soc*. **2005**, 127, 1854.

Hammawa, H; Wanke, S. E.; Gas-phase olefin polymerization over supported metallocene/MAO catalysts: influence of support on activity and polydispersity, *Polym. Int.*, **2006**, 55, 426.

Harrane, A.; Meghabar, R.; Belbachir, M. A.; Protons Exchanged Montmorillonite Clay as an Efficient Catalyst for the Reaction of Isobutylene Polymerization, *Int. J. Mol. Sci.*, **2002**, 3, 790.

Hasegawa, N.; Kawasumi, M.; Kato, M.; Usuki, A.; Okada, A.; Preparation and properties of EPDM–clay hybrids, *J. Appl. Polym. Sci.*, **1998**, 67, 87.

Heinemann, J.; Peichert, P.; Thomann, R.; Mulhaupt, R.; Polyolefin nanocomposites formed by melt compounding and transition metal catalyzed ethene homo- and copolymerization in the presence of layered silicates, *Macromol. Rapid Commun.*, **1999**, 20. 423.

Hirooka, M.; Yabuuchi, H.; Morita, S.; Kawasumi, S.; Nakaguchi, K.; Complex copolymerization. I. Novel equimolar copolymers of acrylonitrile and olefins, *J. Polym. Sci., Polym. Lett.*, **1967**, B5, 47..

Hlatky, G. G.; *"Supported Metallocene Catalysts for Olefin Polymerization" in Metallocene-based polyolefins*, Ed. J. Scheirs and W. Kaminsky, John Wiley & Sons, West Sussex, **2000**, 1, 201.

Hlatky, G. G.; Heterogeneous Single-Site Catalysts for Olefin Polymerization, *Chem. Rev*., **2000**, 100, 1347.

Houg, S. C.; Ban, H. T.; Kishi, N.; Jim, J.; Uozumi, T.; Soga, K.; "Ethene polymerization with a poly(styrene-co- divinylbenzene) beads supported rac-$Ph_2Si(Ind)_2ZrCl_2$ catalyst", *Macromol. Chem. Phys.*, **1998**, 199, 1393.

Iler, R. K.; *The Chemistry of Silica, 2nd ed.*; Wiley: New York, **1979**; Chapter 6.

Imuta, J.; Toda, Y.; Kashiwa, N.; New Metallocene Catalyst Having an Indenyl Group and a Fluorenyl Group for Ethylene-Polar Monomer Copolymerization, *Chemistry Letters*, **2001**, 710.

Inaba, S. I.; Matsumoto, H.; Rieke, R. D.; Highly Reactive Metallic Nickel: Reductive Homocoupling Reagent for Benzylic Mono- and Polyhalides, *J. Org. Chem.*, **1984**, 49, 2903.

Ittel, S. D.; Johnson, L. K.; Brookhart, M.; Late-Metal Catalysts for Ethylene Homo- and Copolymerization, *Chem. Rev.*, **2000**, 100, 1169.

Jal, P. K.; Patel, S.; Mishra, B. K.; Chemical modification of silica surface by immobilization of functional groups for extractive concentration of metal ions, *Talanta*, **2003**, 62, 1005.

Janiak, J.; Rieger, B.; Silica gel supported zirconocene dichloride/methylalumoxane catalysts for ethylene polymerization: Effects of heterogenation on activity, polymer microstructure and product morphology, *Angew. Makromol. Chem.*, **1994**, 215, 47.

Jin, Y-H; Park H-J; Im, S-S; Kwak, S-Y; Kwak, S.; Polyethylene/clay nanocomposite by in situ exfoliation of montmorillonite during Ziegler-Natta polymerization of ethylene. *Macromol. Rapid Commun.*, **2002**, 23, 135.

Johnson, L. K.; Killian, C.M.; Brookhart, M.; New Pd(II)- and Ni(II)-Based Catalysts for Polymerization of Ethylene and .alpha.-Olefins, *J. Am. Chem. Soc.*, **1995**,117, 6414.

Johnson, L. K.; Mecking, S.; Brookhart, M.; Copolymerization of Ethylene and Propylene with Functionalized Vinyl Monomers by Palladium(II) Catalysts, *J. Am. Chem. Soc.*, **1996**, 118, 267.

Jongsomjit, B.; Praserthdam, P.; Kaewkrajang, P.; A comparative study on supporting effect during copolymerization of ethylene/1-olefins with silica-supported zirconocene/MAO catalyst, *Materials Chem. Phys*., **2004**, 86, 243.

Jordan, J. W.; Organophilic bentonites, *J. Phys. Colloid Chem.*, **1949**, 53, 294.

Jung, K. T.; Hwang, D. K.; Shul, Y. G.; Han, H. S.; Lee, W. S.; The preparation of isotactic polyacrylonitrile using zeolite, *Material Letters*, **2002**, 53, 180.

Kaminsky, W.; Renner, F.; High melting Polypropenes by Silica-supported Zirconocene Catalysts, *Makromol. Chem., Rapid Commun.*, **1993**, 14, 239.

Kato, C.; Kuroda, K.; Misawa, M.; Preparation of Montmorillonite –Nylon Complexes and Their Thermal Properties, *Clays & Clay Minerals*, **1997**, 27, 129.

Kaviratna, P. D.; Pinnavaia, T. J.; Schroeder, P. A.; Dielectric properties of smectite clays, *J. Phys. Chem. Solids*, **1996**, 57(12), 1897.

Kawai, T.; Umemura J.; Takenaka, T.; Kodama, M.; Seki, S.; Fourier transform infrared study on the phase transitions of an octadecyltrimethylammonium chloride-water system, *J. Colloid Interface Sci.*, **1985**, 103, 56.

Kawasumi, M.; Hasegawa, N.; Kato, M.; Usuki, A.; Okada, A.; Preparation and Mechanical Properties of Polypropylene-Clay Hybrids, *Macromolecules*, **1997**, 30, 6333.

Kellum, G. E.; Smith, R. C.; Determination of water, silanol, and strained siloxane on silica surfaces, *Anal. Chem.*, **1967**, 39, 341.

Khalil, H.; Mahajan, D.; Rafailovich, M.; Polymer-montmorillonite clay nanocomposites. Part 1: Complexation of montmorillonite clay with a vinyl monomer, *Polym. Int.*, **2005**, 54, 423.

Killian, C. M.; Tempel, D. J.; Johnson, L. K.; Brookhart, M.; Living Polymerization of  -Olefins Using NiII- -Diimine Catalysts. Synthesis of New Block Polymers Based on  -Olefins, *J. Am. Chem. Soc.*, **1996**, 118, 11664.

Kirk-Othmer; Encyclopaedia of Chemical Technology Home Page. Http://www.mrw.interscience. Wiley.com/kirk/ (accessed June **2006**)

Kitagawa, T.; Uozumi, T.; Soga, K.; Takata, T.; Syndiospecific propene polymerization with polymer-supported metallocene catalyst, *Polymer*, **1997**, 38(3), 615.

Kojima, Y.; Usuki, A.; Kawasumi, M.; Okad, A.; Fukushima, Y.; Kurauchi, T.; Kamigaito, O.; Mechanical properties of nylon 6-clay hybrid. *J. Mater. Res.*, **1993**, 8, 1185.

Kornmann, X; Synthesis and Characterisation of Thermoset-Clay Nanocomposites, Doctoral thesis, Luleå University of Technology, **2001**, 14.

Koten, V.; Vroezek, G.; in Stone FGA, West R editors. Advanced Organometallic Chemistry, vol. 21, New York: Academic Press, **1982**, p. 151.

Krasnogorov, A. I.; Tabalin, YE. N.; Physical Properties of Polyethylene modified by radiation-induced grafting of polyacrylonitrile, *Polymer Science U.S.S.R.*, **1978**, 20, 510.

Lagaly, G.; The "layer charge" of regular interstratified 2:1 clay minerals, *Clay Miner.*, **1979**, 27, 1.

Lagaly, G; Beneke, K.; Weiss, A.; Magadiite and H-magadiite: II. H-magadiite and its intercalation compounds, *Am. Miner.*, **1975**, 60, 650.

Lan, T.; Pinnavaia, T. J.; Clay-reinforced epoxy nanocomposites, *Chem. Mater.*, **1994**, 6, 2216.

Largaly, G.; Interaction of alkylamines with different types of layered compounds, *Solid State Ionics*, **1986**, 22, 43.

Laus, M.; Camerani, M.; Lelli, M.; Spamacci, K.; Sandrolini, F.; Francescahgeli, O.; Hybrid nanocomposites based on polystyrene and a reactive organophilic clay, *J. Mater. Sci.*, **1998**, 33, 2883.

Lee, D.; Yoon, K.; Noh, S.; Polymerization of ethylene by using zirconocene catalyst anchored on silica with trisiloxane and pentamethylene spacers, *Macromol. Rapid Commun.*, **1997**, 18 427.

Lee, M. K.; Kim, I. B.; Chin, C. S.; Spectra, Formation Constants, Reactions and Catalytic Activities of Nitrogen-Bonded Unsaturated Nitrile Complexes of Rhodium(I), *Journal of Organometallic Chemistry*, **1985**, 290, 115.

Lee, S. H.; Kim, J. E.; Song, H. H.; Kim, S. W.; Thermal Properties of Maleated Polyethylene/Layered Silicate Nanocomposites, *International Journal of Thermophysics*, **2004**, 25, 5, 1585.

Li, D.; Zhang, Y.; Wang, H.; Tang, J.; Wang, B.; Free-Radical Copolymerization kinetics of Acrylonitrile and Methyl Acrylate in [BMIM]BF4, *J. Appl. Polym. Sci.*, **2006**, 102, 4254.

Liang, L.; Liu, J.; Gong, X.; Thermosensitive Poly(N-isopropylacrylamide)-Clay Nanocomposites with Enhanced Temperature Response, *Langmuir*, **2000**, 16, 9895.

Liu, L.; Qi, Z.; Zhu, X.; Studies on nylon 6/clay nanocomposites by melt-intercalation process, *J. Appl. Polym. Sci.*, **1999**, 71, 1133.

Liu, C.; Tang, T.; Huang, B.; Zirconocene catalyst well space inside modified montmorillonite for ethylene polymerization: role of pretreatment and modification of montmorillonite in tailoring polymer properties, *J. Catal.*, **2004**, 221,162.

Marmur, A.; Thermodynamic aspects of contact angle hysteresis, *Adv. Colloid Interface Sci*., **1994**, 50, 121.

Marques, M. M.; Correia, S. G.; Ascenso, J. R.; Ribeiro, A. F. G.; Gomes, P. T.; Dias, A. R.; Foster, P.; Rausch, M. D.; Chien, J. C. W.; Polymerization with TMA-Protected Polar Vinyl Comonomers. I. Catalyzed by Group 4 Metal Complexes with eta5-type Ligand, *Journal of Polymer Science: Part A: Polymer Chemistry*, **1999**, 37, 2457.

Mathieu-Sicaud, A.; Mering, J.; Perrin-Bonnet, I.; Etude au microscope de la montmorillonite et de I'hectorite saturee par differents cations, *Bull. Soc. Miner. Cristal.*, **1951**, 74, 439.

Mathur, R. B.; Bahl, O. P.; Mittal; A new approach to thermal stabilisation of PAN fibres, *Carbon*, **1992**, 30, 657.

Matyjaszewski, K.; Xia, J.; Atom Transfer Radical Polymerization, *Chem. Rev*., **2001**, 101, 2921.

McAtee, J. L.; Inorganic-organic cation-exchange on montmorillonite, *Am. Miner*., **1959**, 44, 1230.

Mecking, S.; Brookhart, M.; Mechanistic Studies of the Palladium-Catalyzed Copolymerization of Ethylene and  -Olefins with Methyl Acrylate, *J. Am. Chem. Soc*., **1998**, 120, 888.

Mering, J.; On the hydration of montmorillonite, *Trans. Faraday Soc*.,**1946**, 42B, 205.

Minagawa, M.; Taira, T.; Yabuta, Y.; Nozaki, K.; Yoshii, F.; Anomalous Tacticity-Crystallinity Relationship: A WAXD Study of Stereoregular Isotactic (83-25%) Poly(Acrylonitrile) Powder Prepared by Urea Clathrate Polymerization, *Macromolecules*, **2001**, 34, 3679.

Minagawa, M.; Takasu, T.; Shinozaki, S.; Yoshii, F.; Morishita, N.; 13C n.m.r. and g.p.c.-low-angle laser light scattering measurements on polyacrylonitrile prepared by urea clathrate polymerization in the solid state for the optimization of tacticity, *Polymer*, **1995**, 36, 2343.

Minagawa, M.; Ute, K.; Kitayama, T.; Hatada, K.; Determination of Stereoregularity of g-Irradiation Canal Polymerized Polyacrylonitrile by 1H 2D J-Resolved NMR Spectroscopy, *Macromolecules*, **1994**, 27, 3669.

Minagawa, M.; Yamada, H.; Yamaguchi, K.; Yoshii, F.; g-Ray Irradiation Canal Polymerization Condition Ensuring highly Stereoregular(>80%) Poly(acrylonitrile), *Macromolecules*, **1992**, 25, 503.

Misono, A; Uchida, Y.; Hidai, M.; Kanai, H.; Acrylonitrile Complexes of Ruthenium Chloride which Catalyze the Dimerization of Acrylonitrile to 1,4-dicyanobut-1-ene, *Chem. Comm*., **1967**, 376.

Monar, K.; Habeschuss, A.; Modeling the principal amorphous halo in quiescent melts of polyethylene and ethylene copolymers using wide-angle X-ray scattering and its implications, *J. Polym. Sci, B, Poly, Physics.*, **1999**, 37, 3401.

Motomatsu M.; Takahashi, T.; Nie, H.-Y.; Mizutani, W. H.; Tokumoto, H.; Microstructure study of acrylic polymer silica nanocomposite surface by scanning force microscopy, *Polymer*, **1997**, 38, 177.

Ogawa, M.; Kuroda, K.; Preparation of inorganic-organic nanocomposites through intercalation of organoammonium ions into layered silicates, *Bull. Chem. Soc. Jpn*., **1997**, 70, 2593.

Okada, A.; Kawasumi, M.; Usuki, A.; Kojima, Y.; Kurauchi, T.; Kamigaito, O.; Nylon 6-clay hybrid, in Schaefer DW, Mark JE editors, *Materials Science Symp. Proceedings*, vol. 171, Pittsburgh: Material Research Society, **1990**, p. 45.

Paavola, S.; Uotila, R.; Lofgren, B.; Seppala, J. V.; Enhanced adhesive properties of polypropylene through copolymerization with 10-undecen-1-ol, *Reactive and Functional Polymers*, **2004**, 61, 53.

Park, D.; Kim, I.; Ha, C.; Crystalline and viscoelastic properties of branched polyethylenes synthesized using bidentate nickel (II) catalyst, *Polymer*, **2003**, 44, 8177-8184

Park, J-. Y.; McKenna, G. B.; Size and confinement effects on the glass transition behavior of polystyrene/o-terphenyl polymer solutions, *Phys. Rev. B*., **2000**, 61, 6667.

Pham, Q.-T.; Petiaud, R.; Spectres RMN des polymers $^{1}H$-$^{13}C$, NMR SPECTRA OF POLYMERS, **1980**, 1, Ed., SCM.

Pinnavaia, T. J.; Intercalated Clay Catalysts, *Science*, **1983**, 220, 4595.

Pinnavaia, T. J.; Lan, T.; Kaviratna, P. D.; Wang, M. S.; Clay-polymer nanocomposites:polyether and polyimide systems, *Mater. Res. Soc. Symp. Proc*., **1994**, 346, 81.

Pinnavaia, T.J.; Beall, G.W.; Polymer-clay Nanocomposites, New York: Wiley, **2000**. Chapter 1.

Preishuber-Pflugl, P.; Brookhart, M.; Highly Active Supported Nickel Diimine Catalysts for Polymerization of Ethylene, *Macromolecules*, **2001**, 35, 6074.

Rabiej, S.; WAXS Investigations of the Amorphous Phase Structure in Linear Polyethylene and Ethylene-1-Octene Homogeneous Copolymers, *Fibres & Textiles in Eastern Europe*, **2005**, 13, No. 5(53), 30.

Resconi, L.; Cavallo, L.; Fait, A.; Piemontesi, F.; Selectivity in propene polymerization with metallocene catalysts, *Chem. Rev*., **2000**, 100(4), 1253.

Rieger, B.; C. Janiak, C.; Silica Gel Supported Zirconocene Dichloride/Methylalumoxane for Ethylene Polymerizations: Effects of Heterogenation on Activity, Polymer Microstructure and Product Morphology, *Angew. Makromol. Chem*., **1996**, 215, 45.

Rosenblum, M.; Turnbull, M. M.; Begum, M. K.; η[2]-Acrylonitrile cyclopentadienyldicarbonyliron (II) tetrafluoroborate: an unusual high-valent transition metal complex, *J. Organomet. Chem*. **1987**, 321, 67.

Ruckenstein, E.; Yuan, Y.; Nanocomposites of rigid polyamide dispersed in flexible vinyl polymer, *Polymer*, **1997**, 38, 3855.

Schaper, F.; Foley, S. R.; Jordan, R. F.; Acrylonitrile Polymerization by $Cy_3PCuMe$ and $(Bipy)_2FeEt_2$, *J. Am. Chem. Soc*., **2004**, 126, 2114.

Shi, H.; T. Lan, T.; Pinnavaia, T. J.; Interfacial effects on the reinforcement properties of polymer organoclay nanocomposites, *Chem. Mater*., **1996**, 8, 1584.

Shin, S. Y. A.; Simon, L. C.; Soares, J. B. P.; Scholz, S. G.; Polyethylene–clay hybrid nanocomposites: in situ polymerization using bifunctional organic modifiers, *Polymer*, **2003**, 44(18), 5317.

Sides, G.; Barden, L.; The microstructure of dispersed and flocculated samples of kaolinite, illite and montmorillonite, *Can. Geotech. J.*,**1971**, 8, 391.

Simanke, A. G.; Alamo, R. G.; Galland, G. B.; Mauler, R. S.; Wide-Angle X-ray Scattering of Random Metallocene-Ethylene Copolymers with Different Types and Concentration of Comonomer, *Macromolecules*, **2001**, 34, 6959.

Simon, L. C.; Soares, J. B. P.; R. F. de Souza.; Polyethylene Made with In Situ Supported Ni-Diimine/SMAO: Replication Phenomenon and Effect of Polymerization Conditions on Polymer Microstructure and Morphology, *Macromol. Chem. Phys*., **2001**, 202, 3237.

Simon, L. C.; Souza, R. F. D.; Soares, J. B. P.; Mauler, R. S.; Effect of molecular structure on dynamic mechanical properties of polyethylene obtained with nickel-diimine catalysts, *Polymer*, **2001**, 42, 4885.

Simon, L. C.; Williams, C. P.; Soares, J. B. P.; R. F. de Souza.; Effect of polymerization temperature and pressure on the microstructure of Ni-diimine-catalyzed polyethylene: parameter identification for Monte-Carlo simulation, *Chem. Eng. Sci*., **2001**, 56(13), 4181.

Snyder, R. G.; Strauss, H. L.; Elliger, C. A.; Carbon-hydrogen stretching modes and the structure of n-alkyl chains. 1. Long, disordered chains, *J. Phys. Chem.*, **1982**, 86, 5145.

Soares, J. B. P.; Hamielec, A. E.; General dynamic mathematical modelling of heterogeneous and homogeneous Ziegler-Natta copolymerization with multiple site types and mass and heat transfer resistances. *Polym. React. Eng.*, **1995**, 3, 261

Soga, K.; Arai, T.; Hoang, B. H.; Uozumi, T.; Olefin polymerization with metallocene catalysts supported on polysiloxane derivatives, *Macromol. Rapid Commun.*, **1995**, 16, 905.

Strying, M. G.; Hamielec, A. E.; Determination of Molecular Weight, Edited: A. R. Cooper, John Wiley & sons. Inc., **1989**, Chap. 10.

Suh, M. P.; Oh, Y.; Kwak, C.; Synthesis of a Dimethylcobalt(III) Complex Containing Di-2-pyridylamine Ligands and Catalytic Studies on Polymerization of Acrylonitrile, *Organometallics*, **1987**, 6, 411.

Sun, T.; Graces, J. M.; High-performance polypropylene-clay nanocomposites by in-situ polymerization with metallocene/clay catalysts, *Adv. Mater.*, **2002**, 14, 128.

Sun, Y.; Shao, Z.; Hu, P.; Yu, T.; Hydrogen Bonds in Silk Fibroin-Poly(acrylonitrile-co-methyl acrylate) Blends; FT-IR Study, *J. Poly. Sci. B.:Polym. Phys*. 1997, 35, 1405.

Szabo, M. J.; Jordan, R. F.; Michalak, A.; Piers, W. E.; Weiss, T.; Yang, S. Y.; Zielger, T.; Polar Copolymerization by a Palladium-Diimine-Based Catalyst. Influence of the catalyst Charge and Polar Substituent on catalyst Poisoning and Polymerization Activity. A Density functional Theory Study, *Organometallics*, **2004**, 23, 5565.

Theng, B. K. G.; *Formation and properties of clay-polymer complexes*, Elsevier, Amsterdam, **1979**, p.133.

Thunemann, A. F.; Ruland, W.; Lamellar Mesophases in Polyacrylonitrile: A Synchrotron Small-Angle X-ray Scattering Study, *Macromolecules*, **2000**, 33, 2626.

Tien, Y. I.; Wei, K. H.; "High-Tensile-Property Layered Silicates/Polyurethane Nanocomposites by Using Reactive Silicates as Pseudo Chain Extenders, *Macromolecules*, **2001**, 34, 9045.

Tsutsui, T.; Kashiwa, N.; Kinetic study on ethylene polymerization with $Cp_2ZrCl_2$/ methylaluminoxane catalyst system, *Polym. Commun*., **1988**, 29(6), 180.

Tudor, J.; O'Hare, D.; Stereospecific propene polymerisation catalysis using organometallic modified mesoporous silicate, *Chem. Comm*., **1997**, 603.

Tudor, J.; Willington, L.; O'Hare, D.; Royan, B.; Intercalation of catalytically active metal complexes in polysilicates and their application as propene polymerisation catalysts, *Chem. Comm*., **1996**, 2031.

Tyan, H. L.; Leu, C. M.; Wei, K. H.; Effect of Reactivity of Organics-Modified Montmorillonite on the Thermal and Mechanical Properties of Montmorillonite/Polyimide Nanocomposites, *Chem. Mater.*, **2001**, 13, 222.

Uozumi, T.; Soga, K.; Copolymerization of olefins with Kaminsky-Sinn-type catalysts, Die *Makromol. Chem*., **1992**, 193, 823.

Usuki, A.; Kato, M.; Okada, A.; Kurauchi, T.; Synthesis of polypropylene-clay hybrid, *J. Appl. Polym. Sci.*, **1997**, 63, 137.

Usuki, A.; Kojima, Y.; Kawasumi, M.; Okada, A.; Fukushima, Y.; Kurauchi, T.; Kamigaito, O.; Swelling behavior of montmorillonite cation exchanged for ω-amino acids by ε-caprolactam, *J. Mater. Res.*, **1993**, 8, 1174.

Vaia, R. A.; Ishii, H.; Giannelis, E. P.; Synthesis and Properties of Two-Demensional Nanaocstructures by Direct Intercalation of Polymer Melts in layered Silicates. *Chem. Mater.*, **1993**, 5, 1694.

Vaia, R. A.; Teukolsky, R. K.; Giannelis, E. P.; Interlayer Structure and Molecular Environment of Alkylammonium Layered Silicates, *Chem. Mater.*, **1994**, 6, 1017.

Vaia, R. A.; Basudevan, S.; Kravied, W.; Scanlon, L. G.; Gannelis, E. P.; New polymer electrolyte nanocomposites: Melt intercalation of poly(ethylene oxide) in mica-type silicates, *Adv. Mater.*, **1995**, 7, 154.

Vaia, R. A.; Jandt, K. D.; Kramer, E. J.; Giannelis, E. P.; Microstructural evolution of melt intercalated polymer-orgnically modified layered silicates nanocomposites, *Chem. Mater.*, **1996**, 2628.

van Koten, G.; Vrieze, K.; in Stone FGA, West R editors, *Advanced Organometallic Chemistry*, vol.21, New York: Academic Press , **1982**, p. 151.

Wang, W.; Li, L.; Xi, S.; A Fourier Transform Infrared Study of the Coagel to Micelle Transition of Cetyltrimethylammonium Bromide, *J. Colloid Interface Sci*., **1993**, 155, 369.

Wang, Z.; Pinnavaia, T. J.; Nanolayer reinforcement of elastomeric polyurethane, *Chem. Mater*., **1998**, 10, 3769.

Webb, S. W.; Weist E. L.; Chiovetta, M. G.; Laurence, R. L.; Conner, W. C.; *Can. J. Chem. Eng*., **1991**, 69, 665.

Weimer, M. W.; Chen, H.; Giannelis, E. P.; Sogah, D. T.; Direct synthesis of dispersed nanocomposites by in-situ living free radical polymerization using a silicate-anchored initiator, *J. Am. Chem. Soc.*, **1999**, 121, 1615.

Weiss, A.; Organic derivatives of mica-type layer silicates, *Angew. Chem. Inter. Ed*., **1963**, 2, 134.

Weiss, K.; Wirth-Pfeifer, C.; Hofmann, M.; Botzenhardt, S.; Lang, H.; Bruning, K.; Meichel, E.; Polymerisation of ethylene or propylene with heterogeneous metallocene catalysts on clay minerals, *Journal of Molecular Catalysis A: Chemical*, **2002**, 182-183, 143.

Wendy, L.; Frans, H. J. M.; Patric, J.; Melt-compounded salt-containing poly(ethylene oxide)/clay nanocomposites for polymer electrolyte membranes, *Polymer*, **2005**, 46, 7334.

White, D. M.; Stereospecific Polymerization in Urea Canal Complexes, *J. Am. Chem. Soc*., **1960**, 82, 5678.

Worall, W. E.; Clays: their nature, origin and general properties, Maclaren & sons, London (**1968**)

Wrana, C.; Reinartz, K.; Winkelbach, H. R.; Therban, Ò.; The High Performance Elastomer for the New Millennium, *Macromol. Mater. Eng*., **2001**, 286, 657.

Wu, C. R.; Liedberg, B.; Infrared Reflection-Absorption Spectroscopy of Polyacrylonitrile on Copper and Aluminium Surfaces, *J. Polym. Sci.: Part B: Polym. Phys*., **1988**, 26, 1127.

Wu, F.; Foley, S. R.; Burns, C. T.; Jordan, R. F.; Acrylonitrile Insertion Reactions of Cationic Palladium Alkyl Complexes, *J. Am. Chem. Soc*., **2005**, 127, 1841.

Xie, W.; Gao, Z.; Pan, W.; Hunter, D.; Singh, A.; Vaia, R.; Thermal Degradation Chemistry of Alkyl Quaternary Ammonium Montmorillonite, *Chem. Mater*., **2001**, 13, 2979.

Yamamoto, A.; Ikeda, S.; A Coordination Compound of Diethyldipyridylnickel with Acrylonitrile, A polymerization catalyst of Acrylonitrile, *J. Am. Chem. Soc*., **1967**, 89, 5989.

Yamamoto, T.; Yamamoto, A.; Ikeda, S.; Organo (dipyridyl) nickel complexes. I. Stability and activation of the alkyl-nickel bonds of dialkyl (dipyridyl) nickel by coordination with various substituted olefins, *J. Am. Chem. Soc*., **1971**, 93, 3350.

Yamamoto, T.; Yamamoto, A.; Ikeda, S.; Study of Orano(dipyridyl)nickel Complexes. II. Stabilities of Olefin-Nickel Bonds in Olefin-Coordinated Dipyridylnickel and Dialkyl (dipyridyl) nickel Complexes, *J. Am. Chem. Soc*., **1971**, 93, 3360.

Yang, P.; Chan, B. C. K.; Baird, M. C.; Is $FeEt_2$(2,2'-dipyridyl)$_2$ a Ziegler Catalyst for Polymerization of the Polar Monomer Acrylonitrile, *Organometallics*, **2004**, 23, 2752.

Ye, Z.; Zhu, S.; Wang, W.-J.; AlSyouri, H.; Lin, Y. S.; "Morphological and mechanical properties of nascent polyethylene fibers via ethylene extrusion polymerization with MCM-41 supported metallocene catalyst", *Journal of Polymer Science, Part B, Polymer Physics*, **2003**, 41, 2433.

Zambelli, A.; Ammendola, P.; Grassi, A.; Longo, P.; Proto, A.; 13C-Enriched end groups of polypropylene and poly(1-butene) prepared in the presence of bis(cyclopentadienyl) titanium diphenyl and methylalumoxane, *Macromolecules*, **1986**, 19, 2703.